In vivo identification of brain structures functionally involved in spatial learning and strategy switch
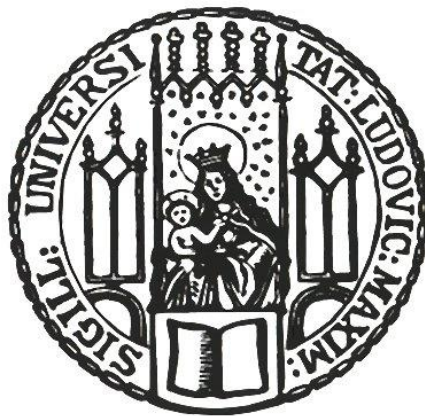
Dissertation der Fakultät für Biologie

der Ludwig-Maximilians-Universität München

Suellen de Almeida Corrêa

München 2018

In vivo identification of brain structures functionally involved in spatial learning and strategy switch

Diese dissertation wurde angefertigt unter Leitung meines Doktorvaters
PD Dr. rer. nat. Carsten T. Wotjak am Max-Planck Insitut für Psychiatrie und der
Ludwig-Maximiliam-Universität München.

Erstgutachter: PD Dr. rer. nat. Carsten T. Wotjak

Zweitgutachter: Prof. Dr. Christian Leibold

Tag der Abgabe: 17.10.2018

Tag der mündlichen Prüfung: 28.03.2019

ERKLÄRUNG

Ich versichere hiermit an Eides statt, dass meine Dissertation selbständig und ohne unerlaubte Hilfsmittel angefertigt worden ist.

Die vorliegende Dissertation wurde weder ganz, noch teilweise bei einer anderen Prüfungskommission vorgelegt.

Ich habe noch zu keinem früheren Zeitpunkt versucht, eine Dissertation einzureichen oder an einer Doktorprüfung teilzunehmen.

München, den 29.03.2019

Suellen de Almeida Corrêa

To A.C.A., A.C. and J.D., with love.

CONTENTS

LIST OF FIGURES

LIST OF TABLES

ABBREVIATIONS

2-DG   2-deoxyglucose

AP   antero-posterior

BLA   basolateral amygdala or basal-lateral amygdala

BMA   basomedial amygdala

BST   bed nuclei of the stria terminalis (also referred to as BNST)

BOLD   blood oxygen level dependent signal

CA1   Cornu Ammonis 1

CA3   Cornu Ammonis 3

ChR2   channel-rhodopsin2

CNO   clozapine N-oxide

DAPI   4',6-diamidino-2-phenylindole

DG   dentate gyrus

dHPC   dorsal hippocampus

DMSO   dimethyl sulfoxide

DREADD   Designer Receptor Exclusively Activated by Designer Drug

DV   dorso-ventral

E   east

ECT   ectorhinal area (cortex)

ENTl   entorhinal area (cortex) – lateral part

FDR	false discovery rate
FG	fluorogold
FL	free learning
fMRI	functional magnetic resonance imaging
FWE	family wise error
GECIs	genetically encoded calcium indicators
GFP	green fluorescent protein
GR	glucocorticoid receptor
HC	home cage
HPC	hippocampus
IC	inferior colliculus
IEG	immediate early gene
IHC	immunohistochemistry
IL	infralimbic area (cortex)
i.p.	intraperitoneal
ISH	*in situ* hybridization
ITI	inter-trial interval
L	left
LS	lateral septal nucleus
MEMRI	manganese enhanced magnetic resonance imaging
ML	medial-lateral
MOB	main olfactory bulb

mPFC	medial prefrontal cortex
MPI	Max Planck Institute
MR	mineralocorticoid receptor
MRI	magnetic resonance imaging
MWM	Morris water maze
N	north
NGS	normal goat serum
NMDA	N-methyl D-aspartate
OFC	orbitofrontal cortex
ORB	orbital area (also referred to as orbital frontal cortex, OFC)
PAG	periaqueductal gray
PBS	Phosphate-Buffered Saline
PERI	perirhinal area (cortex)
PET	positron emission tomography
PFA	paraformaldehyde
PFC	prefrontal cortex
PIR	piriform area (cortex)
PL	place learning
PrL	prelimbic area (cortex)
R	right
RL	response learning
ROI	region of interest

RSP   retrosplenial area (cortex)

S   south

SNr   substantia nigra, reticular part

SSp-bfd   primary somatosensory area – barrel field (also referred to as barrel cortex)

vHPC   ventral hippocampus

VIS   visual area (cortex)

VPM   ventral posteromedial nucleus of the thalamus

W   west

WCM   water cross maze

YFP   yellow fluorescent protein

ABSTRACT

Spatial learning is a complex behavior which includes, among others, encoding of space, sensory and motivational processes, arousal and locomotor performance. Today, our view on spatial navigation is largely hippocampus-centrist. Less is known about the involvement of brain structures up- and downstream, or out of this circuit. Here, I provide the first *in vivo* assessment of the neural matrix underlying spatial learning, using functional manganese-enhanced MRI (MEMRI) and voxel-wise whole brain analysis. Mice underwent place-learning (PL) vs. response-learning (RL) in the water cross maze (WCM) and its readout was correlated to the Mn^{2+} contrasts. Thus, I identified structures involved in spatial learning largely overlooked in the past, due to methods focused on region of interest (ROI) analyses. These structures include several sensory-related structures and differ between place-learners and response-learners, with the former (PL) comprising mostly structures involved in different properties of visual processing, such as horizontal gaze (e.g. nucleus prepositus) and saccade (e.g. fastigial nucleus), or provide vision-input and eye movement information from parahippocampal (e.g. presubiculum, perirhinal, postrhinal and ectorhinal areas) and other regions (e.g. orbital area, superior colliculus and vestibular ocular-reflex from the vestibular nucleus) likely to head-direction, grid- and place-cells; and the latter (RL) presenting structures related to more basic rodent sensory computations, like odor (e.g main and accessory olfactory bulb, cortical amygdala, piriform, endopiriform and postpiriform areas) and acoustic stimuli representation (e.g. auditory area, nucleus of the lateral lemniscus and superior olivary complex), or sensory-motor properties, such as body representation (e.g. somatosensory area – upper limbs) and head-direction signal. Add-on experiments pointed to preferential Mn^{2+} accumulation towards projection terminals, suggesting that our mapping was mostly formed by projection sites of the originally activated structures. This is corroborated by in-depth analysis of MEMRI data after WCM learning showing mostly downstream targets of the hippocampus. These differ between fornical

afferences from vCA1 and direct innervation from dCA1/iCA1 (for PL), and structures along the longitudinal association bundle originating in vCA1 (for RL).

To elucidate the pattern of Mn^{2+} accumulation seen on the scans, I performed *c-fos* expression analyses following learning in the WCM. This helped me identify the structures initially activated during spatial learning and its underlying connectivity to establish the matrix.

Finally, to test the causal involvement of selected structures from our previous findings I inhibited them (through DREADDs) while mice performed the WCM task. I also focused on the causal involvement of the vHPC-mPFC circuit on strategy switch during WCM learning.

I believe that this study might shed light into new brain structures involved in spatial learning and strategy switch and complement the current knowledge on these circuits' connectivity. Moreover, I elucidated some functional mechanisms of MEMRI, clarifying the interpretation of data obtained with this method and its possible future applications.

ZUSAMMENFASSUNG

Räumliches Lernen ist ein komplexes Verhalten, das die Kodierung der Umgebung, Motivations- und sensorische Prozesse, Arousal und Fortbewegung umfasst. Unsere heutige Sicht auf räumliche Navigation ist hauptsächlich Hippocampus-zentristisch. Über die Beteiligung von vor- und nachgeschalteten Hirnstrukturen oder solche, die nicht Teil dieses Schaltkreises sind, ist weit weniger bekannt. Unter der Nutzung von funktioneller manganverstärkter Magnetresonanztomographie (Functional Manganese-Enhanced MRI (MEMRI)) und voxelweiser Analyse des ganzen Gehirnes, lege ich die erste *in vivo*-Untersuchung der neuronalen Matrix, die dem räumlichen Lernen bei Mäusen zugrunde liegt, vor.

Mäuse durchliefen im Water Cross Maze (WCM) zwei Strategien: räumliches Lernen (place learning (PL)) und sensomotorisches Lernen (response learning (RL)). Die Ergebnisse wurden mit den Mangankationkontrasten (Mn^{2+}) korreliert. Ich konnte Hirnstrukturen identifizieren, die am räumlichen Lernen beteiligt sind. Diese wurden in der Vergangenheit unter der Nutzung von Methoden, die auf der Analyse von zuvor ausgewählten Interessenregionen (ROIs) basieren, weitgehend übersehen. Diese Regionen umfassen mehrere sensorische Strukturen, die sich zwischen räumlichem Lernen und sensomotorischem Lernen unterscheiden. Erstere (PL) umfassen hauptsächlich Strukturen, die an verschiedenen Eigenschaften der visuellen Verarbeitung beteiligt sind, wie zum Beispiel dem horizontalen Blick (z.B. Nucleus praepositus) und Sakkaden (z.B. Nucleus fastigii), oder eingehende visuelle Signale und Informationen zur Augenbewegung von parahippocampalen (z.B. Präsubikulum, perirhinalen, postrhinalen und ektorhinalen Regionen) und anderen Regionen (z.B. orbitaler Bereich, Colliculi superiores und Vestibular-Okular-Reflex von den Nuclei vestibulares) wahrscheinlich an sogenannte Head Direction Cells (Kopfrichtungszellen), Grid Cells (Rasterzellen) und Place Cells (Ortszellen) weitergeben. Letztere (RL) zeichnen sich durch Hirnstrukturen aus, die mit fundamentaleren sensorischen Verrechnungen bei Nagetieren zusammenhängen, wie Geruch (z.B. Haupt- und akzessorischem Riechkolben,

kortikale Amygdala, piriforme, endopiriforme und postpiriforme Regionen) und Repräsentationen von akustischen Signalen (z.B. auditorischer Bereich, Nukleus des Lemniscus lateralis und Nucleus olivaris superior) oder sensormotorischen Eigenschaften, wie Körperrepräsentation (z.B. somatosensorische Region – obere Gliedmaßen) und Kopfrichtungssignalen.

Zusätzliche Experimente weisen auf einen Trend zur Ansammlung von Mn2+ an den Projektionsterminalen hin, was darauf hindeutet, dass unsere Kartierung hauptsächlich auf Projektionsregionen der ursprünglich aktivierten Strukturen basiert. Dies wurde durch eine detaillierte Analyse der MEMRI-Daten, die nach dem Lernen im WCM entstanden, bekräftigt, da diese hauptsächlich nachgeschaltete Ziele des Hippocampus anzeigen. Diese unterscheiden sich zwischen fornikalen Afferenzen von vCA1 und direkter Innervation von dCA1/iCA1 (bei PL) und Strukturen entlang des longitudinalen Assoziationsbündels, das aus der vCA1 entstammt (für RL).

Um das Muster der Mn^{2+} -Ansammlung, das sich auf den Scans zeigt, zu erklären, habe ich eine Analyse von c-fos-Expression nach dem Lernen im WCM durchgeführt. Dadurch konnte ich zum anderen Strukturen identifizieren, die ursprünglich während des räumlichen Lernens aktiviert waren, einschließlich efferenter Hirnstrukturen.

Um schließlich einen kausalen Zusammenhang zwischen erhöhter neuronaler Aktivität und dem Verhalten herzustellen, habe ich ausgewählte Hirnstrukturen mit DREADDs inhibiert, während die Mäuse das WCM durchlaufen haben. Dies beinhaltete insbesondere die Rolle des vHPC-mPFC-Schaltkreises in Bezug auf Strategiewechsel während des WCM-Lernens.

Zusammengefasst gewährt diese Studie Aufschluss über neue Hirnareale, die eine Rolle in räumlichem Lernen und Strategiewechsel spielen und die den aktuellen Kenntnisstand über die Konnektivität dieser Schaltkreise ergänzen. Des Weiteren habe ich einige funktionelle Mechanismen von MEMRI aufgedeckt, die die Interpretation der mit dieser Methode erhaltenen Daten und ihre Anwendung in der Zukunft erleichtern werden.

1.   INTRODUCTION

Learning can be defined as the process through which subjects acquire and encode information, stored as new knowledge or skills, in order to elicit appropriate behavioral responses to further external inputs. The storage of information or experiences is the process termed memory (Squire, 1986). Learning and memory are interconnected cognitive processes that involve, among others, attention, arousal, sensory and motivational processes, synaptic plasticity, etc. These features may affect different types of learning and memory in distinct ways, as it will be discussed below.

Memory processes are segmented in different phases, namely: acquisition, consolidation, retention and retrieval. The acquisition phase is the moment when individuals compute information received from the environment, thus, when learning occurs. Consolidation is the initial storage of the information learned and retention is the maintenance phase of this process. Retrieval can be defined as the act of recollecting learned experiences.

Learning may be divided in different categories according to the type of stimuli presented (e.g. cognitive/declarative learning for new information and events or procedural learning for new motor actions) (Cohen et al., 1985), to the content of information acquired (e.g. fear learning or spatial learning), etc. Each different type of learning relies on specific brain structures and networks (for example see (Cho et al., 1999)), but it may share some common molecular processes. In this work we will focus on spatial learning.

1.1. Spatial learning and learning strategies

To explore the environment and orient oneself in different locations is of outmost importance for individual's success in life. Without the ability to navigate from one point to the other and knowing your way back, subjects would be limited to a small radius of exploration around their home base. This

would decrease their possibilities of foraging, mating, among others. Therefore, spatial navigation is an important ability conserved across several species.

Spatial learning enables animals to encode information of their surroundings, through representation of the spatial features of the environment in relation to each other and/or to the subject. In this way, animals can guide themselves to navigate different environments and learn relevant locations, increasing their success in searching for food, shelter, social and sexual partners and avoiding predators.

There are two main spatial learning strategies that co-exist among individuals: one cognitive and another habitual (Tolman et al., 1946). These strategies can be used in different situations where one or another would be optimal for the individual's success. On the one hand, cognitive spatial learning involves the formation of a cognitive map of the environment, allowing flexible navigation of the space from different start positions (O'Keefe and Dostrovsky, 1971; O'Keefe and Nadel, 1978). It counts on cues of the environment and the representation of the cues in relation to each other on that given context – an allocentric view (O'Keefe, 1991; Compton et al., 1997). This type of allocentric learning is also known as place learning (PL), as it uses the "place" or location of the cues as landmarks for the orientation of the subject. On the other hand, procedural spatial learning focuses on the representation of the self within a given context – an egocentric view (Cook and Kesner, 1988). The body representation of the subject, its direction and movements are the key features of this type of navigation (Matin and Li, 1995). For instance, the subject learns to turn right instead of heading west (as it would be the case for place learning) from a specific location to navigate to its target. As this egocentric learning is based on a motor response (body movement) of the subject relative to the environment, it is also known as response learning (RL).

On a first view, place learning might seem more advantageous, since it is flexible and allows individuals to navigate in an environment independently of their initial position. This holds true in many situations. However, if one has to navigate the same path multiple times, without any change in the environment, response learning might be more suitable, since it is easier to learn and

cognitively less demanding. This means that when adopting this learning strategy, the individual needs less attention and focus on the navigation task itself and it is free to respond to other inputs or even perform other tasks in combination. A shift from place to response learning after overtraining was already demonstrated to happen in rodents (e.g. (Packard and McGaugh, 1996; Chang and Gold, 2003; Colombo et al., 2003; Jacobson et al., 2012). Another scenario where response learning would be the preferable strategy over place learning is during stressful situations. If the individual is under stress it should reserve its attention to the possible threat, or stimuli causing distress, and should be able to readily escape from the unwanted situation. Therefore, response learning would be an advantageous strategy to use in this case. The shift from place to response learning strategies for individuals under stress was already shown for mice and human subjects (Packard and Wingard, 2004; Schwabe et al., 2007; Elliott and Packard, 2008; Schwabe et al., 2008; Schwabe and Wolf, 2009).

Place and response learning can also be differentiated considering the underlying brain structures involved in the performance of either strategy. While place learning is hippocampus-dependent (Becker et al., 1980), response learning is striatum-dependent (Cook and Kesner, 1988). Numerous studies have already confirmed these initial findings from rodents (Morris et al., 1982) in non-human primates (Rolls et al., 1997) and human subjects (Iaria et al., 2003), indicating that these learning strategies and their neural anatomical substrates are conserved across different species, including humans. However, other brain structures and networks that are involved in the performance of each specific strategy are not yet fully elucidated. Grid cells in the medial entorhinal cortex were already described to be an important input (Moser and Moser, 2008) and to work in concert with hippocampal place cells (Bush et al., 2014; Renno-Costa and Tort, 2017) in processing contextual information necessary for the formation of the cognitive map of the environment. Therefore, the medial entorhinal cortex is also a key structure for place learning. In contrast, since response learning is based on a strong body representation of the individual in the environment and its body movements within the space

where it is inserted, it is not surprising that the somatosensory and the motor cortices (McNaughton et al., 1994) are also implicated in this navigational strategy. The head direction cells in the retrosplenial cortex, pre- and parasubiculum also seem to be involved in the body orientation and directionality of the subjects performing response learning (Taube, 1998).

Nevertheless, most of the information regarding neuroanatomical bases of spatial learning in general or of either place- or response learning specifically, was acquired with lesions or inactivation studies of pre-defined brain regions or with *ex vivo analysis* of brain sections also focusing in candidate brain regions. More broad analyses of the whole brain *in vivo* are still missing, which can be partly ascribed to difficulties in analyzing learning processes over the course of repeated training and to the lack of appropriate methods which allow for a holistic view with sufficient spatial resolution.

1.2. Assessment of spatial learning and memory in mice

Spatial learning can be assessed in rodents through a number of tests, as the T-maze (Tolman et al., 1946), radial arm maze (Olton and Samuelson, 1976), the Barnes maze (Barnes, 1979) and the popular Morris water maze (MWM; (Morris, 1984)), to name a few. The _T-maze_ consists of three corridors (arms) displayed in a T shape with enclosure walls. Animals are placed inside the maze in the edge of the long arm of the T and are expected to find a food reward at the end of one of the other arms, left or right to the starting arm. On a classic protocol of this task, the spatial alternation test, the animals should alternate their visits to the arms so they will always get a reward (Tolman et al., 1946). This is a working memory test, since it counts on the animal's ability to remember the previously baited arm and navigate to the opposite arm on the next trial. The _radial arm maze_ is a more complex variation of the T-maze, given that it is usually composed of 8 arms (variable number) arranged in a radial orientation from the center area. The test counts on a similar principle of alternating among the arms to find the food reward. This test also assesses reference memory in addition to working memory. For this evaluation, after the

initial training for testing working memory, half of the arms in the maze should be baited in a fixed manner (always the same arms for a given subject) and the exploration behavior of the animals in the maze should be analyzed. If the animals visit unbaited arms this would count as a reference memory error, while revisiting previously baited arms would count as a working memory error (Wenk, 2001). The _Barnes maze_ takes advantage of the aversion rodents have for open and bright spaces, as it is composed of an open flat well-lit board with holes around its edge which the animals use to escape. Nonetheless, only 1 of the 20 holes (variable number) is an actual escape hole, and the animals have to learn the location of this target based on distal cues of the environment (Barnes, 1979). The _Morris water maze_ consists of a large round water tank filled with water at 23°C (+/- 1°C) with a submerged platform (in one of its main protocols) that the animals have to find using many possible navigational strategies. Given that mice avoid open spaces, as mentioned above, they usually prefer to stay close to the maze walls (at least initially), adopting a strategy named thigmotaxis – where they swim around the tank along the wall, sometimes repeating this circular movement multiple times. This strategy is highly stressful and not effective, since the escape platform is not positioned close to the wall and the animals do not learn the platform position by simply swimming along the wall and not encoding information of the environment. With training through multiple days, mice start to adopt different strategies, as random swim, scanning and chaining, that indicate that animals are less anxious about the open space of the tank, but still not actively using spatial cues to locate the platform (Ruediger et al., 2012). Only after an extensive training period, animals seem to use spatial strategies to guide themselves on the maze and find the escape platform (Ruediger et al., 2012). Another drawback of this task is that the solid walls of the maze do not allow animals to see the extra maze cues when swimming close to the enclosures. Moreover, animals can establish the distance of the platform and the wall as a landmark, instead of learning the real position of the platform within the environment (Baldi et al., 2003; Hamilton et al., 2009).

The tests described here are well established and informative to investigate many aspects of spatial learning. However, most of these tasks were developed for rats. Given that the behavior of mice and rats can be remarkably different, care should be taken when choosing an appropriate test for mice.

The water cross maze (WCM)

The water cross maze (WCM) is comprised of 4 arms arranged in a cross shape with a central area connecting the arms. The maze is filled with water up to 1.5 cm above a submerged escape platform located in the distal part of one of the arms. Since the arm opposed to the start arm is blocked with a guillotine door, the maze is transformed in a T maze adaptable for each trial, according to the start position of the animal. This maze combines high motivation to perform (i.e., escape from the water) with the corridor enclosures of the arms. In that way, the stress level of the animals is decreased compared to the open MWM and the number of possible strategies that can be used to perform is limited and easy to evaluate from day 1. Furthermore, the simplicity of the test allows for short trials, decreasing the time animals spend in the water. Since the task is not based on food rewards it does not require that the animals are food deprived, adding up to the argument of decreased stress load compared to other mazes. Moreover, the WCM is made of transparent acrylic glass walls, allowing the animals to see the whole surroundings of the maze and encoding distal cues independently of the animal's position in the apparatus. Therefore, this maze, which was established in the lab for mouse testing (Kleinknecht et al., 2012), is an optimal alternative to study different spatial navigation strategies in mice. Specially, this maze allows the experimenter to impose a specific training strategy (e.g. place learning or response learning) by adapting some features of the apparatus, such as start position, arm blockade placement and platform location, according to the intended protocol (for details please check *Materials and Methods*). Additionally, this task allows scoring of interesting behavioral measurements not possible to extract from other mazes (e.g. accuracy: percentage of correct trials within a day), given that trials can be

6

easily and objectively scored as correct or incorrect (see Materials and Methods).

1.3. **The "hippocampus centrist view" and beyond**

By means of lesion and pharmacological studies, *in vivo* recordings, among other methods, the hippocampus could be characterized as a fundamental brain structure involved in several types of learning , including allocentric spatial learning (Morris et al., 1982) – place learning –, and declarative episodic learning (learning of events) by humans (Squire, 1987, 1992). The description of cells that code for locations (place cells) in the hippocampus (O'Keefe, 1976) and other cell types involved in directionality (head direction cells) and different features of spatial coding (grid and border cells) in parahippocampal regions corroborates the importance of the hippocampus in spatial cognition. These spatial-related cells in parahippocampal regions serve, among other functions, as inputs for different categories of information to place cells, and functional modulation of these cells' activity disrupts place cells' coding, either leading to remapping or decreased spatial tuning (Fyhn et al., 2007; Monaco and Abbott, 2011).

Due to its leading role in spatial learning processing, the hippocampus became the main focus of many researchers studying learning and memory, and different brain structures that might contribute to these cognitive domains were simply overshadowed. We can refer to this problem as a conceptual bias. Thus, it would be informative to obtain a broader overview on brain structures implicated in spatial navigation, learning and memory other than hippocampus, preferentially at a whole brain level. This last point is also important to address due to a methodological bias which increases the single-structure analysis issue (hippocampus-centrist, in this discussion). Given that traditional methods to proof causal involvement of brain structures have restricted analysis of pre-defined regions this type of study-bias was only reinforced. Therefore, it is necessary to look at the brain in broader way. In that effort, we decided to

employ a whole-brain analysis, instead of localized approaches, to pin-point structures possibly related to different spatial learning strategies (e.g. place learning and response learning).

1.4. **Methods for functional imaging in mice**

In the following paragraphs I will go over some methods for functional imaging in mice, depicting their advantages and limitations. For a structured overview of these and other methods please see figure 1.

Analysis of immediate early genes (IEG), such as c-Fos and Arc is traditionally the method of choice for identification of structures involved in specific cognitive processes (Guzowski et al., 2005; Kubik et al., 2007; Sauvage et al., 2013). However, this method is only optimal for analyses performed after a limited number behavioral tasks, notably the ones acquired in a single or few trials, since (i) the activation of the IEG is transient (Shires and Aggleton, 2008; Barry and Commins, 2011) and (ii) mice may acquire the task with different learning profiles (Ohl et al., 2001) (i.e. a mouse may learn the task in 2 days, another mouse in 3, 4 or 5 days, etc). This makes it extremely difficult to define the cutting point for IEG analysis.

A more recent strategy to optimize IEG analysis is named Targeted Recombination in Active Populations (TRAP) (Guenthner et al., 2013). The method consists on the use of transgenic mouse lines that express the tamoxifen-dependent recombinase $CreER^{T2}$ in an activity dependent manner from the loci of the immediate early genes Arc or Fos. In the absence of tamoxifen recombination cannot occur in the cells because the $CreER^{T2}$ transgene will be locked in the cytoplasm. However, when tamoxifen is present Cre-mediated recombination is released and occurs in active cells expressing $CreER^{T2}$, which will then express the effector gene (usually a fluorophore) permanently. Thus, the activated cells will be marked ("TRAPed") by the expression of the fluorophore and can be further identified. This is an advantage to the traditional IEG analysis because it allows a temporal integration of the

8

activity marker expression (once "TRAPed" forever "TRAPed"), decreasing the chances of false positives due to delays of ideal time-point analysis with transient expression. The most used method for the identification of these cells is histology of brain slices under a fluorescence microscope. This relies on the pre-selection of candidate structures (ROIs) to be analyzed and might filter out other possibly interesting structures not listed for analysis. Another option for identification of "TRAPed" cells is the use of cleared brain approaches, such as the iDISCO (Renier et al., 2014) and Clarity (Chung and Deisseroth, 2013; Chung et al., 2013). However, these approaches are expensive, hard to implement and their semi-automatic analysis routines are still in their infancy, thus making it not easily accessible. Furthermore, all of these alternatives require the removal of the brain for analysis, blocking the possibility of longitudinal studies.

Another alternative to overcome the timing issue of IEG analysis would be to measure the accumulation of glucose derivatives (e.g. 2-deoxyglucose, 2-DG) (Bontempi et al., 1999). These metabolites can be used as radioactively labeled tracers and be later identified by autoradiography. An additional approach is based on measurements of changes in brain energy supply by cytochrome-c oxidase analysis (Miranda et al., 2006; Conejo et al., 2007).
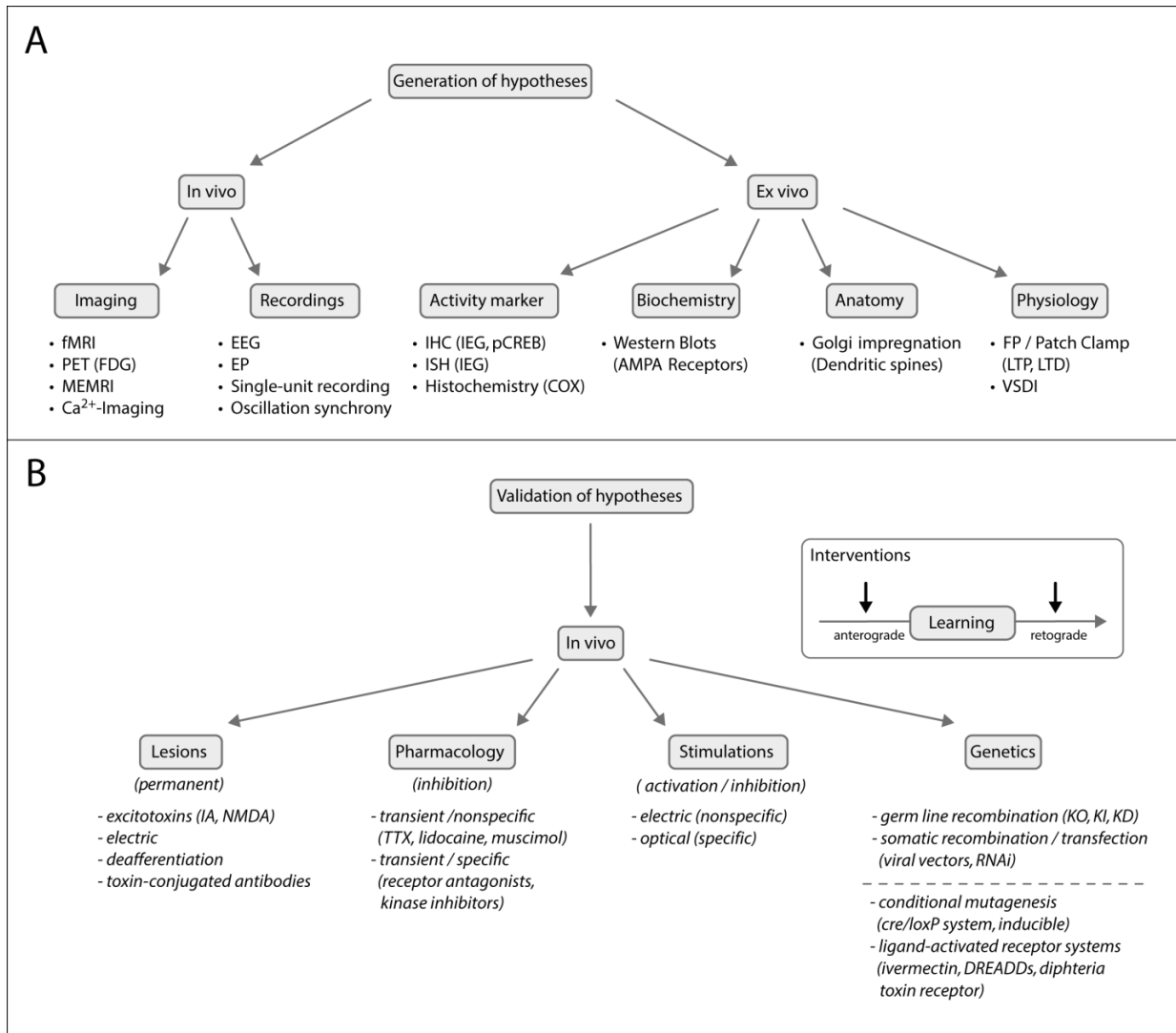
Figure 1: *Schematic overview of methods for identification (generation of hypotheses) and modulation (validation of hypotheses) of neuronal circuits related to given behavior outputs* (reproduced from (Wotjak and Pape, 2013))

None of these methods provides *in vivo* functional assessment of the neuroanatomical substrates of spatial learning. One way to overcome this limitation would be the use of functional magnetic resonance imaging (fMRI). However, to perform fMRI in mice one needs to anesthetize the animals, which leads to brain activity alterations due to the different state of arousal, therefore, compromising the acquired data. Additionally, the classical functional analysis of MRI requires that the task or manipulation of interest is performed in parallel to

the scanning procedure, while the subjects are inside the scanner. Needless to say that this is not suitable for our investigation of behaving animals performing a spatial learning task in the water cross maze.

Modern techniques as 2-photon microscopy (Denk et al., 1994) combined with calcium imaging (Carter and Sabatini, 2004; Yasuda et al., 2004) might come to mind when considering alternative tools for functional imaging of neurons in mice. The latter technique is based on the property of neuronal Ca^{2+} intake upon cellular activation (Cummings et al., 1996). With the recent development of genetically encoded calcium indicators (GECIs; e.g. GCaMPs; (Hires et al., 2008; Sun et al., 2013; Lin and Schnitzer, 2016), it became possible to observe neuronal calcium events (a proxy of action potential firing) online under a microscope, given that the indicators emit fluorescence upon changes in cellular Ca^{2+} concentration. These events can be monitored with high temporal and cellular resolution, allowing a precise analysis of individual neuronal activation state. Moreover, these calcium indicators can be genetically targeted to a specific neuronal population of interest (Tian et al., 2012), refining the study. Nevertheless, this tool also has its limitations. Namely, 2-photon imaging is an invasive method that requires the removal of brain tissue above the area to be imaged (Attardo et al., 2015). This also limits the depth of the region of study and the choice of this region, given that the removal of some cortical regions might cause tremendous behavioral and motor alterations (e.g. (Barth et al., 1982; Jeannerod et al., 1994; Peterson and Arezzo, 1994). Additionally, a major challenge to employ this technique to our investigations is the spatial window limitation. As we discussed before, our aim is to have a whole brain analysis of neuronal activity, and the use of the 2-photon microscopy for calcium imaging would limit our study to pre-defined regions of interest of few mm^3.

Another technique developed for brain-wide functional analysis is the positron emission tomography (PET) (Depresseux, 1977). PET is a nuclear medicine technique used to image cellular glucose metabolism employing radiotracers (e.g ^{18}F-FDG). This is a well-established and highly used tool for

imaging human subjects. It can be applied on pathophysiology studies (e.g. detection of tumors or alteration in brain blood flow) (Schelbert, 1985; Goldman et al., 1997) or functional analysis of sensory stimuli in healthy individuals (Reivich et al., 1983). However, its low spatial resolution for small animals, as mice, limits its use in pre-clinical research. Nevertheless, PET is employed in studies investigating tau-protein aggregates in mouse models of Alzheimer disease (e.g. (Brendel et al., 2016)) and blood flow and metabolic alterations caused by infections (e.g. (Buursma et al., 2005; Weinstein et al., 2014) or neuroinflammation (e.g. (Semmler et al., 2008)) in rodents, to name a few. In the past two decades, there has been an effort to overcome the poor resolution issue with the development of different radiotracers (e.g. (Dedeurwaerdere et al., 2009; Andres et al., 2012; Schrigten et al., 2012) and special scanners for this purpose (e.g. (Chatziioannou et al., 1999; Del Guerra and Belcari, 2002; Tai et al., 2003). Unfortunately, the advances in the field were still not sufficient to achieve desirable imaging resolution to anatomically identify structures in the mouse brain with high confidence. Moreover, similar to fMRI, perfusion- or glucose-based PET is usually acquired in the sedated animal, further limiting its use in animal research. Furthermore, the rather short half-life time of the tracer does not permit the accumulation of the signal over the course of extended training protocols.

An interesting approach to circumvent all the limitations described here is the combination of MRI with an activity tracer that acts both as a functional activity marker and as a contrast enhancer, improving the resolution of the acquired images. This approach was established for rodents using manganese ions (Mn^{2+}) as the activity tracer, exploiting its biophysical similarity to Ca^{2+}, which allows its entrance in active neurons through calcium channels. This technique is named manganese-enhanced magnetic resonance imaging (MEMRI).

Manganese enhanced magnetic resonance imaging (MEMRI)

The need to non-invasively analyze brain morphology and function *in vivo* led to the development of magnetic resonance imaging (MRI). This method was first developed for human subjects and later adapted to non-human primates and rodents (Denic et al., 2011). MRI is based on the physical properties of hydrogen nuclei, which are ubiquitous present in animal soft tissue due to its high water content, to interact with magnetic fields. That is, when exposed to an external magnetic field hydrogen nuclear spins interact with it by adapting two different energy states. Using external radiofrequency pulses, these energy states can be perturbed, and spins will return to their equilibrium state by two fundamental relaxation processes: longitudinal relaxation and transverse relaxation, represented by the relaxation times T_1 and T_2, respectively. The response of the nuclear spins can be recorded by the receiver coil of the scanner and will eventually form an image of the body or organ under study (Schröder and Faber, 2011). The values of the relaxation times (T_1 and T_2) are constant to a given tissue in physiological conditions and may differ among tissues. For that reason, they are also referred to as time constants of specific tissues. The distinct time constants of different tissues result in different image contrasts, allowing the segregation and identification of different structures within the sample. Pathological conditions, such as the presence of tumors alter the concentration of water and/or lipids of the tissue, therefore also altering its time constants, leading to a modification of its contrast acquired by MRI. For that reason, MRI is a valuable clinical tool to assess pathological alterations in tissue, such as to detect tumors. Moreover, MRI can also detect brain function (functional MRI or fMRI) using blood oxygen levels as a hallmark of cellular activity. Thus, brain structures with higher blood oxygen level dependent (BOLD) signal would be detected as more active at that specific time point and could be correlated to specific actions performed by the subject at that moment. This is a vastly used and popular method which can be applied in diverse investigations of brain function and possibly related behaviors. However, as discussed in the previous section, technical limitations, such as the need to perform the task of interest inside the scanner and the required immobility of

the subject's head (mandatory anesthesia for mice) during scanning, do not allow us to implement this method in our investigation. An alternative approach that fits all our technical demands is manganese-enhanced MRI (MEMRI).

MEMRI has the potential to non-invasively map whole-brain activity and identify structures possibly related to a specific task (Chen et al., 2007; Bissig and Berkowitz, 2009; Eschenko et al., 2010; Bangasser et al., 2013; Chen et al., 2013; Hoch et al., 2013; Tang et al., 2016; Laine et al., 2017) since Mn^{2+} enters active neurons through voltage-gated calcium channels (Drapeau and Nachshen, 1984) (e.g., $Ca_v1.2$; (Bedenk et al., 2018)), and is transiently kept intracellularly (Gavin et al., 1990). Mn^{2+} shortens the T1 relaxation time of water (Spiller et al., 1988; Nordhoy et al., 2004) leading to a contrast increase in T_1-weigthed images (Pautler and Koretsky, 2002). Brain structures that accumulate Mn^{2+} can be detected as hotspots in T_1-weighted images, indicating higher neuronal activity in these areas (Lin and Koretsky, 1997). This technique modality is also referred to as activation-induced manganese-dependent MRI (AIM-MRI) (Tambalo et al., 2009). If the integrity of the blood-brain barrier is disrupted, even dynamic accumulation of Mn^{2+} can be observed in a single experimental session (DAIM-MRI) (Aoki et al., 2002).

MEMRI is also used for tract-tracing (for review see (Pautler et al., 2003)), since Mn^{2+} can be axonally transported to neuronal terminals after local $MnCl_2$ administration (Sloot and Gramsbergen, 1994; Pautler et al., 1998), revealing the underlying circuitry of the injection target. During this process, Mn^{2+} may cross one or more synapses (Pautler et al., 1998). We have recently shown that Mn^{2+} preferentially accumulates in projection terminals of the active entrance sites after systemic $MnCl_2$ administration (Bedenk et al., 2018). This feature of Mn^{2+} allows for the combination of activity-induced dissection of structures related to a specific behavior, and the connectomics analysis of the neuronal pathways underlying these brain structures. In that way, MEMRI does not only provide a snapshot of the structures active in response to a given task, but also reveals the downstream connectivity of these brain structures. This results in a functional connectivity map. Furthermore, the possibility of scanning the same

animals at different time points allows for dynamic investigations of the functional circuitry in a within-subject fashion, thus reducing the number of required subjects while increasing the power of such studies (thus subserving the 3-Rs principle for ethical use of animals in testing).

Despite those features, MEMRI is still not widely used, partially due to risk of potential toxic side effects, but also due to insufficient information regarding Mn^{2+} dynamics in the brain, confounding the interpretation of the results. Some properties, such as activity dependent entrance into cells via voltage-gated calcium channels (Drapeau and Nachshen, 1984), transient intracellular storage (Gavin et al., 1990), and preferential accumulation in projection terminals (Bedenk et al., 2018) have previously been reported. However, other properties such as the influence of neuronal activity state on intracellular Mn^{2+} storage and axonal transport have been debated in the literature with inconclusive findings. Therefore, a more explicit description of Mn^{2+} dynamics in the brain is still lacking and needs to be investigated.

1.5. Causal involvement of brain structures in given functions and modulation of neuronal circuits

In order to identify structures possibly involved in a specific action-outcome one needs to carefully tell apart correlation from causality. Correlation might suggest involvement but does not imply causality. Two correlated factors (A and B) might be caused by a third one (C) not causally connecting the two first. In this case, C causes A and also causes B. So, C and A are causally involved, and C and B as well, but A and B are not. The correlation between factors A and B might be positive or negative, depending on how C affects each of the individual factors. Therefore, one can extract possible candidate factors (effectors or outcomes) from correlations but needs to analyze each factor independently in order to check for causality. In the framework of neuroscience, causality (is the structure of interest necessary, essential or only sufficient?) might be tested by manipulations of brain activity of certain structures and/or neuronal populations and analyses of its outcomes, as it will be discussed in the

following paragraphs. For a structured overview of the methods presented below (and others) please see figure 1.

The first attempts to identify brain structures putatively involved in given functions (cognitive, motor, etc) employed mechanical lesion techniques (e.g. stab wounds or surgical extraction) (e.g. (Lashley, 1950)) of the structure under study. The crudeness of these methods made it difficult to establish the implications of the specific structures since it affected many other regions of the brain, either directly by co-removal or de-afferentiation (McWiliams and Lynch, 1978), or indirectly by compensatory mechanisms or inflammation secondary to the lesion (Dusart and Schwab, 1994). Nevertheless, valuable information, such as the involvement of the hippocampus in memory formation, could be acquired by the pioneer studies of Brenda Milner with a famous neuroscience subject in history, Henry Molaison (H.M.; 1926-2008), whose hippocampi (and parahippocampal regions) were surgically removed for treating a persistent case of temporal lobe epilepsy (Augustinack et al., 2014). Interestingly, H.M. could not form new explicit memories from the day of his surgery, but had his past and implicit memories unaffected (Milner and Penfield, 1955; Scoville and Milner, 1957; Penfield and Milner, 1958). This indicated that the hippocampus was fundamental for retaining new information, but it was not necessary for the storage of previous experiences. However, this successful case of investigation of brain function through removal of a specific structure is an exception, and the methods for such types of studies are constantly evolving to make the manipulations as specific and controlled as possible.

Following-up after the mechanical lesion methods previously used, electrolytic and excitotoxic lesions (e.g. (Agid et al., 1974)) were also employed (and are still, currently) for the inactivation of specific brain structures. The main principal of these methods is the functional inactivation (silencing) of a given brain region by the local administration of a current or excitotoxin, respectively for each method, which will alter the intracellular balance of the neurons leading to cell death. Some examples of commonly used excitotoxins are ibotenic acid and N-methyl-D-aspartate (NMDA) (Winn et al., 1984; Wang et

16

al., 1991). Despite its extensive use, these methods lack precision since the extent of the lesion caused by these manipulations is hard to limit and define, and the lesions are nonspecific in their effects on different cell types. Furthermore, these interventions may cause inflammation in brain regions far from but connected to the lesion site (Block et al., 2005). Additionally, electrolytic lesions might also affect traversing fibers from other brain regions near the lesion site (Kirby et al., 2012). Moreover, the lesions caused by these methods are permanent.

Aiming at reversibility of the manipulations the pharmacological approach was developed. With pharmacological inactivation (also referred to as pharmacological lesion or transient lesion) silencing of the brain region of interest is transient (variable duration from minutes to hours depending of the drug used), allowing longitudinal studies and within-subject comparisons, on top of decreasing possible compensatory mechanisms. However, the temporal control of this manipulation might not be ideal for many types of investigations and the drugs used might affect different neuronal populations. Also, these manipulations might be hard to delineate and limit to the target region. In addition, despite the transient aspect of the interventions, these approaches might be problematic when repeated treatment is necessary, given their extended invasive nature which causes tissue trauma.

Lesions and pharmacological inactivation result in a more or less complete omission of neuronal activity in the target brain structures. But, how could one study the impact of increased neuronal activity? Until some years ago, this was virtually impossible. However, a recently developed technique, named optogenetics (Deisseroth, 2011), allows performing such investigations. Optogenetics employs light-activated proteins (rhodopsins) extracted from algae, or bacteria, which can work as a switch (on or off) of neuronal activity. The rhodopsin genes can be either inserted in viral vectors to be injected in target brain structures or be genetically encoded in transgenic mouse lines (e.g. Nex-Cre-ChR2, used in this work). The transfected cells carry rhodopsins and can be controlled by specific focal light stimulation with so far unprecedented

temporal (millisecond scale) and spatial precision. Moreover, the rhodopsins might be targeted to specific cell-types, depending of the promotor of the viral vector or specific transgenic mouse line. Even though optogenetics is an elegant technique it has also some limitations. Its modulation effect is mostly categorical, i.e. neuronal activity is either turned on or off, with few gradual states. Moreover, the light is delivered by a focused light beam, which has a small diameter (approximately 200 μm), making it difficult to be employed for the analysis of bigger areas or entire brain structures. Furthermore, the laser stimulation also creates an artificial synchronized activity in the target areas, which is not necessarily present under natural conditions. Lastly, this it is an invasive technique, requiring the implantation of an optical fiber above the target area.

A novel pharmacogenetic (also referred to as chemogenetics) tool may help to overcome these disadvantages: Designer Receptor Exclusively Activated by Designer Drug (DREADDs) (Armbruster et al., 2007; Farrell and Roth, 2013; Roth, 2016). This technique is based on mutated G protein-coupled muscarinic receptors, which are selectively activated by a designer drug, clozapine-N-oxide (CNO), but not by endogenous acetylcholine. This allows the non-invasive modulation of cell activity in a bidirectional manner (depending on the type of receptor, activator or inhibitor). Another advantage of the DREADDs is the control of the cell activity in a gradual manner, not only by switching on or off. Moreover, it allows the experimenter to affect larger brain structures and even multiple brain structures at the same time, either by targeting it by viral vector injections or in a cell type specific manner with transgenic mouse lines (Roth, 2016).

The different techniques described here might be useful to answer multiple questions related to the causal involvement of specific brain structures in a given behavior, for example. However, it is important to note that these artificial manipulations (specially the activation) only inform us of what the brain structure or neuronal populations might do and not what they really do in physiological situations. Therefore, one needs to be careful with the

interpretation of such results and should not overlook the fact that the brain is a complex and integrated organ that needs all its parts to work well and timed in order to keep balance and produce normal behavior.

One possible interesting target for neural manipulation and causal testing of its involvement on spatial cognition is the medial prefrontal cortex (mPFC) and two of its main pathways mPFC-HPC and mPFC-BLA, as described below.

1.6. The medial prefrontal cortex and basolateral amygdala involvement in strategy switch

The prefrontal cortex (PFC) is involved in a variety of cognitive functions, such as decision making (for review see (Euston et al., 2012)), attentional processing (Dalley et al., 2004; Kesner and Churchwell, 2011), working memory (for review see (Funahashi and Kubota, 1994; Jones, 2002)) and goal directed behavior (Feierstein et al., 2006) Interestingly, the PFC is not a homogeneous structure and is divided in several sub-regions along its dorsal-ventral axis (Delatour and Gisquet-Verrier, 2000). These are anatomical distinct sub-regions which sub-serve specific functional properties (Cook and Kesner, 1988; Seamans et al., 1995; Heidbreder and Groenewegen, 2003; Cassaday et al., 2014; Hardung et al., 2017). In the spatial learning framework, different prefrontal sub-regions of rodents, as the orbitofrontal cortex (OFC) and the pre- (PrL) and infralimbic (IL) cortices were already described to be involved in distinct processes of behavioral flexibility. More specifically, the OFC mediates reversal learning of a previously acquired rule (McAlonan and Brown, 2003), while the medial PFC (mPFC) regions PrL and IL are necessary for strategy switch (or rule shift) (Ragozzino et al., 1999; Rich and Shapiro, 2007) but not for reversal learning (Ragozzino et al., 1999). This means that the OFC mediates learning of a new location target (e.g. escape platform or reward location in a maze), using the same rule as used to learn the old location. In contrast, the mPFC mediates learning of a new rule to find the novel location target (e.g. a place strategy instead of response strategy).

The mPFC receives direct innervation from the hippocampus (Jay and Witter, 1991; Thierry et al., 2000; Hoover and Vertes, 2007) and it modulates learning and memory (Doyere et al., 1993) by altering hippocampal computations, such as place field spatial tuning and stability (Kyd and Bilkey, 2003). Therefore, the mPFC seems to coordinate information received from the hippocampus and inhibit associations that are no longer relevant for the situation, allowing adaptation of behavior (Oualian and Gisquet-Verrier, 2010) – also known as behavioral flexibility. Lesions or inactivation of the mPFC do not affect learning of a rule (Ragozzino, 2007) but lead to perseverance in an outdated strategy (Ragozzino et al., 1999; Block et al., 2007), decreasing performance success when the requirements of the environment are changed. Recordings of mPFC neurons confirm their selective coding of strategy switches (Rich and Shapiro, 2009).

The basolateral nucleus of the amygdala (BLA) is also involved in the shift of different spatial navigation strategies. As mentioned before, during stressful situations, or upon anxiogenic drugs administration, mice and men tend to adopt response-based strategies more frequently then place-based strategies when given free choice (Packard and Wingard, 2004; Elliott and Packard, 2008; Schwabe et al., 2008). It was already described that corticosteroids and concurrent noradrenergic activation are responsible for this unidirectional shift (Schwabe et al., 2010c; Schwabe et al., 2010a). The release of stress hormones and its binding to glucocorticoid receptors (GR) and mineralocorticoid receptors (MR) in response to stress exposure (Schwabe et al., 2010b; Vogel et al., 2016) alter functional connectivity of brain networks favoring striatal pathways (that support response learning) in detriment of hippocampal pathways (that support place learning) (Schwabe et al., 2013; Vogel et al., 2015). This functional connectivity shift is mediated by the BLA (Packard et al., 1994; Kim et al., 2001; Elliott and Packard, 2008), which is anatomically connected to both hippocampus (for review see (Pitkanen et al., 2000; McDonald and Mott, 2017)) and striatum (Kita and Kitai, 1990), and is where the interaction between glucocorticoids and noradrenaline takes places (Schwabe et al., 2010a). Thus,

the BLA is a key modulator structure of different memory systems and fundamental for the switch of learning strategies under stress.

When trained to find a hidden reward in a dry maze, animals generally have an initial preference for allocentric strategies (place learning) and tend to switch for habitual strategies (response learning) with extensive training (Packard and McGaugh, 1996; Chang and Gold, 2003; Colombo et al., 2003; Jacobson et al., 2012). In contrast, the opposite is observed when dual solution water based tasks are used (Kleinknecht et al., 2012; Asem and Holland, 2013). There are speculative reasons for these opposing behaviors observed with the two different types of spatial tests: (i) is perhaps due to the stress caused by the water, leading to a shift to the preferable use of response learning; (ii) by the need to search in a broader way for food (hidden in diverse locations, in a real-life setting), requiring the formation of a cognitive map of the environment, in comparison to the need of an immediate response to escape from water (Asem and Holland, 2013). Independently of the reasons behind it, the mechanisms supporting this switch during learning of the tasks are still not known.

Despite all the information of the involvement of the mPFC and the BLA on strategy switch after initial learning, when the requirements of the environment change, the possible roles of these structures on strategy switch during initial learning are still not described.

1.7. **Aim and objectives**

The aim of this study was to identify the brain structures involved in different spatial learning strategies in mice *in vivo* in a whole brain voxel-wise manner.

More specifically, we had the following objectives:

1. Investigate Mn^{2+} dynamics (neuronal activity-dependent entrance, accumulation and transport) in the mouse brain using manganese-enhanced MRI (MEMRI);

2. Visualize *in vivo* with MEMRI, in a whole brain voxel-wise manner, the brain structures involved in learning in the water cross maze (WCM) through either place learning (PL) or response learning (RL) strategies;

3. Functionally test selected brain structures (identified in the previous objective) through neuronal activity manipulation (stimulation/inhibition) via chemo- and optogenetics in combination with the WCM.

4. Functionally test the involvement of the vHPC-mPFC pathway in strategy switch during learning in the WCM.

2. **MATERIALS AND METHODS**

All experiments were carried out according to the European Community Council Directive 2010/63/EEC. All experimental procedures were approved by the local government of Upper Bavaria (AZ 142-12). Every effort was done to keep the number of experimental subjects at a minimum and to avoid animal suffering.

2.1. **Animals**

A total number of 171 adult male C57BL/6N, Nex-Cre-ChR2-YFP or Nex-Cre mice, from our local breeding stock (Max Planck Institute of Biochemistry, Martinsried, Germany), were used in the experiments of this thesis. Mice were 2 to 6 months of age at the time of experiments. They were single housed (except where indicated otherwise) and maintained in a room with controlled humidity and temperature, under a 12h dark/light cycle, with water and food *at libitum*. After transfer to the local animal facility at the Max Planck Institute of Psychiatry, mice were allowed to get accustomed to the holding conditions (standard macrolon cages type II; 267 × 207 × 140 mm, floor area 370 cm^2; Tecniplast, Italy) for at least 10 days before experiments started.

Generation of transgenic mouse lines

The generation of the Nex-Cre and Nex-Cre-ChR2-YFP mouse lines was performed as previously described (Reichel et al., 2016)*.* Briefly, the Nex-Cre driver line was generated by a *knock-in* of Cre into the Nex-locus (Goebbels et al., 2006). This allowed the selective expression of Cre in forebrain glutamatergic neurons. The Nex-Cre-ChR2-YFP mouse line was generated by breeding heterozygous Nex-Cre mice to homozygous Ai32 mice (Madisen et al., 2012) purchased from the Jackson Laboratory; Ai32:Nex-Cre). This crossing

resulted in a mouse line which selectively expresses ChR2 tagged with YFP in forebrain glutamatergic neurons.

2.2. Drugs

- Vetalgin (MSD Animal Health, Unterschleißheim, Germany) was dissolved in 0.9% NaCl to a final concentration of 50 mg/ml.

- Metacam (Boehringer Ingelheim Vetmedica GmbH, Germany) was dissolved in 0.9% NaCl to a final concentration of 0.1 mg/ml.

- $MnCl_2 \times 4H_2O$ (Sigma-Aldrich, Steinheim, Germany) was dissolved in 0.9% NaCl to a final concentration of 50 mM (4947.5 mg−500 mL saline). The pH was adjusted to 6.95 with NaOH.

- Ketamine + xylazine solution: 138 mg of ketamine and 6.8 mg of xylazine/10 mL solution (0.9% NaCl).

- Clozapine N-Oxide (Tocris Biosciences, Bristol, UK) was dissolved in DMSO 1% (0.9% NaCl solution) to a final concentration of 5 mg/ml.

2.3. Viral vectors

- AAV5-CamKII-ArchT-GFP (UNC Vector core, Chapel Hill, USA); titer: 4.00 x 10^{12} gc/ml;

- AAV8-CamKII-hM4D(Gi)-mCherry (Addgene, Cambridge, USA); titer: 2.64 x 10^{12} gc/mL;

- pAAV8-hSyn-DIO-hM4D(Gi)-mCherry (Addgene, Cambridge, USA); titer: 2.06 x 10^{12} gc/ml;

- pAAV8-hSyn-DIO-mCherry (Addgene, Cambridge, USA); titer: 3.07 x 10^{12} gc/ml.

2.4. **Preparation of optic fiber implants**

Optic fiber implants for optogenetics were manufactured in house by the experimenter. The preparation procedure (adapted from (Sparta et al., 2011)) is fully described in the *Appendix* of this thesis. Briefly, the implants were comprised of an optic fiber (0.39 NA, Ø200 µm Core Multimode Optical Fiber, ThorLabs, Newton, NJ, USA) fixed to a ceramic ferrule (Ø1.25 mm Multimode LC Ceramic Ferrule, Ø230 µm Hole Size, ThorLabs, Newton, NJ, USA). The length of the fiber was adapted to the need of each experiment, depending on the depth of the implantation target (e.g. dHPC or vHPC).

2.5. **Surgeries**

Animals received an intraperitoneal injection of an analgesic (200 mg/kg Vetalgin, MSD Animal Health, Unterschleißheim, Germany), before being anesthetized. Next, they were anesthetized with an isoflurane-oxygen mixture (4.5% for induction and 1.5.% for maintenance, with an oxygen flow of 1.0–1.4 L/min) and mounted in a stereotactic frame (Kopf Instruments, Tujunga, CA, USA) where they were head fixed (frontal teeth, snout and ear bones). Eyes were protected from drying by the application of an eye cream (Bepanthen, Bayer Vital, Leverkusen, Germany). Body temperature was maintained by a water-based heating pad positioned under the mice. Following animal's stabilization and verification of surgical tolerance, the hair on top of his head was shaved and a local anesthetic (10% Lidocaine spray, AstraZeneca, Wedel, Germany) was applied on the skin. After 5 min, a longitudinal incision was made on the skin, extending from behind the eyes line until just before the ears line. The coordinates for lambda and bregma were set as references in order to reach the target coordinates. Small holes were carefully drilled on the skull above the target coordinates and the dura mater (if still present) was removed with a sterile 25 G needle. The injection needle (Hamilton neuro syringe, Hamilton Company, Planegg, Germany) – or fiber tip, in case of implantation of optic fibers – was slowly lowered until the specific depth, determined by the dorso-

ventral coordinate (DV), and the injection started. The correct volumes and injection rates were achieved with the use of a microinfusion pump (for specific injection volumes and rates see detailed injection protocols below). The needle was left in place for 5 min, to avoid reflux, before it was slowly pulled up. The procedure was repeated for the next hemisphere. Following the end of the second injection (or fiber implantation), animals received an intraperitoneal injection of analgesic (0.5 mg/kg Metacam, Boehringer Ingelheim Vetmedica, Rohrdorf, Germany) and the head incision was sutured and disinfected (Braunol, Braun Melsungen, Melsungen, Germany). Animals were placed in a clean warm cage until waking up.

In the first 5 days after surgery, the health status of the animals was daily inspected on basis of predefined parameters (body weight, motility, general behavior, wound appearance, etc) in score sheets and treated with pain medication (subcutaneous, 0.5 mg/kg Metacam, Boehringer Ingelheim Vetmedica, Rohrdorf, Germany). The post-surgery recovery time before follow-up experiments was at least 7 days.

For coordinates, injection volume, rate and complimentary procedures, please check below.

Injection of viral vectors

General surgery procedures are described above. Specifically, the injection targets, volumes and injection rate of the viral vectors were the following:

- The CA3 region of the dorsal hippocampus. Coordinates used for injection were: AP: - 1.8, ML: +/-2.4, DV: - 2.2; 500 nL of the viral vector AAV5-CamKII-ArchT-GFP were injected at a rate of 100 nL/min.
- The CA3 region of the ventral hippocampus. Coordinates used for injection were: AP: - 2.8, ML: +/- 3.2, DV: - 4.0; 500 nL of the viral vector AAV5-CamKII-ArchT-GFP were injected at a rate of 100 nL/min;

- The CA1 region of the dorsal hippocampus. Coordinates used for injection were: AP: - 2.30, ML: +/- 1.65, DV: - 1.40; 300 nL of the viral vector AAV8-CamKII-hM4D(Gi)-mCherry were injected at a rate of 50 nL/min;

- The CA1 region of the ventral hippocampus. Coordinates used for injection were: AP: - 2.9, ML: +/- 2.8, DV: - 4.5; 300 nL of the viral vector AAV8-CamKII-hM4D(Gi)-mCherry were injected at a rate of 50 nL/min;

- The infralimbic cortex (IL). Coordinates used for injection were: AP: + 1.60, ML: +/-0.30, DV: - 2.9; 300 nL of the viral vector pAAV8-hSyn-DIO-hM4D(Gi)-mCherry or the control pAAV8-hSyn-DIO-mCherry were injected at a rate of 50 nL/min.

For each viral vector, at least 3 animals were injected and histologically verified for transfection efficacy (pilot studies not shown here) and localization before the injections of bigger cohorts was performed. All the coordinates were based on the on "The Mouse Brain in Stereotaxic Coordinates" (Franklin and Paxinos, 2007) and tested in our apparatus. Some adjustments were made to match specific needs for different mouse lines. AP, ML and DV values are described in reference to bregma, midline and surface the skull, respectively.

Optic fibers implantation

General surgery procedures are described above. After the optic fiber tip was lowered until its target, the implant was fixed to the skull with dental cement carefully placed to avoid covering lambda and bregma and the upper half of the implant's ferrule. After the dental cement was dry and hard, the procedure was repeated (including the setting of lambda and bregma) in the next hemisphere. Finally, the whole surface of exposed skull was covered by dental cement.

Specifically, the optic fiber implants were targeted at:

- The CA1 region of the dorsal hippocampus. Coordinates used for implantation were: AP: - 2.30, ML: +/- 1.65, DV: - 1.30;
- The CA3 region of the dorsal hippocampus. Coordinates used for implantation were: AP: - 1.8, ML: +/-2.4, DV: - 2.0;
- The CA3 region of the ventral hippocampus. Coordinates used for implantation were: AP: - 2.8, ML: +/- 3.2, DV: - 3.8.

For the experiments where optogenetics was combined with behavioral tests, in addition to the fiber implants, 4 small metal screws were also fixed to the skull of the mice during surgery. The screws were placed in the rostral part of the skull, 2 per hemisphere, and were fixed superficially to the skull only, not protruding down to the brain. The screws were used to increase the stability of the fiber implants fixation and avoid that the construct mounted on the skull would fall. This surgery stage was not performed for the experiment where optogenetics was combined with MEMRI, because animals cannot be scanned when they have metal parts on their bodies.

Injection of retrograde tracer (fluorogold)

General surgery procedures are described above. Specifically, bilateral injections of fluorogold (FG; Fluorochrome, Denver, USA; 1% in distilled H_2O) were targeted at the infralimbic cortex (IL). The coordinates used for injections were: AP: + 1.60, ML: +/-0.30, DV: - 2.9. The total volume of 250 nL was injected in a rate of 25 nL/min.

2.6. **Histology**

Histological verification of fluorophores

The viral vectors used in this work carried a fluorophore (GFP or mCherry, indicated for each experiment) to allow histological verification of transfection efficacy and location.

After the end of the behavioral experiments, animals injected with the viral vectors at least 4 weeks before were sacrificed, had their brains removed and snap frozen in chilled methyl-butane. Brains were kept frozen at -80°C until sliced with a cryostat into 30 μm sections and collected onto a glass slide. The slides were stored at -20°C until microscopic analysis. For microscopic analysis the slides were mounted with the antifade mounting medium Vectashield hard set with DAPI (Vector Laboratories, Burlingame, CA, USA) and coversliped. After hardening, the slides were checked under an epifluorescence microscope (Axioplan 2 Imaging, Zeiss, Oberkochen, Germany) with the appropriate filters for each fluorophore wavelength and for DAPI. Pictures of the brain sections were made using a digital camera (AxioCam MRm, Zeiss, Oberkochen, Germany) coupled to the microscope.

Histological verification of fluorogold

Five to six days after fluorogold injections, mice were transcardially perfused with 4% PFA-PBS and had their brains removed. Brains were post-fixed overnight in 4% PFA-PBS and later cryoprotected with a 30% sucrose solution (with 0.5% PFA). Samples were stored at 4° C for at least 2 days until further processing for histological verification of the fluorescent tracer. Fixed brains were sliced in a vibratome into 30 μm sections and collected onto a glass slide. For microscopic analysis the slides were mounted with a 50% glycerol-PBS solution, coversliped and sealed with transparent nail polish on its borders. After drying, the slides were checked under an epifluorescence microscope (Axioplan

2 Imaging, Zeiss, Oberkochen, Germany) with the appropriate filter for fluorogold (DIC filter). Pictures of the brain sections were made using a digital camera (AxioCam MRm, Zeiss, Oberkochen, Germany) coupled to the microscope.

2.7. **Water Cross Maze (WCM)**

Apparatus, room setup and general procedure

The water cross maze (WCM; figure 2) consists of a transparent acrylic glass apparatus with four arms (50 cm long, 10 cm wide and 30 cm high) arranged in a cross shape and a center zone (10 cm x 10 cm) that connects the four arms. The arms were labeled North (N), East (E), South (S) and West (W) in clockwise order. The apparatus and its removable pieces were custom made at the MPI of Psychiatry, Munich. A removable guillotine door (arm blockade) of transparent acrylic glass was used to transform the cross maze into a T maze (Tolman et al., 1946), always blocking the arm opposite to the start arm (see *Protocols* below for details). A transparent acrylic glass platform (8 cm x 8 cm, 10 cm high) was placed inside maze, by the end of one of its arms (W or E), as indicated in the protocols below.

The maze was placed on top of a desk 65 cm elevated from the floor, in the middle of the experimental room (3 m x 4 m). The room displayed several visual cues arranged in a fixed and unspecific order, as a door to an adjacent room where the animals where housed, a sink with a cabinet below it, an emergency exit door, ventilation tubes on the ceiling and a small desk with a computer. As indicated by pilot tests (not shown here), there were no dominant cues or a preferred wall/side by the animals. There were no overt acoustic or odor cues in the room. Background noise consisted of air conditioning sound. The room was dimly lit with two table lamps fixed to the side walls and with light directed to the walls, not to the maze.

In the beginning of every testing day the maze was filled with tap water at 22°C (+/- 1°C) to the height of 11.5 cm above the maze floor. The surface of the escape platform, placed in the end of the one of the arms (W or E; see details under *Protocols*), was 1.5 cm under the water and it was not visible to the mice. The guillotine door was placed opposite to the start arm, in order to block this arm directly in front of the starting point, forcing the animals to swim left or right instead of straight ahead. The cages of single-housed mice were individually transported from the adjacent holding room to the test room and placed on top of the sink bench. Mice were gently taken out of the cage and placed on the water, facing the wall of the start arm of the maze. The experimenter stood still, approximately 20 cm behind the start arm wall, for the duration of the trial. Mice were given up to 30 s to swim and climb to the escape platform and were allowed to remain there for 20 s (for testing days 1 and 2) before being taken out (with a texturized small shovel) by the experimenter. If the mice did not find the platform within 30 s they were guided to it. Mice were given 6 trials per day, with the start arm positions North (N) or South (S) allocated in a pseudo-random order (e.g. N-S-S-N-N-S or S-N-N-S-S-N). The walls of the maze were wiped with a soft towel between every trial and the water was stirred every 6 trials to avoid possible odor cues of urine. For full-day experiments, part of the water of the maze was renewed in the break between morning and afternoon sessions. After each trial, mice were taken out of the maze and placed back in the home cage which was returned to the holding room and partially positioned under red warm light, so the animals could dry and recover their temperature. The behavioral parameters (see description below) were recorded manually on site by the experimenter.
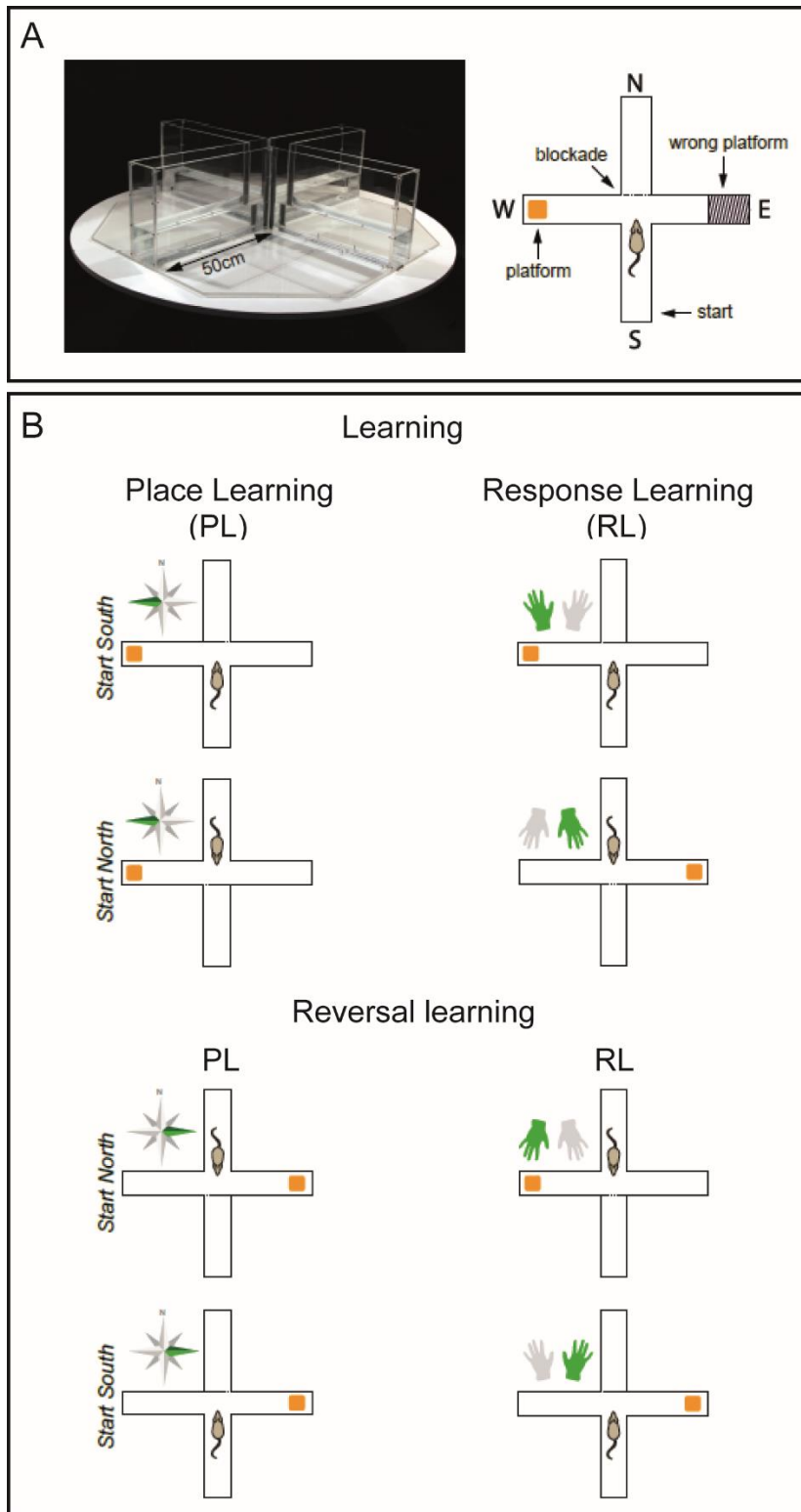
Figure 2: *Water cross maze (WCM) setup and learning protocols.* (A) Picture of the apparatus filled with water, indicating the length of the arms (50 cm); representative image (upper view) of the maze, indicating the orientation of the arms (N, E, S and W) and location of platform, blockade and wrong platform sector for a trial

starting in the S arm. (B) Representation of the learning protocols (upper panel), place learning (PL) and response learning (RL), starting from south (S) and north (N); and reversal learning protocols following PL or RL. (modified from (Kleinknecht et al., 2012)).

Protocols

Animals underwent 6 trials per day (as described in details below) for up to 7 consecutive days (d1-d7, week 1; indicated in each experiment), following a specific learning protocol: place learning (PL) or response learning (RL). For the experiments in which the WCM was combined with MEMRI the behavioral protocol was extended to 8 days (d1-d8). In case of animals that were also subjected to reversal learning (see below), this protocol was applied in the second week of experiments (d9-d11, week 2; indicated in each experiment). For the experiments in which the WCM was combined with optogenetic inhibition of the hippocampus the second week (d9-d13, week 2) of WCM had the same protocol as the first week, and it was considered a recall week.

Place learning (PL): in this learning protocol animals count on visual extra-maze distal cues to orient themselves and form a cognitive map of the environment. Therefore, they should be able to find the escape platform independently of the start location. Since the walls of the maze are transparent, mice can see the room cues from inside the maze and use it in order to learn where the platform is. For this protocol, the platform location was fixed (end of W or E arm, balanced between groups; except for WCM+MEMRI experiment, where the platform was always in the W arm) throughout the duration of the experiment (6 trials per day, up to 8 days) and the start positions varied between N or S in a pseudo-random order (e.g. day 1: N-S-S-N-N-S, day 2: S-N-N-S-S-N, etc). The arm opposite to the start arm was always blocked by a removable transparent guillotine door.

Response learning (RL): in this learning protocol animals rely on their body movements (either turn right or left) in order to navigate to the escape platform. Learning the position of the extra-maze cues is not necessary for performing this protocol. The start positions varied between N or S in a pseudo-

random order (e.g. day 1: N-S-S-N-N-S, day 2: S-N-N-S-S-N, etc) and the platform location varied according the start arm, always in a specific combination (e.g. start arm N, platform E and start arm S, platform W, for animals learning to turn left). The arm opposite to the start arm was always blocked by a removable transparent guillotine door.

Reversal learning: this is a sub-protocol of the previously described PL and RL, designed to test the animal's behavioral flexibility. To perform this protocol correctly, animals had to update the platform location learned the week before. Specifically, animals that underwent place leaning with the platform location on the W during week 1, had to learn the new platform location on the E during week 2, and vice-versa. Conversely, animals that underwent response learning with a left turn during week 1, had to learn to turn right in order to find the platform during week 2.

Spaced training: mice were trained in cohorts of 5-6 (unless otherwise stated) in a spaced manner (mouse 1 trial 1, …, mouse 6 trial 1, mouse 1 trial 2, etc; figure 3A), allowing an inter-trial interval (ITI) of approximately 10-15 min for each mouse. This is the standard training protocol and it was used for most experiments (if not stated otherwise) shown here.

Massed training: mice were trained individually in a massed manner (mouse 1 trial 1, mouse 1 trial 2, …, mouse 1 trial 6, mouse 2, trial 1, etc; figure 3B), allowing an inter-trial interval (ITI) of approximately 3 min for each mouse. This training protocol was used when optogenetic approaches were combined with the WCM to avoid that the animals would have cables connected/disconnected multiple times within the same day. Cables were connected only once daily, 10 min before the recall trials (week 2) started. Animals had this time to get accustomed to the connecting cables and to rest before the test started. During these 10 min animals were maintained in their home cages (without a lid) placed inside a black bucket (blind box) on top of a small stool positioned in front of the start arm of the maze. In between trials animals were maintained in the same cage and the stool was moved to face the new start arm, when it was the case.

Massed alternated training: mice were trained in cohorts of 2 in massed alternated manner (mouse 1 trial 1, mouse 2 trial 1, mouse 1 trial 2, etc; figure 3C), allowing an inter-trial interval (ITI) of approximately 3 min for each mouse. This training protocol was used when chemogenetic approaches (DREADDs) were combined with the WCM to facilitate the logistics of CNO injections and WCM training in parallel.
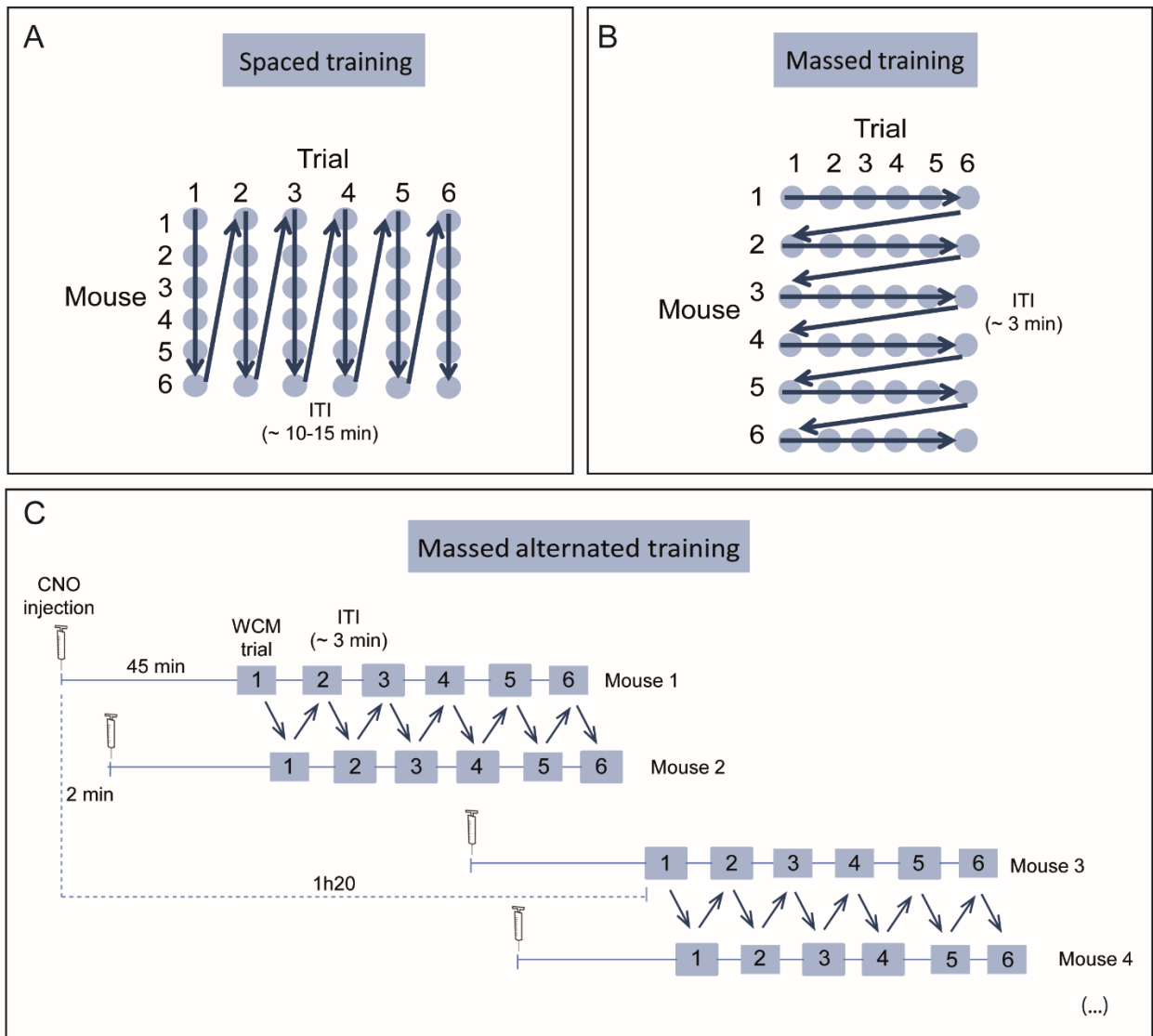
Figure 3: *Training protocols with different distribution of the trials.* (A) Spaced training: each trial is performed by all mice (cohorts of up to 6 mice) before the next trial starts (i.e., mouse 1 trial 1, …, mouse 6 trial 1, mouse 1 trial 2, etc), allowing an

inter-trial interval (ITI) of approximately 10-15 min for each mouse. (B) Massed training: each mouse performs all daily trials (1-6) before the next mouse starts (i.e., mouse 1 trial 1, mouse 1 trial 2, …, mouse 1 trial 6, mouse 2, trial 1, etc), allowing an inter-trial interval (ITI) of approximately 3 min for each mouse. Since the training is individual, the cohort size is variable and the number given here (6) is only an example. (C) Massed alternated protocol: the trials are performed in an alternated manner by 2 mice and only after these individuals finish all 6 daily trials the next two mice start (ie., mouse 1 trial 1, mouse 2 trial 1, mouse 1 trial 2, mouse 2 trial 2, etc), allowing an inter-trial interval (ITI) of approximately 3 min for each mouse.

Performance parameters

Accuracy: accuracy was defined as the percentage of correct trials among the 6 trials in one day. Animals were arbitrarily considered "accurate" if they reached above 83% accuracy (correct performance in at least 5 out of 6 trials). A trial was considered correct if the animal swam directly to the target arm and climbed the platform. If, after leaving the start arm, the animal swam to the arm opposite to where the platform was, swam back to the start arm or swam to the target arm but did not climb the platform the trial was considered incorrect (inaccurate).

Latency: latency was measured as the time it took the animals to climb the platform. If the animal did not find or did not climb the platform within 30 s (total trial time), its latency was considered 31 s. The latency displayed on the graphs is the daily average of the individual trials.

Number of wrong platform visits: if an animal swam all the way to the distal end of the arm (last 1/3 part of the arm) opposite to where the platform was located a "wrong platform visit" was counted. Note that, in some cases, animals swam out and back again multiple times to this incorrect location within the trial duration (30 s). The number of wrong platform visits displayed on the graphs is the daily sum of the individual trials.

Accurate learners: this parameter was derived from the accuracy, described above. It was simply the percentage of accurate animals (accuracy above 83%) within a specific experimental group in a given day.

Start bias: this parameter was derived from the accuracy, described above. The start bias score was calculated as the module of the difference in number of correct trials starting from N and starting from S, for each testing day: start bias score = |(# of correct trials N) - (# of correct trials S)|. If an animal would perform all trials correctly in a given day, it would have a start bias score of zero (3-3=0); while, if an animal would correctly perform only the trials from either side, N or S, it would have a start bias score of 3 (3-0=3 or |0-3|=3) and it would be considered as a "side biased" animal. This is an informative parameter to indicate animals trained under PL that adopt RL instead of the correct strategy.

Good performers versus bad performers: for the segregation of mice under good or bad performers the individual accuracy of animals was averaged across all training days (d1-d8) and these values were divided by a median split. All mice which the accuracy values were above or at the median were considered "good performers"; all mice which the accuracy values were under the median were considered "bad performers".

2.8. **Manganese enhanced magnetic resonance imaging (MEMRI)**

All MEMRI experiments were conducted on a 7T Avance Biospec 70/30 scanner (Bruker BioSpin, Ettlingen, Germany). In brief, essentially as described before (Almeida-Correa et al., 2018; Bedenk et al., 2018), mice were fixed in supine position on a saddle-shaped receive-only coil. Head fixation was achieved using a stereotactic device and the frontal teeth were fixed with a surgical fiber. Once fixed in the coil, mice were kept anesthetized with an isoflurane oxygen mixture (1.0–1.5 vol %, with an oxygen flow of 1.2–1.4 L/min) (Delta Select, Germany). A rectal thermometer was used for body temperature monitoring (Thermalert TH-5, Physitemp Instruments, USA). Body temperature was kept between $36.5°C$ and $37.5°C$ using a water-based heating pad. Pulse rate was continuously monitored by a plethysmographic pulse oximeter (Nonin 8600V, Nonin Medical Inc., USA).

2.9. *In situ* hybridization (ISH)

Radioactive *in situ* hybridization for the detection of c-fos mRNA was performed as previously described elsewhere (Schmidt et al., 2007). Mice underwent learning in the water cross maze (WCM), were sacrificed by decapitation 15 min after the last trial on the day they "learned" the task (performed at least 5 out of 6 correct trials) and had their brains extracted. This time point was set individually for each animal. An even number of home cage controls were time-matched. Immediately upon extraction, brains were snap frozen in chilled methyl-butane and stored at -80°C. Frozen brains were cut on a cryostat in 20 μm sections and mounted on Super Frost Plus glass slides. Slides were stored at -20°C until further processing.

Briefly, for riboprobe in situ hybridization sections were fixed in 4% paraformaldehyde (at 4°C), rinsed in PBS/DEPC (3 x 5 min) and acetylated in 0.25% acetic anhydride in 0.1M triethanolamine/HCl. Next, slides were rinsed in 2xSSC/DEPC (2 x 5 min) and brain sections were dehydrated in increasing concentrations of ethanol (60% / 75% / 95% / 100% EtOH), dipped in chloroform and once more in 100% EtOH. Slides were vertically placed in a rack and were air dried (dust free) over night.

The antisense cRNA probes for c-fos were transcribed from a linearized plasmid. Tissue sections were saturated with 100μl of hybridization buffer containing approximately 1.4×10^6cpm ^{35}S-labeled riboprobe. Brain sections were coverslipped and incubated overnight at 55°C. The following day the sections were rinsed in 2×SSC (standard saline citrate), treated with RNAse A (20mg/l) and washed in increasingly stringent SSC solutions at room temperature. Finally, sections were washed in 0.1×SSC for 1h at 65°C and dehydrated through increasing concentrations of alcohol.

The slides were exposed to an autoradiography film (Kodak Biomax MR films; Eastman Kodak Co., Rochester, NY) and developed after 48h. Images of the brain sections were obtained by digitalizing the original film.

2.10. **Immunohistochemistry (IHC)**

Immunohistochemistry (IHC) for detection of c-Fos positive cells was performed as described below. Briefly, 90 min after Y maze exposure, mice were transcardially perfused with 4% PFA-PBS and had their brains removed. Brains were post-fixed overnight in 4% PFA-PBS and later cryoprotected with a 30% sucrose solution (with 0.5% PFA). Samples were stored at $4^{o}C$ for at least 2 days until further processing for IHC against c-Fos. Fixed brains were sliced in a vibratome into 30 μm sections and collected into wells (24 well plates) filled with cryoprotectant solution (125 mL glycerol + 125 mL ethylenglycol + 250 mL 1xPBS, for 500 mL solution) and stored at $-20^{o}C$ until processing. The next steps were performed under gentle shaking (orbital shaker) in room temperature. Brain slices were thoroughly washed (3 x 10 min) in PBS before being blocked in 10% normal goat serum (NGS) for 1h. Next, slices were washed in PBS (3 x 5 min) and incubated with the primary antibody anti-c-Fos (abl90289; AbCam, Cambridge, United Kingdom) 1:500 in PBS + 1.5% NGS for 12h. Slices were washed in PBS (3 x 5 min) and incubated with the secondary antibody, biotinylated goat anti-rabbit IgG (BA-1000, Vector Laboratories, Burlingame, CA, USA) 1:500 in PBS + 1.5% NGS for 1h. Further, slices were washed in PBS (3 x 5 min) again and then activated in AB complex (VC-PK-6100, Vectastain ABC, Vector Laboratories, Burlingame, CA, USA) for 1h. The following steps were still performed in room temperature, but not under gentle shaking. After being washed in PBS (3 x 5 min), slices we stained for DAB with Peroxidase Substrate Kit (VC-SK-4100) in distilled water. Brain sections were stained for 30 min and reaction was stopped in petri dishes filled with tap water. Another round of washes was performed (2 x 5 min in tap water and 1 x 5 min in distilled water). Next, sections were mounted in microscopy slides (Super Frost Plus glass slides), dehydrated in an ethanol series (70% / 96% / 100% EtOH) and cover-slipped with DPX. Slides were stored horizontally overnight for drying.

Afterwards, brain slides were analyzed under a microscope and bright field images (5x and 10x) of the dorsal hippocampus were acquired by a

camera. c-Fos positive cells were then manually quantified by the experimenter from the microcopy images (10x).

2.11. Definition of Brain Structures

Brain structures shown in the figures of this thesis and listed in tables 1 and 2 were defined using the Allen Mouse Brain Atlas (Lein et al., 2007) (http://mouse.brain-ap.org/experiment/thumbnails/100048576?image_type=atlas) as reference. The exceptions are the "islands of Calleja," (Figure 6 and table 1) and the hippocampus subfields on the retrograde tracing experiment with fluorogold (figure 21) defined based on "The Mouse Brain in Stereotaxic Coordinates" (Franklin and Paxinos, 2007).

2.12. IHC and ISH image analyses

Analyses of ISH digitalized images and IHC microscopy images were performed with ImageJ (http://rsweb.nih.gov/ij/). Regions of interest (ROIs) were manually defined for: (i) automatic pixel analysis (greyscale brightness of the ROI minus brightness of a control region) for ISH images; (ii) manual quantification of c-Fos positive cells after IHC DAB staining. ROIs for IHC were delineated by comparing the fluorescent images with the DAB stained images of each individual animal. A ROI was defined as the region where fluorophore expression was observed.

2.13. **Specific procedures**

Experiment 1: MnCl₂ administration and optogenetic stimulation

Nex-Cre-ChR2-YFP mice (n = 8) were bilaterally implanted with optic fiber constructs at the CA1 region of the hippocampus (as described under *Surgeries*). After 7 days of recovery, mice received the first of eight intraperitoneal injections of 20 mg/kg $MnCl_2$ (Sigma-Aldrich, Steinheim, Germany; 8 x 20/24 h). 16-20h after each $MnCl_2$ injection, animals were anesthetized with an isoflurane-oxygen mixture (4.5% for induction and 1.0-1.2% for maintenance, with an oxygen flow of 1.0–1.4 L/min) and mounted in a stereotactic frame where they were loosely fixed (frontal teeth were fixed and ear bars were protected with thick plastic foam blocks in order to keep the head stable without making pressure to the skull). The body temperature of the animals was maintained by a water-based heating pad positioned under the mice. Following animal stabilization, the cap sleeve of the laser cable was carefully connected to the ferrule (cannula) of the optic fiber implant in the right hemisphere only. The laser stimulation protocol applied was, as follows: blue laser (470 nm), 0.75 mW, 2s, 10 repetitions, 60s intervals (0.016 Hz). This stimulation protocol was already tested by our group (Dine et al., 2016) and proved to be sufficient for local increase of neuronal activity. After the end of the stimulation the laser cable was carefully disconnected and anesthesia was gradually reduced until 0.5%. The animals were taken out of the frame and maintained in a heating pad until waking up. 40 min after the end of the stimulation the animals were anesthetized with a mix of ketamine + xylazine (as described under *Drugs*; 0.1 mL/ 10 g of mouse) and transferred to the MRI room, where they were prepared for scanning. For graphic representation of the experimental design see Figure 5A.

Experiment 2: Enriched housing, MnCl₂ administration and sensory deprivation

C57BL/6N mice (n = 9; 3/cage) were housed in large type III cages (425 × 266 × 155 mm, floor area 820 cm^2; Tecniplast, Italy) enriched with extra nesting material, plastic hair curlers of two different sizes (2 big, 36 mm radius; 3 medium, 36 mm radius), used as texturized tunnels (textures on the inner and outer part), and a hanging thread at the metal lid with a another small hair curler/tunnel (28 mm radius). Mice were kept in the same group under this condition for 8 days, until scanned (scan 1), followed by another 7 days of enriched housing and a second scan (scan 2).

All mice received intraperitoneal injections of 20 mg/kg MnCl₂ (Sigma-Aldrich, Steinheim, Germany) every 24 h for eight consecutive days (8 x 20/24 h), in order to minimize physiological side effects (adapted from (Grunecker et al., 2010; Bedenk et al., 2018). Mice were always weighted immediately before injections to monitor animal's health status and to guarantee the correct dose would be injected every day.

On day 8, animals (3 per day) were individually anesthetized with a mixture of ketamine and xylazine (i.p., injection of 0.1 mL/10 g mice) and transferred to the MRI room. With ketamine we aimed to block NMDA receptors (Anis et al., 1983) and thus, to avoid further Mn^{2+} neuronal entrance (Itoh et al., 2008) during the transport of the animals between rooms. For the scanning procedure, see above. This first MRI scanning (scan 1) took place twelve to twenty-four hours after the last of 8 daily MnCl₂ injections.

Immediately after scan 1, and still under sedation, animals had all their whiskers trimmed close to the skin on the left side of the snout. The right side was untouched. After trimming, animals were put back in the enriched cages. The trimming procedure was repeated every 2 days (under light isoflurane anesthesia) to avoid re-growth of the whiskers. After scan 1, animals received no further MnCl₂ injections.

On the last day of enrichment after scan 1, animals (3 per day) were again individually anesthetized with a mixture of ketamine and xylazine (i.p., injection of 0.1 mL/10 g mice) and transferred to the MRI room for scan 2. Scans 1 and 2 were performed 7 days apart. For graphic representation of the experimental design see figure 6A.

We interrogated the contrast scan 1 > scan 2 using a strict family-wise error corrected threshold of p $_{FWE,cluster}$ < 0.05, with a collection threshold of p $_{uncorrected}$ < 0.001 (Woo et al., 2014), which is in accordance with other MEMRI studies (Lutkenhoff et al., 2012; Laine et al., 2017). Due to expected dilution of Mn^{2+} concentrations after cessation of the $MnCl_2$ injections, relative local increases of Mn^{2+} accumulation in the second scan (scan 2 > scan 1) were only assessed qualitatively at an uncorrected threshold of p < 0.05 (cluster extent 20).

Experiment 3: WCM + MEMRI

Two different cohorts of C57BL/6N mice were trained in the WCM under the place learning (PL; n = 20) or the response learning (RL; n = 24) spaced protocols during 8 consecutive days (d1-d8). $MnCl_2$ injections (i.p.; 20 mg/kg) were performed for 8 days, approximately twelve hours before the behavioral (WCM) sessions. 10 min after the last trial (trial 6 of day 8), accurate learners (PL: 18/20; RL 22/24) were anesthetized with a mixture of ketamine + xylazine (as described under *Drugs*) and transferred to the MRI facility for scanning. The behavioral and scanning procedures are described above.

Experiment 4: IEG analysis after WCM learning

As previously discussed in the introduction, the time-point to sacrifice the animals for IEG analysis is hard to establish, given that its expression is short and transient. Moreover, the behavioral task I use here might take several days to acquire and its learning time differs among animals, complicating things

further. In order to sharpen our cut-off without overlooking the inter-individual differences in learning I defined the following rules: (i) animals would be sacrificed 15 minutes after learning in the WCM (and a similar number of home cage controls would be time-matched); (ii) learning (performing the task accurately: at least 5 out of 6 trials correct) would be considered in an individual basis; (iii) only the top 2 days where most of the animals learned the task would be considered for the cut-off to avoid further variability.

Mice were divided in 3 groups (figure 4): RL, trained in the WCM under the response learning (RL) spaced protocol; PL, trained in the WCM under the place learning (PL) spaced protocol; HC, home cage controls remained in their home cages for the duration of the behavioral task. Brains were processed for radioactive ISH mRNA analysis of the IEG c-fos (as described above), as a marker of cellular activity. I performed a region of interest (ROI) analysis and group comparison in selected brain structures. The individual values displayed here refer to the brightness (image intensity per ROI area) of the ROI minus the brightness of a background region arbitrarily chosen.
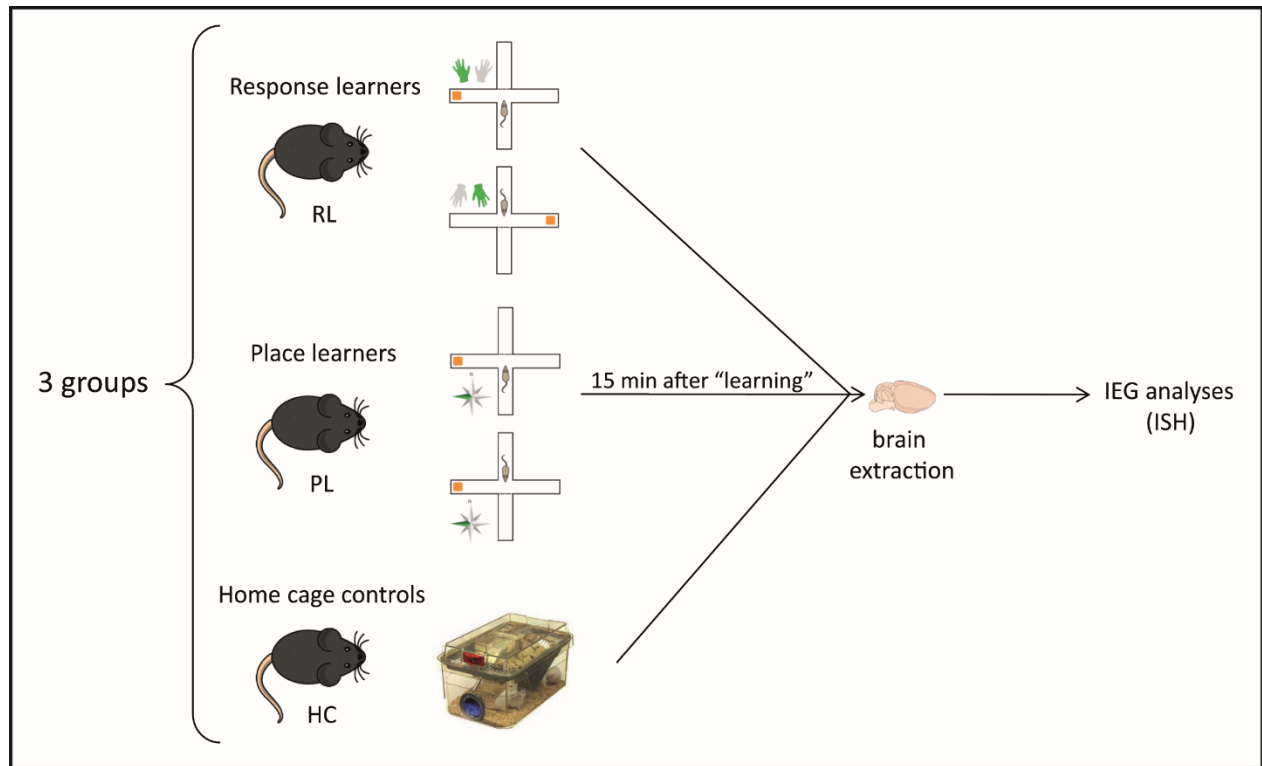
Figure 4: *Experimental design for experiment 4: IEG analysis after WCM learning.* Mice were divided into 3 groups: PL, underwent learning in the WCM under the place learning protocol; RL, underwent learning in the WCM under the response learning protocol; HC, home cage controls, remained in their home cages for the duration of the behavioral task. 15 min after animals from the PL or RL groups leaned the task (performed at least 5 out of 6 trials correctly) they were killed and had their brain removed and snap frozen for future immediate early gene (IEG) analysis by *in situ* hybridization (ISH). The same number of home cage control animals was time-matched with their WCM-trained counterparts.

Experiment 5: Optogenetic inhibition of dHPC during WCM recall

C57BL/6N mice (n = 21) previously bilaterally injected in the dHPC (dCA3; see S*urgeries* for details) with a viral vector transducing the inhibitory opsin ArchT (AAV5-CamKII-ArchT-GFP) and implanted with optic fibers just above the injections targets, were trained in the WCM under the place learning (PL) massed protocol (see detailed description of massed protocol above and on figure 3) during 7 consecutive days (d1-d7). Animals were not connected to the laser cables during the training period. After 1 day of rest, animals which were accurate learners (n = 17) by day 7 (last day of training) started the recall tests

(same behavioral protocol as training) which lasted for 4 days (d9-d12). On the recall days animals were connected to the laser cables once daily (always 10 min before the tests) and remained connect for the whole testing period (6 trials). Animals had this 10-min time to get accustomed to the connecting cables and to rest before the tests started. During this period animals were maintained in their home cages (without a lid) placed inside a black bucket (blind box) on top of a small stool positioned in front of the start arm of the maze. In between trials animals were maintained in the same cage and the stool was moved to face the new start arm, when it was the case.

The laser stimulation (green laser, 532 nm, 22-26 mW) was only performed on day 11 (laser on), for the duration of the trials (for each trial: laser switched on immediately before the animal was placed in the maze, and switched off immediately after the animal was removed from the maze; total duration / trial ~ 10s).

For simplified timeline of experimental procedures see figure 15A.

Experiment 6: Optogenetic inhibition of vHPC during WCM recall

Experimental design and procedures were similar to the ones described above for experiment 5. The following exceptions apply:

(i)   viral vectors were injected in the vHPC (vCA3);
(ii)   the recall tests lasted for 5 days (d9-d13);
(iii) laser stimulation was performed on days 11 and 12.

For simplified timeline of experimental procedures see figure 16A.

Experiment 7: Chemogenetic inhibition of dHPC during WCM learning

C57BL/6N mice (n = 15) previously injected in the dHPC (dCA1; see *Surgeries* for details) with a viral vector transducing the inhibitory DREADD hM4D (AAV8-CamKII-hM4D(Gi)-mCherry) were trained in the WCM under the

place learning (PL) massed alternated protocol (see detailed description of massed alternated protocol above and on figure 3) during 6 consecutive days (d1-d6). Behavioral training was paired with a daily intraperitoneal injection of CNO (5 mg/kg; n = 9) or vehicle (n = 6) 45 min before the beginning of trials. On day 6 the treatment groups were inverted, meaning all animals injected with CNO from d1-d5 received a vehicle injection on d6, and vice-versa. After one day of rest, animals were trained for reversal learning during 2 days (d8-d9) under the same treatment regime of d1-d5.

After 1 week of rest, mice were exposed to an unfamiliar context (Y maze) for 10 min under dim light to induce an increase in hippocampal activity, and to analyze if locomotion of the animals was affected by CNO. 45 min before Y maze exposure mice were injected with either CNO (i.p., 5 mg/kg) or vehicle (same groups as established for the WCM). 90 min after the start of exposure, mice were transcardially perfused with 4% PFA-PBS and had their brains removed. Brains were post-fixed and cryoprotected before sectioning. Fixed brains were sliced in a vibratome into 30 μm sections, in 2 series. One of the series was mounted in glass slides and coverslipped with Vecta Shield Hard set with DAPI for fluorophore analysis (see *Histology* for details), while the other series was further processed for IHC against c-Fos (see *Immunohistochemistry* for details).

For simplified timeline of experimental procedures see figure 18A.

Experiment 8: Chemogenetic inhibition of vHPC during WCM learning

Experimental design and procedures were similar to the ones described above for experiment 7. The following exceptions apply:

(i)   viral vectors were injected in the vHPC (vCA1);

(ii) the reversal learning lasted for 3 days (d8-d10);

(iii) the experiment was finalized after reversal learning in the WCM. There was no exposure to the Y maze and no IHC analysis performed afterwards.

For simplified timeline of experimental procedures see figure 19A.

Experiment 9: Chemogenetic inhibition of IL during WCM learning

Nex-cre mice (n = 12) previously injected in the infralimbic cortex (IL; see *Surgeries* for details) with a viral vector transducing the inhibitory DREADD hM4D in a Cre-dependent manner (pAAV8-hSyn-DIO-hM4D(Gi)-mCherry; hM4D group, n= 5), or a control viral vector (pAAV8-hSyn-DIO-mCherry; mCherry group, n = 7), were trained in the WCM under the place learning (PL) massed alternated protocol (see detailed description of massed alternated protocol above and on figure 3) during 7 consecutive days (d1-d7). Behavioral training was paired with a daily intraperitoneal injection of CNO (5 mg/kg), for all animals, 45 min before the beginning of trials.

For simplified timeline of experimental procedures see figure 20A.

Experiment 10: Retrograde analysis of the IL-HPC pathway

Bilateral fluorogold (FG) injections targeting the infralimbic cortex (IL) of naïve C57BL/6N mice (n = 4) were performed as previously described (see *Surgeries*). 5 to 6 days after injections, mice were transcardially perfused, had their brains removed and processed for histological analysis (see *Histology* for details), focusing on the hippocampus.

2.14. **Statistical analysis**

MEMRI analyses

Significance was accepted after family wise error (FWE) correction on the cluster level p $_{FWE, cluster}$ < 0.05. This was determined by collecting the clusters of the uncorrected threshold of p < 0.001 or p < 0.005, adjusting the size of the cluster.

Voxel-wise analysis of the MR images was performed in SPM8 (www.fil.ion.ucl.ac.uk/spm). Graphics of activation maps have been created in MRICro (www.cabiatl.com/mricro). All images were ultimately arranged in Adobe Illustrator 10.0.3 (Adobe Systems Inc., NY, USA).

Behavioral analyses and other comparisons

Behavioral parameters and other data (e.g. quantification of ISH and IHC), were compared using:

(i)   Unpaired t-test, for 2 groups' comparison and non-repeated measures;

(ii)   1-way ANOVA, for single group comparison of repeated measures (e.g. different time-points) or for multiple groups' comparison and non-repeated measures (e.g. IEG analysis of RL vs PL vs HCC);

(iii) 2-way ANOVA, for multiple groups' comparison and repeated measures;

(iv) χ^2 test, for multiple groups' comparison of contingencies (e.g. leaners vs non-learners).

The statistical test (and post-hoc test, when applicable) used for each individual analysis is indicated in the results section and the figure legend relative to each specific investigation. Data are presented as mean ± s.e.m. Significance was accepted as p < 0.05 and a trend was considered for p < 0.06.

Graphs were created and analyses were performed at GraphPad Prism 7 (GraphPad Software, La Jolla, CA, USA).

3. RESULTS

3.1. Experiment 1: Optogenetic stimulation and its effects on local MEMRI signal

To confirm the debated activity-dependent entrance of Mn^{2+} into neurons I analyzed the signal intensity of the hippocampus with MEMRI, comparing the hemisphere which was optogenetically stimulated (once per day for 8 consecutive days; for detailed protocol please *Materials and Methods* and figure 5) versus the hemisphere which contained a light fiber but did not receive light stimulation. Importantly, ChR2 was selectively expressed in cortical glutamatergic neurons in both hemispheres (Nex-Cre-ChR2-YFP mouse line). I observed a significantly higher signal in the stimulated site compared to its mirrored image (figure 5; within subject, between hemispheres comparison; collection threshold $p < 0.01$, $K_e > 20$ voxels). This cluster was not significant after correction for whole-brain analysis and it is shown qualitatively.

This result indicates that increased neuronal activity after direct optogenetic stimulation results in higher MEMRI signal (reflecting increased Mn^{2+} accumulation) when compared to an unstimulated region (contralateral dorsal hippocampus) that also expresses Channelrhodopsin 2 (ChR2). Therefore, I confirmed that Mn^{2+} enters, and at least transiently accumulates, in activated neurons.
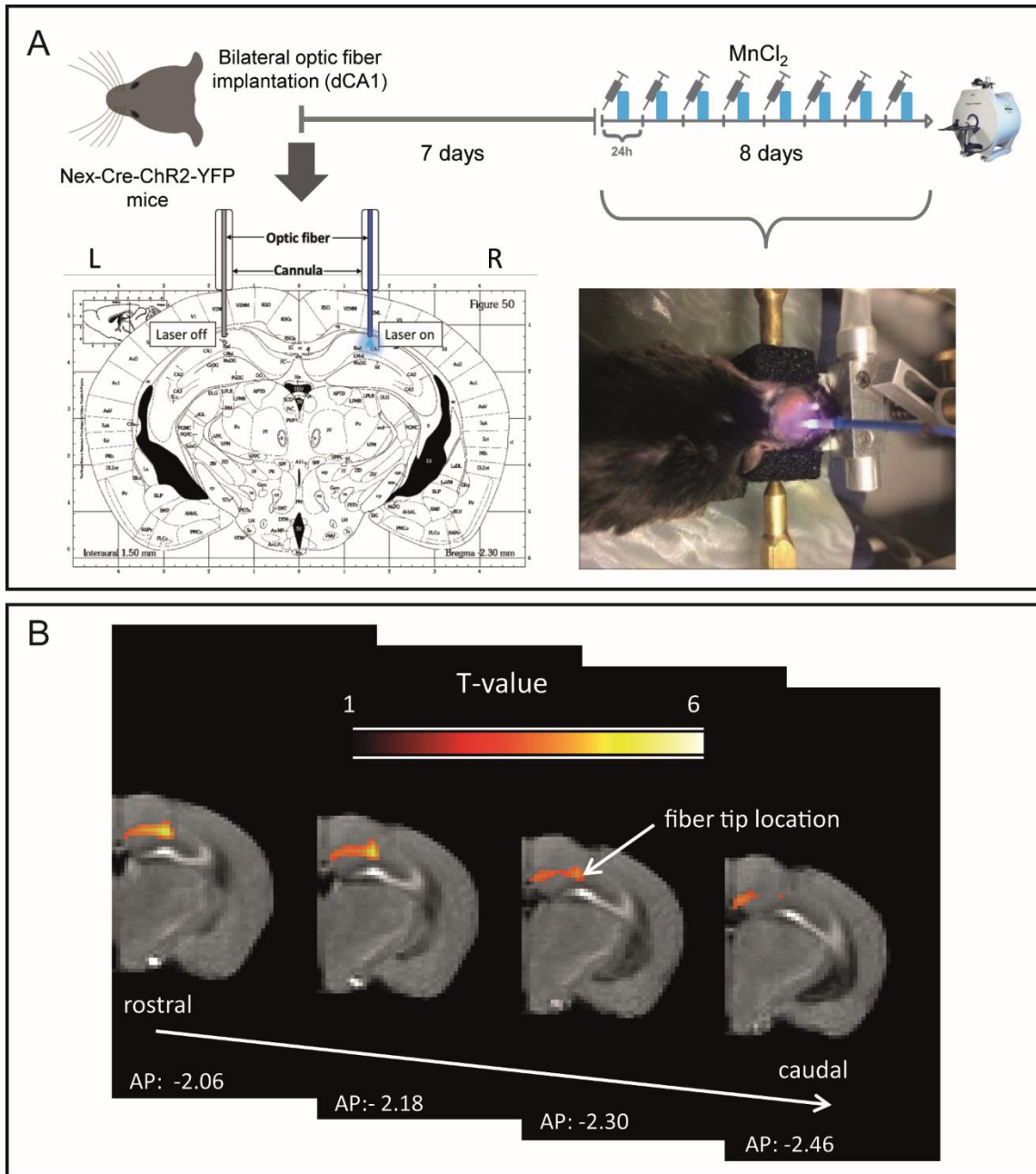
Figure 5: *Mn²⁺ entrance in neurons is activity dependent.* (A) Nex-Cre-ChR2-YFP mice were bilaterally implanted with optic fibers directly above the dorsal hippocampus subfield CA1 (dCA1). After 7 days of recovery, animals were subjected to an 8-day protocol of daily $MnCl_2$ injections (i.p., 20 mg/kg) followed by a direct unilateral (right hemisphere only) optogenetic stimulation [blue laser (470 nm), 0.75 mW, 2s, 10 repetitions, 60s intervals (0.016 Hz)] of the dCA1 16-20 h after. The injections were performed 24h apart. 40 min after the last optogenetic stimulation animals were anesthetized with a mix of ketamine + xylazine (i.p. 0.1 ml/g of mouse; for details see *drugs*) and transferred to the MRI facility for scanning. (B) The comparison between hemispheres (native image vs vertically flipped image; for details see *materials and methods*) showed a significant cluster with stronger signal at the right dHPC (collection threshold $p < 0.01$, $K_e > 20$ voxels; not significant after whole-brain correction;

qualitative representation), adjacent to the fiber tip location. This cluster can be visualized in several plates on the rostral-caudal extent (e.g., from AP -2.06 to -2.46) and it indicates that increased MEMRI signal (as a consequence of Mn^{2+} accumulation) is activity-dependent.

3.2. **Experiment 2: Mn^{2+} dynamics in the brain after partial sensory deprivation (whiskers trimming)**

To investigate the possible influence of neuronal activity on Mn^{2+} accumulation and transport in neurons after its entrance, I designed the following experiment (figure 6A). After 8 daily injections of $MnCl_2$ (i.p.; 20 mg/kg; 24h intervals) and a baseline scan (scan 1), all $MnCl_2$ injections were stopped and animals were subjected to partial sensory deprivation (unilateral whiskers trimming). 7 days later the animals were re-scanned (scan 2). From the first day of $MnCl_2$ injections until the last scan (scan 2) animals were housed in a sensory enriched environment. For the detailed description of the experimental design and procedures please check *Materials and Methods*.

Due to the interval between the two MEMRI scans (7 days) unspecific signal decay was expected, and it was corrected by adding the global image intensities as another nuisance regressor, together with the CSF (Grunecker et al., 2013). After correction, I observed only one cluster with higher signal in scan 1 compared to scan 2 (scan 1 > scan 2). This cluster was located in the left barrel cortex ($p_{FWE, cluster}$ = 0.009, cluster extent 236 voxel), which represents the untrimmed whiskers (figure 6; Table 1). On the opposite comparison (scan 1 < scan 2) a large number of brain structures could be observed (due to partly unspecific dilution of Mn^{2+} between scan 1 and scan 2, I used a threshold of $p < 0.05$, uncorrected. The results are therefore qualitative only): olfactory bulbs, orbital area, islands of Calleja, supplemental somatosensory area, medial thalamic nuclei, caudoputamen, temporal association area, anterior pretectal nucleus, nucleus of the optic tract, anterolateral visual area, perirhinal area, temporal association area, ectorhinal area, subiculum — ventral part, dentate gyrus — ventral part, pontine nuclei, retrosplenial area, superior vestibular nucleus, cerebellum (figure 6B and table 1). Strikingly, 85% of these structures

are efferent of the barrel cortex (table 1), according to previous reports in the literature.

These findings suggest that specific neuronal activity elicited by the remaining whiskers accelerates the transport of Mn^{2+} to efferent structures of the entrance site in the brain. Conversely, the activity blockade resulting from the sensory deprivation seems to lead to decreased or slowed Mn^{2+} transport to projection sites. Taken together, these results point to an activity-dependent axonal transport of Mn^{2+}. Additionally, the fact that not only first-order, but also second order efferents from the barrel cortex showed higher signal intensities in scan 2 compared to scan 1 points to an activity-dependent transsynaptic transport of Mn^{2+}.

For a complete description of the theoretical background leading to this experiment, its experimental design, results and discussion please refer to the published manuscript (Almeida-Correa et al., 2018) in the appendix.

RESULTS Experiment 2: Mn2+ dynamics in the brain after partial sensory deprivation (whiskers trimming)
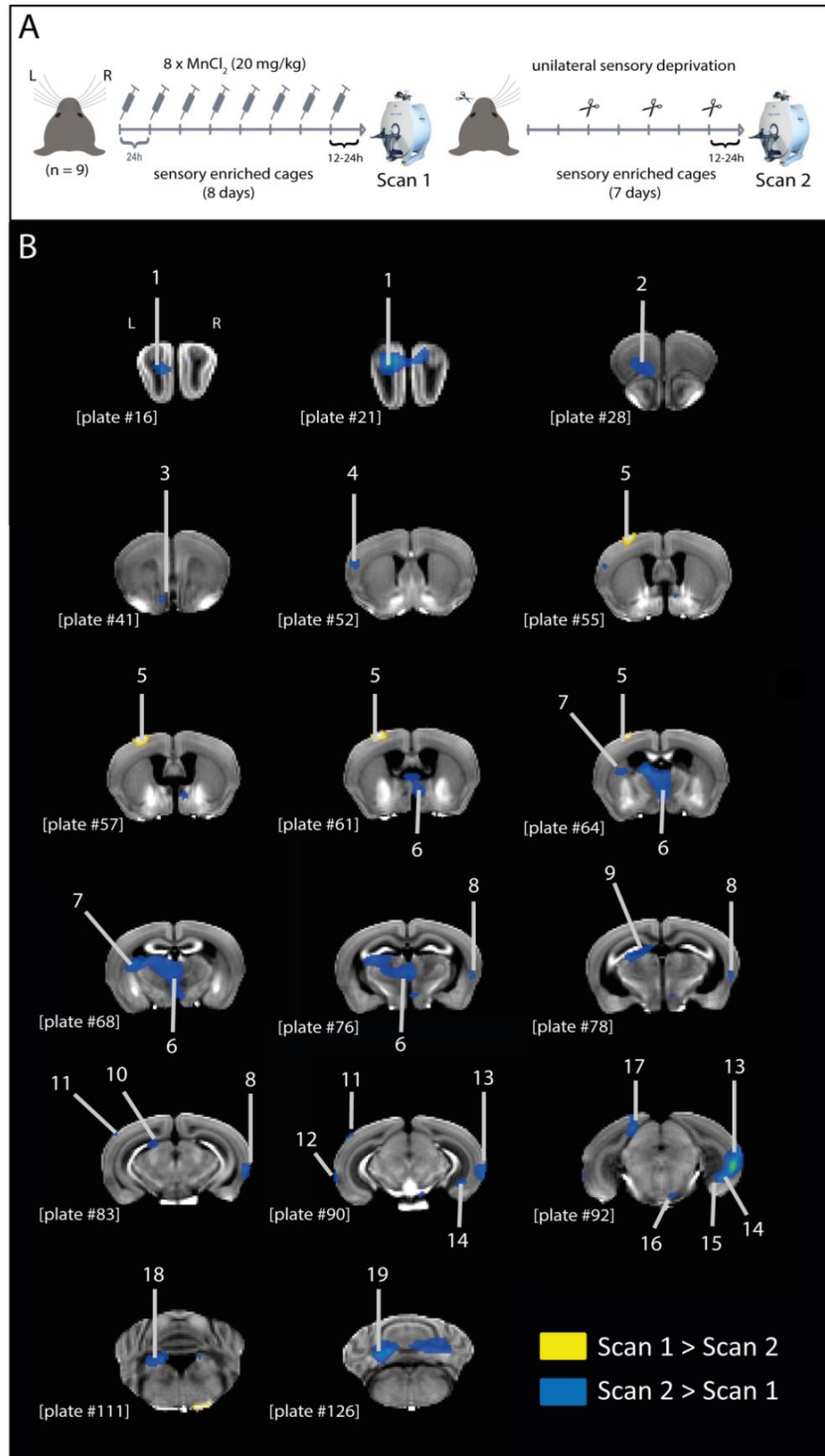
Figure 6: *MEMRI contrast differences after unilateral sensory deprivation.* (A) Graphic representation of experimental design. Mice were treated with MnCl2 (20 mg/kg; i.p.) for 8 days, while housed in a sensory enriched environment, until scan 1.

Immediately after scan 1, mice had their left whiskers trimmed (procedure repeated every 2 days) and remained in the sensory enriched environment for 7 more days without further MnCl$_2$ injections, until scan 2. (B) Representative coronal brain slices indicating the structures showing differential MEMRI signal in scans 1 and 2 (yellow: scan 1 > scan 2; blue: scan 2 > scan 1). Brain structures indicated in the figure: 1, olfactory bulb; 2, orbital area; 3, islands of Calleja; 4, supplemental somatosensory area; 5, barrel cortex; 6, medial thalamic nuclei; 7, caudoputamen; 8, temporal association area; 9, anterior pretectal nucleus; 10, nucleus of the optic tract; 11, anterolateral visual area; 12, perirhinal area; 13, temporal association area + ectorhinal area + perirhinal area; 14, subiculum — ventral part; 15, dentate gyrus — ventral part; 16, pontine nuclei; 17, retrosplenial area; 18, superior vestibular nucleus; 19, cerebellum. Plate numbers under brain slices correspond to the reference plate of the Allen Mouse Brain Atlas used to define the structures. (reproduced from (Almeida-Correa et al., 2018))

Table 1: *List of structures showing differential MEMRI signal between scans 1 and 2 (figure 6), ipsi or contralateral to the reference point (left barrel cortex).* (reproduced from (Almeida-Correa et al., 2018))

Brain structures	# on Figure 1	MEMRI signal ≠		Barrel cortex efferent?*	
		ipsi (L)	contra (R)	ipsi (L)	contra (R)
Olfactory bulb—anterior	1	blue			
Olfactory bulb—posterior	1	blue	blue		
Orbital area	2	blue		green	
Islands of Calleja (striatum)	3	blue			
Supplemental somatosensory area	4	blue		green	green
BARREL CORTEX	**5**	yellow			
Medial thalamic nuclei—anterior	6		blue	green	green
Medial thalamic nuclei—posterior	6	blue	blue	green	green
Caudoputamen	7	blue		green	green
Temporal association areas	8		blue		
Lateral posterior nucleus of the thalamus	6	blue		green	
Dorsal part of the lateral geniculate complex	6	blue		gray	
Parafascicular nucleus	6	blue		gray	
Posterior complex of the thalamus	6	blue		green	
Anterior pretectal nucleus	9	blue			
Lateral posterior nucleus of the thalamus	6	blue		green	
Nucleus of the optic tract	10	blue			
Anterolateral visual area	11	blue		green	
Perirhinal area	12	blue		green	green
Ectorhinal area	13		blue		green
Subiculum—ventral part	14		blue		
Dentate gyrus—ventral part	15		blue		
Pontine nuclei	16		blue	green	
Retrosplenial area	17	blue		green	
Superior vestibular nucleus (medulla)	18	blue			
Cerebellum	19	blue	blue		
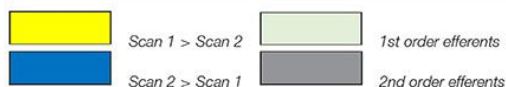
Legend:
- yellow: Scan 1 > Scan 2
- blue: Scan 2 > Scan 1
- light green: 1st order efferents
- gray: 2nd order efferents

*based on the following references: (White and DeAmicis, 1977; Ohara et al., 1980; Montero and Scott, 1981; Ohara and Lieberman, 1981, 1985; Hoogland et al., 1987; Cornwall and Phillipson, 1988; Welker et al., 1988; Hoogland et al., 1991; Chen et al., 1992; Raos and Bentivoglio, 1993; Bourassa et al., 1995; Hazrati et al., 1995; Pinault et

al., 1995; Pinault and Deschenes, 1998; Veinante et al., 2000; Wright et al., 2000; Aronoff et al., 2010; Zakiewicz et al., 2014; Tang et al., 2016; Guo et al., 2017; Sumser et al., 2017)

3.3. Experiment 3: *In vivo* spatial learning matrices (for PL and RL) revealed by MEMRI

WCM PL + MEMRI

As reported before and confirmed by our experiment 1, MEMRI reflects Mn^{2+} signal correspondent to neuronal activity. Therefore, this technique can be used in combination with a behavioral task to detect brain structures that are more active during behavioral performance, and likely learning processes. With that in mind, I combined intraperitoneal injections of 20 mg/kg $MnCl_2$ (Sigma-Aldrich, Steinheim, Germany) every 24 h for eight consecutive days (8 x 20/24 h) to C57BL/6N mice, with 8 days of learning in the water cross maze (WCM) under the protocol of place learning (PL). 18 out of 20 mice learned the task, as indicated by accuracy scores above 83% by the end of training. These mice were included into further analysis (figure 7).

The whole brain voxel-wise analyses of MEMRI signal was divided into 3 parts, using different behavioral scores as regressors: (i) latency from days 1 to 4 (collection threshold $p < 0.01$, $K_e > 50$); (ii) latency from days 5 to 8 (collection threshold $p < 0.01$, $K_e > 65$); (iii) accuracy from days 1 to 8 (collection threshold $p < 0.01$, $K_e > 65$ for positive/direct correlation, $K_e > 90$ for negative/inverse correlation). With these analyses I was able to identify brain structures whose signal correlated with the behavioral measures. Namely, the signal in the dorsal hippocampus, subfield CA3 (dCA3; $p_{FWE-corr} = 0.007$, $K_e = 105$, T-value = 8.78), left hemisphere, inversely correlated with early latency (d1-d4; steep learning phase). The same brain structure, dHPC, subfields CA2 and CA3, was also inversely correlated with late latency (d5-d8; plateau learning phase). This time, however, the correlation was found for both hemispheres

60

RESULTS Experiment 3: In vivo spatial learning matrices (for PL and RL) revealed by MEMRI

(left: $p_{\text{FWE-corr}}$ = 0.052, K_e = 69, T-value = 5.25; right: $p_{\text{FWE-corr}}$ = 0.001, K_e = 138, T-value = 5.59). Additionally, a positive correlation was found between the late latency (d5-d8) and the periaqueductal grey (PAG; $p_{\text{FWE-corr}}$ = 0.049, K_e = 70, T-value = 5.10). For accuracy, an inverse correlation was found with the basolateral amygdala (BLA, left hemisphere; $p_{\text{FWE-corr}}$ = 0.011, K_e = 94, T-value = 5.89) and at the visual cortex (VIS, right hemisphere; $p_{\text{FWE-corr}}$ = 0.008, K_e = 99, T-value = 6.86); a positive correlation was found for the ventral hippocampus (vHPC; $p_{\text{FWE-corr}}$ = 0.049, K_e = 69, T-value = 7.90), left hemisphere. Interestingly, when directly comparing the MEMRI signal of the BLA with the vHPC I found a strong inverse correlation (r = 0.82; p < 0.0001), indicating that these structures might be working in concert, in opposite directions, during performance and learning of this task. There was also a inverse correlation between the VIS and the vHPC (r = 0.59; p < 0.01), even if not as strong.
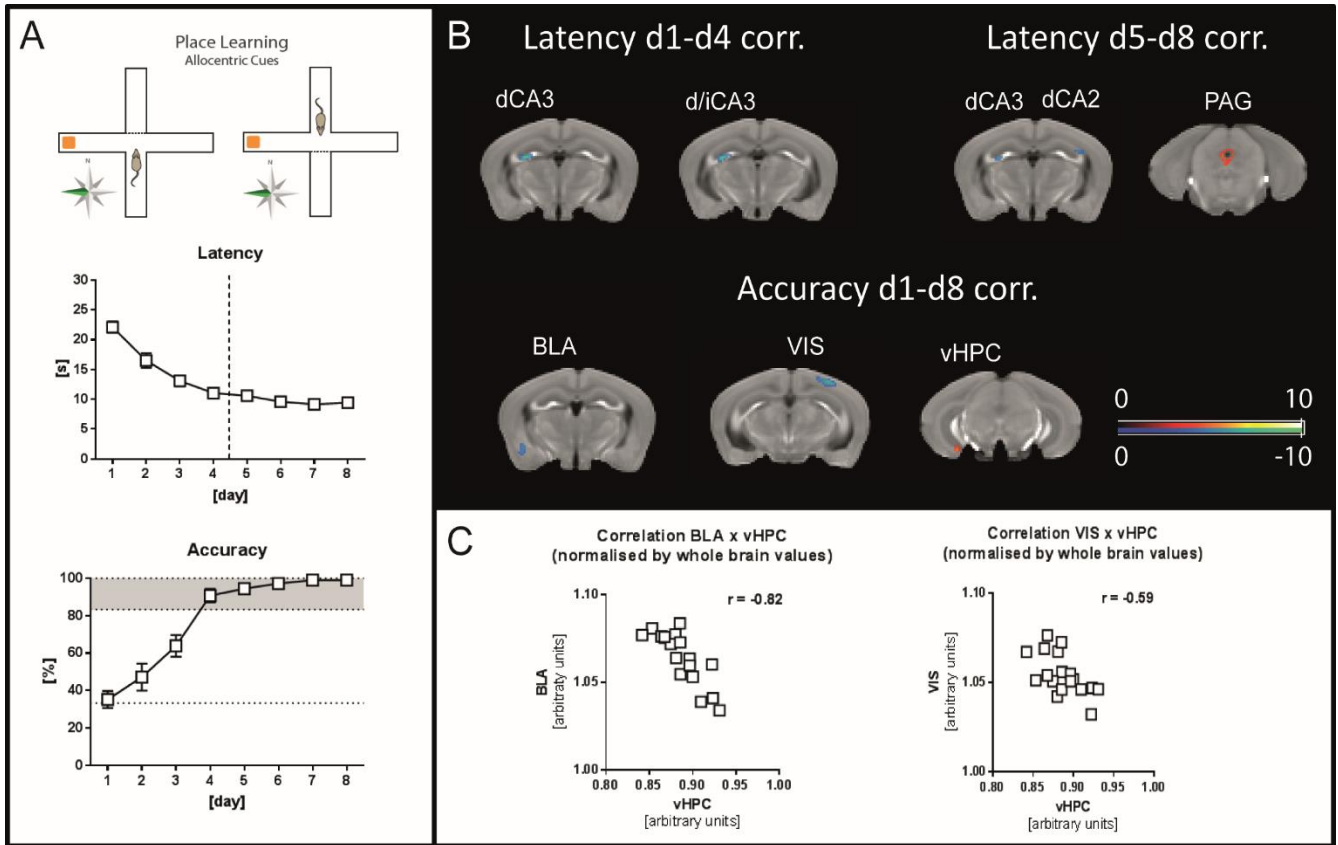
Figure 7: *WCM PL + MEMRI.* (A) Animals (n = 18) were trained in the WCM under the place learning (PL) protocol. Latency and accuracy are displayed for the duration of training (d1-d8). (B) Latency values were dived into early (d1-d4) and late (d5-d8) and correlated with MEMRI contrasts in a whole brain voxel-wise manner (with the unspecific whole brain intensity used as a nuisance regressor). Latency d1-d4 inversely correlates with a cluster on the left dorsal hippocampus subfield CA3 (dCA3; $p_{FWE-corr}$ = 0.007, K_e = 105, T-value = 8.78). Latency d5-d8 inversely correlates with the left dorsal hippocampus subfield CA3 (dCA3) and right dorsal hippocampus subfield CA2 (dCA2) (left: $p_{FWE-corr}$ = 0.052, K_e = 69, T-value = 5.25; right: $p_{FWE-corr}$ = 0.001, K_e = 138, T-value = 5.59) and directly correlates with the periaqueductal grey (PAG; $p_{FWE-corr}$ = 0.049, K_e = 70, T-value = 5.10). Accuracy inversely correlates with the left basolateral amygdala (BLA; $p_{FWE-corr}$ = 0.011, K_e = 94, T-value = 5.89) and right visual area (VIS; $p_{FWE-corr}$ = 0.008, K_e = 99, T-value = 6.86), and directly correlates with the ventral hippocampus (vHPC; $p_{FWE-corr}$ = 0.049, K_e = 69, T-value = 7.90). Color coding depicts t-values. (C) Correlation of MEMRI signal intensities among structures depicted in the lower panel of B, normalized to the individual's whole brain signal intensity. Left: correlation between BLA and vHPC (r = 0.82). Right: correlation between VIS and vPHC (r = 0.59). For A: data are presented as mean ± s.e.m.

These results are in line with the already described hippocampus involvement in place learning in the water cross maze (Kleinknecht et al., 2012).

Thus, they can be used as a proof of concept of the validity of MEMRI on the identification of brain structures related to a given task.

Good vs bad performers

To further investigate the possible interplay of performance level and specific activation in given brain structures, I first assigned the mice into good or bad performers according to their behavioral performance using median split. As explained in detail before (see *materials and methods*), the accuracy score of the animals was calculated as the average of all 8 days of training, and the segregation into two groups was made by a median split of this data. All animals with accuracy score above or at the median were considered good performers, all animals with accuracy score below the median were considered bad performers (figure 8).

In the analysis of the standard behavioral parameters in the WCM (figure 8A) I observed a significant difference in accuracy levels (interaction: $F_{(7, 112)}$ = 5.9, p < 0.0001; group: $F_{(1, 16)}$ = 72.6, p < 0.0001; 2-way ANOVA for repeated measures). Post-hoc analysis revealed that this group difference was related to accelerated learning in the beginning of training with the performance of both groups converging in the end (figure 8). Accordingly, the percentage of accurate learners was significantly higher in the good performers group at day 2 ($\chi^2_{2, N=18}$ test = 5.143, p = 0.023) and day 3 ($\chi^2_{2, N=18}$ test = 11.45, p = 0.0007), and there was a trend to difference in day 4 ($\chi^2_{2, N=18}$ test = 3.6, p = 0.058) (figure 8). Interestingly, group assignment on basis of accuracy scores did not reflect a similar segregation of escape latencies (see latency score in figure 8). This indicates that latency alone is not a reliable parameter to evaluate how well animals perform the task. Moreover, it does not relate to the subsequently described group differences in Mn^{2+} accumulation.

I next compared the MEMRI contrasts of good and bad performers. To determine clusters showing cluster-based FWE-corrected p values < 0.05, I used a collection threshold of p < 0.005 and minimum cluster size of 200 voxels. Only

one cluster was found, showing significantly stronger signal in bad performers compared to good performers (bad > good; figure 8B; $p_{FWE-corr} = 0.024$, $K_e = 201$, T-value = 6.34). This cluster is centered on the basolateral amygdala (BLA), extending rostrally to the perirhinal (PERI), entorhinal (ENTl, lateral part) and piriform (PIR) cortical areas. There was no significant cluster in the inverse comparison (bad < good).
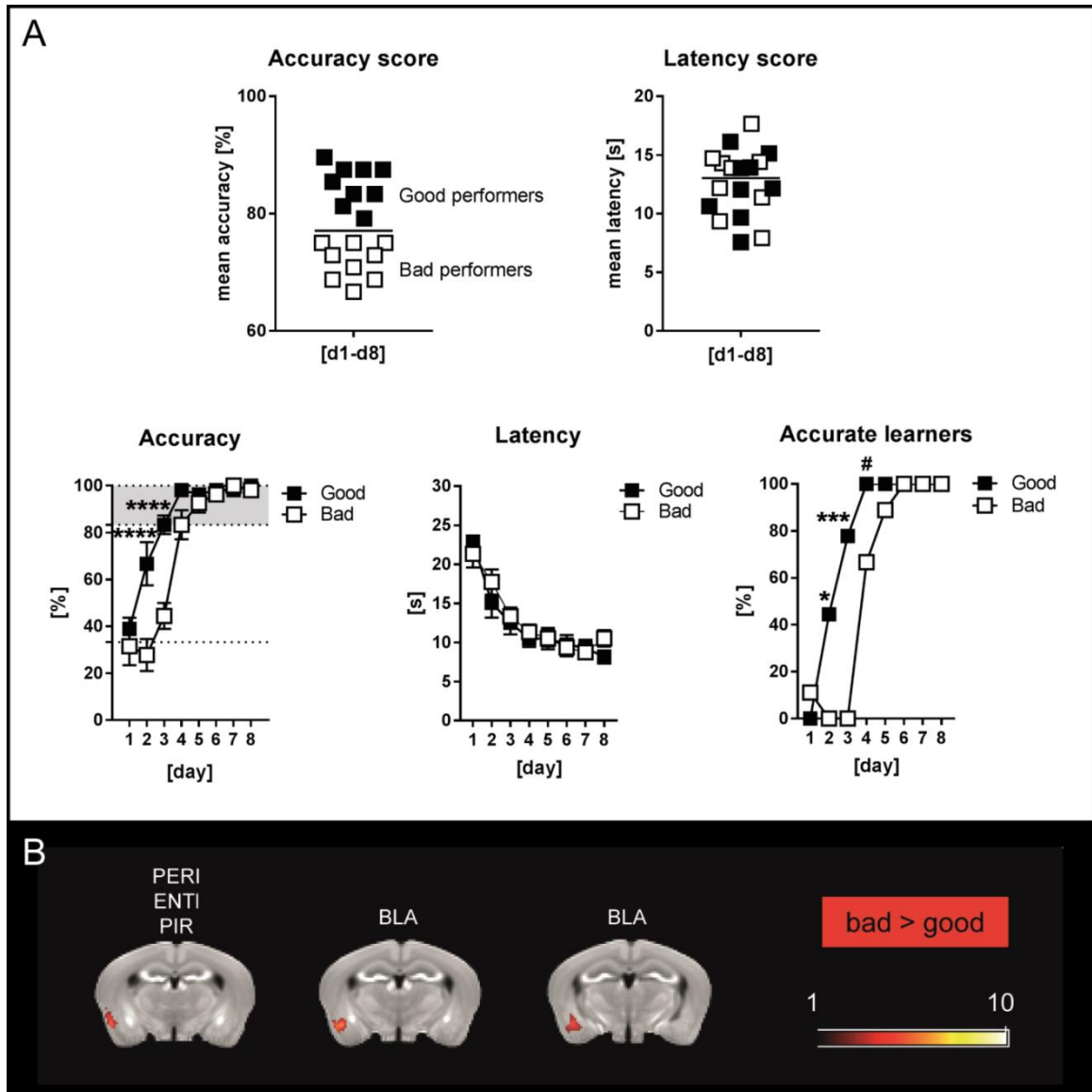
Figure 8: *WCM PL – good vs bad performers.* (A) Animals (n = 18) were categorized as good or bad performers by median split on basis of their accuracy score (top left), which was not reflected by differences in latency (top right). Assessed over the course of training, accuracy was higher for good performers in the beginning of training, with both groups converging in the end. # p < 0.06 (trend); * p < 0.05; *** p < 0.001; **** p <

0.0001 (2-way ANOVA followed by Sidak's post-hoc test or χ^2 test). (B) Representative coronal brain slices showing the results of the comparison of MEMRI contrasts of good vs bad performers (collection threshold $p_{uncorrected} < 0.005$; $p_{FEW\text{-}corr}$ values < 0.05, $K_e > 200$). Only one cluster was found for bad > good ($p_{FWE\text{-}corr} = 0.024$, Ke = 201, T-value = 6.34). This cluster is centered on the basolateral amygdala (BLA) and it comprises the perirhinal (PERI), entorhinal (ENTl, lateral part) and piriform (PIR) cortical areas. No significant cluster in the inverse comparison (bad < good) was found. For A: data are presented as mean ± s.e.m.

WCM RL + MEMRI

Aiming to distinguish the specific brain structures involved in place and response learning, I repeated the experiment in a new cohort of mice using the response learning (RL) protocol. This time 22 out of 24 mice learned the task, as indicated by accuracy scores above 83% by the end of training. These mice were included into further analysis.

After performing a whole brain voxel-wise analysis, as described above (collection threshold $p < 0.001$, $K_e > 90$ voxels), I identified several structures which MEMRI signal correlated with the latency measures (figure 9). More specifically, a cluster in the hippocampus, subfield CA3 ($p_{FWE\text{-}corr} = 0.001$, $K_e = 200$, T-value = 5.18), was inversely correlated with early latency (d1-d4). This cluster extended from the dorsal part (dCA3) to the ventral part (vCA3) of the hippocampus, including the intermediate part (iCA3). For the late latency (d5-d8) there were <u>inverse correlations</u> with the piriform area (PIR; right hemisphere; $p_{FWE\text{-}corr} < 0.001$, $K_e = 309$, T-value = 5.77), the lateral septal nucleus (LS; right hemisphere; $p_{FWE\text{-}corr} = 0.035$, $K_e = 98$, T-value = 4.76), the primary somatosensory area – barrel field (SSp-bfd; left hemisphere; $p_{FWE\text{-}corr} < 0.001$, $K_e = 530$, T-value = 7.65), the ectorhinal and perirhinal areas (ECT + PERI; right hemisphere; $p_{FWE\text{-}corr} = 0.002$, $K_e = 164$, T-value = 4.95), the visual area (VIS; left hemisphere; $p_{FWE\text{-}corr} < 0.001$, $K_e = 211$, T-value = 6.13), the ventral part of the hippocampus subfields CA1 and CA3 and the substantia nigra – reticular part (vCA1 + vCA3 + SNr; right hemisphere; $p_{FWE\text{-}corr} = 0.011$, $K_e = 126$, T-value = 5.45). <u>Direct correlations</u> were found with the main olfactory bulb, the orbital area (MOB + ORB; right hemisphere; $p_{FWE\text{-}corr} = 0.004$, $K_e =$

151, T-value = 7.14), the bed nucleus of the stria terminalis (BST; right hemisphere; p $_{FWE-corr}$ = 0.002, K$_e$ = 173, T-value = 4.93), the retrosplenial area (RSP; midline region; p $_{FWE-corr}$ = 0.003, K$_e$ = 158, T-value = 6.22), the basomedial amygdala (BMA; right hemisphere; p $_{FWE-corr}$ = 0.048, K$_e$ = 91, T-value = 6.40), the dentate gyrus of the hippocampus (DG; left hemisphere, p $_{FWE-corr}$ = 0.046, K$_e$ = 92, T-value = 5.93), the ventral posteromedial nucleus of the thalamus (VPM; left hemisphere; p $_{FWE-corr}$ = 0.040, K$_e$ = 95, T-value = 4.81) and the inferior colliculus (IC; right hemisphere; p $_{FWE-corr}$ = 0.027, K$_e$ = 104, T-value = 7.70). There was no correlation with accuracy.
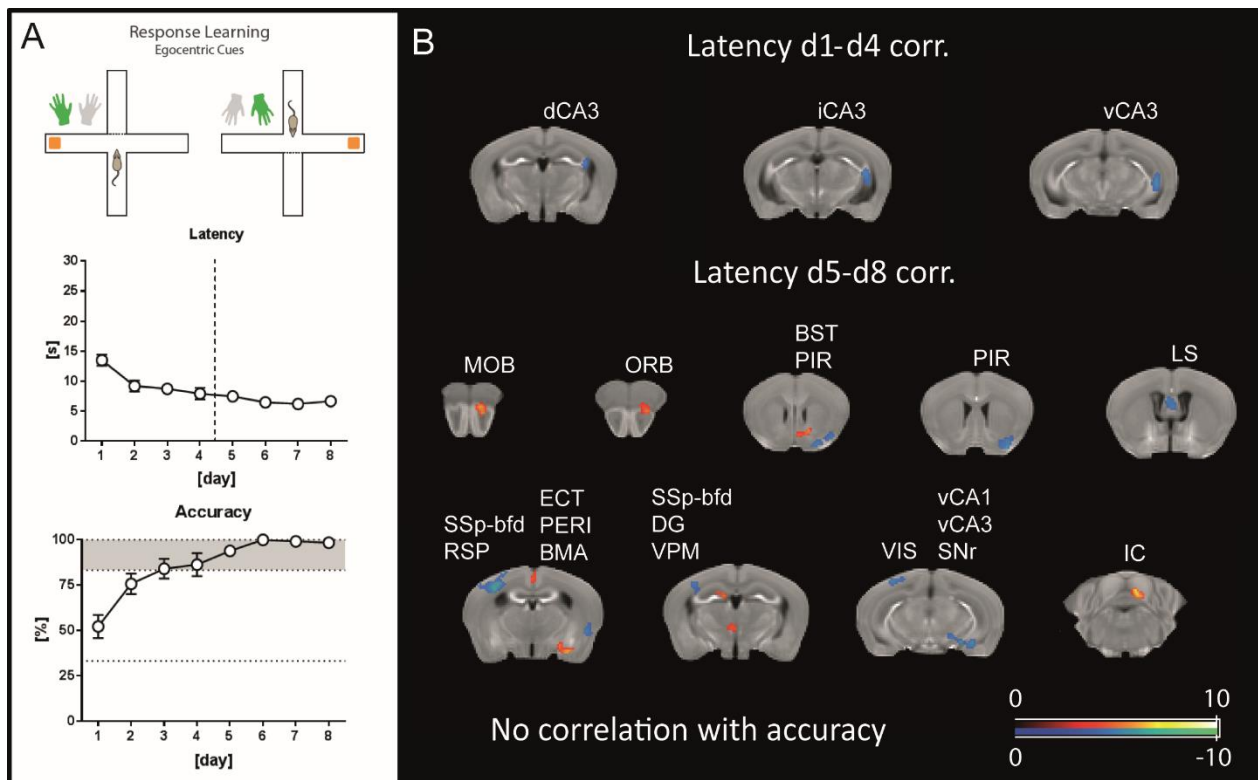
Figure 9: *WCM RL + MEMRI.* (A) Animals (n = 22) were trained in the WCM under the response learning (RL) protocol. Latency and accuracy are displayed for the duration of training (d1-d8). (B) Latency d1-d4 inversely correlates with a cluster comprising the right hippocampus subfield CA3 dorsal (dCA3), intermediate (iCA3) and ventral (vCA3) parts (p $_{FWE-corr}$ = 0.001, K$_e$ = 200, T-value = 5.18). Latency d5-d8 inversely correlates with the right piriform area (PIR; p $_{FWE-corr}$ < 0.001, K$_e$ = 309, T-value = 5.77), the lateral septal nucleus (LS; p $_{FWE-corr}$ = 0.035, K$_e$ = 98, T-value = 4.76), the left primary somatosensory area – barrel field (SSp-bfd; p $_{FWE-corr}$ < 0.001, K$_e$ = 530, T-value = 7.65), the right ectorhinal and perirhinal areas (ECT + PERI; p $_{FWE-corr}$ = 0.002, K$_e$ = 164,

T-value = 4.95), the left visual area (VIS; p $_{FWE-corr}$ < 0.001, K_e = 211, T-value = 6.13), the right ventral hippocampus subfields 1 (vCA1) and 3 (vCA3) and the substantia nigra, reticular part (SNr) (vCA1 + vCA3 + SNr; p $_{FWE-corr}$ = 0.011, K_e = 126, T-value = 5.45). The clusters directly correlated to latency d5-d8 were the right main olfactory bulb (MOB) and orbital area (ORB) (MOB + ORB; p $_{FWE-corr}$ = 0.004, K_e = 151, T-value = 7.14), the right bed nucleus of the stria terminalis (BST; p $_{FWE-corr}$ = 0.002, K_e = 173, T-value = 4.93), the medial retrosplenial area (RSP; p $_{FWE-corr}$ = 0.003, K_e = 158, T-value = 6.22), the right basomedial amygdala (BMA; p $_{FWE-corr}$ = 0.048, K_e = 91, T-value = 6.40), the left dentate gyrus (DG; p $_{FWE-corr}$ = 0.046, K_e = 92, T-value = 5.93), the left ventral posteromedial nucleus of the thalamus (VPM; p $_{FWE-corr}$ = 0.040, K_e = 95, T-value = 4.81) and the right inferior colliculus (IC; p $_{FWE-corr}$ = 0.027, K_e = 104, T-value = 7.70). There was no correlation with accuracy levels. Color coding depicts t-values. For A: data are presented as mean ± s.e.m.

Good vs bad performers

Similarly to the add-on investigation of performance level presented for mice which underwent PL on the WCM, I also split the mice which underwent RL on the WCM in two groups (good performers and bad performers) on basis of their accuracy scores using median split.

I observed a significant difference between groups for accuracy levels (interaction: $F (7, 140) = 5.849$, $p < 0.0001$; group: $F (1, 20) = 35.07$, $p < 0.0001$; 2-way ANOVA for repeated measures). Post-hoc analysis revealed that this group difference was related to an accelerated learning of good performers until day 4 of training with the performance of both groups converging in the end (figure 10). The latency values were significantly lower for good performers (interaction: $F (7, 140) = 5.272$, $p < 0.0001$; 2-way ANOVA for repeated measures) in the first 2 days of training. The percentage of accurate learners was significantly higher for good performers on day 1 ($\chi^2_{2, N=22}$ test = 5.712, p = 0.017), day 2 ($\chi^2_{2, N=22}$ test = 8.564, p = 0.003), day 3 ($\chi^2_{2, N=22}$ test = 4.09, p = 0.043) and day 4 ($\chi^2_{2, N=22}$ test = 7.062, p = 0.008).

When comparing the MEMRI contrasts of good and bad performers I did not find any significant difference.
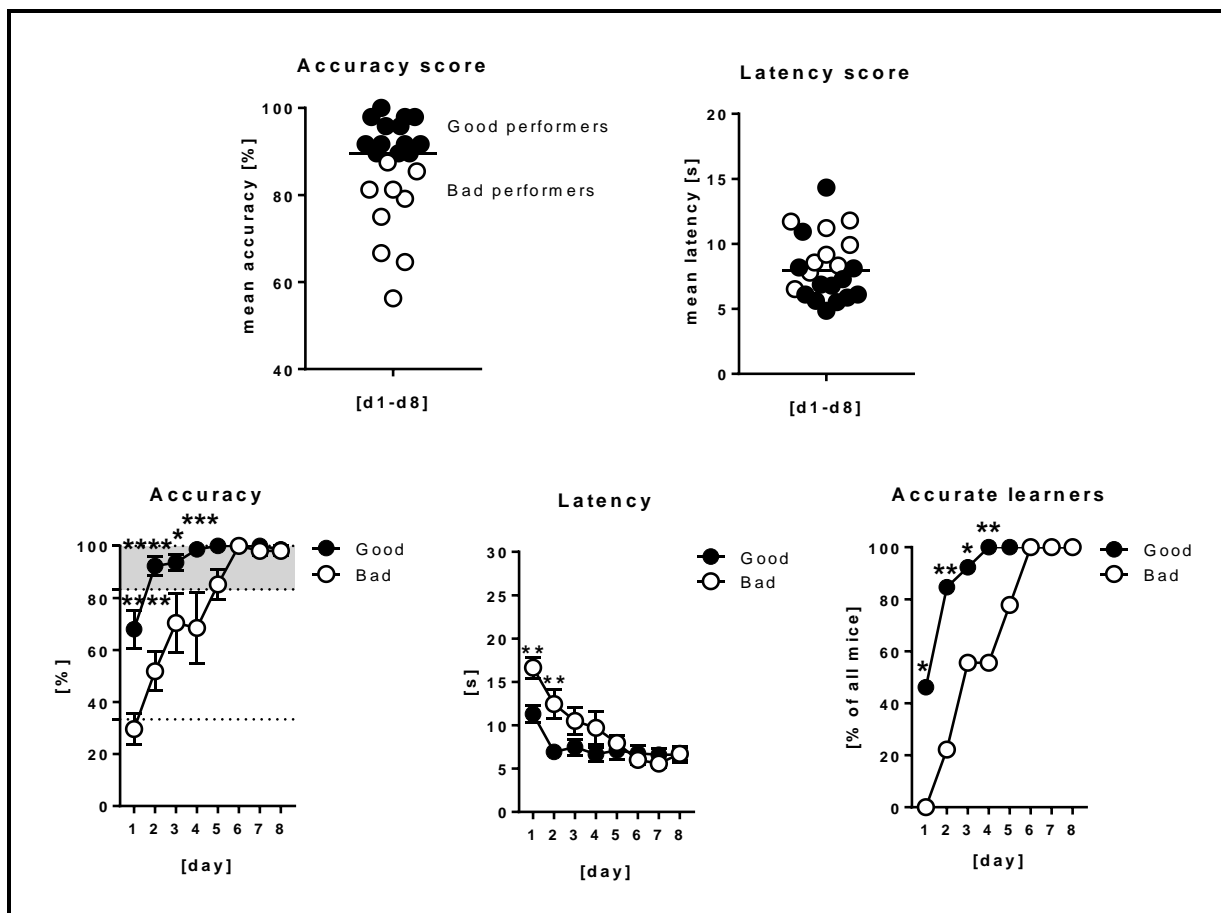
Figure 10: *WCM RL – good vs bad performers.* Animals (n = 22) were split into good or bad performers based on their accuracy score (top left) as described in figure 8 (PL). Latency score is also shown (top right). Accuracy was higher for good performers on the first half of training (day 1, **** $p < 0.0001$; day 2, **** $p < 0.0001$; day 3, * $p < 0.05$; day 4, *** $p = 0.001$; 2-way ANOVA followed by Sidak's post-hoc test). Latency values were significantly lower for good performers also in the beginning of the training period (day 1, ** $p < 0.01$; day 2, ** $p < 0.01$; 2-way ANOVA followed by Sidak's post-hoc test). Additionally, the percentage of accurate learners was significantly higher in the good performers group (day 1, * $p < 0.05$; day 2, ** $p < 0.01$; day 3, * $p < 0.05$; day 4, ** $p < 0.01$; χ^2 test). Data are presented as mean ± s.e.m.

Behavioral performance PL vs RL

Before I compared MEMRI results between the two experimental groups, I first compared their behavioral performance (figure 11). The latency was significantly lower in RL than in PL animals (interaction: $F_{(7, 266)} = 6.676$, $p < 0.0001$; group: $F_{(1, 38)} = 28.37$, $p < 0.0001$; 2-ANOVA for repeated

measures). Post-hoc analyses revealed that this difference was stronger on days 1, 2 and 3. Accuracy levels were significantly higher for the RL group (interaction: $F_{(7, 266)} = 4.959$, $p < 0.0001$; group: $F_{(1, 38)} = 6.086$, $p = 0.018$; 2-way ANOVA for repeated measures), specially on the first 3 days of training. This was also reflected in the percentage of accurate learners on day 2 ($\chi^2_{2, N=40}$ test = 5.507, $p = 0.019$) and day 3 ($\chi^2_{2, N=40}$ test = 6.077, $p = 0.014$). The number of wrong platform visits did not differ between groups.

Additionally, I calculated the latency and accuracy scores (as described in *Materials and Methods*) for the individual groups and observed significant differences in both parameters. Namely, the latency was lower for RL ($t_{38} = 5.206$, $p < 0.0001$; unpaired t-test,) and the accuracy was higher for the same group ($t_{38} = 2.467$, $p = 0.0182$; unpaired t-test).

Taken together, these results indicate that animals learn faster under the RL protocol compared to PL. This is reflected by the difference in accuracy levels and number of accurate learners until day 3. Nevertheless, from day 4 on there was no difference between groups, suggesting that animals trained under either protocol can learn the task if the training duration is of at least 4 days.
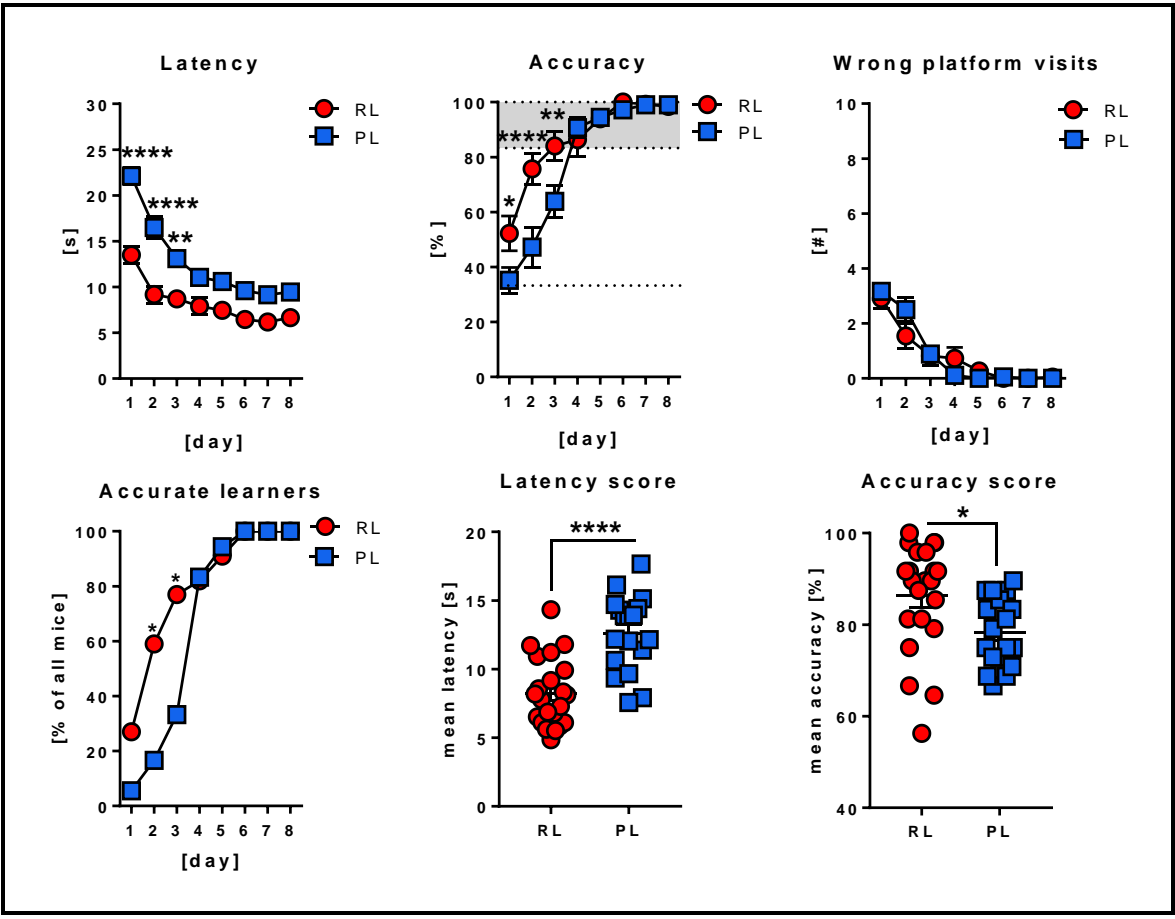
Figure 11: *Mice trained under the RL protocol learn the WCM task faster.* Animals were trained in the WCM using either PL (n = 18) or RL (n = 22) protocols. Latency was significantly lower for RL animals in the beginning of training (day 1, **** $p < 0.0001$; day 2, **** $p < 0.0001$; day 3, ** $p < 0.01$). Conversely, accuracy levels were significantly higher for the RL group (day 1, * $p < 0.05$; day 2, **** $p < 0.0001$; day 3, ** $p < 0.01$; 2-way ANOVA followed by Sidak's post-hoc test). The number of wrong platform visits did not differ between groups. The percentage of accurate learners was significantly higher for the RL group (day 2, * $p < 0.05$; day 3, * $p < 0.05$; χ^2 test). Latency scores were lower (**** $p < 0.0001$; unpaired t-test) and accuracy scores were higher (* $p < 0.05$, unpaired t-test) for the RL group. Data are presented as mean ± s.e.m.

MEMRI PL vs MEMRI RL

To identify the specific neuroanatomical substrates of place learning (PL) versus response learning (RL) I directly compared the MEMRI contrasts. I performed a whole brain voxel-wise analysis with the individual's whole brain intensity values as regressor of no interest, with collection p value < 0.005,

minimum voxel size (K_e) of 20 voxels and FDR correction. I found higher contrast intensities (MEMRI signal) after response learning (RL > PL) in the following brain structures (figure 12 and table 2): accessory olfactory bulb, piriform area, lateral olfactory tract, anterior cingulate area, bed nucleus of the stria terminalis, anterior hypothalamic nuclei, thalamic nuclei, dorsal fornix, retrosplenial area, posterior parietal association area, cortical amygdala, auditory areas, endopiriform nucleus, postpiriform transition area, posterior nucleus of the amygdala, basomedial nucleus of the amygdala, subiculum – ventral part, subiculum – dorsal part, pontine grey, tegmental reticular nucleus, pontine reticular nucleus, periaqueductal grey, pons (nucleus of the lateral lemniscus and superior central nucleus raphe), superior cerebellar peduncle decussation and peduncle pontine nucleus.

The other way around, place learning coincided with higher contrast intensities (RL < PL; figure 12 and table 2) in prelimbic cortex, orbital area, taenia tecta, infralimbic area, lateral septal nucleus, stria terminalis, ventral posterior nucleus of the thalamus, geniculate complex, anterior pretectal nucleus, susbtantia nigra, zona incerta, ectorhinal cortex, perirhinal cortex, presubiculum, temporal association area, medulla (medial vestibular nucleus, nucleus prepositus, nucleus raphe magnus, facial motor nucleus, medial and spinal vestibular nucleus, parvicellular nucleus and intermediate reticular nucleus), cerebellum (interposed nucleus and fastigial nucleus) and nucleus of the solitary tract.

Some structures were present in both comparisons (RL > PL and RL < PL; figure 12 and table 2) in different slices across the rostral caudal extent: main olfactory bulb, motor cortex, piriform area, substantia innominata, lateral entorhinal cortex, simple lobule of the cerebellum.
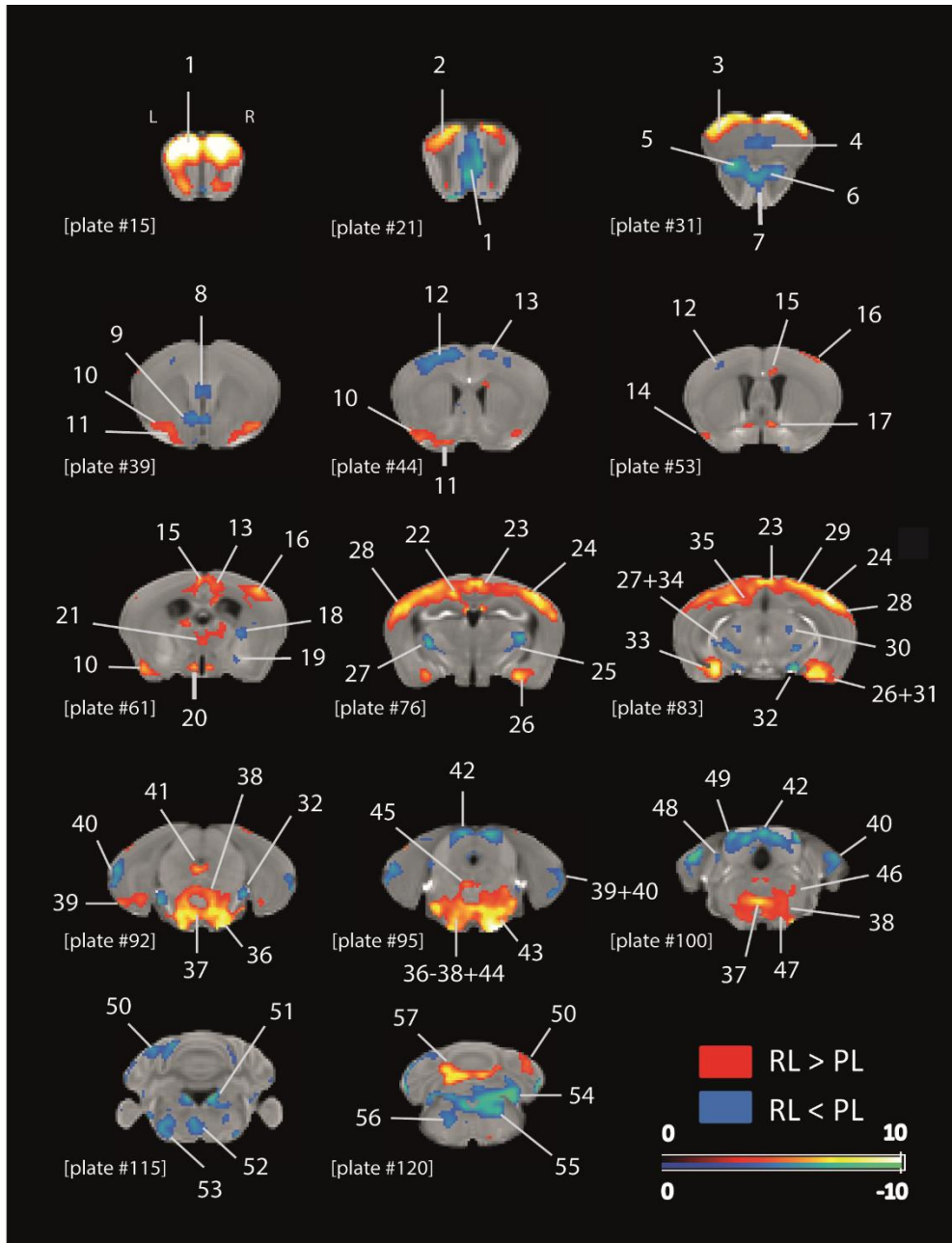
Figure 12: *MEMRI contrast differences for mice trained in the WCM with either the PL or RL protocol.* Representative coronal brain slices indicating the structures showing differential MEMRI signal for RL and PL groups (red/orange/yellow: RL > PL; blue/green: RL < PL). Brain structures indicated in the figure are listed in table 2. Plate numbers under brain slices correspond to the reference plate of the Allen Mouse Brain Atlas which was used to define the structures. Color coding depicts t-values.

Table 2: *List of structures showing differential MEMRI signal between scans of mice trained under the PL protocol vs mice trained under the RL protocol in the WCM*

Brain structure	# on Figure 12	MEMRI signal ≠	$p_{\text{FDR corr}}$	T-value
Main olfactory bulb	1	Red/Blue	<0.001	15.38 / 7.99
Accessory olfactory bulb	2	Red	<0.001	13.16
Motor cortex	3, 13	Red/Blue	<0.001	7.72 / 4.88
Prelimbic cortex	4	Blue	<0.001	4.82
Orbital area	5	Blue	<0.001	7.74
Piriform area	6, 10	Red/Blue	<0.001	5.81 / 4.37
Taenia tecta	7	Blue	<0.001	5.85
Infralimbic cortex	8	Blue	<0.001	5.40
Lateral septal nucleus	9	Blue	<0.001	6.24
Substantia innominata	11, 19	Red/Blue	<0.001	4.83 / 4.56
Somatosensory area	12	Blue	<0.001	5.70
Lateral olfactory tract	14	Red	<0.001	5.40
Anterior cingulate area	15	Red	<0.001	5.20
Somatosensory area – upper limbs	16	Red	<0.001	5.28
Bed nucleus of the stria terminalis	17	Red	<0.001	5.53
Stria terminalis	18	Blue	=0.001	4.36
Anterior hypothalamic nuclei	20	Red	0.001	7.28
Thalamic nuclei	21	Red	<0.001	7.53
Dorsal fornix	22	Red	<0.001	7.53
Retrosplenial area	23	Red	<0.001	9.45
Posterior parietal association area	24	Red	<0.001	9.25
Ventral posterior nucleus of the thalamus	25	Blue	=0.001	4.23
Cortical amygdala	26	Red	<0.001	7.25
Geniculate complex	27	Blue	<0.001	10.82
Auditory areas	28	Red	<0.001	7.76
Visual areas	29	Red	<0.001	7.36
Anterior pretectal nucleus	30	Blue	=0.001	4.40
Endopiriform nucleus	31	Red	<0.001	8.16
Postpiriform transition area	31	Red	<0.001	8.16
Susbtantia nigra	32	Blue	<0.001	8.97
Posterior nucleus of the amygdala	33	Red	<0.001	9.25
Basomedial nucleus of the amygdala	33	Red	<0.001	9.25
Subiculum- ventral part	33	Red	<0.001	9.25
Zona incerta	34	Blue	=0.001	4.61
Subiculum – dorsal part	35	Red	<0.001	5.77
Pontine grey	36	Red	<0.001	13.70
Tegmental reticular nucleus	37	Red	<0.001	8.71
Pontine reticular nucleus	38	Red	<0.001	6.68
Lateral entorhinal cortex	39	Red/Blue	<0.001	7.59 / 6.72
Ectorhinal cortex	40	Blue	<0.001	6.72
Perirhinal cortex	40	Blue	<0.001	6.72
Periaqueductal grey	41	Red	<0.001	6.52
Superior colliculus	42	Blue	<0.001	10.17
Pons: nucleus of the lateral lemniscus	43	Red	<0.001	13.70

Pons: superior central nucleus raphe	44		<0.001	9.18
Superior cerebellar peduncle decussation	45		<0.001	5.73
Peduncle pontine nucleus	46		<0.001	6.29
Superior olivary complex + periolivary region	47		<0.001	7.66
Presubiculum	48		<0.001	6.32
Temporal association area	49		<0.001	10.17
Cerebellum: simple lobule	50		<0.001	5.07 / 6.43
Medulla: medial vestibular nucleus	51		<0.001	7.35
Medulla: nucleus prepositus	51		<0.001	7.35
Medulla: nucleus raphe magnus	52		<0.001	6.36
Medulla: facial motor nucleus	53		<0.001	7.12
Cerebellum: interposed nucleus	54		<0.001	9.00
Cerebellum: fastigial nucleus	54		<0.001	9.00
Medulla: medial and spinal vestibular nucleus	55		<0.001	7.03
Medulla: parvicellular nucleus	55		<0.001	7.03
Nucleus of the solitary tract	55		<0.001	7.03
Medulla: intermediate reticular nucleus	56		<0.001	5.91
Cerebellar commissure and arbor vitae	57		<0.001	8.27

RL > PL and RL < PL, depending on the plate across the rostral caudal extent
RL > PL
RL < PL

3.4. Experiment 4: IEG (c-fos) analysis after learning in the WCM

To elucidate the pattern of Mn^{2+} accumulation seen on the scans I analyzed c-fos expression after learning (at least 5 out of 6 correct trials in one day) in the WCM (PL vs RL vs home cage/HC controls). With this, I aimed at differentiating the structures initially activated during spatial learning (high density of c-fos positive cells) and its underlying connectivity (structures with higher Mn^{2+} signal in the previous experiment) to establish a spatial learning matrix.

Based on the previous results pointing at the hippocampus as the source of signal to its downstream targets (where I observed Mn^{2+} accumulation), this was the first choice of structure to be analyzed. The dorsal and ventral portions of the hippocampus (CA1 subfield) were analyzed as separate ROIs. I found a significant difference between right dorsal hippocampus (dCA1) of the RL group compared to HC (figure 13; group: $F_{(2, 17)} = 3.671$, $p = 0.0473$; 1-way

ANOVA). This difference was not observed when considering values averaged over both hemispheres. There was no difference between the PL group and the other two groups for dCA1. For the ventral hippocampus ROI (vCA1), I observed a significant difference on the left hemisphere between the PL group and HC (figure 13; group: $F_{(2, 13)} = 5.256$, $p = 0.0212$; 1-way ANOVA). Once more, this difference was not observed when both hemispheres were considered. No difference was found between the RL group and the other two groups.

Given my interest in strategy switch during performance in the WCM, and the putative role of the medial prefrontal cortex (mPFC) on this process, I selected its sub-regions, the prelimbic (PrL) and infralimbic (IL) cortices, as ROIs. At the PrL I found a significant difference in the left (figure 13; group: $F_{(2, 22)} = 4.696$, $p = 0.0200$; 1-way ANOVA) and in the right (group: $F_{(2, 22)} = 3.59$, $p = 0.0447$; 1-way ANOVA) hemispheres between the RL group and HC. However, the right hemisphere comparison did not survive multiple comparison correction (Tukey's post-hoc test, $p = 0.0546$, trend). The significant difference was also present when both hemispheres were considered (PrL total, figure 13; group: $F_{(2, 22)} = 5.935$, $p = 0.0087$; 1-way ANOVA). There was no difference considering the PL group. For the IL ROI, there was a significant difference (figure 13; group: $F_{(2, 14)} = 4.662$, $p = 0.0281$; 1-way ANOVA) between the PL group and the HC in the left hemisphere. This difference was also observed when both hemispheres were considered (IL total, figure 13; group: $F_{(2, 14)} = 3.776$, $p = 0.0488$; 1-way ANOVA). No difference was found for the RL group.

These results suggest that all structures analyzed were affected by training in the WCM under either the PL or RL protocols. This corroborates our hypothesis that these are at least some of the structures initially activated upon spatial learning. Moreover, they demonstrate that the hippocampus is activated during learning under both protocols.
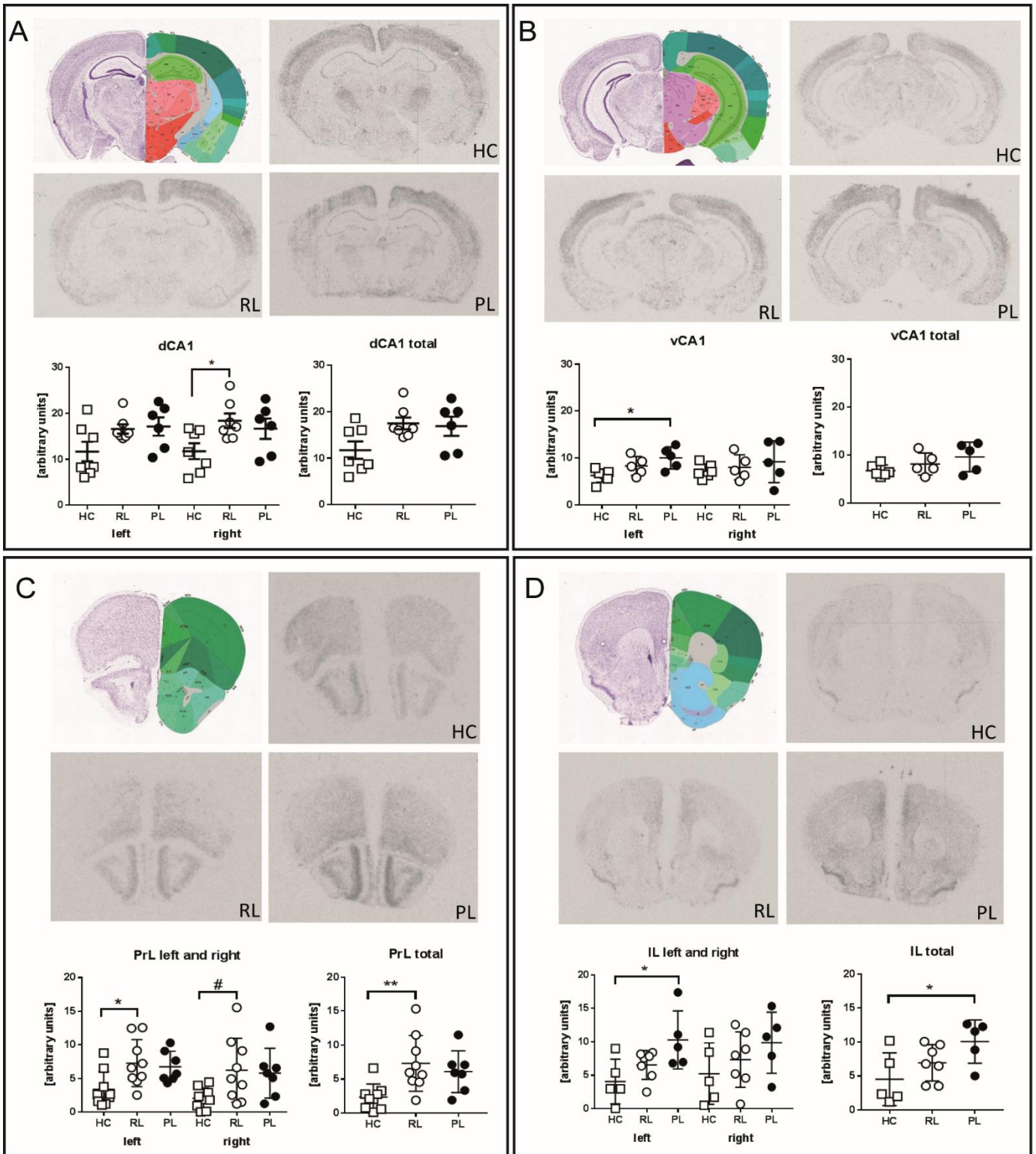
Figure 13: *IEG (c-fos) analysis after WCM learning.* (A-D) Upper panels: representative images of the atlas plates (top left) used as references to define the structures of interest, and the ISH brain slices of the three groups analyzed: HC, home cage controls; RL, mice trained under the response learning protocol; PL, mice trained

under the place learning protocol. Lower panels: quantification of the data. (A) dCA1: HC (n = 7), RL (n = 7) and PL (n = 6). The values of the RL group were significantly higher than those of the HC group on the right dorsal hippocampus (dCA1) (* $p < 0.05$). There was no difference when both hemispheres were considered. There was no difference between the PL group and the other two groups. (B) vCA1: HC (n = 6), RL (n = 5) and PL (n = 5). The values of the PL group were significantly higher than those of the HC group on the left hemisphere (* $p < 0.05$). This difference was not observed when both hemispheres were considered. No difference was found between the RL group and the other two groups. (C) PrL: HC (n = 9), RL (n = 9) and PL (n = 7). There was a significant difference in the left (* $p < 0.05$) and trend to difference in the right hemisphere (# $p < 0.06$) between the RL group and HC. This difference was also present for total PrL (both hemispheres) (** $p < 0.01$). There was no difference considering the PL group. (D) IL: HC (n = 5), RL (n = 7) and PL (n = 5). The values of the PL group were significantly higher than those of the HC in the left hemisphere (* $p < 0.05$). This difference was also observed when both hemispheres were considered (IL total, * $p < 0.05$). No difference was found for the RL group. Data are presented as mean ± s.e.m. For all analyses: 1-way ANOVA followed by Tukey's post-hoc test. dCA1, dorsal hippocampus subfield CA1; vCA1, ventral hippocampus subfield CA1; PrL, prelimbic area/cortex; IL, infralimbic area/cortex.

3.5. **Spaced vs massed training in the WCM**

As previously described under *materials and methods*, when optogenetic modulation of behavior was combined with performance in the WCM, mice underwent a modified training protocol (regarding the distribution of the 6 daily trials) when compared to the "traditional" spaced protocol used in the experiments so far. This modification from spaced to massed trials protocol was necessary to avoid that animals would be connected/disconnect with the optic fiber cables multiple times during the day, thus increasing their stress levels and the chance that the head implants would be displaced or would fall off. For a graphical representation of the different training protocols please see figure 3.

To check if animals could learn the task under the massed protocol, with the short inter-trial interval (ITI) of 3 min (as opposed to the 10-15 min ITI of the spaced protocol), I assigned mice to two groups. The first group was subjected to spaced PL ("spaced" group) with the regular ITI of 10-15 min, the second group was subjected to massed PL on the WCM ("massed" group) with the shorter ITI of 3 min, and behavioral performance was compared.

There was no difference between groups on latency, accuracy or number of wrong platform visits (figure 14; statistics not shown). There was a significant higher number of accurate learners in group at day 3 ($\chi^2_{2, N=16}$ test = 4, p = 0.045), but not at any other days. Therefore, I consider that both training protocols are appropriate for testing spatial learning behavior and might be applied indistinctively for a training period of at least 4 days.
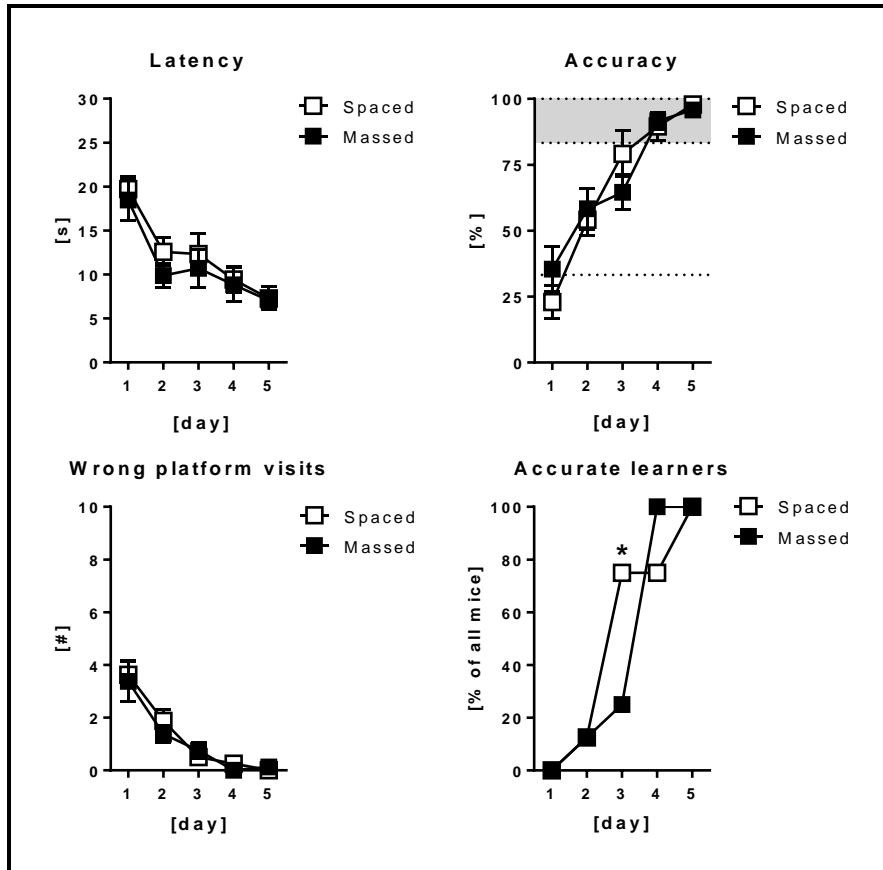
Figure 14: *Place learning in the WCM is largely unaffected by massed training and decreased inter-trial interval.* Animals trained in the WCM under spaced (n = 8) or massed (n = 8) protocols had their behavioral performance compared. There was no significant difference between groups on latency values, accuracy levels or number of wrong platform visits. The percentage of accurate learners was higher for the spaced group on day 3 (* p < 0.05, χ^2 test) but not on the other days. Data are presented as mean ± s.e.m.

3.6. **Experiment 5: dHPC optogenetic inhibition during WCM (PL) recall**

As a "proof of concept" experiment to validate the combination of the WCM with optogenetic manipulation in our setup, I bilaterally injected a viral vector transducing the inhibitory opsin ArchT in the dorsal hippocampus CA3 subfield (dCA3 / dHPC) of C57BL/6N mice and 3 weeks after implanted optic fibers directly above the viral injection target. Following recovery, animals (n = 21) were trained in the WCM for 7 days under the PL protocol without connection to the laser cables. The animals that were accurate learners by day 7 (n = 17 out of 21; figure 15) followed up for the next stage of the experiment. After 1 day of rest, animals were tested for recall of the task, under the same protocol as training, but at this time connected to the laser cables without laser activation in order to habituate them to the intervention procedure. Thus, the analysis presented here does not consider the behavioral data from day 9 (habituation only). On day 10 behavioral performance did not seem to be affected by the cable connections (laser off) anymore and most of the animals could perform the task normally (accurate learners = 90.9%). On day 11, I optogenetically inhibited the dHPC of the animals with green laser (532 nm, 22-26 mW) for the duration of each trial (~ 10 s). I did not observe a significant drop of accuracy or number of accurate learners, other than expected. The latency values or number of wrong platform visits did not significantly differ from days 10 and 11 either. Finally, on day 12, I tested the animals once more with the cables connected and laser off, and also did not observe significant differences in behavior.

Despite the fact that these results are not in line with our expected outcomes for HPC inhibition during a spatial memory test, they brought awareness of the possible impact of the optic fiber implantations on learning the task. This issue is dealt with in more detail later (see figure 17).
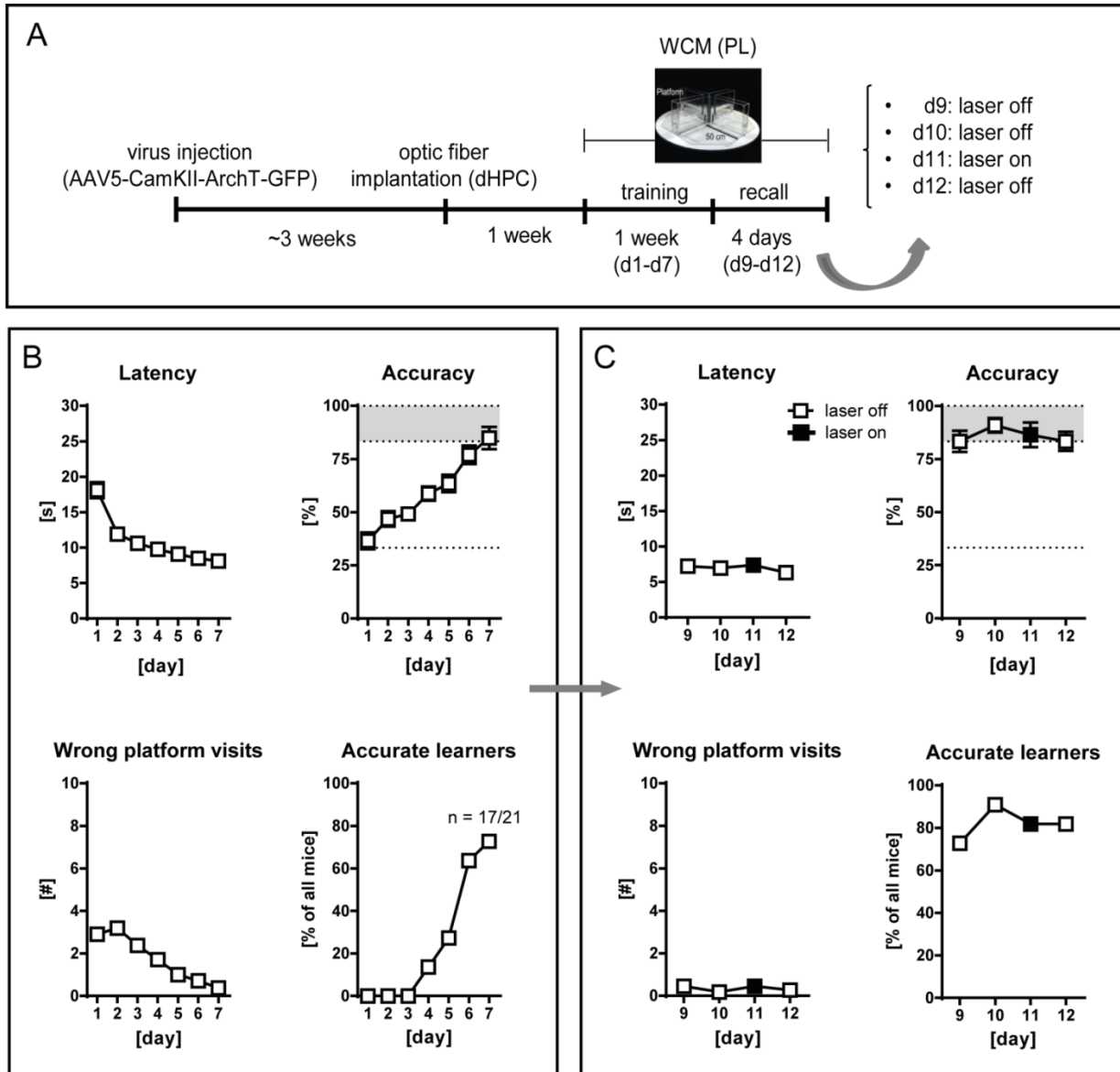
Figure 15: *Optogenetic inhibition of dHPC during spatial memory recall.* (A) Experimental timeline, highlighting the time-points and intervals of different experimental procedures and the laser regime for the recall tests (d9-d12). (B) Behavioral performance of the mice (n = 21) on the training week (d1-d7) in the WCM under the PL protocol. 17 out of 21 mice learned (were considered accurate learners) the task by d7 and followed-up for the recall week. (C) Behavioral performance of the mice (n = 17) during the recall testing period (d9-d12) in the WCM under the PL protocol. There was no significant difference on any of the behavioral parameters between laser on days and laser off day. Data are presented as mean ± s.e.m.

3.7. **Experiment 6: vHPC optogenetic inhibition during WCM (PL) recall**

In line with the previous experiment, and to further investigate the involvement of the ventral HPC, especially the CA3 subfield (which showed a strikingly strong MEMRI signal and correlation with behavioral measurements in experiment 3) in spatial memory in the WCM, I repeated the previous experiment in a new group of mice, this time targeting the ventral CA3 region. Additional differences in the protocol were the duration of recall tests (5 days, d9-d13; instead of 4, as before) and the number of days with optogenetic inhibition (laser on; 2 days, d11 and d12; instead of 1 day, as before).

From a total number of 20 mice which were trained in the WCM for 7 days (d1-d7), 8 have acquired the task in the end of training (figure 16). Only these mice followed up for the recall tests (d9-d13). During the recall period I observed a significant drop in accuracy levels (F (2.455, 17.18) = 5.056, p = 0.0144; 1-way ANOVA), especially from day 10 (laser off) to day 11 (laser on), as revealed by the post-hoc analysis. There was no significant difference in accuracy among the other days or on the other behavioral parameters.

These results indicate a possible role of the vHPC in recall of spatial memory in the WCM, as it was already pointed out by other studies (see *Discussion*). Nevertheless, the small number of subjects in the recall tests limited the power of our analysis and was likely the reason why no further differences between days were observed (e.g. drop in number of accurate learners from days 10 to 11).
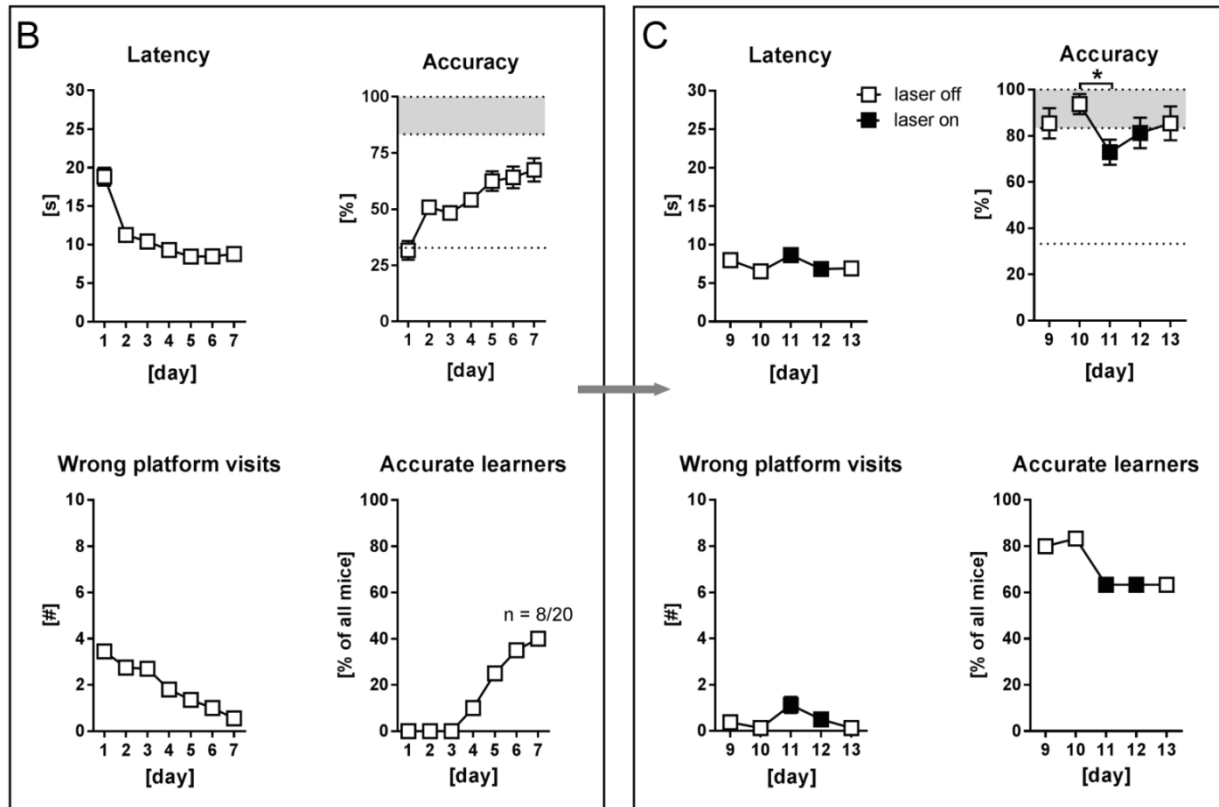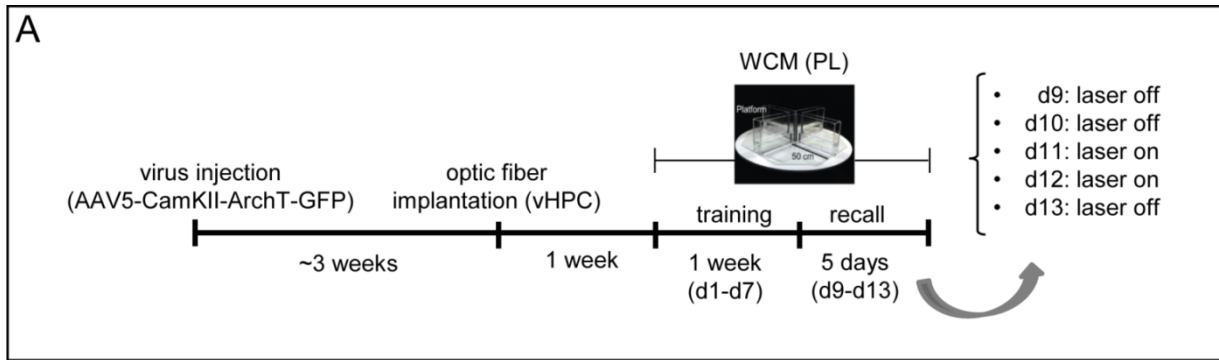
Figure 16: *Optogenetic inhibition of vHPC during spatial memory recall.* (A) Experimental timeline, highlighting the time-points and intervals of different experimental procedures and the laser regime for the recall tests (d9-d13). (B) Behavioral performance of the mice (n = 20) on the training week (d1-d7) in the WCM under the PL protocol. 8 out of 20 mice learned (were considered accurate learners) the task by d7 and followed-up for the recall week. (C) Behavioral performance of the mice (n = 8) during the recall testing period (d9-d13) in the WCM under the PL protocol. There was a significant drop in accuracy from day 10 (laser off) to day 11 (laser on) * p < 0.05 (1-way ANOVA followed by Tukey's post-hoc test). There was no significant difference on the other behavioral parameters between laser on and laser off days. Data are presented as mean ± s.e.m.

3.8. **dHPC vs vHPC implantations and its effects on WCM learning**

Under normal conditions, naïve C57BL/6N mice learn the WCM PL task in 4 to 7 days (e.g. see figure 7, figure 9 and figure 14). Thus, the training duration of this task is up to 7 days, unless a specific investigation requires a prolongation of the protocol, as in experiments 3, for example. Nevertheless, in the last two experiments, not all animals learned the WCM task by day 7. vHPC implanted mice, especially, showed a considerable decrease in accuracy and percentage of accurate learners by day 7. For that reason, I hypothesized that a lesion caused by the fiber implantation itself could have been responsible for the decreased accuracy and percentage of accurate learners from the last two experiments. Therefore, I directly compared the behavioral data of the two implanted groups (dHPC implanted and vHPC implanted) and naïve (non-implanted mice, trained under the same massed PL protocol for 5 days; same cohort shown as "massed" group in figure 14) to better understand this issue (figure 17).

Statistical analyses of behavioral performance from d1 to d5 failed to reveal significant differences in latency, but not the other parameters. Specifically, group differences were observed towards the end of training for accuracy levels (interaction: $F_{(8, 184)} = 3.342$, $p = 0.0013$, group: $F_{(2, 46)} = 17.73$, $p < 0.0001$; 2-way ANOVA), number of wrong platform visits (interaction: $F_{(8, 184)} = 2.798$, $p = 0.0060$, group: $F_{(2, 46)} = 13.54$, $p < 0.0001$; 2-way ANOVA) and percentage of accurate learners (day 4: $\chi^2_{3, N=49}$ test = 26.57, $p < 0.0001$; day 5 $\chi^2_{3, N=49}$ test = 15.15, $p = 0.0005$).

In the analysis of days 1 to 7 between the implanted groups (dHPC vs vHPC) I did not observe any differences for latency or number of wrong platform visits. However, the accuracy levels of the two groups showed a trend to significance (interaction: $F_{(6, 234)} = 2.057$, $p = 0.0591$; 2-way ANOVA) and post-hoc analysis revealed a significant difference on the last day (day 7), with the vHPC implanted showing lower values. Additionally, the percentage of accurate learners was significantly lower for vHPC implanted animals (day 6: $\chi^2_{2, N=41}$ test = 4.111, $p = 0.043$; day 7: $\chi^2_{2, N=41}$ test = 7.22, $p = 0.007$).

These results suggest that the HPC implantation by itself, without further manipulation (e.g. cable connection or optogenetic inhibition, i.e. laser on), disrupts learning in the WCM. The effect was more pronounced for the vHPC implanted group and precluded further optogenetic experiments targeting the HPC.
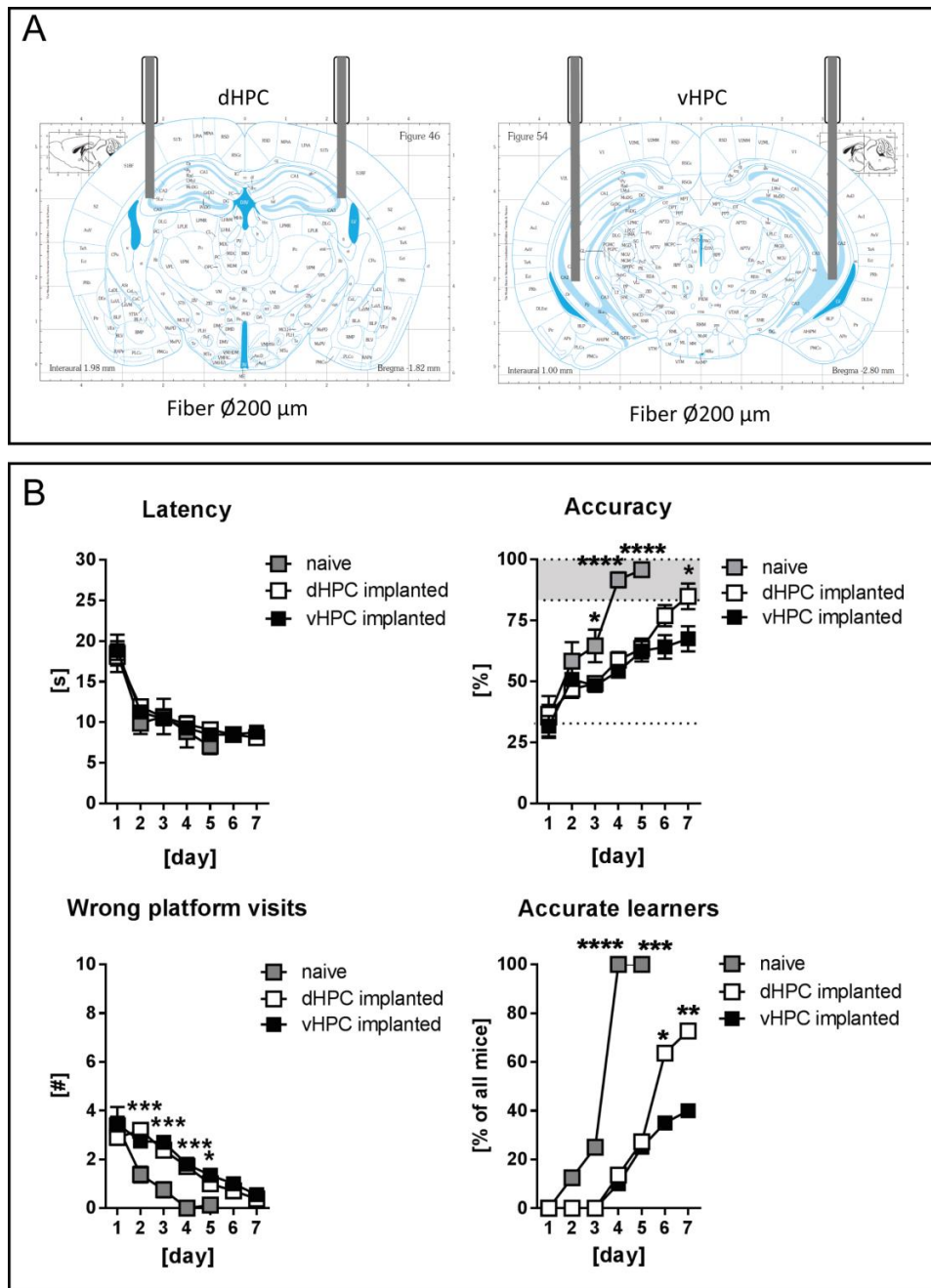
Figure 17: *Optic fiber implantation in the HPC affects place learning in the WCM.* (A) Representative images of mouse brain plates (adapted from the Mouse Brain in Stereotaxic Coordinates) indicating location of the optic fiber implants and its caliber/diameter (200 µm, in scale). (B) Behavioral performance of naïve mice (n= 8), dHPC implanted (n = 21) and vHPC implanted (n = 20). Latency values did not differ among the groups. In the three groups' comparison from d1-d5, accuracy was higher for naïve mice on day 3 (naïve vs vHPC, * p < 0.05), day 4 (naïve vs dHPC and naïve vs vHPC, **** p < 0.0001) and day 5 (naïve vs dHPC and naïve vs vHPC, **** p < 0.0001). The number of wrong platform visits was significantly lower for naïve animals on day 2 (naïve vs dHPC,*** p < 0.001; naïve vs vHPC, ** p < 0.01), day 3 (naïve vs

dHPC, ** $p < 0.01$; naïve vs vHPC, **** $p < 0.0001$), day 4 (naïve vs dHPC, *** $p < 0.001$; naïve vs vHPC, *** $p < 0.001$) and day 5 (naïve vs vHPC, * $p = 0.05$) (2-way ANOVA followed by Tukey's post-hoc test). The percentage of accurate learners was significantly higher for naïve animals (day 4, **** $p < 0.0001$; day 5, *** $p < 0.001$; χ^2 test). In the comparison between implanted groups (dHPC vs vHPC) from d1-d7, there was no difference for latency or number of wrong platform visits. Accuracy was significantly higher for dHPC implanted mice on day 7 (* $p < 0.05$; 2-way ANOVA followed by Tukey's post-hoc test). The percentage of accurate learners was significantly lower for vHPC implanted animals (days 6, * $p < 0.05$; day 7, ** $p < 0.01$; χ^2 test). Data are presented as mean ± s.e.m.

3.9. Experiment 7: dHPC chemogenetic inhibition during WCM (PL) learning

After the technical problems described in experiments 5 and 6 (also see figure 17), that affected the number of animals that learned the task, I changed our approach for neuronal inhibition: instead of using optogenetics I employed chemogenetics (DREADDs). C57BL/6N mice were injected in the dorsal hippocampus subfield CA1 (dCA1) with a viral vector transducing the inhibitory DREADD hM4D and after 3 weeks started training in the WCM under the PL protocol paired with daily CNO (i.p., 5 mg/kg; 45 min before the behavioral task) or vehicle injections for 5 days (d1-d5). On day 6 animals received the inverted treatment when compared to the previous 5 days; the behavioral protocol (see figure 18A) was unchanged. After 1 day of rest, animals were tested for reversal learning on 2 days (d8-d9) under the same treatment regime received on the initial 5 days (d1-d5).

There was no difference in the behavioral parameters between the two groups (CNO vs vehicle) in the training period (d1-d6; figure 18B) or in the reversal learning period (d8-d9; figure 18C).

Figure 18: *Chemogenetic inhibition of dHPC during learning in the WCM (PL).* (A) Timeline of experimental procedures, including a schematic representation of the injection sites for the viral vector (AAV8-CamKII-hM4Di-mCherry) aimed at the dCA1 pyramidal layer. (B) Behavioral performance of the mice trained under the place learning protocol in the WCM, treated with CNO (n = 9; i.p., 5 mg/kg, 45 min before behavioral task) or vehicle (n = 6) during the training/learning period (d1-d6). Note that on day 6 (d6) animals received inverted treatment compared to the one from the initial 5 days.

There was no difference between groups on the behavioral parameters evaluated. (C) Behavioral performance of the same mice during the reversal learning period (d8-d9). Latency, accuracy and number of wrong platform visits and percentage of accurate learners were not different between groups. (D) Left panel: locomotion of the animals treated with CNO (i.p, 5 mg/kg, n = 7) or vehicle (n = 6) 45 min before a 10 min-exposure to a new context (Y maze). Middle and right: c-Fos expression on the dCA1 of animals killed 80 min after Y maze exposure. Middle panel: IHC image, indicating an example ROI of the area (individually defined) used for cell counting. Right panel: quantification of cells positive for c-Fos. There was no difference between groups. Values are shown as density of cells per area, in arbitrary units. Data are presented as mean ± s.e.m.

Given the known involvement of the dorsal hippocampus in spatial navigation and learning, and this lack of difference between groups, I hypothesized that the chemogenetic approach used here either: (i) was not sufficient to inhibit a large enough portion of the hippocampus to affect behavioral performance; or (ii) the DREADDs were not functional (i.e., did not lead to inhibition of the target neurons upon activation with CNO). In order to clarify the problem I analyzed the density of c-Fos positive cells in the transfected hippocampal area (tagged with mCherry of the viral vector) after the exposure of the mice previously treated with CNO or vehicle (45 min before) to a new context (which should induce activation of the dHPC). There was no significant difference between the groups (figure 18D), indicating that the DREADDs used here did not sufficiently inhibit the transfected target area.

3.10. **Experiment 8: vHPC chemogenetic inhibition during WCM (PL) learning**

Similarly to the experiment described above, I tested the effects of chemogenetically inhibiting the ventral hippocampus subfield CA1 of animals learning the WCM under the PL protocol. Again, there were no differences in the behavioral parameters between groups during either training/learning (d1-d6) or reversal learning (d8-d10) (figure 19). I attribute the lack of differences to a possible mal function of the chemogenetic approach used here, as described in the previous experiment which has been performed in parallel to this one.

Figure 19: *Chemogenetic inhibition of vHPC during learning in the WCM (PL).*
(A) Timeline of experimental procedures, including a schematic representation of the injection sites for the viral vector (AAV8-CamKII-hM4Di-mCherry) aimed at the vCA1 pyramidal layer and vCA1. (B) Behavioral performance of the mice trained under the place learning protocol in the WCM, treated with CNO (n = 7; i.p., 5 mg/kg, 45 min before behavioral task) or vehicle (n = 6) during the training/learning period (d1-d6). Note that on day 6 (d6) animals received inverted treatment compared to the one from the initial 5 days. There was no difference between groups on the behavioral parameters evaluated. (C) Behavioral performance of the same mice during the reversal learning period (d8-d10). Latency, accuracy, number of wrong platform visits and percentage of accurate learners were not different between groups. Data are presented as mean ± s.e.m.

3.11. **Experiment 9: IL chemogenetic inhibition during WCM (PL) learning – focus on strategy switch**

Since the mPFC is implicated in strategy switch, as discussed in the introduction, I hypothesized that it might also be involved in this switch from RL to PL during initial learning (under the spatial strategy) in the WCM, and not only switching from strategies fully learned before. To test this hypothesis I injected the infralimbic cortex (IL) of Nex-Cre mice with either a DIO viral vector transducing the inhibitory DREADD hM4D or a control viral vector transducing mCherry only. 3 weeks after, mice were subjected to place learning (PL) in the water cross maze (WCM) under CNO administration (5 mg/kg; i.p.; 45 min before the behavioral task).

I observed reduced accuracy on the hM4D group around the middle of the training period, only revealed by post-hoc analysis (figure 20; interaction: $F_{(6, 60)} = 2.04$, $p = 0.0741$; 2-way ANOVA followed by Sidak's post-hoc test). The accuracy values for both groups converged in the end. This was reflected in the percentage of accurate learners (day 5: $\chi^2_{2, N=12}$ test $= 5.182$, $p = 0.0228$). The percentage of side biased animals differed in the first day (day1: $\chi^2_{2, N=12}$ test $= 5.6$, $p = 0.0180$) and it was comparable on the other training days.

Figure 20. *Chemogenetic inhibition of IL during learning in the WCM (PL) – focus on strategy switch*. (A) Timeline of experimental procedures, including a schematic representation of the injection sites for the viral vectors (control: AAV8-hSyn-DIO-mCherry, n = 7; or AAV8-hSyn-DIO-hM4D(Gi)-mCherry, n = 5) aimed at the IL (bilaterally). (B) Behavioral performance of the mice trained under the place learning protocol in the WCM, treated with CNO (i.p., 5 mg/kg, 45 min before behavioral task) during the training/learning period (d1-d7). Accuracy was significant higher for the control (mCherry) group on day 5 (** $p < 0.01$; 2-way ANOVA followed by Sidak's post-hoc test). The percentage of accurate learners was higher for this group on the same

day (day 5, * < 0.05; χ^2 test). The percentage of side biased animals was higher on the experimental (hM4D) group on the first day (day 1, * < 0.05; χ^2 test). There was no difference between groups on the other behavioral parameters evaluated. Data are presented as mean ± s.e.m. IL, infralimbic cortex.

3.12. **Experiment 10: Retrograde tracing of IL with fluorogold**

It has been previously described that the hippocampus (HPC) and the medial prefrontal cortex (mPFC) are functionally and anatomically interconnected (see *Introduction* for more information). Given the interplay of the mPFC and the HPC in strategy selection and spatial navigation (Hok et al., 2005; Martinet et al., 2011; Negron-Oyarzo et al., 2018), I also hypothesized that activity of the HPC-mPFC pathway is necessary for the initial strategy switch during learning in the WCM. However, to determine the exact projection subfields of the hippocampus to the infralimbic cortex (IL) in the mouse brain, I analyzed the fluorescence of the retrograde tracer fluorogold (FG) after its injection in the target area (IL; figure 21) of 4 mice. I observed fluorescent signal in the dorsal and intermediate parts of the CA3 subfield (figure 21) and ventral part of the CA1 subfield (figure 21), indicating that these hippocampal regions project directly to the IL area. No fluorescence was observed in the dorsal part of CA1.

This anatomical pathway analysis was used as the basis of the experimental design of the specific functional modulation of the vCA1-IL pathway, described in the *Outlook* (see figure 24).
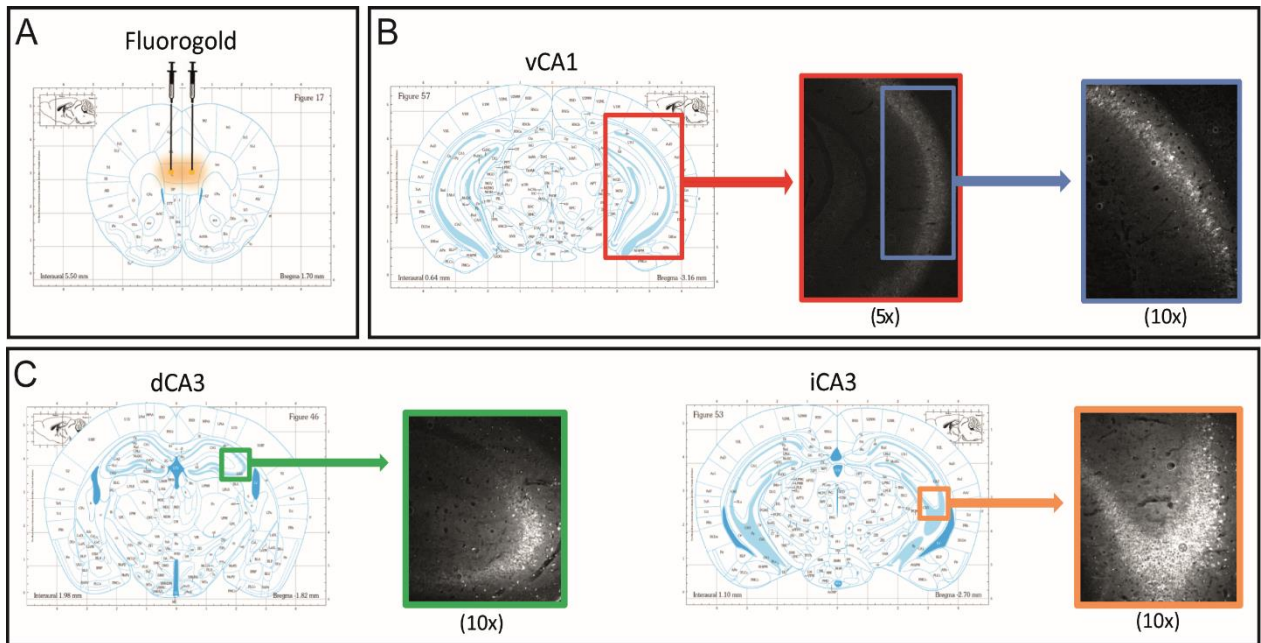
Figure 21: *IL Retrograde tracing of the infralimbic cortex (IL) to the hippocampus.* (A) The retrograde tracer, fluorogold (FG), was bilaterally injected into the IL. (B) Ventral hippocampus at the level where FG signal was found with representative microscopy images (5x and 10x) of vCA1. (C) Dorsal and intermediate hippocampus at the level where FG signal was found, with representative microscopy images (10x) of dCA3 and iCA3.

4. **DISCUSSION**

In this thesis I revealed the neuronal matrix underlying spatial navigation under the place and response learning strategies in the water cross maze (WCM) task using manganese-enhanced MRI (MEMRI) and whole brain voxel-wise analysis. In this context I elucidated important functional properties of MEMRI in order to better interpret our results, including the influence of neuronal activity on (i) Mn^{2+} cellular uptake, followed by transient accumulation at this site, and (ii) increased axonal and transsynaptic transport after cellular uptake.

Moreover, I compared the results obtained with MEMRI after training in the WCM with IEG expression to tell apart the likely structures initially activated by the task from the output structures where Mn^{2+} preferentially accumulates.

I also attempted to prove the causal involvement of selected structures with spatial learning and strategy switch in the WCM. Follow-up experiments in this direction will be discussed in the outlook.

4.1. **Advantages of MEMRI over other tools**

As I showed here, manganese-enhanced MRI is an interesting tool for analyzing brain activity in small animals given its good resolution that allows the delineation of brain structures not possible with other techniques, like PET scan. Additionally, since Mn^{2+} is taken-up in activity manner (Lin and Koretsky, 1997), and transiently accumulates at the uptake structure (Gavin et al., 1990), it can be detected after the performance of a behavioral task (or intervention) of interest (Chen et al., 2007; Bissig and Berkowitz, 2009; Eschenko et al., 2010; Bangasser et al., 2013; Chen et al., 2013; Hoch et al., 2013; Tang et al., 2016; Laine et al., 2017). This makes it possible to combine it with freely moving behavioral tasks out of the scanner and even with tasks that require multiple trials (over days) to be accomplished (e.g. WCM). Moreover, since MEMRI is non-invasive and performed in live animals, it brings the possibility to run longitudinal studies and follow-up animals with the simple passage of time (e.g.

aging studies) or before and after a specific manipulation (Almeida-Correa et al., 2018). Furthermore, MEMRI has the advantage of allowing voxel-wise whole brain analyses (Yu et al., 2008; Soma et al., 2011) instead of pre-defined ROI analyses, or small windows for imaging (e.g. calcium imaging techniques). Lastly, this technique can also be used for connectomics analyses, either after a direct intracerebral injection for tract tracing investigations (for review see (Pautler, 2004)) or after a systemic injection with baseline and follow-up scans for comparison (Almeida-Correa et al., 2018).

4.2. **MEMRI functional mechanisms**

Aiming at better understanding and interpreting the results obtained with MEMRI, I carried out investigations addressing functional mechanisms of this technique. These investigations were complementary to previous work from our lab and others.

MEMRI studies have already employed different routes for Mn^{2+} administration, such as intracerebral injections (Pautler et al., 2003; Watanabe et al., 2004; Yang et al., 2011), intranasal aerosols (Henriksson et al., 1999; Pautler and Koretsky, 2002; Lehallier et al., 2012), intravitreal injection (Pautler et al., 1998; Bearer et al., 2007; Luo et al., 2012), and topic eye application (Lin et al., 2014). These methods are however invasive and often toxic (Bearer et al., 2007; Luo et al., 2012; Lin et al., 2014). Systemic injections have a reduced risk of toxicity if fractionated (Grunecker et al., 2010), or continuously delivered with osmotic mini pumps (Sepulveda et al., 2012; Poole et al., 2017). The delayed and limited diffusion of Mn^{2+} to the brain should also be considered. In each case, care must be taken to find an optimal balance between a sufficient dose to reach the best contrast while minimizing the potential side/toxic effects of Mn^{2+} in the brain. The use of systemic methods for delivering of $MnCl_2$ has clear advantages, e.g., in case of prolonged behavioral procedures. In some cases, however, systemic treatment has to be combined with the disruption of the blood-brain barrier (BBB), e.g., by mannitol injection (Lin and Koretsky,

1997; Aoki et al., 2002) or by ultrasound (Howles et al., 2010), in order to allow the Mn^{2+} to quickly reach the brain. In these cases, a single $MnCl_2$ spike injection can be applied. Even with the use of relatively small doses for a single injection that did not cause major apparent side/toxic effects, small impairments as transient motor deficit in skilled reaching, rears, and activity were already described in rats (Alaverdashvili et al., 2017). This limitation should be considered, especially when designing studies with behavioral experiments where fine motor skills are necessary. For long-term investigations (from many hours to days) the disruption of the BBB is not necessary (Yu et al., 2005; Kuo et al., 2006), given that Mn^{2+} can reach the brain and accumulate in a activity-dependent manner in the structures related to the challenge/task performed at least few hours after systemic administration. This applies in particular to the paradigm used here in experiment 2, where I "pre-loaded" the cells with Mn^{2+} before the experimental intervention (whiskers trimming). My data suggest that this procedure might also be used for acute behavioral challenges where mice could be first treated with $MnCl_2$ to reach sufficient contrast, followed by repeated scanning before and after the challenge. One should also not overlook clearance of Mn^{2+} in the brain when scans are performed long (more than 24 h) after the $MnCl_2$ injections have stopped. Our lab has previously reported that the half-life of Mn^{2+}, after an 8×30 mg/kg $MnCl_2$ i.p. injection protocol, is about 5–7 days, depending on the brain structures (Grunecker et al., 2013). This point was taken into consideration in my analysis comparing scans 1 and 2 in experiment 2, which were performed 1 week apart.

Another recent work from our lab has shown that an important entrance site for Mn^{2+} in neurons are $Ca_v1.2$ channels (Bedenk et al., 2018), supporting data in the literature pointing at Mn^{2+} entrance in neurons via calcium channels (Drapeau and Nachshen, 1984). In the same study we were able to additionally show a preferential accumulation of Mn^{2+} in projection sites of the neurons (Bedenk et al., 2018). This has to be kept in mind while interpreting the findings of my thesis. Experiments 1 and 2 of this thesis are in line with the findings of Bedenk et al (Bedenk et al., 2018) and extend the knowledge of Mn^{2+} dynamics in the brain. In experiment 1, I provide the first direct evidence of the coupling

between increased neuronal activity (triggered by focal unilateral optogenetic stimulation of dCA1) and Mn^{2+} accumulation, as reflected by increased MEMRI signal intensity. This finding supports previous investigations using pharmacological block or stimulation of specific targets to establish the involvement of neuronal activity in Mn^{2+} cellular uptake (Wang et al., 2015). Nevertheless, this does not preclude the possibility that Mn^{2+} can enter neurons also in the absence of activity (Bearer et al., 2007; Lowe et al., 2008; Wang et al., 2015), possibly mediated by the binding of this ion to the divalent metal transporter, DMT1 (Roth and Garrick, 2003; Bartelle et al., 2013). However, these tests were mostly performed *in vitro* or with intracerebral $MnCl_2$ injections and used much higher concentrations of $MnCl_2$ then the ones used in the current work. Our finding also suggests that Mn^{2+} accumulates, at least transiently, at the entrance site (stimulated target) upon artificial direct stimulation. I acknowledge that a limitation of my experimental design is the unilateral stimulation, given that the laser might cause heating (or burning) of the tissue, masking or confusing the results. However, the protocol of optogenetic stimulation used here was previously tested and proved to be sufficient to increase local neuronal firing without causing neuronal damage (Dine et al., 2016). Nevertheless, a solution for the possible heating problem would be the use of wild-type mice injected in one hemisphere with a viral vector transducing ChR2, while the other hemisphere would be injected with a control viral vector (transducing fluorophore only), and stimulating both hemispheres equally. However, this alternative experimental design brings another limitation. That is, only one of the hemispheres would express ChR2. One might argue that the expression of the opsin itself might alter cell permeability to Mn^{2+} or lead to other unknown /unspecific modifications that would be hard to control and to detect. For that reason, I chose the protocol used here.

In experiment 2 I went on to investigate the involvement of neuronal activity in Mn^{2+} transport after its entrance in the cells. I found that neuronal activity elicited by sensory stimulation (whisking) led to accelerated transport of Mn^{2+} to projections sites (figure 22). Additionally, I found that this transport is both axonal and transsynaptic, given that I observed differential MEMRI signal in

first and second order efferents from the target structure (barrel cortex) (table 1). These results are in line with the findings from Bedenk et al (Bedenk et al., 2018) and significant extend them by showing that Mn^{2+} may cross synapses and increase MEMRI signal in second order efferents. This experiment is a nice example of how MEMRI can be applied to longitudinal studies that investigate the effects of a challenge / manipulation (e.g. whiskers trimming) using a combination of baseline and follow-up scans. For a detailed description of this experiment please check the published manuscript (Almeida-Correa et al., 2018) enclosed in the annex of this document.
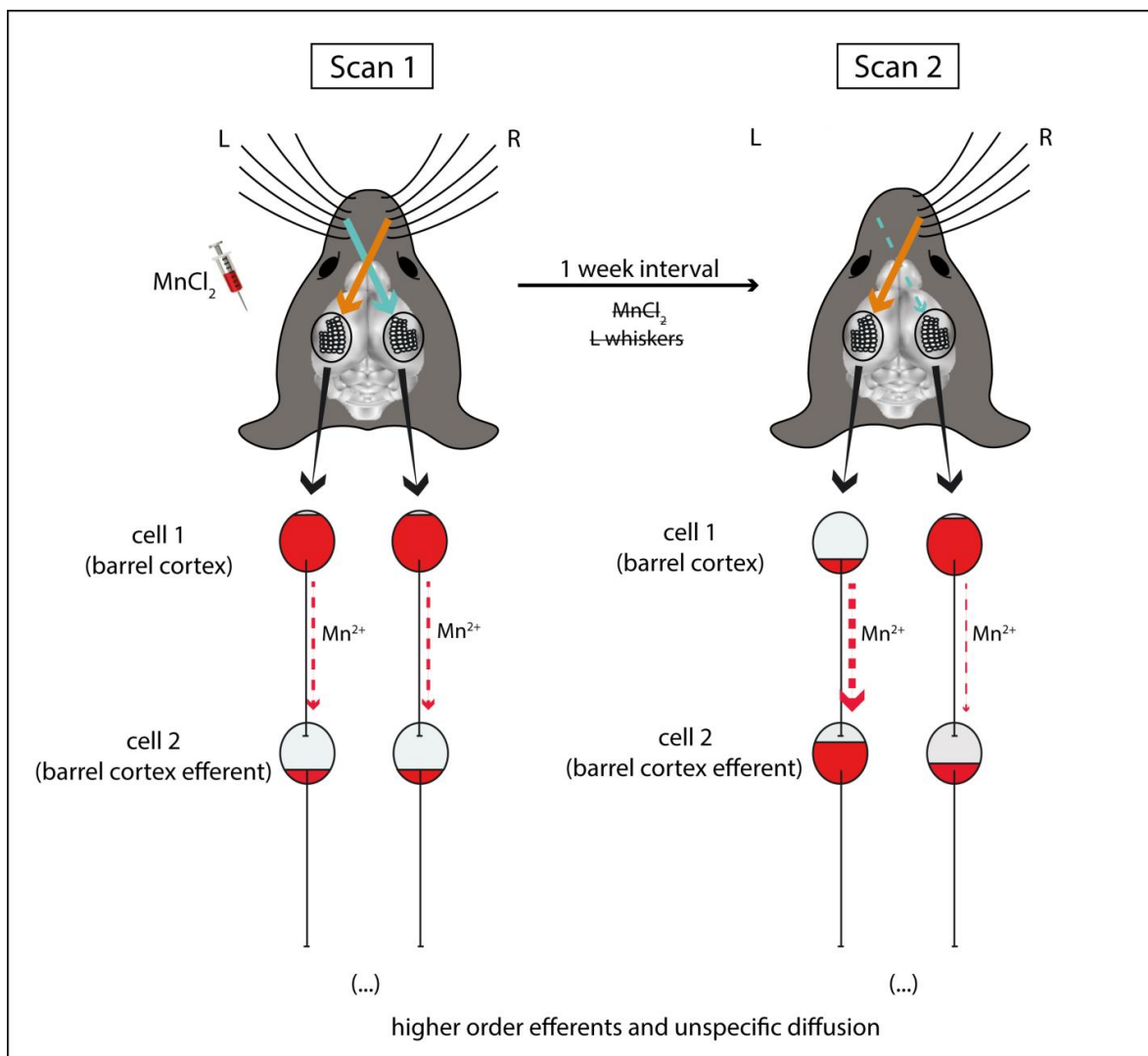
Figure 22*: Schematic explanation for the differences in Mn^{2+} accumulation observed after unilateral sensory deprivation.* In the end of sensory enriched housing with intact whiskers and repeated $MnCl_2$ injections, MEMRI (scan 1) reveals

equal bilateral accumulation of Mn^{2+} in the barrel cortices. 1 week later (scan 2) after unilateral sensory deprivation (left side), Mn^{2+} is cleared from the left but not right barrel cortex (cell 1), due to ongoing sensory inputs from the intact whiskers of the contralateral right side. At the same time, Mn^{2+} is accumulated in efferent brain structures downstream to the left barrel cortex (cell 2) following activity-dependent axonal/transsynaptic transport. For simplicity reasons, this scheme does not depict the afferences from brain stem structures and the thalamus which relay sensory information from the whiskers to the barrel cortex. (reproduced from (Almeida-Correa et al., 2018))

   Previous studies already investigated the possible role of neuronal activity in Mn^{2+} axonal and transsynaptic transport in specific pathways with different protocols and obtained, somewhat, contradicting results. These studies were confined to local Mn^{2+} application. For instance, it was shown that Mn^{2+} is co-released with neurotransmitters after stimulation with high K^+ (Takeda et al., 1998), indicating that Mn^{2+} transport is dynamically linked to neural signaling. Later, many groups mapped sensory system activation in response to specific odors (Pautler et al., 1998; Pautler and Koretsky, 2002; Chuang et al., 2009; Lehallier et al., 2012), visual (Bissig and Berkowitz, 2009), or acoustic stimulation (Yu et al., 2005), supporting the idea that Mn^{2+} transport is activity-dependent. One of these studies (Bearer et al., 2007) employed transgenic blind mice to investigate activity-dependency in Mn^{2+} dynamics after intravitreal $MnCl_2$ injection and concluded that "Mn^{2+} is not transmitted efficiently across synapses in the absence of electrical activity in this system," whereas uptake and axonal transport remained intact. This last conclusion is supported by the results of Lowe et al. (Lowe et al., 2008) showing no difference in MEMRI signal intensity in the visual system between groups treated with $MnCl_2$ only or in combination with cell activity blockers (APB or TTX). On the other hand, accelerated Mn^{2+} transport after $MnCl_2$ co-treatment with AMPA was already described (Wang et al., 2015), indicating that axonal transport of Mn^{2+} is dynamically modulated by neuronal activity. In fact, pharmacological blockage of calcium channels also blocked this accelerated transport (Wang et al., 2015). Using the song control system in song birds as a model of neuronal plasticity (for review see (Van der Linden et al., 2004)), Tindemans et al. (Tindemans et al., 2003) were able to show an activity-dependent transsynaptic transport of Mn^{2+} from the site of local cerebral injection of Mn^{2+} in the HVC (high vocal center; a relay region of the song control system) to more downstream regions

100

[such as the nucleus robustus arcopallialis (RA) and the striatal area X].Using dynamic MEMRI, the authors reported that both regions showed a more rapid accumulation of Mn^{2+} in the stimulated birds. After about 10 h, this difference to non-stimulated birds vanished only for RA, but not for area X, suggesting a differential functional connectivity of the two regions in the song circuitry. Considering these previous reports and the results presented here, I conclude that, even in the case of systemic $MnCl_2$ injection, axonal and transsynaptic transport of Mn^{2+} is modulated by the activity state of the neuronal pathway. My results further suggest that reduced neuronal activity due to blockage of sensory inputs attenuates the transport of Mn^{2+} from its initial accumulation site, while continuous neuronal activity promotes the transport of Mn^{2+} between neurons.

4.3. Why choosing the water cross maze (WCM)

The water cross maze (WCM) was my behavioral task of choice to investigate spatial navigation, learning and memory in mice for multiple reasons. First, this task is very easy to establish, easy for the animals to learn and to record the data from trial 1 on. Also, the learning protocols are well defined and clearly identified by performance of the animals, allowing the investigation and comparison of hippocampus-dependent vs hippocampus-independent learning. Another advantage of the WCM over other spatial navigation tasks is the strong motivation that animals have to escape from the water, which is comparable between animals. This might not be the case for dry mazes, where the motivation to search for food can differ from one individual to the other. When compared to the Morris water maze, the WCM has the advantage of the enclosed corridors that limit the path of the animals, avoiding chaining, random search, etc, making it easier to identify the strategy search of the subjects. Furthermore, the enclosed corridors decrease the stress of the animals when compared to exposure to open environments. Additionally, there is a large variety of information that can be acquired from the animal's behavior in the WCM, such as latency, accuracy, number of wrong platform visits, start bias, etc (Kleinknecht et al., 2012). These behavioral measures can be used as

regressors for correlation analyses of functional MEMRI data, as I showed here in experiment 3. This combination of methods provides new interesting data that helps unravel the structures involved in performance of the WCM, thus involved in spatial navigation and learning and memory, and its underlying connectivity.

Nevertheless, as any other method, the WCM also has its limitations. The most important to note was already mentioned before as an advantage: the task is very easy to learn. Even though this might be a beneficial characteristic, given that it reduces the stress load of the animals within few trials and allows an efficient training paradigm, it is also a disadvantage given that a "ceiling effect" of learning is usually reached after few days of training. Thus, manipulations that aim at improving spatial learning should not be tested in the WCM. Additionally, the maze set-up with its transparent walls is also advantageous and disadvantageous in different perspectives. It is advantageous given that it allows animals to see the extra maze cues from any position inside the maze, helping the individuals to orient themselves. And it is disadvantageous since even when animals do not require the hippocampus to perform the task (e.g. trained under RL) they acquire information of the surrounding to enhance their orientation capabilities as well, which might mask the detection of brain structures involved in one or another learning protocol. This was likely the reason why I did not see the hippocampus among the structures with differential MEMRI signal in our comparison between PL- and RL-trained animals. Moreover, since hippocampal functions are very redundant it is only possible to see the manipulation effects when hippocampal volume loss (caused by lesions or transient inactivation) is major (Moser et al., 1993; Kleinknecht et al., 2012). This "cognitive reserve" mediated effect was directly investigated in a longitudinal study which combined imaging and behavioral testing over the course of 16 months until senescence (Reichel et al., 2017).

4.4. **Spatial learning matrices, brain connectivity and cognitive domains**

The regressor analyses used to identify brain structures putatively related to learning in the WCM (experiment 3) highlighted the hippocampus in the inverse correlation with latency and the direct correlation with accuracy for PL. This is line with the vast literature showing the involvement of the hippocampus with allocentric spatial learning (i.e. place learning) (Becker et al., 1980; Morris et al., 1982). The PAG was directly correlated with latency, perhaps suggesting an impact of fear processing (for review see (Tovote et al., 2015)) in detrimental cognitive performance (i.e., feeling of fear and despair leading to decreased performance in the WCM). In line with this emotional component, the BLA was inversely correlated with accuracy, and BLA MEMRI signal was strongly inversely correlated with vHPC MEMRI signal. These results corroborate the hypothesis of emotional control over cognitive performance. More specifically, in this case, of emotional detrimental effects over spatial learning. This interplay of emotion and learning, likely mediated by the vHPC-BLA circuit (as previously mentioned in the *Introduction*), is really interesting for me and it will be revisited in the outlook. Notably, most of the clusters correlated with behavioral performance were found unilaterally. I believe that the most parsimonious explanation for this finding is the thresholding used in my analysis, which only considers clusters with a relatively large number of voxels (e.g. 50 voxels for experiment 3; check details in the *Results*) in order to avoid false positives. In turn, that has the limitation of missing some smaller clusters possibly involved in the behavioral task. For RL, the hippocampus was the only structure correlated with latency from days 1-4, suggesting that even if not necessary to perform the task (under this specific strategy) animals do count on hippocampal activity, likely to process information of its surroundings before they learn exactly what they have to do to escape the WCM. Several structures were correlated (directly or inversely) with latency from days 5-8. These structures are implicated in different functions, such as sensory processing (e.g. main olfactory bulb, piriform area), stress/emotionality (e.g. bed nucleus of the stria terminalis, basomedial amygdala), etc. This will be further discussed in the

following paragraphs (also see table 3). There was no cluster correlated with accuracy, possibly because of the used analysis threshold, as explained before.

My comparison between the MEMRI signal observed in animals trained under place- or response learning in the WCM revealed several structures with differential contrasts. I analyzed a possible pattern among these structures, taking into consideration our previous results pointing at preferential Mn^{2+} accumulation in projection terminals (Bedenk et al., 2018) and available data in the literature regarding brain connectivity. I found that many of the structures described here to have a stronger MEMRI signal in either comparison (RL > PL or RL < PL) are downstream targets of the hippocampus (figure 23). Their connectivity, however, differs between structures along the longitudinal association bundle originating in vCA1 (for RL > PL) and fornical afferences from vCA1 and direct innervation from dCA1/iCA1 (for RL < PL). These findings support the idea that the MEMRI signal observed in this experiment is mainly comprised of outputs of the initially activated structures and suggest that different hippocampal pathways are involved in the different navigation strategies studied here (PL and RL). This last finding highlights the importance of the whole brain analysis performed here and the need to investigate structures other than the hippocampus, as mentioned before in the introduction. The finding also shows that even if not required to perform the response learning strategy in the WCM (Kleinknecht et al., 2012), the hippocampus is also involved in response learning by recruiting some of its outputs as the retrosplenial cortex and the subiculum, possibly to update head direction signals (Chen et al., 1994; Cho and Sharp, 2001) provided by the vestibular system (Smith, 1997), thus, improving performance of the animals through path integration (McNaughton et al., 1996; Taube, 1998). These results are in line with the previously described differential functional connectivity of the hippocampus and its downstream targets for distinct information computations (e.g. anxiety processing or goal-directed behavior, (Ciocchi et al., 2015).
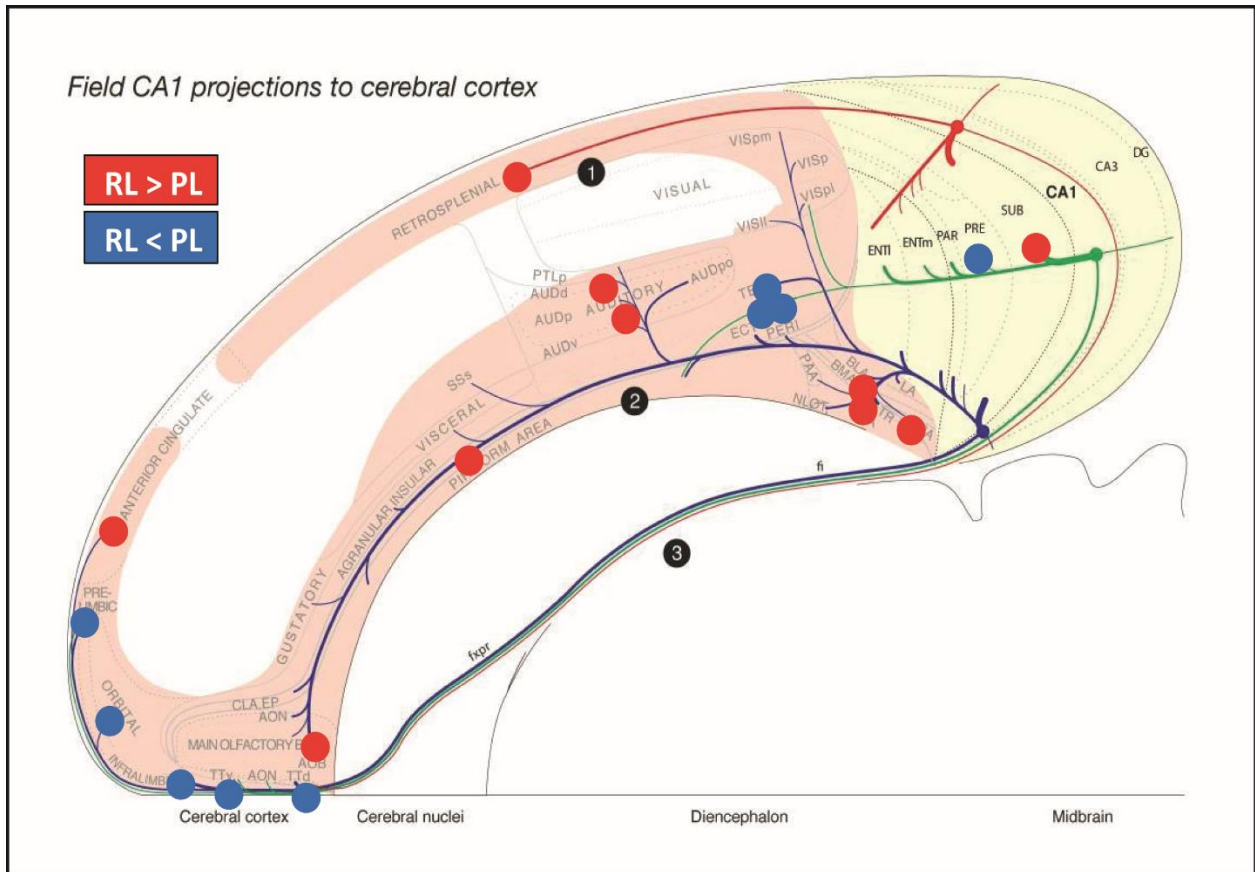
Figure 23*: MEMRI PL vs RL − connectivity matrix of hippocampus and cortical structures.* Schematic representation of cortical outputs of the hippocampus and its different connectivity patterns. 1. Dorsal stream to the retrosplenial area and caudal end of the anterior cingulate area; 2. Ventral stream through the longitudinal association bundle 3. Rostral stream via a cortical-subcortical-cortical pathway involving the fornix system. Red dots represent cortical structures with higher MEMRI signal in the RL group (RL > PL) and blue dots represent cortical structures with higher MEMRI signal in the PL group (RL < PL). The connectivity pattern of the distinct groups differ between structures along the longitudinal association bundle originating in vCA1 (for RL > PL) and fornical afferences from vCA1 and direct innervation from dCA1/iCA1 (for RL < PL). All structures represented with dots were extracted from table 2. (Figure adapted from (Cenquizca and Swanson, 2007)

Moreover, to understand the role of each structure with differential MEMRI signal, based on previous descriptions available in the literature, I categorized them individually into distinct cognitive domains (table 3). Namely: sensory processing, emotion (stress, fear, anxiety, social-related behaviors, etc), executive function (mental planning), memory and attention (adapted from

(Park et al., 2018)). Structures could fall into one or more categories, depending on their involvement in these different cognitive domains.

Table 3: List of structures showing differential MEMRI signal between scans of mice trained under the PL protocol vs mice trained under the RL protocol in the WCM contextualized into different cognitive domains

Brain structure	MEMRI signal ≠	Cognitive domains*				
		Sensory processing	Emotion	Executive function	Memory	Attention
Main olfactory bulb	red/blue	X				
Accessory olfactory bulb	red	X				
Motor cortex	red/blue	X		x		
Prelimbic cortex	blue			x	x	x
Orbital area	blue	X	x	x	x	x
Piriform area	red/blue	X				
Taenia tecta	blue	X				
Infralimbic cortex	blue		x	x	x	x
Lateral septal nucleus	blue		x	x	x	
Substantia innominate	red/blue		x		x	x
Somatosensory area	blue	X				
Lateral olfactory tract	red	X				
Anterior cingulate area	red		x			
Somatosensory area – upper limbs	red	X				
Bed nucleus of the stria terminalis	red		x			
Stria terminalis	blue		x			
Anterior hypothalamic nuclei	red		x			
Thalamic nuclei	red	X	x	x	x	x
Dorsal fornix	red	X		x	x	x
Retrosplenial area	red	X	x	x	x	
Posterior parietal association area	red	X		x		x
Ventral posterior nucleus of the thalamus	blue	X				
Cortical amygdala	red	X				
Geniculate complex	blue	X				
Auditory areas	red	X				
Visual areas	red	X				
Anterior pretectal nucleus	blue	X				
Endopiriform nucleus	red	X				
Postpiriform transition area	red		x			
Susbtantia nigra	blue	X	x			
Posterior nucleus of the amygdala	red		x			
Basomedial nucleus of the amygdala	red		x			
Subiculum- ventral part	red				x	
Zona incerta	blue	X				x
Subiculum – dorsal part	red				x	
Pontine grey	red	X			x	
Tegmental reticular nucleus	red	X			x	
Pontine reticular nucleus	red	X		x	x	
Lateral entorhinal cortex	red/blue	X			x	
Ectorhinal cortex	blue	X			x	

106

Structure						
Perirhinal cortex	🟦	x			x	
Periaqueductal grey	🟥		x			
Superior colliculus	🟦	x				
Pons: nucleus of the lateral lemniscus	🟥	x				
Pons: superior central nucleus raphe	🟥	x	x			
Superior cerebellar peduncle decussation	🟥	x				
Peduncle pontine nucleus	🟥	x				x
Superior olivary complex + periolivary region	🟥	x				
Presubiculum	🟦				x	
Temporal association area	🟦	x				
Cerebellum: simple lobule	🟥🟦	x				
Medulla: medial vestibular nucleus	🟦	x				
Medulla: nucleus prepositus	🟦	x				x
Medulla: nucleus raphe magnus	🟦	x				
Medulla: facial motor nucleus	🟦	x				
Cerebellum: interposed nucleus	🟦	x				x
Cerebellum: fastigial nucleus	🟦	x				x
Medulla: medial and spinal vestibular nucleus	🟦	x				
Medulla: parvicellular nucleus	🟦	x				
Nucleus of the solitary tract	🟦	x	x			
Medulla: intermediate reticular nucleus	🟦	x				
Cerebellar commissure and arbor vitae	🟥					

🟥🟦 **RL > PL and RL < PL**, depending on the plate across the rostral caudal extent
🟥 **RL > PL**
🟦 **RL < PL**

*based on the following references: (Berard et al., 1983; Harris, 1986; Rees and Roberts, 1993; Robinson et al., 1993; Chen et al., 1994; Wiig and Bilkey, 1994; Schoenbaum and Eichenbaum, 1995; Wiig and Bilkey, 1995; Andersen, 1997; Smith, 1997; Maddock, 1999; Bussey et al., 2000; Gaffan et al., 2000; Mook Jo et al., 2002; Dalley et al., 2004; Kobayashi et al., 2004; Comoli et al., 2005; Feierstein et al., 2006; Gittis and du Lac, 2006; Holland and Gallagher, 2006; Trageser et al., 2006; Notsu et al., 2008; Whitlock et al., 2008; Albrechet-Souza et al., 2011; Kesner and Churchwell, 2011; Condes-Lara et al., 2012; Sugai et al., 2012; Lopez Hill et al., 2013; Igarashi et al., 2014; Recio-Spinoso and Joris, 2014; Butler and Taube, 2015; Chee et al., 2015; Escanilla et al., 2015; Li et al., 2015; Tukker et al., 2015; Cordero et al., 2016; Kapoor et al., 2016; Lech et al., 2016; Leitner et al., 2016; Mitra et al., 2016; Chometton et al., 2017; Cui et al., 2017; Nakamura et al., 2017; Vedder et al., 2017; Low et al., 2018; Nishio et al., 2018)

Most of the structures listed are related to sensory processing, alone or in combination with other domains. This is not surprising for mouse data in a behavioral task, given that this species relies on several sensory modalities to acquire information about its surrounding in order to better react to the inputs perceived by them. However, it is interesting to note that within the sensory processing domains I could identify different patterns for the RL and PL groups.

That is, many of the sensory-related structures with stronger signal for PL (RL < PL; blue in table 2 and table 3) are part of the oculomotor system in the brainstem, involved in different properties of horizontal gaze (e.g. nucleus prepositus) and saccade (e.g. fastigial nucleus), or provide vision-input and eye movement information from parahipocampal (e.g. presubiculum, perirhinal, postrhinal and ectorhinal areas) and other brain regions (e.g. orbital area, superior colliculus and vestibular ocular-reflex from the vestibular nucleus) to head-direction, grid- and place-cells. While several sensory-related structures with stronger signal for RL (RL > PL; red in table 2 and table 3) are involved in more basic rodent sensory computations, like odor (e.g main and accessory olfactory bulb, cortical amygdala, piriform, endopiriform and postpiriform areas) and acoustic stimuli representation (e.g. auditory area, nucleus of the lateral lemniscus and superior olivary complex), or sensory-motor properties, such as body representation (e.g. somatosensory area – upper limbs) and head-direction signal (e.g. retrosplenial area and subiculum), supporting path integration-based navigation (Cooper and Mizumori, 2001; Tukker et al., 2015; Vedder et al., 2017). Given that this analysis was based on a direct comparison (higher or lower than) between groups and among brain structures, I cannot rule out the possibility that the "higher" signal in the visual-related structures for PL overshadowed (or actively suppressed) other sensory-related modalities, rendering the ladder biased towards RL. Nevertheless, the use of these different sensory modalities is not striking considering the different requirements for the navigation strategies. On one hand, PL requires visual processing of the extra-maze cues (Fenton et al., 1994; Liu et al., 1994; Robinson et al., 2001)(Chen et al., 2016) and to keep the gaze fixed to those landmarks while navigating the maze, enabling animals to flexibly navigate from different start locations and find the escape platform. On the other hand, RL requires a strong body representation and self-location abilities (Taube et al., 2013; Laurens and Angelaki, 2018) within a given context to allow animals to perform the correct body movement to reach the escape platform, independently of environmental cues. Taken together, this is the first *in vivo* demonstration of different

implication of sensory-related brain structures in PL vs RL on a whole brain level.

Furthermore, I could also observe that most of the structures comprised in the "emotion" category of the cognitive domains have a stronger signal in RL compared to PL. This is in line with the already reported interplay of stress and memory systems (Packard and Wingard, 2004; Elliott and Packard, 2008; Schwabe et al., 2008). That is, the preferential use of rigid navigation strategies (e.g. RL) over cognitive ones (e.g. PL) influenced by emotional or physical distress. In our experiments, the possible role of emotionality on behavioral performance and, more specifically, on strategy choice could not be evaluated given that animals were trained under a specific protocol (PL or RL). Therefore, they were not given a choice of how to perform the task accurately. However, it is interesting to note that even under those circumstances, it was possible to observe that the underlying brain matrix of the animals trained under RL shows structures that match the expected pathways of emotional processing (e.g. basolateral amygdala and bed nucleus of the stria terminalis) that bias the use of this navigation strategy when individuals are given the choice (Packard et al., 1994; Kim et al., 2001; Elliott and Packard, 2008). Thus, it is possible that the rigid navigation strategy recruits this "emotional processing system" by itself, even in the absence of real stress. This could be interpreted as that rigid navigation enables individuals to use their energy and focus in processes other than navigation per se. In that way, one could hypothesize that animals performing under RL (rigid navigation) would have an elevated arousal level that would prime them to successfully react to a stressful event.

Nevertheless, it should be noted that the results discussed here and presented in tables 2 and 3 refer to two separate cohorts of mice (cohort 1: PL; cohort 2: RL). Therefore, there is a possibility that the differential MEMRI signal, including that of the structures categorized as emotion-related, might be due to different stress levels of the cohorts prior to training and might not be related to the behavioral task performance. I cannot rule out such influences, but tried to keep the experimental designs as similar as possible for both cohorts, with the

exception of the training paradigm itself – which defined the different groups –, to reduce possible cohorts differences unrelated to the behavioral task.

Considering the executive function and memory domains, there was no distinct pattern between the different MEMRI signals (RL < PL, eg. prelimbic- and infralimbic areas and lateral septal nucleus; or RL > PL, e.g. thalamic nuclei, retrosplenial area and pontine reticular nucleus), given that these domains are similarly required for the animals to perform both navigation strategies.

Further, the majority of structures categorized as attention-related (e.g. orbital, prelimbic- and infralimbic areas, substantia innominata and zona incerta) have a stronger MEMRI signal for PL. This is expected given that this navigation strategy is flexible and counts on the formation and use of a cognitive map of the environment. Thus, requiring animals to be focused to compute information of the context where they are inserted and update their current location in relation to the goal/target location (Delatour and Gisquet-Verrier, 2000; Dalley et al., 2004). In contrast, animals navigating under RL have only to perform the same body movement (e.g. turn right or left) in order to find the goal location. Therefore, they do not require a high attentional level for navigating, sparing their energy and focus for other functions.

Of note, one should not overlook that learning might be accomplished early during the training protocol, particularly in case of a trivial learning task, as the WCM. Accordingly, activation of the brain structures related to the task might be low and affect only few voxels (below the threshold) which would be filtered out during data analysis. Moreover, MEMRI signal might be shifted to first, second or third order efferent structures (as discussed before).

Importantly, it must be considered that the categorization and discussion about the role of these brain structures (table 3) were based on available data in the literature. Thus, the experimental designs and subjects (e.g. mice, rats, monkeys, humans, etc) might differ among the studies and might account for some inconsistencies about the definition of certain structures (including nomenclature) and their involvement in different brain functions.

4.5. **Manipulation of neuronal circuits**

To prove functional causality for the activation patterns observed, I went on to manipulate their neuronal activity by optogenetic and chemogenetic means. I encountered several technical problems that led the outcomes of the referred experiments to be inconclusive. I will discuss these problems and present alternatives below.

First, in experiments 5 and 6, I tried to inhibit the hippocampus by optogenetics during memory recall. I chose to interfere with an already-formed memory, instead of inhibiting the hippocampus during learning – memory acquisition (which would correspond to the WCM + MEMRI experiment; see experiment 3) – to avoid compensatory processes or that possible unwanted effects of the fiber implantations, tissue burning or overheating by the laser would unspecifically impair animal's performance. In line with that, I observed a striking drop in behavioral performance in the WCM even before laser stimulation. This suggests that the implantation of the optic fiber itself caused damage to the tissue, which in turn led to the poor performance observed with these animals. This hypothesis was corroborated by our direct comparison of behavioral data from naïve (non-implanted) mice, with dHPC- and vHPC-implanted mice (figure 17). In this comparison I observed a significant difference in behavioral performance of implanted and non-implanted animals. The performance drop was more pronounced in the vHPC-implanted animals, likely because the deep implantation caused a large brain lesion at the fiber tract. However, I cannot precise if the behavioral deficit I observed is due to a lesion caused by the fiber implantation, as I propose, or perhaps by a detrimental outcome (e.g. cell death) caused by the viral vector at the site of injection. To disentangle which of the possibilities holds true, an additional group of mice injected with the viral vector and without implantation would be necessary. Nevertheless, I believe that a possible lesion caused by the fiber would be more likely than a lesion caused by the viral vector injection given that the titration of the virus was controlled to not exceed commonly used concentrations (without toxic effects) and histology after the termination of the

behavioral tests showed neurons with apparent intact morphology. Even if precise stainings for detection of inflammation of cell death were not performed, I can exclude large scale necrosis.

Next, I used chemogenetics as an alternative strategy to overcome the problems I faced with the optic fiber implantation. This method also requires the injection of viral vectors to transduce special membrane receptors, however the activation of these receptors, and consequent modulation of the neuronal targets, is achieved upon systemic injection of the specific ligand, clozapine N-oxide (CNO). Therefore, it does not require invasive implantations or laser stimulation. Importantly, in the experiments where chemogenetics was used, the manipulations were performed throughout training and reversal learning. With this, I aimed to evaluate the inhibition of selected structures during learning (in a closer protocol to the one I used for the combination of WCM and MEMRI; see experiment 3). However, there is the shortcoming that this early interference may force compensatory processes aiming self-stabilization of the system.

In my first attempts of implementing chemogenetics for neural activity inhibition (experiments 7 and 8) I injected viral vectors transducing hM4D (the inhibitory DREADD) in wild-type C57BL/6N mice. I did not observe behavioral effects of these manipulations, even if the histological analyses (presence of the fluorophore) suggest that the virus was expressed in the correct target location. Functional investigation of the DREADD was carried by *ex-vivo* electrophysiological recordings of local field potentials and showed an overall increase in neuronal activity in dHPC on the population level (pop-spikes) (data not shown; performed by Dr. Julien Dine, Electrophysiology Core Unit, MPI of Psychiatry). This result contradicts the expected outcome from the manipulation applied here. This contradiction between the expected and observed results with the use of the inhibitory DREADD hM4D was already reported elsewhere (Lopez et al., 2016). In that study the authors compared the behavioral and physiological outcomes of inhibitory DREADD's manipulation of viral vectors with two different promoters: hSyn (neuronal targeted; (Kugler et al., 2003)) or

CamKII (specific to glutamatergic forebrain neurons; (Mayford et al., 1996; White et al., 2011; Scheyltjens et al., 2015). When using the viral vector with hSyn the results were the opposite of what it was expected: neural activity increase instead of inhibition, as observed in the present study for dHPC. When using the viral vector with CamKII the outcome was in line with the expectations: inhibition of neural activity. The authors ascribe these different results to the specificity of the promotor. Thus, the expression of the inhibitory DREADD in both excitatory and inhibitory neurons would result in local overall excitation of the system. While, limiting the expression of the inhibitory DREADD to excitatory neurons would lead to the expected inhibition of the target not only on the cell level, but also at the population level. These are reasonable explanations, however inconsistent with our observations. In our study the promotor used was CamKII and the results observed parallel the ones described by Lopez et al (Lopez et al., 2016) for hSyn. Perhaps the differences observed between these results might be ascribed to the different viral serotypes employed in each study: AAV2.8 for Lopez et al (Lopez et al., 2016), and AAV8 in our study. Nevertheless, it is important to note that our electrophysiological analyses of the outcomes of the same manipulation in the vHPC were in line with the expectations: neural inhibition of the system (data not shown).

The contradictory outcomes from these first DREADD attempts made us move to a more specific alternative. Namely, the use of transgenic mice expressing Cre under the Nex promoter (specific to glutamatergic forebrain neurons; (Goebbels et al., 2006)) injected with a Cre-dependent viral vector. In that way I expected to have a more precise targeting of glutamatergic neurons, thus manipulating the neuronal activity of excitatory neurons only. A preliminary evaluation of the functionality of the system was performed by *ex-vivo* patch clamp recordings after expression of the viral vector at the mPFC (in the border of IL and PrL) and the expected outcome was observed: inhibition of local neural activity (data not shown; performed by Dr. Julien Dine, Electrophysiology Core Unit, MPI of Psychiatry). After this functional test I checked for behavioral effects of the manipulation (hM4D injection at the IL + CNO systemic treatment) in the WCM (experiment 9) and observed significant difference between groups

on accuracy and percentage of accurate learners on day 5, likely due to higher start bias on the hM4D group (however not significantly different because of the small number of animals per group). In line with this hypothesis, the percentage of side-biased animals differed between groups on day 1 and is slightly (but not significantly) higher for the hM4D group from days 2 to 5. Therefore, this preliminary experiment supports my hypothesis of a functional involvement of the IL in initial strategy switch during learning in the WCM. However, this experiment needs to be replicated to increase the number of animals and substantiate the initial findings.

Nevertheless, one should consider that the neuronal activity manipulations (optogenetics and chemogenetics) used here only target a small portion of the brain structures under study. Therefore, compensatory mechanisms might act to stabilize the system and lead to a zero (or small) net effect of the intervention (e.g. experiments 5, 6, 7 and 8). This self-stabilization is a core characteristic of neuronal networks. In particular, in case of evolutionary important capabilities such as spatial navigation, we can expect numerous redundancies and alternative compensatory strategies, which render it very complicated to demonstrate causal involvement of a single brain structure. As an example, Wheeler and colleagues (Wheeler et al., 2013) have demonstrated c-Fos changes upon recall of remote contextual fear memory in a high number of brain structures. However, follow-up individual chemogenetic inhibition of more than 20 of these structures – one by one – revealed "causal involvement" only for a few (Vetere et al., 2017).

4.6. **Conclusions**

Taken together, I believe that the results presented here describe important brain substrates specifically involved in the main navigation strategies used by animals: place learning or response learning. These results extend the list of previously identified brain structures involved in spatial cognition and its downstream targets, complementing the current knowledge on spatial navigation circuits' connectivity. By applying a whole brain voxel-wise analysis of MEMRI signal it was possible to identify structures overlooked in past studies due to the use of region of interest (ROI) analysis or specific local imaging methods limited to a small window of view.

Moreover, I elucidated some key functional mechanisms of MEMRI, such as the influence of neuronal activity in Mn^{2+} cellular entrance and transport along axonal terminals and transsynaptically, clarifying the interpretation of data obtained with this method and its possible future applications.

4.7. **Outlook**

As a follow-up of the studies presented here, I intend to pursue the causal involvement testing of selected structures from tables 2 and 3. More specifically, I am interested in investigating the causal involvement of pathways likely involved in spatial navigation of place or response learning and in the strategy switch from response to place learning during initial training under the place learning protocol.

Background knowledge on strategy switch during spatial learning was already presented in the introductory section of this thesis, and therefore will not be extensively revisited. However, I would like to highlight once more that most studies analyzing the strategy used by animals when they are free to choose how to navigate show that allocentric strategies (place learning) are preferred initially and are substituted by egocentric strategies (response learning) with extensive training (e.g. (Packard and McGaugh, 1996; Chang and

Gold, 2003; Colombo et al., 2003; Jacobson et al., 2012). Nevertheless, our observations in the lab, and partially reported previously (Kleinknecht et al., 2012), show the inverse order: response learning (until up to day 3) and place learning in the following days, under a place learning training. Similar observations were already reported in one study by Asem and Holland (Asem and Holland, 2013). In this work the authors raise interesting points on the possible reasons why their observations differ from the literature. Most importantly, the majority of studies analyzed spatial leaning strategies used for rodents to search for food rewards in dry mazes (for exceptions see (Packard and McGaugh, 1992; Devan and White, 1999; Lee et al., 2008), while they investigated the strategies used to reach an escape platform in a water T-maze. This difference in the experimental design has important consequences that should not be overlooked. First, the ethological explanation for the use of different strategies: food sources are widely distributed in the natural environment and require animals to use complex and refined foraging strategies to increase their chances to successfully navigate and find food. Therefore, allocentric-based navigation would be favored in this setting, because it is flexible and more effective in large and changing environments. In the artificial testing scenario (laboratory dry mazes) the food location is constant and this would facilitate navigation with time, allowing the switch to simpler, rigid response-based navigation strategies maintaining the cost-effectiveness of the choice. Second, in the water mazes the initial contact with water (considering that rodents are not natural swimmers) might cause despair and the need to react quickly to find escape, in a situation similar to fight or flight response. Also it might lead to the release of stress hormones that bias their navigation to the use of an egocentric strategy (Schwabe et al., 2010b; Schwabe et al., 2013; Vogel et al., 2015; Vogel et al., 2016), as discussed before. On top of that, the partial reinforcement of the incorrect choice (50% of correct trials if the animals always make the same body turn when the platform has a fixed location) might be sufficient for animals to persist in the wrong strategy for more than one day, passed the initial arousal/stress caused by water. Our observations with the water cross maze (WCM) are in line with this last study (Asem and Holland,

2013). Even if the possible reasons why this strategy switch occurs within the training days were already debated, the neuroanatomical substrates of this process are not described yet. To investigate this open question I focused on the pathway manipulation of the hippocampal – cortical circuit.

Preliminary results (experiments 9 and 10) presented here are part of our first attempts into this direction. These experiments focused on the dissection of the specific projections from the hippocampus (HPC) to the medial prefrontal cortex (mPFC) in the modulation of strategy switch. I identified the specific target in the vCA1 projecting to the infralimbic cortex (IL) by retrograde tracing and defined this pathway as our focus of study. Next, I aim to target this pathway specifically with a double viral approach (figure 24) for manipulating neuronal activity of the projections from vCA1 to IL and evaluating its effects on initial training in the WCM under the place learning protocol. Namely, I will inject a viral vector for Cre expression in CamKII positive neurons (AAV5-CamKII-Cre-GFP) in the vCA1 and later a retrograde viral vector for hM4D expression in a Cre-dependent manner (CAV2-DIO-hM4D-mCherry) in the IL. In that way I can dissect the specific projections from vCA1 to IL, specifically manipulate this pathway and investigate its functional role on strategy switch during WCM learning.
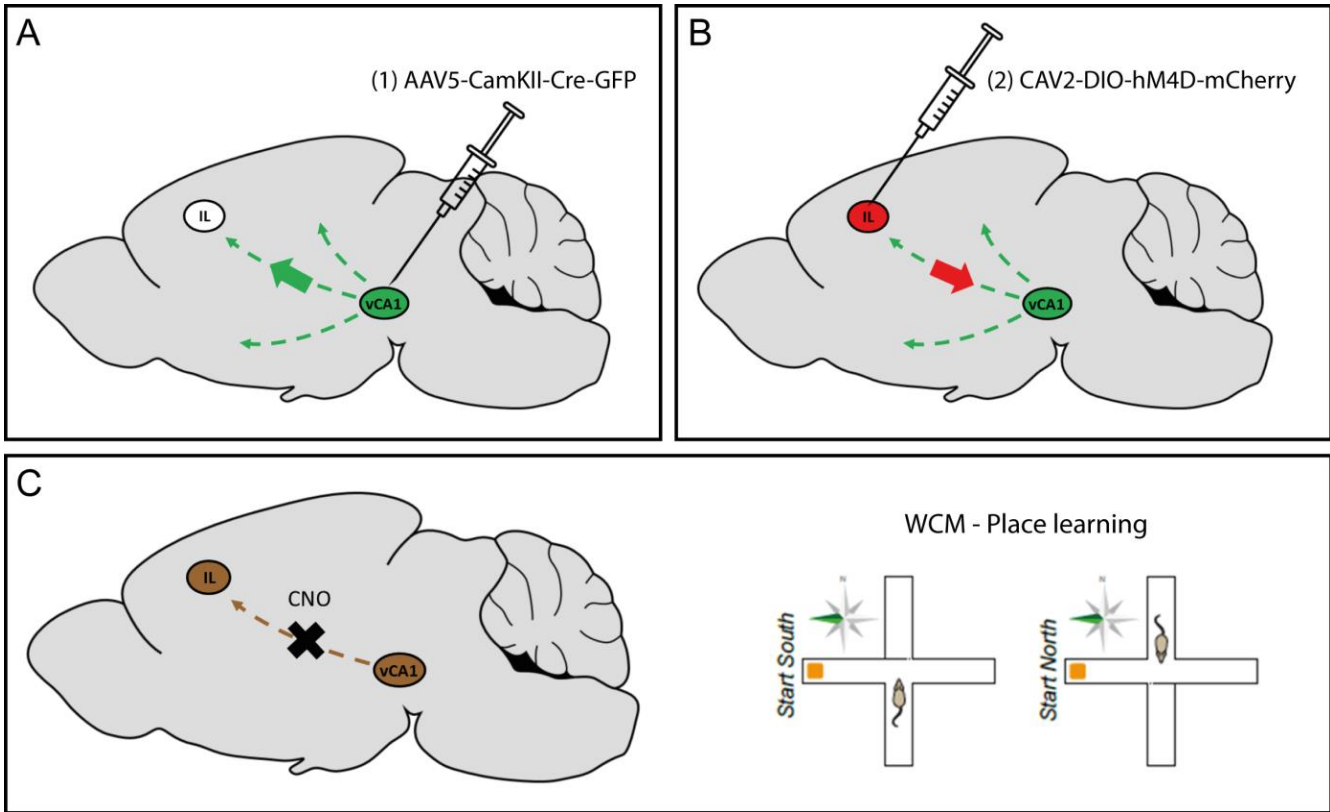
Figure 24*: vCA1-IL pathway modulation − experimental design.* A. Injection of the first viral vector (AAV5-CamKII-Cre-GFP) into the vCA1. B. 3 weeks after the first injection: injection of the second viral vector (CAV-DIO-hM4D-mCherry) into the IL. C. 10 days after the second injection: CNO treatment to inhibit the neuronal activity on the vCA1-IL pathway during training in the WCM under the response learning protocol.

I believe that this investigation will elucidate the brain circuit involved in an important process supporting behavioral control and choice selection aiming at successful navigation of the environment.

Finally, I also intend to use this methodological approach to investigate the vHPC-BLA pathway in the interplay of emotion and spatial learning (as presented in the *Introduction*).

5.   **APPENDIX**

5.1. **Complementary methods**

Preparation of optic fiber implants

Optic fiber implants for optogenetics were manufactured in house by the experimenter. The preparation procedure (adapted from (Sparta et al., 2011)) is, as follows:

- Strip a piece of optic fiber of approximately 25 mm

- Leave a piece of cap of approximately 3 cm adjacent to the exposed segment and cut it with forceps

- Fix the ceramic ferrule (with its flat end up) in a metal arm/holder

- Put a small drop of high temperature glue (should be stored at $-80^{\circ}C$ when not in use) on the upper tip of the ferrule and carefully place the fiber inside, letting it protrude down for approximately 2 mm

- Heat up the glue with heating gun for around 30 s (until the glue gets dark) and cut any remaining piece of fiber that is still protruding using a diamond knife

- Place the new implant with its dead end down in the polishing disc and polish the fiber (above a polishing pad) making an ¨8 (∞) shape¨ 20x for each polishing paper: black - pink - green - white (in this order)

- Cut the fiber tip at the proper length you need using a diamond knife

   The list of materials used and its references are below:

- Fiber (0.39 NA, Ø200 µm Core Multimode Optical Fiber, Low-OH for 400 - 2200 nm, TECS Clad) - reference: FT200EMT (ThorLabs, Newton, NJ, USA).

- Fiber stripping tool (Fiber Stripping Tool, Typical Cladding/Coating: 230 µm / 500 µm) - reference: T12S21 (ThorLabs, Newton, Newton, NJ, USA).

- Ceramic ferrule (Ø1.25 mm Multimode LC Ceramic Ferrule, Ø230 µm Hole Size) - reference: CFLC230-10 (ThorLabs, Newton, NJ, USA).

- High temperature glue (High Temperature & Low CTE Epoxy) - reference: 353NDPK (ThorLabs, Newton, NJ, USA).

- Polishing disc (Bare Ferrule Polishing Puck; FC/PC and SC/PC Ferrule Polishing Disc) – reference: D50-F (ThorLabs, Newton, NJ, USA).

- Polishing pad (Polishing Pad for PC Finishes, 8.75" x 13", 50 Durometer) – reference: NRS913A (ThorLabs, Newton, NJ, USA).

- Polishing paper (Fiber Polishing/Lapping Film for Use with Stainless Steel Ferrules) – references: LF5P (11" x 9" Silicon Carbide Lapping (Polishing) Sheets, 5 µm Grit; black); LF3P (11" x 9" Aluminum Oxide Lapping (Polishing) Sheets, 3 µm Grit; pink); LF1P (11" x 9" Aluminum Oxide Lapping (Polishing) Sheets, 1 µm Grit; green); LF03P (11" x 9" Calcined Alumina Lapping (Polishing) Sheets, 0.3 µm Grit; white) (ThorLabs, Newton, NJ, USA).

- Diamond knife (Diamond Wedge Scribe) – reference: S90W [discontinued] (ThorLabs, Newton, NJ, USA).

5.2. **Contributions**

The author contributed to the design of all studies, conceptualized, performed and analyzed all the WCM experiments (except for the experiment depicted in figures 7 and 8), carried out the MEMRI scans (except for experiment 3), injections of $MnCl_2$ (except for the experiment depicted in figures 7 and 8), viral vectors and fluorogold, production and implantation of the optic fiber constructs, laser stimulation for optogenetics experiments, histological analysis of brains, injections of CNO for chemogenetics experiments and *in situ* hybridization and immunohistochemical analysis.

Dr. Carsten T. Wotjak supervised all experiments and contributed to the design and the interpretation of all data.

Dr. Michael Czisch assisted in the conceptualization of experiment 2, supervised all the MEMRI scanning and performed the analysis of the MEMRI data.

Dr. Benedikt T. Bedenk conceptualized, performed and co-analyzed the experiment depicted in figures 7 and 8.

Dr. Simona Andreea Bura performed the MEMRI scans of the experiment depicted in figure 9 and co-performed the brain removal of the animals from experiment 4.

Dr. Julien Dine assisted in the conceptualization of experiment 1 and performed the electrophysiology experiments for functional testing of the DREADDs, as mentioned in the discussion (data not shown).

Dr. Andreas Genewsky assisted in the conceptualization of experiment 1, in the production and implantation of optic fiber constructs, and laser stimulation for optogenetics experiments.

Tim Ebbert performed the behavioral tests of experiments 7 and 8, and the quantification of the *in situ* hybridization results (experiment 4).

Julia Sulger translated the abstract of this manuscript from English to German.

5.3. **Financial support**

5.4. **Own publications**

Parts of this thesis have already been published in peer review journals (see publications below) and as part of the doctoral thesis of Benedikt Bedenk (figure 7, modified). During the period of my doctoral research I contributed to the following publications:

ALMEIDA-CORRÊA, SUELLEN; CZISCH, MICHAEL; WOTJAK, CARSTEN T. In vivo visualization of active polysynaptic circuits with longitudinal manganese-enhanced MRI (MEMRI). Frontiers in Neural Circuits, v. 12, article 42, 2018.

BEDENK, BENEDIKT T.; **ALMEIDA-CORRÊA, SUELLEN**; JURIK, ANGELA; DEDIC, NINA; GRÜNECKER, BARBARA; GENEWSKY, ANDREAS; KALTWASSER, SEBASTIAN F.; RIEBE, CAITLIN J.; DEUSSING, JAN M.; CZISCH, MICHAEL; WOTJAK, CARSTEN T. Mn2+ dynamics in manganese-enhanced MRI (MEMRI): CAv1.2 channel mediated uptake and preferential accumulation in projection terminals. NeuroImage, v. 169, p. 374-382, 2018.

REICHEL, JUDITH M.; BEDENK, BENEDIKT T.; GASSEN, NILS C.; HAFNER, K.; BURA, S. ANDREEA; **ALMEIDA-CORRÊA, SUELLEN**; GENEWSKY, ANDREAS; DEDIC, NINA; GIESERT, F.; AGARWAL, AMIT; NAVE, K.-A.; REIN, THEO; CZISCH, MICHAEL; DEUSSING, JAN M. AND WOTJAK, CARSTEN T. Beware of your Cre-Ation: lacZ expression impairs neuronal integrity and hippocampus-dependent memory. Hippocampus, v. 26, issue 10, p. 1250–1264, 2016.

Part of the data presented in this thesis (figure 6, table 1 and figure 22) has already been published in Almeida-Corrêa et al 2018. For that reason, it is reprinted in full below. Following, Bedenk et al 2018 is also reprinted to assist the reader in some of the interpretations of the *Discussion* of this thesis.

Almeida-Corrêa et al 2018

In Vivo Visualization of Active Polysynaptic Circuits With Longitudinal Manganese-Enhanced MRI (MEMRI)

Suellen Almeida-Corrêa[1], Michael Czisch[2] and Carsten T. Wotjak[1]*

[1] Department of Stress Neurobiology & Neurogenetics, Max Planck Institute of Psychiatry, Munich, Germany, [2] Core Unit Neuroimaging, Max Planck Institute of Psychiatry, Munich, Germany

Manganese-enhanced magnetic resonance imaging (MEMRI) is a powerful tool for *in vivo* non-invasive whole-brain mapping of neuronal activity. Mn^{2+} enters active neurons via voltage-gated calcium channels and increases local contrast in T_1-weighted images. Given the property of Mn^{2+} of axonal transport, this technique can also be used for tract tracing after local administration of the contrast agent. However, MEMRI is still not widely employed in basic research due to the lack of a complete description of the Mn^{2+} dynamics in the brain. Here, we sought to investigate how the activity state of neurons modulates interneuronal Mn^{2+} transport. To this end, we injected mice with low dose $MnCl_2$ 2. (i.p., 20 mg/kg; repeatedly for 8 days) followed by two MEMRI scans at an interval of 1 week without further $MnCl_2$ injections. We assessed changes in T_1 contrast intensity before (scan 1) and after (scan 2) partial sensory deprivation (unilateral whisker trimming), while keeping the animals in a sensory enriched environment. After correcting for the general decay in Mn^{2+} content, whole brain analysis revealed a single cluster with higher signal in scan 1 compared to scan 2: the left barrel cortex corresponding to the right untrimmed whiskers. In the inverse contrast (scan 2 > scan 1), a number of brain structures, including many efferents of the left barrel cortex were observed. These results suggest that continuous neuronal activity elicited by ongoing sensory stimulation accelerates Mn^{2+} transport from the uptake site to its projection terminals, while the blockage of sensory-input and the resulting decrease in neuronal activity attenuates Mn^{2+} transport. The description of this critical property of Mn^{2+} dynamics in the brain allows a better understanding of MEMRI functional mechanisms, which will lead to more carefully designed experiments and clearer interpretation of the results.

Keywords: manganese-enhanced MRI, neuroimaging, brain connectomics, Mn^{2+} transport, barrel-cortex, whiskers, sensory deprivation

INTRODUCTION

The dissection of neuronal pathways involved in specific brain networks underlying distinct behavioral outputs is of outmost interest to modern neuroscience. Currently employed methods in basic research include local brain injections of neuronal anterograde (Gerfen and Sawchenko, 1984; Veenman et al., 1992) and retrograde tracers (Arvidson, 1977; Schmued and Fallon, 1986; Quattrochi et al., 1989) or viral vectors (Wickersham et al., 2007; Zeng et al., 2017; Zingg et al., 2017). They rely on the investigation of the pathways *post-mortem*, via histological analysis of

brain slices or cleared brains when employing CLARITY based protocols for example (Chung et al., 2013). Moreover, these methods are limited to pre-defined regions of interest, given that they require targeted brain injections. A lot has been learned about neuronal circuits employing these tools, however, a non-invasive technique that would allow follow-up investigations comparing the same animals overtime is still desirable. Here, we focus on manganese-enhanced magnetic resonance imaging (MEMRI) as a powerful alternative.

MEMRI has the potential to non-invasively map whole-brain activity and identify structures related to a specific task (Chen et al., 2007, 2013; Bissig and Berkowitz, 2009; Eschenko et al., 2010; Bangasser et al., 2013; Hoch et al., 2013; Tang et al., 2016; Laine et al., 2017) since Mn^{2+} enters active neurons through voltage-gated calcium channels (Drapeau and Nachshen, 1984) (e.g., Ca$_v$1.2; Bedenk et al., 2018), and is transiently kept intracellularly (Gavin et al., 1990). Mn^{2+} shortens the T$_1$ relaxation time of water (Spiller et al., 1988; Nordhøy et al., 2004) leading to a contrast increase in T$_1$-weigthed images (Pautler and Koretsky, 2002). Brain structures that accumulate Mn^{2+} can be detected as hotspots in T$_1$-weighted images, indicating higher neuronal activity in these areas (Lin and Koretsky, 1997). This technique modality is also referred to as activation-induced manganese-dependent MRI (AIM-MRI) (Tambalo et al., 2009). If the integrity of the blood-brain barrier is disrupted, even dynamic accumulation of Mn^{2+} can be observed in a single experimental session (DAIM-MRI) (Aoki et al., 2002).

MEMRI is also used for tract-tracing (for review see Pautler, 2004), since Mn^{2+} can be axonally transported to neuronal terminals after local MnCl$_2$ administration (Sloot and Gramsbergen, 1994; Pautler et al., 1998), revealing the underlying circuitry of the injection target. During this process, Mn^{2+} may cross one or more synapses (Pautler et al., 1998).

We have recently shown that Mn^{2+} preferentially accumulates in projection terminals of the active entrance sites after systemic MnCl$_2$ administration (Bedenk et al., 2018). This feature of Mn^{2+} allows for the combination of activity-induced dissection of structures related to a specific behavior, and the connectomics analysis of the neuronal pathways underlying these brain structures. In that way, MEMRI does not only provide a snapshot of the structures active in response to a given task, but also reveals the downstream connectivity of these brain structures. This results in a functional connectivity map. Furthermore, the possibility of scanning the same animals at different time points allows for dynamic investigations of the functional circuitry in a within-subject fashion, thus reducing the number of required subjects while increasing the power of such studies (3-Rs principle for ethical use of animals in testing).

Despite those features, MEMRI is still not widely used, partially due to toxic side effects, but also due to insufficient information regarding Mn^{2+} dynamics in the brain, confounding the interpretation of the results. Some properties, such as activity-dependent entrance into cells via voltage-gated calcium channels (Drapeau and Nachshen, 1984), transient intracellular storage (Gavin et al., 1990), and preferential accumulation in projection terminals (Bedenk et al., 2018) have previously been reported. However, other properties such as the influence of neuronal

activity state on intracellular Mn^{2+} storage and axonal transport have been debated in the literature with inconclusive findings. Therefore, a complete description of Mn^{2+} dynamics in the brain is still lacking.

To address this, we conducted a longitudinal within-subject study to investigate whether, following systemic injections of MnCl$_2$, the transport of Mn^{2+} is dependent on neuronal activity elicited by sensory stimulation. As a model pathway for this study we chose the whiskers-barrel cortex system, based on its well-described and defined connectivity (for examples see Chmielowska et al., 1989; Aronoff et al., 2010; Zakiewicz et al., 2014) and the property of sensory stimulation by whisking resulting in a strong and specific increase on neuronal activity at the corresponding contralateral barrel cortex (Woolsey and Van der Loos, 1970; Axelrad et al., 1976; Peron et al., 2015). As such, we aimed to compare the contrast patterns observed with MEMRI (i) following systemic MnCl$_2$ injections in mice with intact whiskers in enriched sensory housing conditions, and (ii) after the same mice were partially sensory deprived (unilateral whisker trimming). We hypothesized that ongoing sensory input would lead to accelerated clearance of Mn^{2+} in the corresponding barrel cortex with a concomitant relative increase in Mn^{2+} accumulation in efferent structures.

MATERIALS AND METHODS

All experiments were carried out according to the European Community Council Directive 2010/63/EEC. All experimental procedures were approved by the local government of Upper Bavaria (AZ 142-12). Every effort was done to keep the number of experimental subjects at a minimum and to avoid animal suffering.

Animals

Adult male C57BL/6N mice ($n = 9$) from our local breeding stock (Max Planck Institute of Biochemistry, Martinsried, Germany) were kept in groups of 3 per cage with food and water *ad libitum*, under a 12 h dark/light inverted cycle (lights on at 07h30), in a room with controlled temperature and humidity. After transfer to the local animal facility at the Max Planck Institute of Psychiatry, mice were allowed to get accustomed to the holding conditions (standard macrolon cages type II; 267 × 207 × 140 mm, floor area 370 cm^2; Tecniplast, Italy) for at least 10 days before experiments started. Mice were 3 to 4 months old at the time of experiments. Intraperitoneal injections described next were conducted between 16h00 and 20h00.

Drugs

- MnCl$_2$ × 4H$_2$O (Sigma-Aldrich, Steinheim, Germany) was dissolved in 0.9% NaCl to a final concentration of 50 mM (4947.5 mg−500 mL saline). The pH was adjusted to 6.95 with HCl and NaOH.
- Ketamine + xylazine solution: 138 mg of ketamine and 6.8 mg of xylazine/10 mL solution (0.9% NaCl).

Experimental Procedures

Mice (3/cage) were housed in large type III cages ($425 \times 266 \times 155$ mm, floor area 820 cm^2; Tecniplast, Italy) enriched with extra nesting material, plastic hair curlers of two different sizes (2 big, 36 mm radius; 3 medium, 36 mm radius), used as texturized tunnels (textures on the inner and outer part), and a hanging thread at the metal lid with a another small hair curler/tunnel (28 mm radius). Mice were kept in the same group under this 8. condition for 8 days, until scanned (scan 1), followed by another 7 days of enriched housing and a second scan (scan 2).

All mice received intraperitoneal injections of 20 mg/kg MnCl$_2$ (Sigma-Aldrich, Steinheim, Germany) every 24 h for eight consecutive days (8 x 20/24 h), in order to minimize physiological side effects (adapted from Grünecker et al., 2010; Bedenk et al., 2018). Mice were always weighted immediately before injections to monitor animal's health status and to guarantee the correct dose would be injected every day.

On day 8, animals (3 per day) were individually anesthetized with a mixture ketamine and xylazine (i.p., injection of 0.1 mL/10 g mice) and transferred to the MRI room. With ketamine we aimed to block NMDA receptors (Anis et al., 1983) and thus, to avoid further Mn^{2+} neuronal entrance (Itoh et al., 2008) during the transport of the animals between rooms. For the scanning procedure, see below.

Immediately after scan 1, and still under sedation, animals had all their whiskers trimmed close to the skin on the left side of the snout. The right side was untouched. After trimming, animals were put back in the enriched cages. The trimming procedure was repeated every 2 days (under light isoflurane anesthesia) to avoid re-growth of the whiskers. After scan 1, animals received no further MnCl$_2$ injections.

On the last day of enrichment after scan 1, animals (3 per day) were again individually anesthetized with a mixture of ketamine and xylazine (i.p., injection of 0.1 mL/10 g mice) and transferred to the MRI room for scan 2. For graphic representation of the experimental design see **Figure 1A**.

Manganese-Enhanced Magnetic Resonance Imaging (MEMRI)

Twelve to twenty-four hours after the last of 8 daily MnCl$_2$ injections, a first MRI scanning took place (scan 1). Seven days after scan 1, the second MRI scanning took place (scan 2).

All MEMRI experiments were conducted on a 7T Avance Biospec 70/30 scanner (Bruker BioSpin, Ettlingen, Germany). In brief, essentially as described before (Bedenk et al., 2018), mice were fixed in supine position on a saddle-shaped receive-only coil. Head fixation was achieved using a stereotactic device and the frontal teeth were fixed with a surgical fiber. Once fixed in the coil, mice were kept anesthetized with an isoflurane-oxygen mixture (1.0–1.5 vol %, with an oxygen flow of 1.2–1.4 L/min) (Delta Select, Germany). A rectal thermometer was used for body temperature monitoring (Thermalert TH-5, Physitemp Instruments, USA). Body temperature was kept between 36.5 and 37.5°C using a water-based heating pad. Pulse rate was continuously monitored by a plethysmographic pulse oxymeter (Nonin 8600V, Nonin Medical Inc., USA).

T$_1$-weighted (T1w) brain images were acquired using a 3D gradient echo pulse sequence [TR = 50 ms, TE = 3.2 ms, matrix size = $128 \times 106 \times 106$ zero filled to $128 \times 128 \times 128$, field of view (FOV) = $16 \times 16 \times 18$ mm^3, number of averages = 10, resulting in a spatial resolution of $125 \times 125 \times 140.6$ µm^3].

MRI Data Post-processing

Images were reconstructed in Paravision (Bruker, BioSpin, Ettlingen, Germany) and transferred to standard ANALYSE format. Further post-processing was performed using SPM 8 (www.fil.ion.ucl.ac.uk/spm). T1w-images were bias-corrected using the algorithm implemented in SPM8, minimizing the entropy of the image histogram. In this way we could remove intensity gradients introduced by differences in the distance between surface receiver coil and the brain structures (Milchenko et al., 2006). For each individual subject the brain was then extracted using the RATS software (https://www.estima.com/ratsmain.shtml). Images were spatially normalized in two steps: In the first step, we generated a study-specific group template. For this purpose, we initially normalized all individual brain extracted images to a representative single subject image of good quality. The study-specific template image was then calculated as the mean image of all normalized images of this first step. In a second normalization step, this study-specific template was then used as the new target image for normalization. Doing so, we aimed at minimizing individual regional discrepancies in the final normalized images (Huang et al., 2010). Finally, all normalized images were smoothed with a Gaussian kernel of eight-times the image resolution ($1.0 \times 1.0 \times 1.124$ mm^3 at full-width half maximum). Data were analyzed using a paired t-test (scan 1 and scan 2), along with cerebrospinal fluid (CSF) intensities as a nuisance regressor. To account for unspecific global intensity changes due to Mn^{2+} wash-out between the two measurements (Grünecker et al., 2013), global image intensities were added as another nuisance regressor. Calculation of the global mean regressor was automatically performed in the generation of the ANCOVA model in SPM8: the global mean is calculated as the mean intensity of all voxel inside the standard analysis mask. By default, this mask includes all voxels which show an intensity larger than 1/8*(mean of all image voxels).

Definition of Brain Structures

All the brain structures shown in **Figure 1** and listed in **Table 1** were defined using the Allen Mouse Brain Atlas (Lein et al., 2006) (http://mouse.brain-map.org/experiment/thumbnails/100048576?image_type=atlas) as a reference. The only exception is the "islands of Calleja," defined based on "10. The Mouse Brain in Stereotaxic Coordinates" (Franklin and Paxinos, 2007).

Statistics and Data Presentation

We interrogated the contrast scan 1 > scan 2 using a strict family-wise error corrected threshold of $p_{FWE,cluster} < 0.05$, with a collection threshold of $p_{uncorrected} < 0.001$ (Woo et al., 2014), which is in accordance with other MEMRI studies (Lutkenhoff et al., 2012; Laine et al., 2017). Due to expected dilution of Mn^{2+} concentrations after cessation of the MnCl2 injections, relative

FIGURE 1 | MEMRI contrast differences after unilateral sensory deprivation. **(A)** Graphic representation of experimental design. Mice were treated with MnCl$_2$ (20 mg/kg; i.p.) for 8 days, while housed in a sensory enriched environment, until scan 1. Immediately after scan 1, mice had their left whiskers trimmed (procedure repeated every 2 days) and remained in the sensory enriched environment for 7 more days without further MnCl$_2$ injections, until scan 2. **(B)** Representative coronal brain slices indicating the structures showing differential MEMRI signal in scans 1 and 2 (yellow: scan 1 > scan 2; blue: scan 2 > scan 1). Brain structures indicated in the figure: 1, olfactory bulb; 2, orbital area; 3, islands of Calleja; 4, supplemental somatosensory area; 5, barrel cortex; 6, medial thalamic nuclei; 7, caudoputamen; 8, temporal association area; 9, anterior pretectal nucleus; 10, nucleus of the optic tract; 11, anterolateral visual area; 12, perirhinal area; 13, temporal association area + ectorhinal area + perirhinal area; 14, subiculum—ventral part; 15, dentate gyrus—ventral part; 16, pontine nuclei; 17, retrosplenial area; 18, superior vestibular nucleus; 19, cerebellum. Plate numbers under brain slices correspond to the reference plate of the Allen Mouse Brain Atlas used to define the structures.
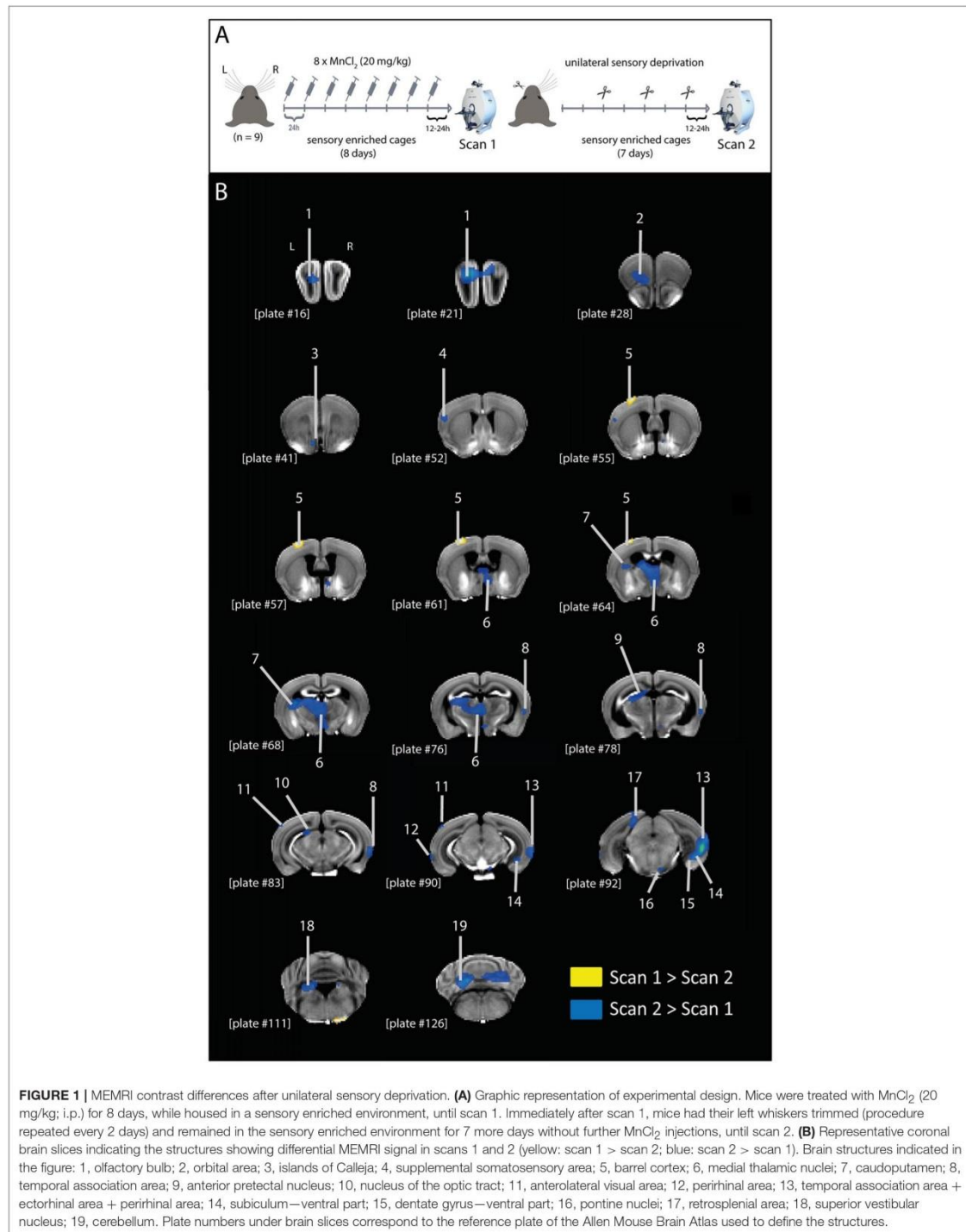
128

TABLE 1 | List of structures showing differential MEMRI signal between scans 1 and 2, ipsi or contralateral to the reference point (left barrel cortex).

Brain structures	# on Figure 1	MEMRI signal ≠		Barrel cortex efferent?*	
		ipsi (L)	contra (R)	ipsi (L)	contra (R)
Olfactory bulb—anterior	1	Scan 2 > Scan 1			
Olfactory bulb—posterior	1	Scan 2 > Scan 1	Scan 2 > Scan 1		
Orbital area	2	Scan 2 > Scan 1		1st order efferents	
Islands of Calleja (striatum)	3	Scan 2 > Scan 1			
Supplemental somatosensory area	4	Scan 2 > Scan 1		1st order efferents	1st order efferents
BARREL CORTEX	**5**	Scan 1 > Scan 2			
Medial thalamic nuclei—anterior	6		Scan 2 > Scan 1	1st order efferents	1st order efferents
Medial thalamic nuclei—posterior	6	Scan 2 > Scan 1		1st order efferents	1st order efferents
Caudoputamen	7	Scan 2 > Scan 1		1st order efferents	1st order efferents
Temporal association areas	8		Scan 2 > Scan 1		
Lateral posterior nucleus of the thalamus	6	Scan 2 > Scan 1		1st order efferents	
Dorsal part of the lateral geniculate complex	6	Scan 2 > Scan 1		2nd order efferents	
Parafascicular nucleus	6	Scan 2 > Scan 1		2nd order efferents	
Posterior complex of the thalamus	6	Scan 2 > Scan 1		1st order efferents	
Anterior pretectal nucleus	9	Scan 2 > Scan 1		1st order efferents	
Lateral posterior nucleus of the thalamus	6	Scan 2 > Scan 1		1st order efferents	
Nucleus of the optic tract	10	Scan 2 > Scan 1			
Anterolateral visual area	11	Scan 2 > Scan 1			
Perirhinal area	12	Scan 2 > Scan 1		1st order efferents	1st order efferents
Ectorhinal area	13		Scan 2 > Scan 1	1st order efferents	1st order efferents
Subiculum—ventral part	14		Scan 2 > Scan 1		
Dentate gyrus—ventral part	15		Scan 2 > Scan 1		
Pontine nuclei	16		Scan 2 > Scan 1	1st order efferents	
Retrosplenial area	17	Scan 2 > Scan 1		1st order efferents	
Superior vestibular nucleus (medulla)	18	Scan 2 > Scan 1			
Cerebellum	19	Scan 2 > Scan 1	Scan 2 > Scan 1		

Legend:
- Yellow: *Scan 1 > Scan 2*
- Blue: *Scan 2 > Scan 1*
- Light green: *1st order efferents*
- Gray: *2nd order efferents*

based on the following references: White and DeAmicis, 1977; Ohara et al., 1980; Montero and Scott, 1981; Ohara and Lieberman, 1981, 1985; Hoogland et al., 1987, 1991; Cornwall and Phillipson, 1988; Welker et al., 1988; Chen et al., 1992; Raos and Bentivoglio, 1993; Bourassa et al., 1995; Hazrati et al., 1995; Pinault et al., 1995; Pinault and Deschenes, 1998; Veinante et al., 2000; Wright et al., 2000; Wang et al., 2005; Aronoff et al., 2010; Zakiewicz et al., 2014; Tang et al., 2016; Guo et al., 2017; Sumser et al., 2017.

129

local increases of Mn^{2+} accumulation in the second scan (scan 2 > scan 1) were only assessed qualitatively at an uncorrected threshold of $p < 0.05$ (cluster extent 20).

Voxel-wise analysis of the MR images was performed in SPM8 (www.fil.ion.ucl.ac.uk/spm). Graphics of activation maps have been created in MRICro (www.cabiatl.com/mricro). All images were ultimately arranged in Adobe Illustrator 10.0.3 (Adobe Systems Inc., NY, USA).

RESULTS

After correcting for the unspecific global decrease of Mn^{2+} between the experimental time points, we identified only a single cluster showing higher Mn^{2+} intensity in the first scan compared to the second (scan 1 > scan 2). This cluster was located in the left barrel cortex ($p_{FWE,cluster} = 0.009$, cluster extent 236 voxel), representing activity of the untrimmed whiskers (**Figure 1B**; **Table 1**).

In the inverse contrast (scan 2 > scan 1), a number of brain structures could be detected to show a stronger intensity at time point 2 (**Figure 1B**; **Table 1**), mainly located in the left hemisphere.

The higher signal in the left barrel cortex (corresponding to the untrimmed whiskers) in scan 1 compared to scan 2, and the lack of difference in the right barrel cortex (corresponding to the trimmed whiskers) suggests that the sensory blockage by whisker trimming attenuated the Mn^{2+} transport to projection terminals. This hypothesis is further supported by the clusters showing higher Mn^{2+} intensity in the second measurement compared to the first (scan 2 > scan 1), which include a large number (85% of total) of efferents of the left barrel cortex (**Table 1**). Therefore, we conclude that Mn^{2+} is transported from the uptake site to its projection terminals, in an activity-dependent manner.

DISCUSSION

Here we show that, after systemic $MnCl_2$ injections, both intra- and interneuronal transport of Mn^{2+} is accelerated by the continuous activity of the afferent cells in the brain, when compared to a unilaterally sensory deprived pathway. This conclusion was based on the following observations: (i) only the barrel cortex of the corresponding untrimmed whiskers showed higher MEMRI signal in scan 1 compared to scan 2; (ii) most of the structures that showed higher MEMRI signal in scan 2 compared to scan 1 are efferent to the barrel cortex (**Table 1**; **Figure 2**).

The Whisker-Barrel Cortex System

The mouse barrel-cortex system was chosen as a model due to its well characterized connectivity (Woolsey and Van der Loos, 1970; Welker, 1976) and because of its property of strong and defined neuronal activation in the barrel cortex contralateral to its specific sensory input (Woolsey and Van der Loos, 1970; Axelrad et al., 1976; Peron et al., 2015). Therefore, it is the perfect model system to study changes in neuronal activity due to sensory stimulation or deprivation, and the underlying Mn^{2+} dynamics related to neuronal activation. This pathway was already used elsewhere
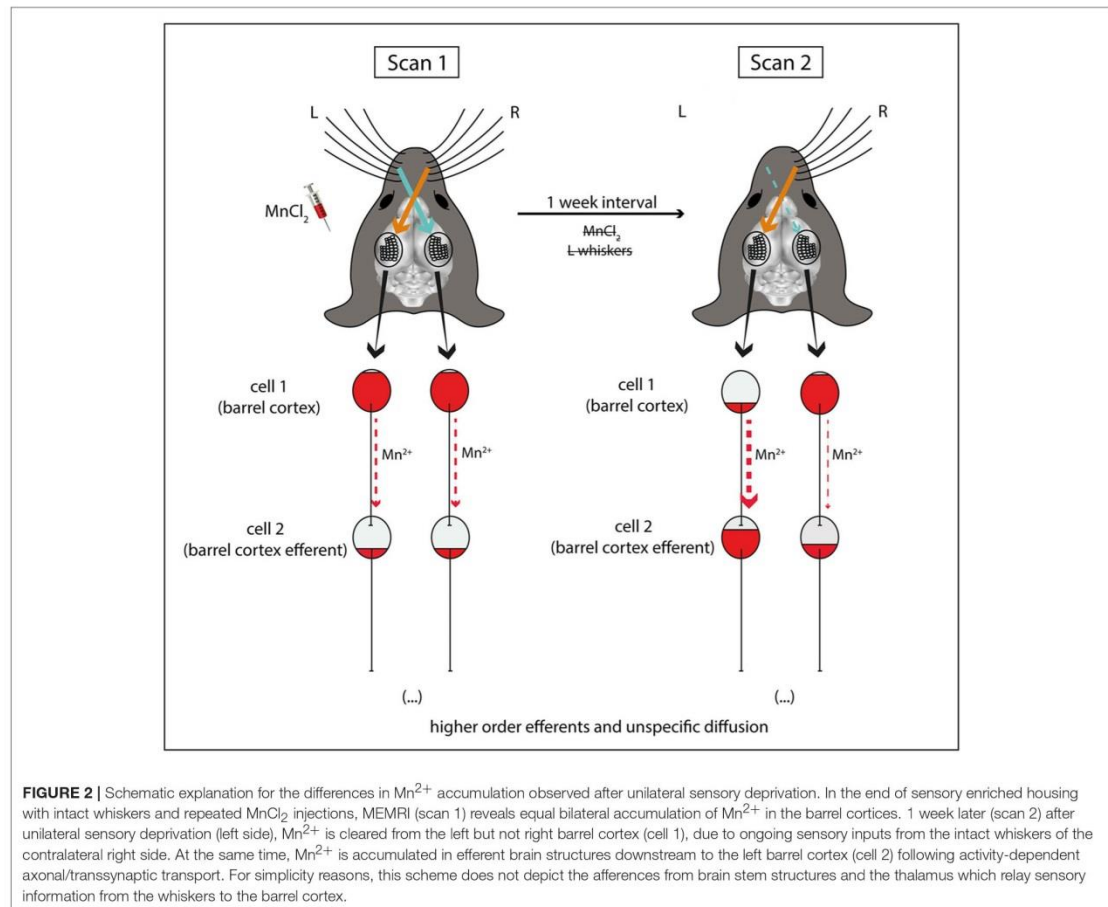
to map tactile sense-evoked activity with MEMRI (Weng et al., 2007), BOLD (Lu et al., 2004; de Celis Alonso et al., 2012) and CBV fMRI (Lu et al., 2004) after mechanical whisker stimulation in rats; also with MEMRI after blood-brain barrier ultrasonic disruption and mechanical whisker stimulation in mice (Howles et al., 2010).

For the sake of simplicity, in our conclusion scheme (**Figure 2**) we represented neurons of the barrel cortex as cell 1 (reference point). These neurons are the cortical representation of a mouse's contralateral whiskers (Woolsey and Van der Loos, 1970; Ferezou et al., 2006). However, it is worth highlighting that after stimulation of the whiskers, sensory information is initially processed by the trigeminal nuclei of the brainstem, followed, in parallel, by the ventroposterior medial (VPM)—lemniscal and extralemniscal pathways—and the posterior medial (POm) nuclei of the thalamus—paralemniscal pathway—before reaching the barrel cortex (for review Petersen, 2007; Diamond et al., 2008). Therefore, the barrel cortex cells are already downstream to other brain structures which may take up Mn^{2+} in an activity-dependent manner.

Most of the brain structures which showed higher Mn^{2+} levels in scan 2 compared to scan 1 turned out to be efferent to the left barrel cortex, including monosynaptic (1st order) and polysynaptic (2nd order) projection sites (**Table 1**). This connectivity analysis and assignment was made taking the vast barrel cortex connectivity data in the literature into account (for examples see Aronoff et al., 2010; Zakiewicz et al., 2014). Second order efferents were here defined as the projections from either of the two main outputs of the barrel cortex, namely: the thalamic reticular nucleus and the posterior complex of the thalamus (Hoogland et al., 1987; Wright et al., 2000). Some brain structures, especially medial thalamic nuclei, are both 1st and 2nd order efferents. In these cases, they were just assigned as 1st order efferents.

An important point to mention is that most of the whisker-barrel connectivity literature is based on rat experiments. Large part of this data (Ohara et al., 1980; Montero and Scott, 1981; Ohara and Lieberman, 1981, 1985; Cornwall and Phillipson, 1988; Chen et al., 1992; Raos and Bentivoglio, 1993; Bourassa et al., 1995; Hazrati et al., 1995; Pinault et al., 1995; Pinault and Deschenes, 1998; Veinante et al., 2000; Wright et al., 2000; Wang et al., 2005; Zakiewicz et al., 2014) was included in our analysis to assign structures as barrel cortex efferents. Given the similarities of the rat and mouse nervous system, we do not believe that inter-species differences could falsely or significantly impact the connectivity analysis presented here. However, we acknowledge that small differences between the barrel system connectivity of these species were already reported (Kichula and Huntley, 2008).

The results shown here included most, but not all the barrel cortex efferents previously described. In fact, some of its main outputs, such as the motor cortex or the thalamic reticular nucleus, did not show a differential MEMRI signal in scan 2 compared to scan 1. This might be ascribed to the fact that Mn^{2+} can be transsynapticaly transported, as already reported elsewhere (Saleem et al., 2002; Pautler et al., 2003; Murayama et al., 2006; Bearer et al., 2007), and also shown here by the geniculate and parafascicular nuclei of the thalamus, which

130

FIGURE 2 | Schematic explanation for the differences in Mn^{2+} accumulation observed after unilateral sensory deprivation. In the end of sensory enriched housing with intact whiskers and repeated MnCl$_2$ injections, MEMRI (scan 1) reveals equal bilateral accumulation of Mn^{2+} in the barrel cortices. 1 week later (scan 2) after unilateral sensory deprivation (left side), Mn^{2+} is cleared from the left but not right barrel cortex (cell 1), due to ongoing sensory inputs from the intact whiskers of the contralateral right side. At the same time, Mn^{2+} is accumulated in efferent brain structures downstream to the left barrel cortex (cell 2) following activity-dependent axonal/transsynaptic transport. For simplicity reasons, this scheme does not depict the afferences from brain stem structures and the thalamus which relay sensory information from the whiskers to the barrel cortex.

represent 2nd order efferents from the barrel cortex and 1st order efferents from the reticular nucleus. This might lead to an additional dilution of the Mn^{2+} contrast, hindering its detection by voxel wise brain analysis. Another possibility is that the MEMRI signal might have been filtered out in large structures which receive diffused rather than focused projections, such as the motor cortex, because the signal intensity tends to be higher in compact and densely connected structures (Aoki et al., 2004; Bedenk et al., 2018).

It is important to note that our protocol of partial sensory deprivation (whisker trimming) was applied to adult mice only (3–4 months old) and did not include follicle removal or cauterization. Moreover, considering the short duration of the deprivation (7 days), we do not believe that the results of this study are a consequence of cortical map plasticity, widely described in neurodevelopmental and plasticity studies using the barrel-cortex system model (Van der Loos and Woolsey, 1973; Woolsey and Wann, 1976; Levin and Dunn-Meynell, 1991; Dunn-Meynell et al., 1992; Siucinska and Kossut, 1994; Melzer

and Smith, 1996; Kossut and Juliano, 1999; Fox, 2002; Allen et al., 2003; Rema et al., 2003; Schierloh et al., 2003; Shepherd et al., 2003; Dubroff et al., 2005; Fox and Wong, 2005; Shoykhet et al., 2005; Frostig, 2006; Lee et al., 2007; Schubert et al., 2007; Drew and Feldman, 2009; Wu et al., 2011; Gainey et al., 2016; Jacob et al., 2017).

Mn^{2+} Administration, Toxicity, and Decay

MEMRI studies have already employed different routes for Mn^{2+} administration, such as intracerebral injections (Pautler et al., 2003; Watanabe et al., 2004; Yang et al., 2011), intranasal aerosols (Henriksson et al., 1999; Pautler and Koretsky, 2002; Lehallier et al., 2012), intravitreal injection (Pautler et al., 1998; Bearer et al., 2007; Luo et al., 2012), and topic eye application (Lin et al., 2014). These methods are however invasive and often toxic (Bearer et al., 2007; Luo et al., 2012; Lin et al., 2014). Systemic injections have a reduced risk of toxicity if fractionated (Grünecker et al., 2010), or continuously delivered with osmotic mini pumps (Sepulveda et al., 2012; Poole et al., 2017). The

delayed and limited diffusion of Mn^{2+} to the brain should also be considered. In each case, care must be taken to find an optimal balance between a sufficient dose to reach the best contrast while minimizing the potential side/toxic effects of Mn^{2+} in the brain. The use of systemic methods for delivering of $MnCl_2$ has clear advantages, e.g., in case of prolonged behavioral procedures. In some cases, however, systemic treatment has to be combined with the disruption of the blood-brain barrier (BBB), e.g., by mannitol injection (Lin and Koretsky, 1997; Aoki et al., 2002) or by ultrasound (Howles et al., 2010), in order to allow the Mn^{2+} to quickly reach the brain. In these cases, a single $MnCl_2$ spike injection can be applied. Even with the use of relatively small doses for a single shot that did not cause major apparent side/toxic effects, small impairments as transient motor deficit in skilled reaching, rears, and activity was already described in rats (Alaverdashvili et al., 2017). This limitation should be considered, especially when designing studies with behavioral experiments where fine motor skills are necessary. For longer term investigations (from many hours to days) the disruption of the BBB is not necessary (Yu et al., 2005; Kuo et al., 2006), given that Mn^{2+} can reach the brain and accumulate in a activity-dependent manner in the structures related to the challenge/task performed at least few hours before. This applies in particular to the paradigm used here, where we "pre-loaded" the cells with Mn^{2+} before the experimental intervention (whiskers trimming). Our data suggest this procedure might also be used for acute behavioral challenges where mice could be first treated with $MnCl_2$ to reach sufficient contrast, followed by repeated scanning before and after the challenge.

One should also not overlook clearance of Mn^{2+} in the brain when scans are performed long (more than 24 h) after the $MnCl_2$ injections have stopped. We previously reported that the half-life of Mn^{2+}, after an 8×30 mg/kg $MnCl_2$ injection protocol, is about 5–7 days, depending on the brain structures (Grünecker et al., 2013). This point was taken into consideration in our analysis comparing scans 1 and 2, which were performed 1 week apart.

The Interplay of Neuronal Activity and Mn^{2+} Axonal and Transsynaptic Transport

Previous studies already investigated the possible role of neuronal activity in Mn^{2+} axonal and transsynaptic transport in specific pathways with different protocols and obtained, somewhat, contradicting results. For instance, it was shown that Mn^{2+} is co-released with neurotransmitters after stimulation with high K^+ (Takeda et al., 1998), indicating that Mn^{2+} transport is dynamically linked to neural signaling. Later, many groups mapped sensory system activation in response to specific odors (Pautler et al., 1998; Pautler and Koretsky, 2002; Chuang et al., 2009; Lehallier et al., 2012), visual (Bissig and Berkowitz, 2009), or acoustic stimulation (Yu et al., 2005), supporting the idea that Mn^{2+} transport is activity-dependent. One of these studies (Bearer et al., 2007) employed transgenic blind mice to investigate activity-dependency in Mn^{2+} dynamics after intravitreal $MnCl_2$ injection and concluded that "Mn^{2+} is not transmitted efficiently across synapses in the absence of electrical activity in this system," whereas uptake and axonal transport remained intact. This last conclusion is supported

by the results of Lowe et al. (2008) showing no difference in MEMRI signal intensity in the visual system between groups treated with $MnCl_2$ only or in combination with cell activity blockers (APB or TTX). On the other hand, accelerated Mn^{2+} transport after $MnCl_2$ co-treatment with AMPA was already described (Wang et al., 2015), indicating that axonal transport of Mn^{2+} is dynamically modulated by neuronal activity. In fact, pharmacological blockage of calcium channels also blocked this accelerated transport (Wang et al., 2015). Using the song control system in song birds as a model of neuronal plasticity (for review see Van der Linden et al., 2004), Tindemans et al. (2003) were able to show an activity dependent transsynaptic transport of Mn^{2+} from the site of local cerebral injection of Mn^{2+} in the HVC (high vocal center; a relay region of the song control system) to more downstream regions [such as the nucleus robustus arcopallialis (RA) and the striatal area X]. Using dynamic MEMRI, the authors reported that both regions showed a more rapid accumulation of Mn^{2+} in the stimulated birds. After about 10 h, this difference to non-stimulated birds vanished only for RA, but not for area X, suggesting a differential functional connectivity of the two regions in the song circuitry. Considering these previous reports and the results presented here, we conclude that, even in the case of systemic $MnCl_2$ injection, axonal and transsynaptic transport of Mn^{2+} is modulated by the activity state of the neuronal pathway. Our results further suggest that reduced neuronal activity due to blockage of sensory inputs attenuates the transport of Mn^{2+} from its initial accumulation site, while continuous neuronal activity promotes the transport of Mn^{2+} between neurons.

Ketamine and NMDA Receptor Blockage

We used ketamine in an anesthetic dose (138 mg/kg) (Buitrago et al., 2008) in order to block NMDA receptor-related neuronal activity (Anis et al., 1983) and, thus, to avoid further entrance of Mn^{2+} in neurons (Itoh et al., 2008), which might be caused by transportation of the animals from the vivarium to the scanning room and/or their fixation inside the scanner. We are aware of the fact that ketamine has complex and not fully understood mechanisms of action and might lead to unspecific effects which are unrelated to anesthesia such as hyperlocomotion (Hayase et al., 2006) or antidepressant-like effects in low doses (Kavalali and Monteggia, 2012). However, in the present study we can exclude that ketamine has affected MEMRI signal intensities by itself, due to: (i) $MnCl_2$ treatment was given chronically for 8 days and finished at least 12 h before ketamine injection; (ii) there was only a short interval (~30 min) between ketamine administration and the scanning procedure; and (iii) the within-subject design used here (ketamine treatment before both first and second scans).

CONCLUSION

Taken together, we provide evidence for neuronal activity-dependent accelerated transport of Mn^{2+} to projection terminals and across synapses. This observation allows for a more careful design of the experiments using systemic $MnCl_2$ treatment. At the same time, it adds another layer of components to the interpretation of the results obtained by MEMRI.

132

AUTHOR CONTRIBUTIONS

FUNDING

ACKNOWLEDGMENTS

REFERENCES

Alaverdashvili, M., Lapointe, V., Whishaw, I. Q., and Cross, A. R. (2017). Manganese-enhanced magnetic resonance imaging and studies of rat behavior: transient motor deficit in skilled reaching, rears, and activity in rats after a single dose of MnCl2. *Magn. Reson. Insights* 10, 1178623–17706878. doi: 10.1177/1178623X17706878

Allen, C. B., Celikel, T., and Feldman, D. E. (2003). Long-term depression induced by sensory deprivation during cortical map plasticity *in vivo*. *Nat. Neurosci.* 6, 291–299. doi: 10.1038/nn1012

Anis, N. A., Berry, S. C., Burton, N. R., and Lodge, D. (1983). The dissociative anaesthetics, ketamine and phencyclidine, selectively reduce excitation of central mammalian neurones by N-methyl-aspartate. *Br. J. Pharmacol.* 79, 565–575. doi: 10.1111/j.1476-5381.1983.tb11031.x

Aoki, I., Tanaka, C., Takegami, T., Ebisu, T., Umeda, M., Fukunaga, M., et al. (2002). Dynamic activity-induced manganese-dependent contrast magnetic resonance imaging (DAIM MRI). *Magn. Reson. Med.* 48, 927–933. doi: 10.1002/mrm.10320

Aoki, I., Wu, Y. J., Silva, A. C., Lynch, R. M., and Koretsky, A. P. (2004). *In vivo* detection of neuroarchitecture in the rodent brain using manganese-enhanced MRI. *Neuroimage* 22, 1046–1059. doi: 10.1016/j.neuroimage.2004.03.031

Aronoff, R., Matyas, F., Mateo, C., Ciron, C., Schneider, B., and Petersen, C. C. (2010). Long-range connectivity of mouse primary somatosensory barrel cortex. *Eur. J. Neurosci.* 31, 2221–2233. doi: 10.1111/j.1460-9568.2010.07264.x

Arvidson, B. (1977). Retrograde axonal transport of horseradish peroxidase from cornea to trigeminal ganglion. *Acta Neuropathol.* 38, 49–52. doi: 10.1007/BF00691276

Axelrad, H., Verley, R., and Farkas, E. (1976). Responses evoked in mouse and rat SI cortex by vibrissa stimulation. *Neurosci. Lett.* 3, 265–274. doi: 10.1016/0304-3940(76)90053-7

Bangasser, D. A., Lee, C. S., Cook, P. A., Gee, J. C., Bhatnagar, S., and Valentino, R. J. (2013). Manganese-enhanced magnetic resonance imaging (MEMRI) reveals brain circuitry involved in responding to an acute novel stress in rats with a history of repeated social stress. *Physiol. Behav.* 122, 228–236. doi: 10.1016/j.physbeh.2013.04.008

Bearer, E. L., Falzone, T. L., Zhang, X., Biris, O., Rasin, A., and Jacobs, R. E. (2007). Role of neuronal activity and kinesin on tract tracing by manganese-enhanced MRI (MEMRI). *Neuroimage* (37 Suppl. 1), S37–S46. doi: 10.1016/j.neuroimage.2007.04.053

Bedenk, B. T., Almeida-Corrêa, S., Jurik, A., Dedic, N., Grünecker, B., Genewsky, A. J., et al. (2018). Mn2+ dynamics in manganese-enhanced MRI (MEMRI): Cav1.2 channel-mediated uptake and preferential accumulation in projection terminals. *Neuroimage* 169, 374–382. doi: 10.1016/j.neuroimage.2017.12.054

Bissig, D., and Berkowitz, B. A. (2009). Manganese-enhanced MRI of layer-specific activity in the visual cortex from awake and free-moving rats. *Neuroimage* 44, 627–635. doi: 10.1016/j.neuroimage.2008.10.013

Bourassa, J., Pinault, D., and Deschênes, M. (1995). Corticothalamic projections from the cortical barrel field to the somatosensory thalamus in rats: a single-fibre study using biocytin as an anterograde tracer. *Eur. J. Neurosci.* 7, 19–30. doi: 10.1111/j.1460-9568.1995.tb01016.x

Buitrago, S., Martin, T. E., Tetens-Woodring, J., Belicha-Villanueva, A., and Wilding, G. E. (2008). Safety and efficacy of various combinations of injectable anesthetics in BALB/c mice. *J. Am. Assoc. Lab. Anim. Sci.* 47, 11–17.

Chen, K. H., Chen, D. Y., and Liang, K. C. (2013). Functional connectivity changes during consolidation of inhibitory avoidance memory in rats: a manganese-enhanced MRI study. *Chin. J. Physiol.* 56, 269–281. doi: 10.4077/CJP.2013.BAB144

Chen, S., Raos, V., and Bentivoglio, M. (1992). Connections of the thalamic reticular nucleus with the contralateral thalamus in the rat. *Neurosci. Lett.* 147, 85–88. doi: 10.1016/0304-3940(92)90780-B

Chen, W., Tenney, J., Kulkarni, P., and King, J. A. (2007). Imaging unconditioned fear response with manganese-enhanced MRI (MEMRI). *Neuroimage* 37, 221–229. doi: 10.1016/j.neuroimage.2007.05.001

Chmielowska, J., Carvell, G. E., and Simons, D. J. (1989). Spatial organization of thalamocortical and corticothalamic projection systems in the rat SmI barrel cortex. *J. Comp. Neurol.* 285, 325–338. doi: 10.1002/cne.902850304

Chuang, K. H., Lee, J. H., Silva, A. C., Belluscio, L., and Koretsky, A. P. (2009). Manganese enhanced MRI reveals functional circuitry in response to odorant stimuli. *Neuroimage* 44, 363–372. doi: 10.1016/j.neuroimage.2008.08.046

Chung, K., Wallace, J., Kim, S.-Y., Kalyanasundaram, S., Andalman, A. S., Davidson, T. J., et al. (2013). Structural and molecular interrogation of intact biological systems. *Nature* 497, 332–337. doi: 10.1038/nature12107

Cornwall, J., and Phillipson, O. T. (1988). Afferent projections to the parafascicular thalamic nucleus of the rat, as shown by the retrograde transport of wheat germ agglutinin. *Brain Res. Bull.* 20, 139–150. doi: 10.1016/0361-9230(88)90171-2

de Celis Alonso, B., Sergeyeva, M., Brune, K., and Hess, A. (2012). Lateralization of responses to vibrissal stimulation: connectivity and information integration in the rat sensory-motor cortex assessed with fMRI. *Neuroimage* 62, 2101–2109. doi: 10.1016/j.neuroimage.2012.05.045

Diamond, M. E., von Heimendahl, M., Knutsen, P. M., Kleinfeld, D., and Ahissar, E. (2008). 'Where' and 'what' in the whisker sensorimotor system. *Nat. Rev. Neurosci.* 9, 601–612. doi: 10.1038/nrn2411

Drapeau, P., and Nachshen, D. A. (1984). Manganese fluxes and manganese-dependent neurotransmitter release in presynaptic nerve endings isolated from rat brain. *J. Physiol.* 348, 493–510. doi: 10.1113/jphysiol.1984.sp015121

Drew, P. J., and Feldman, D. E. (2009). Intrinsic signal imaging of deprivation-induced contraction of whisker representations in rat somatosensory cortex. *Cereb. Cortex* 19, 331–348. doi: 10.1093/cercor/bhn085

Dubroff, J. G., Stevens, R. T., Hitt, J., Maier, D. L., McCasland, J. S., and Hodge, C. J. (2005). Use-dependent plasticity in barrel cortex: intrinsic signal imaging reveals functional expansion of spared whisker representation into adjacent deprived columns. *Somatosens. Mot. Res.* 22, 25–35. doi: 10.1080/08990220500084990

Dunn-Meynell, A. A., Benowitz, L. I., and Levin, B. E. (1992). Vibrissectomy induced changes in GAP-43 immunoreactivity in the adult rat barrel cortex. *J. Comp. Neurol.* 315, 160–170. doi: 10.1002/cne.903150204

Eschenko, O., Canals, S., Simanova, I., Beyerlein, M., Murayama, Y., and Logothetis, N. K. (2010). Mapping of functional brain activity in freely behaving rats during voluntary running using manganese-enhanced MRI: implication for longitudinal studies. *Neuroimage* 49, 2544–2555. doi: 10.1016/j.neuroimage.2009.10.079

Ferezou, I., Bolea, S., and Petersen, C. C. (2006). Visualizing the cortical representation of whisker touch: voltage-sensitive dye imaging in freely moving mice. *Neuron* 50, 617–629. doi: 10.1016/j.neuron.2006.03.043

Fox, K. (2002). Anatomical pathways and molecular mechanisms for plasticity in the barrel cortex. *Neuroscience* 111, 799–814. doi: 10.1016/S0306-4522(02)00027-1

Fox, K., and Wong, R. O. (2005). A comparison of experience-dependent plasticity in the visual and somatosensory systems. *Neuron* 48, 465–477. doi: 10.1016/j.neuron.2005.10.013

Franklin, K. B. J., and Paxinos, G. (2007). *The Mouse Brain in Stereotaxic Coordinates, 3rd Edn.* San Diego, CA: Academic Press; Elsevier.

Frostig, R. D. (2006). Functional organization and plasticity in the adult rat barrel cortex: moving out-of-the-box. *Curr. Opin. Neurobiol.* 16, 445–450. doi: 10.1016/j.conb.2006.06.001

Gainey, M. A., Wolfe, R., Pourzia, O., and Feldman, D. E. (2016). Whisker deprivation drives two phases of inhibitory synapse weakening in layer 4 of rat somatosensory cortex. *PLoS ONE* 11:e0148227. doi: 10.1371/journal.pone.0148227

Gavin, C. E., Gunter, K. K., and Gunter, T. E. (1990). Manganese and calcium efflux kinetics in brain mitochondria. Relevance to manganese toxicity. *Biochem. J.* 266, 329–334. doi: 10.1042/bj2660329

Gerfen, C. R., and Sawchenko, P. E. (1984). An anterograde neuroanatomical tracing method that shows the detailed morphology of neurons, their axons and terminals: immunohistochemical localization of an axonally transported plant lectin, *Phaseolus vulgaris* leucoagglutinin (PHA-L). *Brain Res.* 290, 219–238. doi: 10.1016/0006-8993(84)90 940-5

Grünecker, B., Kaltwasser Sebastian, F., Peterse, Y., Sämann Philipp, G., Schmidt Mathias, V., Wotjak Carsten, T., et al. (2010). Fractionated manganese injections: effects on MRI contrast enhancement and physiological measures in C57BL/6 mice. *NMR Biomed.* 23, 913–921. doi: 10.1002/nbm.1508

Grünecker, B., Kaltwasser, S. F., Zappe, A. C., Bedenk, B. T., Bicker, Y., Spoormaker, V. I., et al. (2013). Regional specificity of manganese accumulation and clearance in the mouse brain: implications for manganese-enhanced MRI. *NMR Biomed.* 26, 542–556. doi: 10.1002/nbm.2891

Guo, C., Peng, J., Zhang, Y., Li, A., Li, Y., Yuan, J., et al. (2017). Single-axon level morphological analysis of corticofugal projection neurons in mouse barrel field. *Sci. Rep.* 7:2846. doi: 10.1038/s41598-017-03000-8

Hayase, T., Yamamoto, Y., and Yamamoto, K. (2006). Behavioral effects of ketamine and toxic interactions with psychostimulants. *BMC Neurosci.* 7:25. doi: 10.1186/1471-2202-7-25

Hazrati, L. N., Pinault, D., and Parent, A. (1995). The thalamic reticular nucleus does not send commissural projection to the contralateral parafascicular nucleus in the rat. *Brain Res.* 679, 123–134. doi: 10.1016/0006-8993(95)00223-D

Henriksson, J., Tallkvist, J., and Tjälve, H. (1999). Transport of manganese via the olfactory pathway in rats: dosage dependency of the uptake and subcellular distribution of the metal in the olfactory epithelium and the brain. *Toxicol. Appl. Pharmacol.* 156, 119–128. doi: 10.1006/taap.1999.8639

Hoch, T., Kreitz, S., Gaffling, S., Pischetsrieder, M., and Hess, A. (2013). Manganese-enhanced magnetic resonance imaging for mapping of whole brain activity patterns associated with the intake of snack food in *ad libitum* fed rats. *PLoS ONE* 8:e55354. doi: 10.1371/journal.pone.0055354

Hoogland, P. V., Welker, E., and Van der Loos, H. (1987). Organization of the projections from barrel cortex to thalamus in mice studied with *Phaseolus vulgaris*-leucoagglutinin and HRP. *Exp. Brain Res.* 68, 73–87. doi: 10.1007/BF00255235

Hoogland, P. V., Wouterlood, F. G., Welker, E., and Van der Loos, H. (1991). Ultrastructure of giant and small thalamic terminals of cortical origin: a study of the projections from the barrel cortex in mice using *Phaseolus vulgaris* leuco-agglutinin (PHA-L). *Exp. Brain Res.* 87, 159–172. doi: 10.1007/BF00228517

Howles, G. P., Qi, Y., and Johnson, G. A. (2010). Ultrasonic disruption of the blood-brain barrier enables *in vivo* functional mapping of the mouse barrel field cortex with manganese-enhanced MRI. *Neuroimage* 50, 1464–1471. doi: 10.1016/j.neuroimage.2010.01.050

Huang, C. M., Lee, S. H., Hsiao, I. T., Kuan, W. C., Wai, Y. Y., Ko, H. J., et al. (2010). Study-specific EPI template improves group analysis in functional MRI of young and older adults. *J. Neurosci. Methods* 189, 257–266. doi: 10.1016/j.jneumeth.2010.03.021

Itoh, K., Sakata, M., Watanabe, M., Aikawa, Y., and Fujii, H. (2008). The entry of manganese ions into the brain is accelerated by the activation of N-methyl-d-aspartate receptors. *Neuroscience* 154, 732–740. doi: 10.1016/j.neuroscience.2008.03.080

Jacob, V., Mitani, A., Toyoizumi, T., and Fox, K. (2017). Whisker row deprivation affects the flow of sensory information through rat barrel cortex. *J. Neurophysiol.* 117, 4–17. doi: 10.1152/jn.00289.2016

Kavalali, E. T., and Monteggia, L. M. (2012). Synaptic mechanisms underlying rapid antidepressant action of ketamine. *Am. J. Psychiatry* 169, 1150–1156. doi: 10.1176/appi.ajp.2012.12040531

Kichula, E. A., and Huntley, G. W. (2008). Developmental and comparative aspects of posterior medial thalamocortical innervation of the barrel cortex in mice and rats. *J. Comp. Neurol.* 509, 239–258. doi: 10.1002/cne.21690

Kossut, M., and Juliano, S. L. (1999). Anatomical correlates of representational map reorganization induced by partial vibrissectomy in the barrel cortex of adult mice. *Neuroscience* 92, 807–817. doi: 10.1016/S0306-4522(98)00722-2

Kuo, Y. T., Herlihy, A. H., So, P. W., and Bell, J. D. (2006). Manganese-enhanced magnetic resonance imaging (MEMRI) without compromise of the blood-brain barrier detects hypothalamic neuronal activity *in vivo*. *NMR Biomed.* 19, 1028–1034. doi: 10.1002/nbm.1070

Laine, M. A., Sokolowska, E., Dudek, M., Callan, S. A., Hyytia, P., and Hovatta, I. (2017). Brain activation induced by chronic psychosocial stress in mice. *Sci. Rep.* 7:15061. doi: 10.1038/s41598-017-15422-5

Lee, S. H., Land, P. W., and Simons, D. J. (2007). Layer- and cell-type-specific effects of neonatal whisker-trimming in adult rat barrel cortex. *J. Neurophysiol.* 97, 4380–4385. doi: 10.1152/jn.01217.2006

Lehallier, B., Coureaud, G., Maurin, Y., and Bonny, J. M. (2012). Effects of manganese injected into rat nostrils: implications for *in vivo* functional study of olfaction using MEMRI. *Magn. Reson. Imaging* 30, 62–69. doi: 10.1016/j.mri.2011.08.009

Lein, E. S., Hawrylycz, M. J., Ao, N., Ayres, M., Bensinger, A., Bernard, A., et al. (2006). Genome-wide atlas of gene expression in the adult mouse brain. *Nature* 445, 168–176. doi: 10.1038/nature05453

Levin, B. E., and Dunn-Meynell, A. (1991). Adult rat barrel cortex plasticity occurs at 1 week but not at 1 day after vibrissectomy as demonstrated by the 2-deoxyglucose method. *Exp. Neurol.* 113, 237–248. doi: 10.1016/0014-4886(91)90180-K

Lin, T. H., Chiang, C. W., Trinkaus, K., Spees, W. M., Sun, P., and Song, S. K. (2014). Manganese-enhanced MRI (MEMRI) via topical loading of Mn(2+) significantly impairs mouse visual acuity: a comparison with intravitreal injection. *NMR Biomed.* 27, 390–398. doi: 10.1002/nbm.3073

Lin, Y. J., and Koretsky, A. P. (1997). Manganese ion enhances T1-weighted MRI during brain activation: an approach to direct imaging of brain function. *Magn. Reson. Med.* 38, 378–388. doi: 10.1002/mrm.1910380305

Lowe, A. S., Thompson, I. D., and Sibson, N. R. (2008). Quantitative manganese tract tracing: dose-dependent and activity-independent terminal labelling in the mouse visual system. *NMR Biomed.* 21, 859–867. doi: 10.1002/nbm.1272

Lu, H., Patel, S., Luo, F., Li, S. J., Hillard, C. J., Ward, B. D., et al. (2004). Spatial correlations of laminar BOLD and CBV responses to rat whisker stimulation with neuronal activity localized by Fos expression. *Magn. Reson. Med.* 52, 1060–1068. doi: 10.1002/mrm.20265

Luo, L., Xu, H., Li, Y., Du, Z., Sun, X., Ma, Z., et al. (2012). Manganese-enhanced MRI optic nerve tracking: effect of intravitreal manganese dose on retinal toxicity. *NMR Biomed.* 25, 1360–1368. doi: 10.1002/nbm.2808

Lutkenhoff, E., Karlsgodt, K. H., Gutman, B., Stein, J. L., Thompson, P. M., Cannon, T. D., et al. (2012). Structural and functional neuroimaging phenotypes in dysbindin mutant mice. *Neuroimage* 62, 120–129. doi: 10.1016/j.neuroimage.2012.05.008

Melzer, P., and Smith, C. B. (1996). Plasticity of metabolic whisker maps in somatosensory brainstem and thalamus of mice with neonatal lesions of whisker follicles. *Eur. J. Neurosci.* 8, 1853–1864. doi: 10.1111/j.1460-9568.1996.tb01329.x

Milchenko, M. V., Pianykh, O. S., and Tyler, J. M. (2006). The fast automatic algorithm for correction of MR bias field. *J. Magn. Reson. Imaging* 24, 891–900. doi: 10.1002/jmri.20695

Montero, V. M., and Scott, G. L. (1981). Synaptic terminals in the dorsal lateral geniculate nucleus from neurons of the thalamic reticular nucleus: a light

134

and electron microscope autoradiographic study. *Neuroscience* 6, 2561–2577. doi: 10.1016/0306-4522(81)90102-0

Murayama, Y., Weber, B., Saleem, K. S., Augath, M., and Logothetis, N. K. (2006). Tracing neural circuits *in vivo* with Mn-enhanced MRI. *Magn. Reson. Imaging* 24, 349–358. doi: 10.1016/j.mri.2005.12.031

Nordhøy , W., Anthonsen, H. W., Bruvold, M., Brurok, H., Skarra, S., Krane, J., et al. (2004). Intracellular manganese ions provide strong T1 relaxation in rat myocardium. *Magn. Reson. Med.* 52, 506–514. doi: 10.1002/mrm.20199

Ohara, P. T., and Lieberman, A. R. (1981). Thalamic reticular nucleus: anatomical evidence that cortico-reticular axons establish monosynaptic contact with reticulo-geniculate projection cells. *Brain Res.* 207, 153–156. doi: 10.1016/0006-8993(81)90685-5

Ohara, P. T., and Lieberman, A. R. (1985). The thalamic reticular nucleus of the adult rat: experimental anatomical studies. *J. Neurocytol.* 14, 365–411. doi: 10.1007/BF01217752

Ohara, P. T., Sefton, A. J., and Lieberman, A. R. (1980). Mode of termination of afferents from the thalamic reticular nucleus in the dorsal lateral geniculate nucleus of the rat. *Brain Res.* 197, 503–506. doi: 10.1016/0006-8993(80)91136-1

Pautler, R. G. (2004). *In vivo*, trans-synaptic tract-tracing utilizing manganese-enhanced magnetic resonance imaging (MEMRI). *NMR Biomed.* 17, 595–601. doi: 10.1002/nbm.942

Pautler, R. G., and Koretsky, A. P. (2002). Tracing odor-induced activation in the olfactory bulbs of mice using manganese-enhanced magnetic resonance imaging. *Neuroimage* 16, 441–448. doi: 10.1006/nimg.2002.1075

Pautler, R. G., Mongeau, R., and Jacobs, R. E. (2003). *In vivo* trans-synaptic tract tracing from the murine striatum and amygdala utilizing manganese enhanced MRI (MEMRI). *Magn. Reson. Med.* 50, 33–39. doi: 10.1002/mrm.10498

Pautler, R. G., Silva, A. C., and Koretsky, A. P. (1998). *In vivo* neuronal tract tracing using manganese-enhanced magnetic resonance imaging. *Magn. Reson. Med.* 40, 740–748. doi: 10.1002/mrm.1910400515

Peron, S. P., Freeman, J., Iyer, V., Guo, C., and Svoboda, K. (2015). A Cellular resolution map of barrel cortex activity during tactile behavior. *Neuron* 86, 783–799. doi: 10.1016/j.neuron.2015.03.027

Petersen, C. C. (2007). The functional organization of the barrel cortex. *Neuron* 56, 339–355. doi: 10.1016/j.neuron.2007.09.017

Pinault, D., Bourassa, J., and Deschênes, M. (1995). Thalamic reticular input to the rat visual thalamus: a single fiber study using biocytin as an anterograde tracer. *Brain Res.* 670, 147–152. doi: 10.1016/0006-8993(94)01303-Y

Pinault, D., and Deschênes, M. (1998). Projection and innervation patterns of individual thalamic reticular axons in the thalamus of the adult rat: a three-dimensional, graphic, and morphometric analysis. *J. Comp. Neurol.* 391, 180–203. doi: 10.1002/(SICI)1096-9861(19980209)391:2<180::AID-CNE3>3.0.CO;2-Z

Poole, D. S., Doorenweerd, N., Plomp, J. J., Mahfouz, A., Reinders, M. J. T., and van der Weerd, L. (2017). Continuous infusion of manganese improves contrast and reduces side effects in manganese-enhanced magnetic resonance imaging studies. *Neuroimage* 147, 1–9. doi: 10.1016/j.neuroimage.2016.09.030

Quattrochi, J. J., Mamelak, A. N., Madison, R. D., Macklis, J. D., and Hobson, J. A. (1989). Mapping neuronal inputs to REM sleep induction sites with carbachol-fluorescent microspheres. *Science* 245, 984–986. doi: 10.1126/science.2475910

Raos, V., and Bentivoglio, M. (1993). Crosstalk between the two sides of the thalamus through the reticular nucleus: a retrograde and anterograde tracing study in the rat. *J. Comp. Neurol.* 332, 145–154. doi: 10.1002/cne.903320202

Rema, V., Armstrong-James, M., and Ebner, F. F. (2003). Experience-dependent plasticity is impaired in adult rat barrel cortex after whiskers are unused in early postnatal life. *J. Neurosci.* 23, 358–366. doi: 10.1523/JNEUROSCI.23-01-00358.2003

Saleem, K. S., Pauls, J. M., Augath, M., Trinath, T., Prause, B. A., Hashikawa, T., et al. (2002). Magnetic resonance imaging of neuronal connections in the macaque monkey. *Neuron* 34, 685–700. doi: 10.1016/S0896-6273(02)00718-3

Schierloh, A., Eder, M., Zieglgänsberger, W., and Dodt, H. U. (2003). Sensory deprivation changes the pattern of synaptic connectivity in rat barrel cortex. *Neuroreport* 14, 1787–1791. doi: 10.1097/00001756-200310060-00006

Schmued, L. C., and Fallon, J. H. (1986). Fluoro-Gold: a new fluorescent retrograde axonal tracer with numerous unique properties. *Brain Res.* 377, 147–154. doi: 10.1016/0006-8993(86)91199-6

Schubert, D., Kötter, R., and Staiger, J. F. (2007). Mapping functional connectivity in barrel-related columns reveals layer- and cell type-specific microcircuits. *Brain Struct. Funct.* 212, 107–119. doi: 10.1007/s00429-007-0147-z

Sepulveda, M. R., Dresselaers, T., Vangheluwe, P., Everaerts, W., Himmelreich, U., Mata, A. M., et al. (2012). Evaluation of manganese uptake and toxicity in mouse brain during continuous MnCl2 administration using osmotic pumps. *Contrast Media Mol. Imaging* 7, 426–434. doi: 10.1002/cmmi.1469

Shepherd, G. M., Pologruto, T. A., and Svoboda, K. (2003). Circuit analysis of experience-dependent plasticity in the developing rat barrel cortex. *Neuron* 38, 277–289. doi: 10.1016/S0896-6273(03)00152-1

Shoykhet, M., Land, P. W., and Simons, D. J. (2005). Whisker trimming begun at birth or on postnatal day 12 affects excitatory and inhibitory receptive fields of layer IV barrel neurons. *J. Neurophysiol.* 94, 3987–3995. doi: 10.1152/jn.00569.2005

Siucinska, E., and Kossut, M. (1994). Short term changes of cortical body maps following partial vibrissectomy in adult mice. *Acta Neurobiol. Exp.* 54, 345–354.

Sloot, W. N., and Gramsbergen, J. B. (1994). Axonal transport of manganese and its relevance to selective neurotoxicity in the rat basal ganglia. *Brain Res.* 657, 124–132. doi: 10.1016/0006-8993(94)90959-8

Spiller, M., Brown, R. D. III, Koenig, S. H., and Wolf, G. L. (1988). Longitudinal proton relaxation rates in rabbit tissues after intravenous injection of free and chelated Mn^{2+}. *Magn. Reson. Med.* 8, 293–313. doi: 10.1002/mrm.1910080307

Sumser, A., Mease, R. A., Sakmann, B., and Groh, A. (2017). Organization and somatotopy of corticothalamic projections from L5B in mouse barrel cortex. *Proc. Natl. Acad. Sci. U.S.A.* 114, 8853–8858. doi: 10.1073/pnas.1704302114

Takeda, A., Kodama, Y., Ishiwatari, S., and Okada, S. (1998). Manganese transport in the neural circuit of rat CNS. *Brain Res. Bull.* 45, 149–152. doi: 10.1016/S0361-9230(97)00330-4

Tambalo, S., Daducci, A., Fiorini, S., Boschi, F., Mariani, M., Marinone, M., et al. (2009). Experimental protocol for activation-induced manganese-enhanced MRI (AIM-MRI) based on quantitative determination of Mn content in rat brain by fast T1 mapping. *Magn. Reson. Med.* 62, 1080–1084. doi: 10.1002/mrm.22095

Tang, X., Wu, D., Gu, L. H., Nie, B. B., Qi, X. Y., Wang, Y. J., et al. (2016). Spatial learning and memory impairments are associated with increased neuronal activity in 5XFAD mouse as measured by manganese-enhanced magnetic resonance imaging. *Oncotarget* 7, 57556–57570. doi: 10.18632/oncotarget.11353

Tindemans, I., Verhoye, M., Balthazart, J., and Van Der Linden, A. (2003). *In vivo* dynamic ME-MRI reveals differential functional responses of RA- and area X-projecting neurons in the HVC of canaries exposed to conspecific song. *Eur. J. Neurosci.* 18, 3352–3360. doi: 10.1111/j.1460-9568.2003.03056.x

Van der Linden, A., Van Meir, V., Tindemans, I., Verhoye, M., and Balthazart, J. (2004). Applications of manganese-enhanced magnetic resonance imaging (MEMRI) to image brain plasticity in song birds. *NMR Biomed.* 17, 602–612. doi: 10.1002/nbm.936

Van der Loos, H., and Woolsey, T. A. (1973). Somatosensory cortex: structural alterations following early injury to sense organs. *Science* 179, 395–398. doi: 10.1126/science.179.4071.395

Veenman, C. L., Reiner, A., and Honig, M. G. (1992). Biotinylated dextran amine as an anterograde tracer for single- and double-labeling studies. *J. Neurosci. Methods* 41, 239–254. doi: 10.1016/0165-0270(92)90089-V

Veinante, P., Lavallée, P., and Deschênes, M. (2000). Corticothalamic projections from layer 5 of the vibrissal barrel cortex in the rat. *J. Comp. Neurol.* 424, 197–204. doi: 10.1002/1096-9861(20000821)424:2<197::AID-CNE1>3.0.CO;2-6

Wang, J., Huo, F. Q., Li, Y. Q., Chen, T., Han, F., and Tang, J. S. (2005). Thalamic nucleus submedius receives GABAergic projection from thalamic reticular nucleus in the rat. *Neuroscience* 134, 515–523. doi: 10.1016/j.neuroscience.2005.04.025

Wang, L., Lu, H., Brown, P. L., Rea, W., Vaupel, B., Yang, Y., et al. (2015). Manganese-enhanced MRI reflects both activity-independent and activity-dependent uptake within the rat habenulomesencephalic pathway. *PLoS ONE* 10:e0127773. doi: 10.1371/journal.pone.0127773

Watanabe, T., Radulovic, J., Spiess, J., Natt, O., Boretius, S., Frahm, J., et al. (2004). *In vivo* 3D MRI staining of the mouse hippocampal system using intracerebral injection of MnCl2. *Neuroimage* 22, 860–867. doi: 10.1016/j.neuroimage.2004.01.028
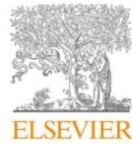
135

Welker, C. (1976). Receptive fields of barrels in the somatosensory neocortex of the rat. *J. Comp. Neurol.* 166, 173–189. doi: 10.1002/cne.901660205

Welker, E., Hoogland, P. V., and Van der Loos, H. (1988). Organization of feedback and feedforward projections of the barrel cortex: a PHA-L study in the mouse. *Exp. Brain Res.* 73, 411–435. doi: 10.1007/BF00248234

Weng, J. C., Chen, J. H., Yang, P. F., and Tseng, W. Y. (2007). Functional mapping of rat barrel activation following whisker stimulation using activity-induced manganese-dependent contrast. *Neuroimage* 36, 1179–1188. doi: 10.1016/j.neuroimage.2007.04.010

White, E. L., and DeAmicis, R. A. (1977). Afferent and efferent projections of the region in mouse SmL cortex which contains the posteromedial barrel subfield. *J. Comp. Neurol.* 175, 455–482. doi: 10.1002/cne.901750405

Wickersham, I. R., Finke, S., Conzelmann, K. K., and Callaway, E. M. (2007). Retrograde neuronal tracing with a deletion-mutant rabies virus. *Nat. Methods* 4, 47–49. doi: 10.1038/nmeth999

Woo, C. W., Krishnan, A., and Wager, T. D. (2014). Cluster-extent based thresholding in fMRI analyses: pitfalls and recommendations. *Neuroimage* 91, 412–419. doi: 10.1016/j.neuroimage.2013.12.058

Woolsey, T. A., and Van der Loos, H. (1970). The structural organization of layer IV in the somatosensory region (SI) of mouse cerebral cortex. The description of a cortical field composed of discrete cytoarchitectonic units. *Brain Res.* 17, 205–242. doi: 10.1016/0006-8993(70)90079-X

Woolsey, T. A., and Wann, J. R. (1976). Areal changes in mouse cortical barrels following vibrissal damage at different postnatal ages. *J. Comp. Neurol.* 170, 53–66. doi: 10.1002/cne.901700105

Wright, A. K., Norrie, L., and Arbuthnott, G. W. (2000). Corticofugal axons from adjacent 'barrel' columns of rat somatosensory cortex: cortical and thalamic terminal patterns. *J. Anat.* 196 (Pt 3), 379–390. doi: 10.1046/j.1469-7580.2000.19630379.x

Wu, C. S., Ballester Rosado, C. J., and Lu, H. C. (2011). What can we get from 'barrels': the rodent barrel cortex as a model for studyingthe

establishment of neural circuits. *Eur. J. Neurosci.* 34, 1663–1676. doi: 10.1111/j.1460-9568.2011.07892.x

Yang, P. F., Chen, D. Y., Hu, J. W., Chen, J. H., and Yen, C. T. (2011). Functional tracing of medial nociceptive pathways using activity-dependent manganese-enhanced MRI. *Pain* 152, 194–203. doi: 10.1016/j.pain.2010.10.027

Yu, X., Wadghiri, Y. Z., Sanes, D. H., and Turnbull, D. H. (2005). *In vivo* auditory brain mapping in mice with Mn-enhanced MRI. *Nat. Neurosci.* 8, 961–968. doi: 10.1038/nn1477

Zakiewicz, I. M., Bjaalie, J. G., and Leergaard, T. B. (2014). Brain-wide map of efferent projections from rat barrel cortex. *Front. Neuroinform.* 8:5. doi: 10.3389/fninf.2014.00005

Zeng, W. B., Jiang, H. F., Gang, Y. D., Song, Y. G., Shen, Z. Z., Yang, H., et al. (2017). Anterograde monosynaptic transneuronal tracers derived from herpes simplex virus 1 strain H129. *Mol. Neurodegener.* 12, 38. doi: 10.1186/s13024-017-0179-7

Zingg, B., Chou, X. L., Zhang, Z. G., Mesik, L., Liang, F., Tao, H. W., et al. (2017). AAV-mediated anterograde transsynaptic tagging: mapping corticocollicular input-defined neural pathways for defense behaviors. *Neuron* 93, 33–47. doi: 10.1016/j.neuron.2016.11.045

136

Bedenk et al 2018

Mn²⁺ dynamics in manganese-enhanced MRI (MEMRI): Caᵥ1.2 channel-mediated uptake and preferential accumulation in projection terminals

Benedikt T. Bedenk [a,b], Suellen Almeida-Corrêa [a], Angela Jurik [a], Nina Dedic [a], Barbara Grünecker [b], Andreas J. Genewsky [a], Sebastian F. Kaltwasser [a], Caitlin J. Riebe [a], Jan M. Deussing [a], Michael Czisch [b,1], Carsten T. Wotjak [a,*,1]

[a] Max Planck Institute of Psychiatry, Dept. Stress Neurobiology & Neurogenetics, Kraepelinstr. 2-10, 80804 Munich, Germany
[b] Max Planck Institute of Psychiatry, Core Unit Neuroimaging, Kraepelinstr. 2-10, 80804 Munich, Germany

ARTICLE INFO

ABSTRACT

Manganese-enhanced magnetic resonance imaging (MEMRI) exploits the biophysical similarity of Ca^{2+} and Mn^{2+} to map the brain's activity *in vivo*. However, to what extent different Ca^{2+} channels contribute to the enhanced signal that MEMRI provides and how Mn^{2+} dynamics influence Mn^{2+} brain accumulation after systemic administration of $MnCl_2$ are not yet fully understood. Here, we demonstrate that mice lacking the L-type Ca^{2+} channel 1.2 (Caᵥ1.2) in the CNS show approximately 50% less increase in MEMRI contrast after repeated systemic $MnCl_2$ injections, as compared to control mice. In contrast, genetic deletion of L-type Ca^{2+} channel 1.3 (Caᵥ1.3) did not reduce signal. Brain structure- or cell type-specific deletion of Caᵥ1.2 in combination with voxel-wise MEMRI analysis revealed a preferential accumulation of Mn^{2+} in projection terminals, which was confirmed by local $MnCl_2$ administration to defined brain areas.

Taken together, we provide unequivocal evidence that Caᵥ1.2 represents an important channel for neuronal Mn^{2+} influx after systemic injections. We also show that after neuronal uptake, Mn^{2+} preferentially accumulates in projection terminals.

Introduction

Manganese-enhanced magnetic resonance imaging (MEMRI) has gained considerable attention in preclinical imaging, both as a method to increase tissue contrast in MRI (Pautler and Koretsky, 2002), and as a proxy for brain activity levels under basal (resting) conditions or due to external stimulation (Yu et al., 2008, 2005). The advantage of MEMRI over BOLD-based fMRI is that manganese (Mn^{2+}) accumulates in an activity-dependent manner in the brain of awake and behaving animals (Berkowitz et al., 2010; Bissig and Berkowitz, 2009; Eschenko et al., 2010; Lehallier et al., 2012; Lin and Koretsky, 1997; Yu et al., 2005), with only the final MRI readout needing to be performed under sedation. In addition, magnetic field susceptibility does not affect the T1-weighted MEMRI images to such an extent as in T2* weighted BOLD-based fMRI (Pohmann, 2011), which is especially advantageous for assessing inferior brain structures such as the amygdala or hypothalamic regions.

Unfortunately, being a heavy metal ion, Mn^{2+} has (neuro-) toxic side effects at higher concentrations (Aschner and Aschner, 1991; Canals et al., 2008; Crossgrove and Zheng, 2004; Eriksson et al., 1987; Normandin and Hazell, 2002; O'Neal and Zheng, 2015; Sloot et al., 1994). To avoid toxicity, low-dose approaches have been proposed, which include fractionated application in several injections (Bock et al., 2008; Grunecker et al., 2010), or continuous delivery using osmotic minipumps (Eschenko et al., 2010; Sepulveda et al., 2012). As a result, systemic treatment with $MnCl_2$ has become feasible in the context of behavioral studies. Despite this advance, the intraneuronal compartmentalization of Mn^{2+} accumulation has remained elusive. There is evidence that Mn^{2+} enters neurons at dendrites and soma in activity-dependent and independent manner (Wang et al., 2015), accumulates in presynaptic terminals after axonal transport (Sloot and Gramsbergen, 1994), and may even serve as a trans-synaptic tracer (for review see: Pautler, 2004).

It is thought that the enhanced MEMRI contrast results from Mn^{2+}

ions influx via Ca^{2+} channels (Drapeau and Nachshen, 1984) and accumulation in neurons following depolarization. Simpson et al. (1995) identified N-methyl-D-aspartic acid (NMDA) receptors and L-type voltage dependent Ca^{2+} channels (LTCCs) as the main activity-dependent entry pathways into neurons. NMDA receptors, which open during cell depolarization and simultaneous agonist binding, are essential for Mn^{2+} influx, with NMDAR agonists increasing the Mn^{2+}-enhanced contrast (Itoh et al., 2008).

The influence of LTCCs (whose activation is dependent on the membrane potential) on MEMRI, and especially of different LTCC subpopulations is not yet fully known. Previous work has shown that Mn^{2+} uptake in the rat retina decreases after administration of nifedipine (an LTCC antagonist), but is unaffected by AMPA or NMDA receptor antagonists (Berkowitz et al., 2011). However, a clear assessment of the different LTCC isoforms' roles in neuronal Mn^{2+} uptake is still lacking. In the central nervous system (CNS), LTCCs have 2 isoforms: $Ca_v1.2$ and $Ca_v1.3$ that are encoded by the CACNA1C and CACNA1D genes, respectively. The majority of the brain's LTCCs are $Ca_v1.2$ (approx. 80%), which are mostly postsynaptic, the rest are primarily neuronal somatic $Ca_v1.3$ channels (Hell et al., 1993; Hetzenauer et al., 2006; Ludwig et al., 1997; Sinnegger-Brauns et al., 2009; Westenbroek et al., 1990).

To address the knowledge gaps, we aimed to demonstrate (i) whether $Ca_v1.2$ and/or $Ca_v1.3$ allows the entry of Mn^{2+} into neurons, and (ii) whether Mn^{2+} accumulation is intraneuronally compartmentalized following fractionated systemic $MnCl_2$ injections. To this end, we first compared MEMRI in mice with a CNS-specific KO of $Ca_v1.2$ ($Ca_v1.2^{CNS-KO}$) or $Ca_v1.3$ ($Ca_v1.3$ KO) with controls. Having identified $Ca_v1.2$ as the main channel for Mn^{2+}, we specifically knocked-out $Ca_v1.2$ expression in the thalamus, a region with predominantly long-distance projection neurons (Hohl-Abrahao and Creutzfeldt, 1991; Tucciarone et al., 2009; Van Horn and Sherman, 2004; Yu et al., 2014, 2012). We then compared the voxel-wise analysis of MEMRI signals in these thalamic $Ca_v1.2$ KO mice with controls. In this way we sought to elucidate whether Mn^{2+} primarily accumulates at sites of $Ca_v1.2$ expression (i.e., the site of local recombination) vs. projection terminals of the affected neurons. We verified our results by measuring time-dependent increases in Mn^{2+} accumulation following thalamic administration of $MnCl_2$. Finally, using conditional deletion of $Ca_v1.2$ in cortical glutamatergic neurons ($Ca_v1.2^{Glu-KO}$) or the entire CNS ($Ca_v1.2^{CNS-KO}$), we confirmed the preferential accumulation of Mn^{2+} in projection terminals.

Materials and methods

All experiments were carried out according to the European Community Council Directive 2010/63/EEC. All experimental procedures were approved by the local government of Upper Bavaria (55.2.1.54-2532-41-09, 44-09 and 142-12).

Animals

Adult male mice (2–5 months old) were single-housed in standard macrolon cages type II, with food and water ad libitum. Mice were maintained on a reversed 12 h:12 h light/dark cycle (lights off at 09:00) in a temperature- and humidity-controlled room. After transfer to the local animal facility, mice were accustomed to the holding conditions for at least 10 days before any experiments started. Intraperitoneal injections described below were conducted between 09:00 and 11:00.a.m.

In the first experiment, we assessed Mn^{2+} accumulation in genetically modified mice either lacking $Ca_v1.2$ in the brain or $Ca_v1.3$ throughout the entire body. Since the complete knockout (KO) of $Ca_v1.2$ is embryonically lethal (Seisenberger et al., 2000), a brain-specific deletion was used. Deletion of $Ca_v1.2$ in the CNS was performed as previously described (Langwieser et al., 2010). Briefly, CNS-specific $Ca_v1.2$ KO mice ($Ca_v1.2^{CNS-KO}$) and control littermates ($Ca_v1.2^{Ctrl}$) were obtained by initially breeding homozygous floxed $Ca_v1.2$ mice ($Ca_v1.2^{f/f}$) to hemizygous Nestin-Cre mice (backcrossed to C57BL/6N for > 10 generations).

Finally, $Ca_v1.2^{f/f}$ mice were bred to $Ca_v1.2^{+/-}$, Nestin-Cre mice to obtain $Ca_v1.2^{CNS-Ctrl}$ ($Ca_v1.2^{+/f}$, Nestin-Cre; n = 6) and $Ca_v1.2^{CNS-KO}$ ($Ca_v1.2^{-/f}$, Nestin-Cre; n = 7) mice. For voxel-wise, whole-brain analysis of Mn^{2+} accumulation, we additionally compared new cohorts of $Ca_v1.2^{CNS-KO}$ (n = 13) and $Ca_v1.2^{Ctrl}$ mice (n = 13; see Experiment 4). Genetic deletion of $Ca_v1.3$ was performed as previously described (Platzer et al., 2000). Briefly, multiple stop codons were introduced via a neo cassette into the CACNA1D gene by means of homologous recombination in mouse embryonic stem cells. Chimeric mice were created by blastocyst injection. The positive F1 progeny was backcrossed with C57BL/6 mice and the F2 heterozygote offspring was bred in order to generate homozygous $Ca_v1.3$ KOs (genotype: $Ca_v1.3^{-/-}$; n = 4). Wild type C57BL/6/N mice (Charles River, Germany) served as controls (n = 5).

In the second experiment, homozygous floxed $Ca_v1.2$ mice ($Ca_v1.2^{f/f}$) were injected directly in the thalamus (as described in the next section) with adeno-associated viruses (AAV) encoding either green fluorescent protein (GFP) fused with a Cre-recombinase (pAAV2.1-CMV-Cre-2A-GFP M4, alias AAV-Cre/GFP; n = 6) or exclusively GFP (pAAV 2.1 sc Ef1a eGFP AAV 2/2, alias AAV-GFP; n = 4). In addition, another control group without any injection was used (n = 4). AAVs were kindly provided by Stylianos Michalakis (Faculty for Chemistry and Pharmacy, Ludwig-Maximilian-University, Munich, Germany). AAV-mediated delivery of the Cre-recombinase by AAV-Cre/GFP allows a time and region specific KO of $Ca_v1.2$ after injection whereas the administration of the control virus AAV-GFP does not influence expression of the floxed gene site.

In the third experiment, a C57BL/6N mouse (Martinsried, Germany) was unilaterally injected with $MnCl_2$ into the thalamus (see below).

In the fourth experiment, inactivation of CACNA1C from forebrain glutamatergic neurons during development was achieved by breeding homozygous floxed Cav1.2 mice to heterozygous Nex-Cre mice (Goebbels et al., 2006) to obtain $Ca_v1.2^{Glu-KO}$ mice ($Ca_v1.2^{f/f,Nex-Cre}$; n = 9) as previously described (Dedic et al., 2017). These animals were compared to the $Ca_v1.2^{CNS-KO}$ mice (n = 13) as well as to the respective control littermates ($Ca_v1.2^{Ctrl}$, n = 13; $Ca_v1.2^{f/f}$, n = 8).

AAV and $MnCl_2$ local injection/surgery

Homozygous floxed $Ca_v1.2$ mice ($Ca_v1.2^{f/f}$) underwent surgery 1 month before the first MRI scan. Mice were anesthetized with isoflurane (DeltaSelect, Germany), mounted to a stereotactic frame (TSE-Systems, Heidelberg, Germany) and kept under inhalation anesthesia by an isoflurane-oxygen mixture (1.5–1.7 vol% with an oxygen flow of 1–1.2 L/min). After exposure of the skull, a hole was drilled and AAVs were injected with a 5 µL micro syringe (Hamilton, Bonaduz, Switzerland) connected to a micro injector pump (UltraMicroPump III, World Precision Instruments Inc., Sarasota USA). 700 nL of the respective AAV was infused into the right ventral posteromedial (VPM) and ventral posterolateral (VPL) nuclei of the thalamus (−1.5 mm posterior, 2.1 mm lateral and 4.0 mm ventral to bregma). The site of injection was verified by magnetic resonance imaging (MRI). Injections were performed at a rate of 50 nL/min followed by 5 min diffusion time, during which the injection needle was left in place.

One C57BL/6N mouse was injected with $MnCl_2$ directly into the right VPM and VPL to track Mn^{2+} transport in the brain. To this end, the mouse was anesthetized and positioned as described above. After drilling, $MnCl_2$ (50 mM, pH = 7.1) was applied iontophoretically (5 µA for 15 min, 7 s on-off interval) into the right VPM and VPL thalamic nuclei (−1.5 mm posterior, 2.1 mm lateral and 4.0 mm ventral to bregma).

In each case, surgical tolerance was achieved by local anesthesia with lidocaine spray and subcutaneous injection with the analgesic Meloxicam (0.5 mg/kg in 0.2 mL saline) 5 min before surgery. Afterwards, the wound was closed with sutures and disinfected with Braunoderm® (B.Braun, Melsungen, Germany). Mice received a subcutaneous injection with the analgesic Meloxicam (0.5 mg/kg in 0.2 mL saline) and were placed back in their home cage. Meloxicam treatment continued for 3 days via the drinking water (0.5 mg/kg in 5 mL tap water).

138

Manganese-enhanced magnetic resonance imaging (MEMRI)

With the exception of the 1 animal which received the local thalamic $MnCl_2$ injection and the conditional KO mice, all animals underwent baseline MRI followed by MEMRI, as previously described (Grunecker et al., 2010). After baseline MRI, mice had 1 week of rest before they received intraperitoneal injections of 30 mg/kg $MnCl_2$ (Sigma, Germany) every 24 h for 8 consecutive days ($8 \times 30/24$ h). This protocol struck a balance between maximal contrast enhancement and minimal physiological side effects (Grunecker et al., 2010). 12–24 h after the last injection, an identical imaging procedure (like during the baseline recording) was performed. For the experiment comparing $Ca_v1.2^{CNS-KO}$ and $Ca_v1.2^{Glu-KO}$ mice, only 1 MEMRI was recorded 24 h after the final injection. The 1 animal which received the local thalamic $MnCl_2$ injection at time point d = 0 was measured 4 times with an approximately 12 h delay between the MRI experiments (at d = 0.53, 1, 1.7, 1.96).

Baseline MRI and MEMRI was conducted on a 7T Avance Biospec 70/30 scanner (Bruker BioSpin, Ettlingen, Germany). Mice were anaesthetized with isoflurane (DeltaSelect, Germany), fixed in supine position on a saddle-shaped receive-only coil and kept under inhalation anesthesia with an isoflurane-oxygen mixture (1.5–1.7 vol% with an oxygen flow of 1.2–1.4 L/min). The head was restrained with a stereotactic device and the frontal teeth were fixed with a surgical fiber to prevent movement artifacts. Body temperature was monitored with a rectal thermometer (Thermalert TH-5, Physitemp Instruments, USA) and kept between 36.5 °C and 37.5 °C using a water-based heating pad. Pulse rate was continuously monitored by a plethysmographic pulse oxymeter (Nonin 8600 V, Nonin Medical Inc., USA).

T_1-weighted (T1w) brain images were acquired using a 3D gradient echo pulse sequence (TR = 50 ms, TE = 3.2 ms, matrix size = 128 × 106 x 106 zero filled to 128 × 128 x 128, field of view (FOV) = 16 × 16 × 18 mm, number of averages = 10, resulting in a spatial resolution of 125 × 125 × 140.6 μm³).

MRI data post-processing

After reconstruction with Paravision Software (Bruker, BioSpin, Ettlingen, Germany), images were transferred to standard ANALYSE format. Further post-processing was performed using SPM 8 (www.fil.ion.ucl.ac.uk/spm) in 2 steps: (i) T1w images were bias corrected in order to remove intensity gradients introduced by the geometric properties of the surface coil and afterwards spatially normalized to a custom-made master template (mean image deriving from 216 individual MEMRI images). For brain extraction, a binary mask of the intracranial vault without large vessels (whole-brain) was manually defined (MRIcro, www.sph.sc.edu/comd/rordon/mricro.html) on the master template and subsequently transformed into the native (co-registered) space of each individual animal (by inverted spatial normalization). For further analysis, whole brains were extracted from bias-corrected T1w images in native space. (ii) Individual whole-brain extracted images (in native space) were spatially normalized from scratch to a whole-brain extracted master template (whole brains extracted from the 216 images).

One technical limitation of our study was the use of T1w images instead of T1 maps, which would be less prone to biases introduced by the coil geometry. However, we opted to improve signal-to-noise in the individual T1w images rather than acquire several images with lower SNR needed for T1 fitting.

Region of interest analysis

Binary masks of the HPC and its sub-regions as well as the cortex and the whole-brain mask were specified on the whole-brain master template according to the anatomical atlas of the C57BL/6 mouse (Paxinos and Franklin, 2012). The bilateral cortical regions of interest (ROIs) included somatomotor, somatosensory, auditory and visual cortices. The whole-brain mask included the brain inside the complete field of view covered, i.e., including olfactory bulb to cerebellum. Masks were then back-transformed into the native space of each animal and intensities of the ROIs were extracted using in-house written IDL scripts (www.creaso.com). To correct for unspecific effects (e.g., R.F. gain and sensitivity effects), ROI intensities were normalized to the whole-brain intensity. When intensity differences in the whole-brain of $Ca_v1.2$ and $Ca_v1.3$ animals were compared, the intensities derived from a ROI of the bilateral extracranial muscle (m. masseter, m. temporalis), running in the rostral-caudal direction approximately from 2.4 to −2.8 mm bregma, was used for intensity normalization. The coefficient of variance (COV) of the ROI intensities was determined by the standard deviation (SD) and the mean intensity of the respective brain region (COV = SD/mean). ROI intensities of Ca_v KOs and controls before and after $MnCl_2$ injection were compared with a one-way ANOVA with repeated measures. Scheffé's method was used for post-hoc analysis, if the ANOVA revealed a significant interaction.

For the 1 animal directly injected into the thalamus, distribution of Mn^{2+} was specified both around the thalamic injection site and in the insular cortex (sphere with a radius of 0.62 mm at the coordinates of the thalamic injection, and at the peak voxel location in the insula of the whole-brain analysis – second experiment, described below). Both ROIs were directly applied to the spatially normalized whole-brain images to extract their intensities. No further intensity normalization was applied. ROI intensities then entered regression analysis. The intensity development over time after intracerebral $MnCl_2$ injection was tested using the Pearson coefficient.

Whole-brain analysis

Brain-extracted spatially normalized images were smoothed with a Gaussian kernel 8× the image resolution (1.0 × 1.0 × 1.124 mm³ at full-width half maximum). Voxel by voxel comparison was implemented in SPM 5 (www.fil.ion.ucl.ac.uk/spm) using the SPM mouse toolbox (http://wbic.cam.ac.uk/~sjs80/spmmouse.html).

For the first experiment, MEMRI images of $Ca_v1.2^{CNS-KO}$ (n = 13) from Experiment 4 were compared to control animals ($Ca_v1.2^{Ctrl}$; n = 13) using a two-sample *t*-test with a global intensity-by-group regressor to account for unspecific basal differences in Mn^{2+} accumulation. To correct for multiple testing, a voxel-wise family-wise error correction was implemented at a threshold of $p_{FWE} < 0.005$.

In the second experiment, smoothed images of homozygous $Ca_v1.2^{fl/fl}$ mice were assigned to a full factorial model comprising a between factor *group* (AAV-GFP/Cre vs. AAV-GFP controls) and a within factor *time point* (baseline MRI = scan 1 before $MnCl_2$ injection, time point 1; and MEMRI = scan 2 after $MnCl_2$ injection, time point 2). For correction of unspecific global intensity differences, an *ANCOVA-by-time point* regressor was included in the model. We tested *group-by-time point* interaction utilizing an F-contrast. Statistical maps were sampled at a threshold of p < .001 and a cluster-based multiple test correction for family-wise error with regard to non-stationary smoothness was employed ($p_{FWE,cluster}$) (Hayasaka et al., 2004). For further visualization, mean contrast estimates were extracted from a sphere with radius 0.22 mm around the peak voxel of statistical significant clusters.

In the third experiment, extracted whole-brain images were spatially normalized to a master template and smoothed with a Gaussian kernel 5× the image resolution (i.e., 625 × 625 × 703 μm³). In addition to the ROI analysis (described above) and to investigate the specificity of the insula cluster, an in-house written routine in Matlab was applied to the images, which fitted the 4-time points voxel-wise using a linear regression (y = A + Bx) by minimizing χ^2-error statistics. The positive slope of the regression was depicted for each voxel at an uncorrected threshold of p < .005 with a minimal cluster extent of 30 voxels.

In the fourth experiment, smoothed images of $Ca_v1.2^{CNS-KO}$ (13) and $Ca_v1.2^{Glu-KO}$ mice (9) and respective littermate controls (13/8) were compared using a full factorial model comprising the between factors *line* (CNS vs. Glu) and *genotype* (control vs. KO), along with global intensities as a nuisance regressor. *Line-by-genotype* interactions were calculated and displayed using whole-brain family-wise error correction ($p_{FWE} < 0.05$,

cluster extent > 20 voxel). Again, for visualization, contrast estimates were extracted for the clusters reaching significance as described above.

Western blot analysis of Ca$_v$1.2 expression after AAV injection

One month after the last imaging session, AAV injected homozygous floxed Ca$_v$1.2 (Ca$_v$1.2$^{f/f}$) mice were killed with an overdose of isoflurane and their brains removed, frozen in 2-methylbutane on dry ice and stored at −80 °C. Following the results of the imaging data analysis, brain tissues of the VPM and VPL thalamic nuclei (primary injection sites) and the site of maximal MEMRI contrast differences (i.e., agranular insular cortex) were punched (using cylindrical punchers with an internal diameter of 0.5 mm and a punch length of ~0.5 mm) in a cryostat microtome at −20 °C for subsequent use in Western blot analysis of Ca$_v$1.2 expression. Brain slices were collected and the dissection site verified by histological analysis.

The tissue punches were suspended in 100 μL lysis buffer per 10 mg tissue (50 mM Tris-HCl, 2% SDS, pH 7.5) and boiled for 10 min. After normalization of protein concentration in each sample (BSA equivalents measured with a NanoDrop spectrophotometer, Thermo Fischer Scientific, Germany), the homogenates were separated by 10% SDS-PAGE. The resulting gels were transferred to PVDF membranes (Immobilion-P, Millipore, Germany) and blocked at 4 °C overnight with 3% BSA and 1% Tween-20 in PBS. They were then incubated for 90 min with Ca$_v$1.2-specific antibody (kindly provided by Franz Hofmann, Institute of Pharmacology and Toxicology, Technical University Munich, Germany) and α-tubulin antibody (Millipore, Germany). Further, the membranes were immersed in chemiluminescence substrate (ECL, Western Lightning Chemiluminescence, Perkin-Elmer, Germany) and digitized with a HP ScanJet scanner ($40 \times 40\,\mu m^2$). A trained investigator blind to the experimental groups quantified the bands with ImageJ (rsbweb.nih.gov/ij). The Ca$_v$1.2 signal was normalized to the α-tubulin signal to get the relative amount of Ca$_v$1.2. A two-sample *t*-test was conducted for each region.

In situ hybridization

In situ hybridization was performed as previously described (Dedic et al., 2017). The *CACNA1C* probe was designed to target the loxP flanked exons 14 and 15 (nucleotides 2307–2427 of GenBank accession no. NM_009781).

Statistics and data presentation

Data were analyzed in SPSS 23 (SPSS, Chicago, IL, USA) and plotted in MRICro and GraphPad Prism 5.0 (GraphPad, San Diego, CA, USA) with the arithmetic mean and the standard error of the mean (SEM). Voxel-wise analysis of the MR images was performed in SPM8 or SPM5 (www.fil.ion.ucl.ac.uk/spm) while the voxel-wise linear regression was performed directly in Matlab 7.7.0 (MathWorks Inc., Natick, MA, USA). Significance was accepted at p < .05, if not stated otherwise. Graphics of activation maps were created in MRICro (www.cabiatl.com/mricro). All final images were displayed in Adobe Illustrator 10.0.3 (Adobe Systems Inc., NY, USA).

Results

Ca$_v$1.2 plays an important role in manganese-dependent contrast increase

We scanned Ca$_v$1.2$^{CNS\text{-}KO}$ and their littermate controls 2 times: before (MRI, scan 1) and after MnCl$_2$ treatment (MEMRI, scan 2; Fig. 1A), and analyzed contrast differences in the whole-brain and 2 ROIs: the hippocampus (HPC) and the cortex. These ROIs were selected as representative regions/structures, given that they (i) can be unequivocally delineated on the scans, (ii) are the focus of many cognitive-related studies and, therefore, of broad interest, and (iii) present a high expression of LTCCs

(Dedic et al., 2017), allowing us to investigate the role of these channels in the MEMRI signal. In the comparison for all ROIs grouped, as well as for the coefficient of covariance (COV) of the whole-brain data, the ANOVA revealed significant main effects of *time point* (MRI, scan 1, before MnCl$_2$ vs MEMRI, scan 2, after MnCl$_2$ administration) (Fig. 1C; $F_{1,11} \geq 34.75$, p < .001) and *genotype* (Ctrl *vs.* KO) ($F_{1,11} \geq 6.02$, p ≤ .032) as well as a significant *time point × genotype* interaction ($F_{1,11} \geq 5.38$, p ≤ .041). In a post-hoc comparison, both Ca$_v$1.2$^{CNS\text{-}KO}$ and controls showed a significant increase in intensity by time point (p ≤ .023), however, the groups differed significantly in MEMRI contrast (p ≤ .002).

Next, we analyzed MRI and MEMRI contrast in Ca$_v$1.3 KOs and wild-type controls. The ANOVA revealed a significant main effect of *time point* (Fig. 1D; $F_{1,7} \geq 24.93$, p < .002) in whole-brain/ROIs and COV. The *genotype* and the interaction were not significant ($F_{1,7} \leq 2.59$, p ≥ .152).

On average, Ca$_v$1.2$^{CNS\text{-}KO}$ mice showed only ~45% of the whole-brain intensity increase observed in their littermate controls, whereas Ca$_v$1.3 KOs displayed intensity increase similar to wild-type animals. Regarding the contrast differences, this already became evident by the observation of the mean images of each group (Fig. 1B).

Voxel-wise whole-brain analysis in new cohorts of mice revealed that Ca$_v$1.2$^{CNS\text{-}KO}$ mice have significantly lower MEMRI intensity not in an ubiquitous, but in a very distinct manner: in the bilateral medial prefrontal cortex (mPFC), bed nucleus of the stria terminalis (BNST), globus pallidus (GP), retrosplenial cortex (RSC) and the CA1 region of the dorsal HPC, as compared to control animals. In addition, unilateral signal reductions were found in the right amygdaloid complex (Amy) and the right CA3, as well as in the left inferior colliculus (IC) (Fig. 1E). The inverted contrast (Ca$_v$1.2$^{CNS\text{-}KO}$ > Ca$_v$1.2^{Ctrl}) revealed no significant differences.

Local depletion of Ca$_v$1.2 inhibits manganese-dependent contrast increase only in the projection terminals of the affected neurons

After we identified Ca$_v$1.2 as a prominent entry point for Mn^{2+} into neurons, we decided to locally KO Ca$_v$1.2 expression in a defined brain structure in order to study the intraneuronal compartmentalization of Mn^{2+} accumulation at uptake (i.e., area of recombination) vs. projection sites (i.e., following uptake and axonal transport). To this end, we injected an AAV encoding for the Cre-recombinase and eGFP into the right VPM and VPL thalamic nuclei of Ca$_v$1.2$^{fl/fl}$ mice (Fig. 2A). Control Ca$_v$1.2$^{fl/fl}$ mice were treated with a control virus encoding for eGFP or remained untreated. We decided to target the thalamus, since thalamic structures not only express Ca$_v$1.2, but also comprise mainly long-distance projecting neurons. In this way we ensured an easier distinction of changes in Mn^{2+} accumulation between uptake sites vs. projection terminals. Given the fact that Ca$_v$1.2 is predominantly expressed in postsynaptic terminals, expression of the Cre-recombinase is expected to result in depletion of Ca$_v$1.2 at the level of the injection site. All animals underwent the fractionated MnCl$_2$ injection protocol over 8 days. Changes in Mn^{2+} accumulation were assessed by voxel-wise whole-brain analysis. After correction for multiple comparisons, only 1 single cluster showed a significant *group-by-time point* interaction: not at the recombination site, but in the agranular insular cortex (cluster extent = 443, F = 32.90, p$_{FWE,cluster}$ = 0.015; Fig. 2B left panel), indicative of lower levels of Mn^{2+} in AAV-Cre/GFP treated mice, compared to AAV-GFP and untreated controls (Fig. 2B right panel). We also compared the AAV-Cre/GFP with the AAV-GFP injected control mice. Again, the same cluster (agranular insular cortex) survived the sampling at p$_{uncorrected}$ < 0.001. This time, however, the cluster did not reach significance after alpha correction due to the relatively small sample size of mice injected with the control virus (n = 4; data not shown; cluster extent = 66, F = 22.64, p$_{FWE,cluster}$ = 0.296, p$_{uncorrected}$ < 0.001).

To understand which effect drives the *group-by-time point* interaction, we compared AAV-Cre/GFP injected mice with AAV-GFP injected and untreated controls separately for MRI and MEMRI in an F-test. Whereas no significant group differences were found for MRI data, MEMRI
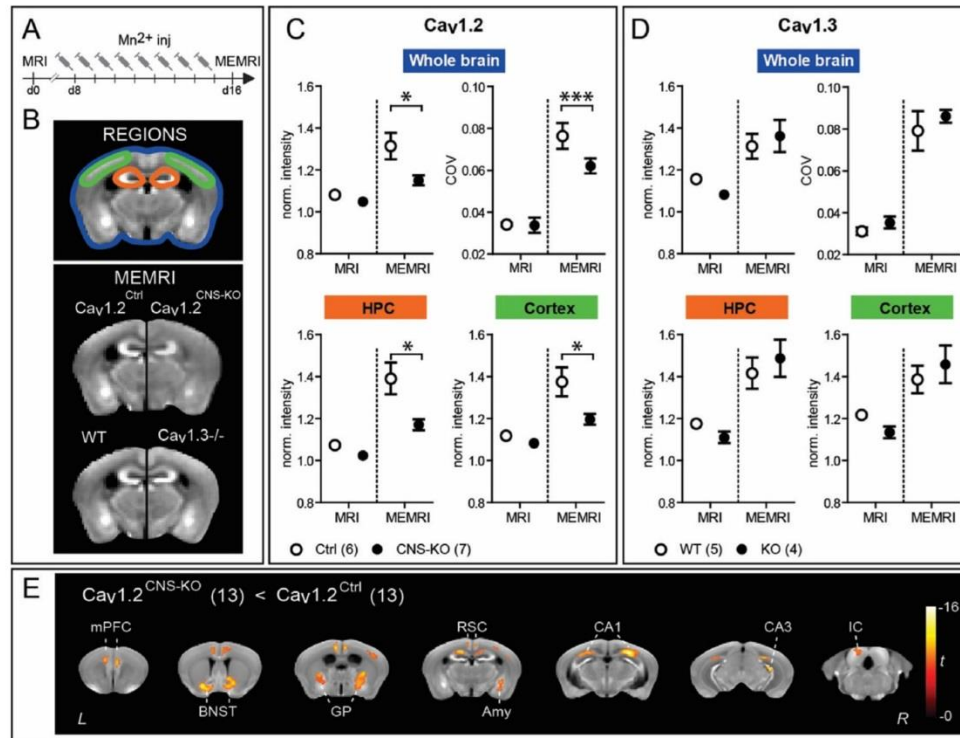
Fig. 1. Deletion of Ca$_v$1.2, but not Ca$_v$1.3, affects manganese-dependent contrast increase. **(A)** Simplified experimental design. Baseline MRI was performed 1 week before the start of MnCl$_2$ injections (i.p., 30 mg/kg, 8×, 24 h apart), which were followed by the MEMRI acquisition (inj: injection; d: day). **(B)** The upper panel shows the analysed brain regions of interest (ROI), exemplified in one slice only. The lower panel depicts mean MEMRI images of calcium channel knockouts (Ca$_v$1.2^{CNS-KO} *top* and Ca$_v$1.3$^{-/-}$ *bottom* KO, right) and their controls (WT, left). As compared with the other groups, Ca$_v$1.2^{CNS-KO} show reduced MEMRI contrast between brain regions. **(C)** Ca$_v$1.2^{CNS-KO} showed weaker intensity and contrast increase after manganese chloride treatment in all ROIs under investigation **(D)** Ca$_v$1.3 KOs did not exhibit differences in manganese-dependent intensity or contrast increase in any of the ROIs analysed (* p < .05, *** p < .001; 2-way ANOVA followed by Newman-Keuls post-hoc test). **(E)** In a voxel-wise, whole-brain analysis of the MEMRI images of new groups of mice (cf. Fig. 3), Ca$_v$1.2^{CNS-KO} showed a basal bilateral intensity reduction in the medial prefrontal cortex (mPFC), bed nucleus of the stria terminalis (BNST), globus pallidus (GP), retrosplenial cortex (RSC) and the CA1 region of the dorsal hippocampus, as compared with Ca$_v$1.2^{Ctrl}. Unilateral signal reductions were measured in the right amygdala (Amy), the right CA3 region and the left inferior colliculus (IC) (t ≥ 8.02; p$_{corrected}$ ≤ 0.005). L/R: left/right. Color bar represents t-values. Sample size in brackets.

analysis revealed the same significant cluster as before (agranular insular cortex; cluster extent = 373, F = 26.21, p$_{FWE,cluster}$ = 0.029; data not shown).

The thalamus is known to project to the agranular insular cortex (Chen et al., 2014), which might explain why the voxel-wise analysis revealed lower levels of Mn^{2+} accumulation in the agranular insular cortex after knock out of Ca$_v$1.2 expression in the thalamus. To exclude the possibility that the AAV-Cre/GFP virus has simply spread to the agranular insular cortex (where it would affect the expression of Ca$_v$1.2 and, thus, uptake of Mn^{2+}), we quantified Ca$_v$1.2 channels in the thalamus and agranular insular cortex by Western blot. Compared to controls, the protein content of Ca$_v$1.2 was significantly reduced only at the recombination site (VPM and VPL thalamic nuclei; t$_{12}$ = 6.70; p < .001; Fig. 2C), but not in the projection site (agranular insular cortex; t$_{12}$ = 1.47; p = .166; Fig. 2C).

We confirmed that the thalamic neurons indeed project to the agranular insular cortex by local administration of MnCl$_2$ into the right VPM and VPL, followed by repeated MEMRI measurements over the course of 2 days (Fig. 2D). ROI analysis showed that while the intensity at the injection site rapidly decreased over time (thalamus; r^2 = 0.837; slope = −0.203; p = .042), the contrast in the projection site increased slightly, but significantly (insular cortex; r^2 = 0.822; slope = 0.031; p = .046). These findings were confirmed by voxel-wise, whole-brain

assessment of Mn^{2+} signal over time, which again revealed an increase of MEMRI intensity in the agranular insular cortex. Whole-brain analysis also showed a trend towards a time-dependent increase in signal intensity in the HPC and the ventral pons with a maximum slope of 0.07 (Fig. 2D).

Knocking out Ca$_v$1.2 by conditional mutagenesis leads to inhibition of manganese-dependent contrast increase in highly dense projection areas but not at the uptake site

To confirm the preferential accumulation of Mn^{2+} accumulation in projection terminals after systemic MnCl$_2$ injections, we compared MEMRI signals in mice with conditional deletion of Ca$_v$1.2 in cortical glutamatergic neurons (Ca$_v$1.2^{Glu-KO}), the entire CNS (Ca$_v$1.2^{CNS-KO}) and their respective wild-type littermates. We employed a two-factorial, voxel-wise, whole-brain analysis with the factors *line* and *genotype* with a focus on factorial interactions. These interactions allowed us to identify the brain structures in which Ca$_v$1.2-mediated Mn^{2+} influx is still preserved in Ca$_v$1.2^{Glu-KO} but not in Ca$_v$1.2^{CNS-KO}. Analyses revealed significant factorial interactions for 3 clusters: the left piriform cortex (T = 7.18, Z = 5.67) and the bilateral globus pallidus (T ≥ 7.96, Z ≥ 6.07; p$_{FWE}$ < 0.05; Fig. 3A). These effects were driven by the selective decrease in signal intensities in Ca$_v$1.2^{CNS-KO} but not Ca$_v$1.2^{Glu-KO} mice (Fig. 3A,
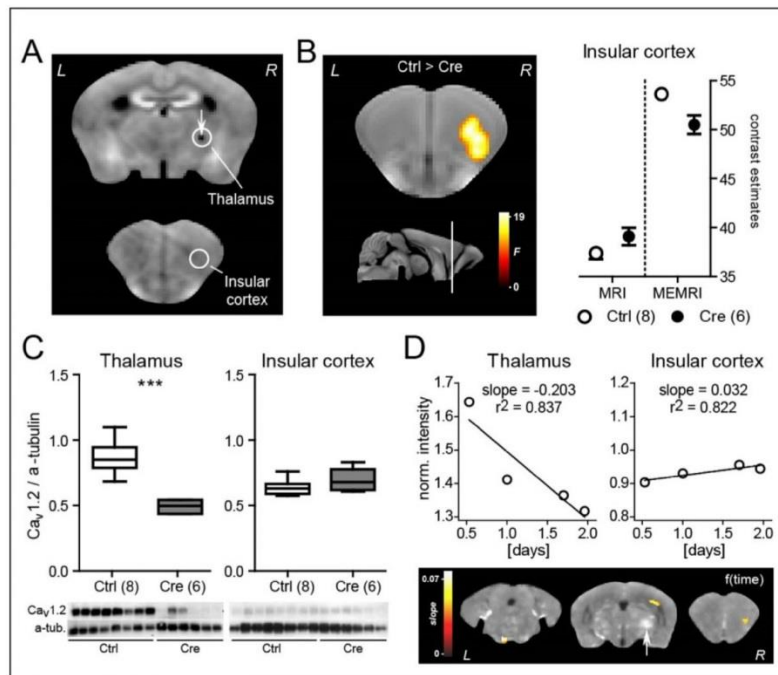
Fig. 2. Mn^{2+} preferentially accumulates in the projection terminals of the affected neurons after local interventions. **(A)** Coronal MEMRI slices (group mean image) depicting the site of injection in the right thalamus of Ca$_v$1.2$^{f/f}$ mice (arrow) that received either (i) a viral vector encoding for the expression of the Cre-recombinase and GFP (Cre, n = 6), (ii) a control virus encoding for GFP only (n = 4), (iii) or no treatment at all (n = 4). White circles outline the brain punches used for Western blot confirmation of Ca$_v$1.2 deletion (see panel C). **(B)** MRI and MEMRI contrasts (following fractionated systemic treatment with MnCl$_2$; cf. Fig. 1A) were compared in a voxel-wise manner between Ca$_v$1.2$^{f/f}$ mice treated with the Cre-expressing virus and controls (Ctrl, collapsed groups (ii) and (iii)). Voxel-wise, whole-brain interaction analysis (time point x group) revealed 1 significant cluster in the agranular insular cortex (F = 32.90, p$_{corrected}$ = 0.015). This interaction was a consequence of the reduction in MEMRI contrast after injection of the Cre-expressing virus, as can be seen in the contrast estimates of a sphere around the peak voxel (right graph). **(C)** Western blot analyses of Ca$_v$1.2 levels in brain punches from the injection site (right thalamus) and the projection site (agranular insular cortex; punching sites are indicated by the white circles in panel A) confirmed reduced Ca$_v$1.2 protein content in Cre-treated mice in the thalamus (t$_{12}$ = 6.70; p < .001) but not in the insular cortex (t$_{12}$ = 1.47; p = .166) compared to controls (Ctrl). **(D)** Within-subject analysis of temporal changes in Mn^{2+} accumulation after administration of MnCl$_2$ into the right thalamus of a control mouse. Lower panel: MEMRI analyses of brain structures with time-dependent increase in Mn^{2+} accumulation following local injection of MnCl$_2$ into the thalamus (injection site indicated by the arrow) revealed the right agranular insular cortex (yellow; right figure), as well as the hippocampus (yellow; middle figure) and ventral pons (yellow; left figure), where a trend of significant signal increase was found. Upper panel: MEMRI signal intensities measured about every 12 h after local injection of MnCl$_2$ decreased at the level of the injection site (thalamus; slope = −0.203, r^2 = 0.837), but increased in the agranular insular cortex (slope = 0.032, r^2 = 0.822) over time. Sample size in brackets.

left panels). Expression analysis of Ca$_v$1.2 mRNA by radioactive *in situ* hybridization (ISH) confirmed the lack of Ca$_v$1.2 in the CNS of Ca$_v$1.2^{CNS-KO} and the specific depletion of this Ca^{2+} channel from cortical glutamatergic neurons of Ca$_v$1.2^{Glu-KO} mice (Fig. 3B). Based on these recombination patterns, one would expect *line x genotype* differences in Ca$_v$1.2-dependent Mn^{2+} accumulation in prominent structures such as the caudoputamen (CPu), where Ca$_v$1.2 expression is preserved in Ca$_v$1.2^{Glu-KO}, rather than in the globus pallidus, which is virtually devoid of Ca$_v$1.2 expression even in wild-type controls. We assume that the lack of Ca$_v$1.2 expression in the CPu of Ca$_v$1.2^{CNS-KO}, but not Ca$_v$1.2^{Glu-KO} mice, results in a reduced influx of Mn^{2+} and, as a consequence, reduced Mn^{2+} accumulation in the projection terminals of the globus pallidus (Allen brain atlas, Experiment 114399934 – CP) (Fig. 3C). Similarly, neurons of the olfactory bulb (which undergo recombination of the Ca$_v$1.2 gene in Ca$_v$1.2^{CNS-KO}, but not Ca$_v$1.2^{Glu-KO} mice) might be the primary sites of reduced Mn^{2+} influx resulting from the reduced Mn^{2+} accumulation in downstream projection sites (i.e., piriform cortex; Allen brain atlas, Experiment 146859480 – MOB).

Discussion

In the present study, we identified Ca$_v$1.2 as an important channel for

Mn^{2+} entry into neurons. Using local knock-down of Ca$_v$1.2 in distinct brain areas together with cell-type specific conditional KO of this ion channel, we demonstrate that MEMRI signals are biased towards projection terminals following systemic MnCl$_2$ injections.

Based on *ex vivo* studies (Pautler and Koretsky, 2002; Simpson et al., 1995) and pharmacological investigations on the rat retina (Berkowitz et al., 2011), it has been suggested that MEMRI contrast depends on LTCCs. Using modern KO techniques, we were able to demonstrate that Ca$_v$1.2, the prevailing LTCC in the brain, provides the major contribution to Mn^{2+}-dependent contrast increase *in vivo*. Taking into account the whole-brain intensity, only about 50% of the Mn^{2+}-induced contrast increase was detectable in the Ca$_v$1.2^{CNS-KO} KOs compared to controls. Another primary modulator of MEMRI intensity is the NMDA receptor (Itoh et al., 2008), which may affect Mn^{2+} influx both directly (as a gate of bivalent cations) and indirectly by altering the neuronal activity of the neurons and, consequently, the activity of voltage-dependent Ca^{2+} channels like Ca$_v$1.2. However, basal activity-independent Mn^{2+}-uptake after local MnCl$_2$ injections has been reported (Bearer et al., 2007; Lowe et al., 2008; Wang et al., 2015), likely mediated by Mn^{2+} binding to the divalent metal transporter, DMT1 (Bartelle et al., 2013, 2015; Roth and Garrick, 2003).

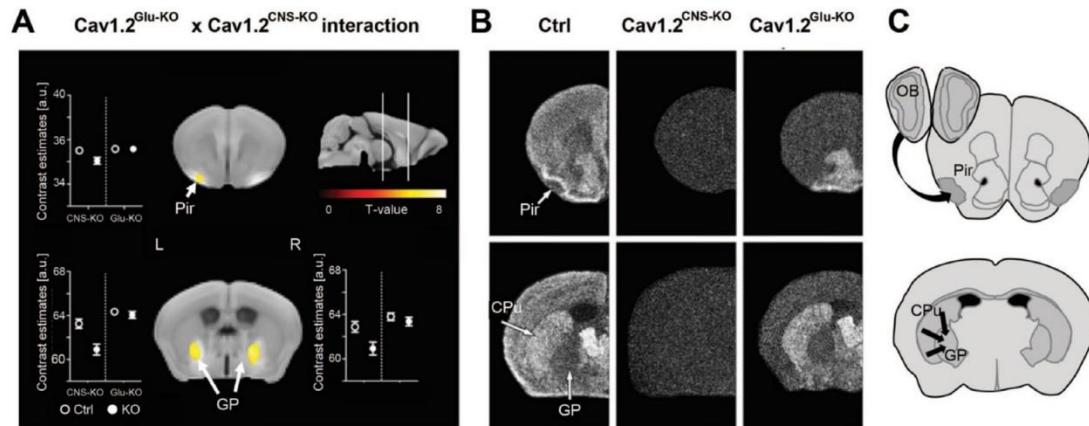A conceivable reason why, in our studies, only Ca$_v$1.2 but not Ca$_v$1.3

Fig. 3. **Conditional Ca$_v$1.2 mutants reveal a preferential accumulation of Mn^{2+} in projection areas.** (A) Voxel-wise, whole-brain analysis of MEMRI data obtained after fractionated systemic MnCl$_2$ treatment revealed 3 clusters (depicted in yellow) with significantly less Mn^{2+} accumulation in Ca$_v$1.2^{CNS-KO} (n = 13) vs. Ca$_v$1.2^{Glu-KO} (n = 9) mice (compared to wild-type controls; n = 13/8): the piriform cortex (left) and bilateral globus pallidus (p$_{FWE}$<0.05). (B) *In situ* hybridization confirmed the total lack of Ca$_v$1.2 expression in the brains of Ca$_v$1.2^{CNS-KO} mice, as compared to controls (Ctrl) and mice with specific Ca^{2+} channel deletion in cortical glutamatergic neurons (Ca$_v$1.2^{Glu-KO}). Arrows indicate the clusters mentioned in (A): piriform cortex (Pir) and globus pallidus (GP), and the caudoputamen (CPu). (C) Representative schemes depicting the putative pathway of Mn^{2+} from possible uptake sites (olfactory bulb, OB, and caudoputamen, CPu) to the clusters indicated in (A) (Pir and GP, respectively).

affected the image intensity could simply be the abundance of each channel: Ca$_v$1.2 makes up the majority of the LTCCs in the brain, whereas Ca$_v$1.3 accounts for less than 15%, with the remaining channels Ca$_v$1.1 and Ca$_v$1.4 contributing just 0.1% (Hetzenauer et al., 2006; Sinnegger-Brauns et al., 2009). Thus, MEMRI might not be sensitive enough to detect a significant contribution of Ca$_v$1.3 to the signal intensity. Another explanation could be the local concentration of Ca$_v$1.2 at the postsynaptic site (Hell et al., 1993; Ludwig et al., 1997; Westenbroek et al., 1990), although there is a report of pre- and postsynaptic localization of these channels in the rat HPC (Tippens et al., 2008). If Mn^{2+} is released pre-synaptically in an activity-dependent manner (Takeda et al., 1998), it would be most concentrated at the proximity of the synaptic cleft and not close to the soma, where Ca$_v$1.3 is dominantly situated (Hell et al., 1993; Ludwig et al., 1997). Finally, Ca$_v$1.3 expression is not evenly distributed in the brain, with more abundant expression in the bed nucleus of the stria terminalis, hypothalamus, central amygdala, locus coeruleus and other mid-/hindbrain structures (Hetzenauer et al., 2006). Ca$_v$1.2, in contrast, is also abundantly expressed in cortical and hippocampal structures (Hetzenauer et al., 2006), i.e., in the ROIs of the first MEMRI experiment.

A general disadvantage of the KO technique used is that life-long inactivation of gene expression may cause unknown developmental alterations, e.g., in the permeability of the blood brain barrier or compensatory changes in the density of other ion channels. For example, it has been shown that deletion of Ca$_v$1.3 causes a compensatory upregulation of Ca$_v$1.2 in the mouse retina (Berkowitz et al., 2015). This might explain why Ca$_v$1.3 KO mice showed a nominally higher, although not significant, Mn^{2+} accumulation as compared to controls in the ROIs studied. In addition, Ca$_v$1.2 KO mice are prone to compensatory changes with a homeostatic switch to Ca^{2+} permeable α-amino-3--hydroxy-5-methyl-4-isoxazolepropionic acid (AMPA) receptor expression (Langwieser et al., 2010), However, our finding that Mn^{2+} accumulation was still strongly reduced in Ca$_v$1.2-KO identifies Ca$_v$1.2 as an important channel for Mn^{2+} into neurons. The potential contribution of Ca$_v$1.3 to MEMRI intensities (e.g., in mid-/hindbrain structures) remains unknown.

After demonstrating the importance of Ca$_v$1.2 for intracerebral Mn^{2+} accumulation, we decided to locally knock-out this ion channel specifically in the thalamus to look for differences in intraneuronal

compartimentalization of Mn^{2+}. Our strategy was as follows: if we reduce the expression of Ca$_v$1.2 selectively in the thalamus - a brain structure with predominantly long-distance projection neurons (Hohl-Abrahao and Creutzfeldt, 1991; Tucciarone et al., 2009; Van Horn and Sherman, 2004; Yu et al., 2014, 2012), the resulting decrease in intraneuronal Mn^{2+} accumulation might reveal differences in MEMRI signal intensities at influx sites and/or in clearly distinguishable projection terminals. Brain structures with predominantly local projections would not enable this distinction. Indeed, voxel-wise, whole-brain analysis revealed a cluster of reduced MEMRI signal far away from the ipsilateral injection site, where no changes in signal intensity could be observed despite a 40% reduction in Ca$_v$1.2 levels. The cluster with significant changes in signal intensity corresponded to the agranular insular cortex, one of the many efferent structures of the thalamic nuclei targeted by the viral vector. As confirmed by Western blot analyses, the decreased Mn^{2+} levels in the agranular insular cortex cannot be due to a local reduction in Ca$_v$1.2. We conclude from these findings that the reduction in Ca$_v$1.2 expression, for instance in thalamic structures, resulted in reduced Mn^{2+} accumulation in projection terminals, such as the agranular insular cortex.

We confirmed the transport of Mn^{2+} away from its entry sites towards axon terminals by longitudinal MEMRI measurements after local injection of MnCl$_2$ into the thalamus. Voxel-wise regression analysis identified 3 brain regions, including the agranular insular cortex, that displayed a significant increase in image intensity over time. This rather specific transport of Mn^{2+} from the thalamus to the agranular insular cortex is surprising in light of the multitude of projections to other brain structures (Chen et al., 2014). As we will discuss later, MEMRI seems to be biased to brain structures with dense and focused projections, whereas more dispersed projections might be filtered out during data analysis. Nevertheless, our findings are consistent with the earlier described phenomenon that Mn^{2+} is transported along the axon of neurons by microtubules to the projection terminals (Sloot and Gramsbergen, 1994; Wang et al., 2016), where it might be released in an activity-dependent manner (Bearer et al., 2007; Pautler et al., 2003; Sloot and Gramsbergen, 1994; Wang et al., 2015; Yang et al., 2011). Here, we significantly extend those observations by demonstrating that Mn^{2+} preferentially accumulates in projection terminals, also after systemic MnCl$_2$ injections.

To further support this conclusion, we looked for differences in Mn^{2+}

accumulation in mice with conditional deletion of $Ca_v1.2$ in cortical glutamatergic neurons ($Ca_v1.2^{Glu-KO}$) vs. the entire brain ($Ca_v1.2^{CNS-KO}$). This approach visualizes Mn^{2+} accumulation in GABAergic neurons which still express $Ca_v1.2$ in $Ca_v1.2^{Glu-KO}$. Indeed, MEMRI analyses of *line × genotype* interactions revealed distinct intensity differences in the striatum. Importantly, such differences were not observed in brain structures with preserved abundant expression of $Ca_v1.2$ in $Ca_v1.2^{Glu-KO}$ (e.g., caudoputamen), but at prominent efferent structures (i.e., globus pallidus). Interestingly, we also observed differences in Mn^{2+} accumulation at level of the piriform cortex where both $Ca_v1.2^{Glu-KO}$ and $Ca_v1.2^{CNS-KO}$ show recombination of $Ca_v1.2$ expression. An explanation could be that the 2 lines differ in recombination of $Ca_v1.2$ expression at level of the olfactory bulb (*cf.* Dedic et al., 2017), whereby the preserved expression of $Ca_v1.2$ in afferent GABAergic projections account for the differences in signal intensities at level of the piriform cortex. In this context, we wish to emphasize that the MEMRI signal seems to be biased towards densely focused projections. Thresholding the results of the voxel-wise, whole-brain analysis by using a family-wise error correction may have filtered out weaker, more dispersed projections. In addition, alterations in Mn^{2+} accumulation in dispersed projections might have lower signal-to-noise ratios and, thus, not survive corrections for multiple testing.

The biased contrast differences towards efferent brain structures (i.e., axon terminals) rather than sites of $Ca_v1.2$ expression (i.e., dendrites or soma) may critically depend on the fractionated Mn^{2+} application employed and/or the time between the last Mn^{2+} injection and scanning. The outcome could be different with application of a single dose of $MnCl_2$ followed by MEMRI scans shortly thereafter, when signal intensities might still be higher at influx sites before efficient axonal transport of Mn^{2+} takes place. However, single injection protocols often require high concentrations of Mn^{2+}, which have adverse and even toxic side effects (Aschner and Aschner, 1991; Daoust et al., 2013, 2014; Lin et al., 2014) such as altered neuronal excitability (Eschenko et al., 2010), impaired astrocyte function (Hazell, 2002), neuronal and glial lesions (Canals et al., 2008) and behavioral distortions (Grunecker et al., 2010). Low-dose, systemic applications, like the fractionated application protocol (Bock et al., 2008; Grunecker et al., 2010) or continuous delivery of small doses of Mn^{2+} via osmotic minipumps (Eschenko et al., 2010; Sepulveda et al., 2012) reduce these side effects, but are likely to result in a Mn^{2+} accumulation pattern that emphasizes the projection routes rather than the primary influx sites. These distinctions have to be kept in mind when interpreting MEMRI data.

Taken together, our data (i) demonstrate the pivotal role of $Ca_v1.2$ in Mn^{2+} influx into neurons, and (ii) reveal strongest accumulation of Mn^{2+} in projection terminals of regions with a high density of $Ca_v1.2$ channels. Given the activity-dependent regulation of $Ca_v1.2$ (Di Biase et al., 2011; Weick et al., 2003), this observation suggests voxel-wise, whole-brain MEMRI analysis as an interesting tool for exploratory studies on changes in brain activity with a connectomics perspective. In light of the close links between genetic polymorphisms of CACNA1C and human psychiatric diseases (e.g., bipolar disorder, attention-deficit hyperactivity disorder, major depressive disorder, autism spectrum disorder, schizophrenia; Cross-disorder group, 2013), this might be of particular interest for studies on animal models of psychopathology.

Acknowledgements

References

Aschner, M., Aschner, J.L., 1991. Manganese neurotoxicity: cellular effects and blood-brain barrier transport. Neurosci. Biobehav. Rev. 15, 333–340.

Bartelle, B.B., Mana, M.D., Suero-Abreu, G.A., Rodriguez, J.J., Turnbull, D.H., 2015. Engineering an effective Mn-binding MRI reporter protein by subcellular targeting. Magn. Reson. Med. 74, 1750–1757. https://doi.org/10.1002/mrm.25566.

Bartelle, B.B., Szulc, K.U., Suero-Abreu, G.A., Rodriguez, J.J., Turnbull, D.H., 2013. Divalent metal transporter, DMT1: a novel MRI reporter protein. Magn. Reson. Med. 70, 842–850. https://doi.org/10.1002/mrm.24509.

Bearer, E.L., Falzone, T.L., Zhang, X., Biris, O., Rasin, A., Jacobs, R.E., 2007. Role of neuronal activity and kinesin on tract tracing by manganese-enhanced MRI (MEMRI). Neuroimage 37 (Suppl 1), S37–S46. https://doi.org/10.1016/j.neuroimage.2007.04.053.

Berkowitz, B.A., Bissig, D., Bergman, D., Bercea, E., Kasturi, V.K., Roberts, R., 2011. Intraretinal calcium channels and retinal morbidity in experimental retinopathy of prematurity. Mol. Vis. 17, 2516–2526.

Berkowitz, B.A., Murphy, G.G., Craft, C.M., Surmeier, D.J., Roberts, R., 2015. Genetic dissection of horizontal cell inhibitory signaling in mice in complete darkness in vivo. Invest. Ophthalmol. Vis. Sci. 56, 3132–3139. https://doi.org/10.1167/iovs.15-16581.

Berkowitz, B.A., Roberts, R., Bissig, D., 2010. Light-dependant intraretinal ion regulation by melanopsin in young awake and free moving mice evaluated with manganese-enhanced MRI. Mol. Vis. 16, 1776–1780.

Bissig, D., Berkowitz, B.A., 2009. Manganese-enhanced MRI of layer-specific activity in the visual cortex from awake and free-moving rats. Neuroimage 44, 627–635. https://doi.org/10.1016/j.neuroimage.2008.10.013.

Bock, N.A., Paiva, F.F., Silva, A.C., 2008. Fractionated manganese-enhanced MRI. NMR Biomed. 21, 473–478. https://doi.org/10.1002/nbm.1211.

Canals, S., Beyerlein, M., Keller, A.L., Murayama, Y., Logothetis, N.K., 2008. Magnetic resonance imaging of cortical connectivity in vivo. Neuroimage 40, 458–472. https://doi.org/10.1016/j.neuroimage.2007.12.007.

Chen, C.-F.F., Zou, D.-J., Altomare, C.G., Xu, L., Greer, C.A., Firestein, S.J., 2014. Nonsensory target-dependent organization of piriform cortex. Proc. Natl. Acad. Sci. U. S. A 111, 16931–16936. https://doi.org/10.1073/pnas.1411266111.

Crossgrove, J., Zheng, W., 2004. Manganese toxicity upon overexposure. NMR Biomed. 17, 544–553. https://doi.org/10.1002/nbm.931.

Daoust, A., Barbier, E.L., Bohic, S., 2013. Manganese enhanced MRI in rat hippocampus: a correlative study with synchrotron X-ray microprobe. Neuroimage 64, 10–18. https://doi.org/10.1016/j.neuroimage.2012.09.025.

Daoust, A., Saoudi, Y., Brocard, J., Collomb, N., Batandier, C., Bisbal, M., Salome, M., Andrieux, A., Bohic, S., Barbier, E.L., 2014. Impact of manganese on primary hippocampal neurons from rodents. Hippocampus 24, 598–610. https://doi.org/10.1002/hipo.22252.

Dedic, N., Pohlmann, M.L., Richter, J.S., Mehta, D., Czamara, D., Metzger, M.W., Dine, J., Bedenk, B.T., Hartmann, J., Wagner, K.V., Jurik, A., Almli, L.M., Lori, A., Moosmang, S., Hofmann, F., Wotjak, C.T., Rammes, G., Eder, M., Chen, A., Ressler, K.J., Wurst, W., Schmidt, M.V., Binder, E.B., Deussing, J.M., 2017. Cross-disorder risk gene CACNA1C differentially modulates susceptibility to psychiatric disorders during development and adulthood. Mol. Psychiatr. https://doi.org/10.1038/mp.2017.133.

Di Biase, V., Tuluc, P., Campiglio, M., Obermair, G.J., Heine, M., Flucher, B.E., 2011. Surface traffic of dendritic CaV1.2 calcium channels in hippocampal neurons. J. Neurosci. 31, 13682–13694. https://doi.org/10.1523/JNEUROSCI.2300-11.2011.

Drapeau, P., Nachshen, D.A., 1984. Manganese fluxes and manganese-dependent neurotransmitter release in presynaptic nerve endings isolated from rat brain. J. Physiol. 348, 493–510.

Eriksson, H., Magiste, K., Plantin, L.O., Fonnum, F., Hedstrom, K.G., Theodorsson-Norheim, E., Kristensson, K., Stalberg, E., Heilbronn, E., 1987. Effects of manganese oxide on monkeys as revealed by a combined neurochemical, histological and neurophysiological evaluation. Arch. Toxicol. 61, 46–52.

Eschenko, O., Canals, S., Simanova, I., Beyerlein, M., Murayama, Y., Logothetis, N.K., 2010. Mapping of functional brain activity in freely behaving rats during voluntary running using manganese-enhanced MRI: implication for longitudinal studies. Neuroimage 49, 2544–2555. https://doi.org/10.1016/j.neuroimage.2009.10.079.

Goebbels, S., Bormuth, I., Bode, U., Hermanson, O., Schwab, M.H., Nave, K.-A., 2006. Genetic targeting of principal neurons in neocortex and hippocampus of NEX-Cre mice. Genesis 44, 611–621. https://doi.org/10.1002/dvg.20256.

Grunecker, B., Kaltwasser, S.F., Peterse, Y., Samann, P.G., Schmidt, M.V., Wotjak, C.T., Czisch, M., 2010. Fractionated manganese injections: effects on MRI contrast enhancement and physiological measures in C57BL/6 mice. NMR Biomed. 23, 913–921. https://doi.org/10.1002/nbm.1508.

Hayasaka, S., Phan, K.L., Liberzon, I., Worsley, K.J., Nichols, T.E., 2004. Nonstationary cluster-size inference with random field and permutation methods. Neuroimage 22, 676–687. https://doi.org/10.1016/j.neuroimage.2004.01.041.

Hazell, A.S., 2002. Astrocytes and manganese neurotoxicity. Neurochem. Int. 41, 271–277.

Hell, J.W., Westenbroek, R.E., Warner, C., Ahlijanian, M.K., Prystay, W., Gilbert, M.M., Snutch, T.P., Catterall, W.A., 1993. Identification and differential subcellular localization of the neuronal class C and class D L-type calcium channel alpha 1 subunits. J. Cell Biol. 123, 949–962.

144

Hetzenauer, A., Sinnegger-Brauns, M.J., Striessnig, J., Singewald, N., 2006. Brain activation pattern induced by stimulation of L-type Ca2+-channels: contribution of Ca(V)1.3 and Ca(V)1.2 isoforms. Neuroscience 139, 1005–1015. https://doi.org/10.1016/j.neuroscience.2006.01.059.

Hohl-Abrahao, J.C., Creutzfeldt, O.D., 1991. Topographical mapping of the thalamocortical projections in rodents and comparison with that in primates. Exp. Brain Res. 87, 283–294.

Itoh, K., Sakata, M., Watanabe, M., Aikawa, Y., Fujii, H., 2008. The entry of manganese ions into the brain is accelerated by the activation of N-methyl-D-aspartate receptors. Neuroscience 154, 732–740. https://doi.org/10.1016/j.neuroscience.2008.03.080.

Langwieser, N., Christel, C.J., Kleppisch, T., Hofmann, F., Wotjak, C.T., Moosmang, S., 2010. Homeostatic switch in hebbian plasticity and fear learning after sustained loss of Cav1.2 calcium channels. J. Neurosci. 30, 8367–8375. https://doi.org/10.1523/JNEUROSCI.4164-08.2010.

Lehallier, B., Rampin, O., Saint-Albin, A., Jerome, N., Ouali, C., Maurin, Y., Bonny, J.-M., 2012. Brain processing of biologically relevant odors in the awake rat, as revealed by manganese-enhanced MRI. PLoS One 7, e48491. https://doi.org/10.1371/journal.pone.0048491.

Lin, T.-H., Chiang, C.-W., Trinkaus, K., Spees, W.M., Sun, P., Song, S.-K., 2014. Manganese-enhanced MRI (MEMRI) via topical loading of Mn(2+) significantly impairs mouse visual acuity: a comparison with intravitreal injection. NMR Biomed. 27, 390–398. https://doi.org/10.1002/nbm.3073.

Lin, Y.J., Koretsky, A.P., 1997. Manganese ion enhances T1-weighted MRI during brain activation: an approach to direct imaging of brain function. Magn. Reson. Med. 38, 378–388.

Lowe, A.S., Thompson, I.D., Sibson, N.R., 2008. Quantitative manganese tract tracing: dose-dependent and activity-independent terminal labelling in the mouse visual system. NMR Biomed. 21, 859–867. https://doi.org/10.1002/nbm.1272.

Ludwig, A., Flockerzi, V., Hofmann, F., 1997. Regional expression and cellular localization of the alpha1 and beta subunit of high voltage-activated calcium channels in rat brain. J. Neurosci. 17, 1339–1349.

Normandin, L., Hazell, A.S., 2002. Manganese neurotoxicity: an update of pathophysiologic mechanisms. Metab. Brain Dis. 17, 375–387.

O'Neal, S.L., Zheng, W., 2015. Manganese toxicity upon overexposure: a decade in review. Curr. Environ. Heal. Reports 2, 315–328. https://doi.org/10.1007/s40572-015-0056-x.

Pautler, R.G., 2004. In vivo, trans-synaptic tract-tracing utilizing manganese-enhanced magnetic resonance imaging (MEMRI). NMR Biomed. 17, 595–601. https://doi.org/10.1002/nbm.942.

Pautler, R.G., Koretsky, A.P., 2002. Tracing odor-induced activation in the olfactory bulbs of mice using manganese-enhanced magnetic resonance imaging. Neuroimage 16, 441–448. https://doi.org/10.1006/nimg.2002.1075.

Pautler, R.G., Mongeau, R., Jacobs, R.E., 2003. In vivo trans-synaptic tract tracing from the murine striatum and amygdala utilizing manganese enhanced MRI (MEMRI). Magn. Reson. Med. 50, 33–39. https://doi.org/10.1002/mrm.10498.

Paxinos, G., Franklin, K., 2012. The Mouse Brain, fourth ed. Academic Press.

Platzer, J., Engel, J., Schrott-Fischer, A., Stephan, K., Bova, S., Chen, H., Zheng, H., Striessnig, J., 2000. Congenital deafness and sinoatrial node dysfunction in mice lacking class D L-type Ca2+ channels. Cell 102, 89–97.

Pohmann, R., 2011. Spatial encoding - basic imaging sequences. In: Schröder, L., Faber, C. (Eds.), In Vivo NMR Imaging. Humana Press, New York Dordrecht Heidelberg London, pp. 23–44. https://doi.org/10.1007/978-1-61779-219-9.

Roth, J.A., Garrick, M.D., 2003. Iron interactions and other biological reactions mediating the physiological and toxic actions of manganese. Biochem. Pharmacol. 66, 1–13.

Seisenberger, C., Specht, V., Welling, A., Platzer, J., Pfeifer, A., Kuhbandner, S., Striessnig, J., Klugbauer, N., Feil, R., Hofmann, F., 2000. Functional embryonic cardiomyocytes after disruption of the L-type alpha1C (Cav1.2) calcium channel gene in the mouse. J. Biol. Chem. 275, 39193–39199. https://doi.org/10.1074/jbc.M006467200.

Sepulveda, M.R., Dresselaers, T., Vangheluwe, P., Everaerts, W., Himmelreich, U., Mata, A.M., Wuytack, F., 2012. Evaluation of manganese uptake and toxicity in mouse brain during continuous MnCl2 administration using osmotic pumps. Contrast Media Mol. Imaging 7, 426–434. https://doi.org/10.1002/cmmi.1469.

Simpson, P.B., Challiss, R.A., Nahorski, S.R., 1995. Divalent cation entry in cultured rat cerebellar granule cells measured using Mn2+ quench of fura 2 fluorescence. Eur. J. Neurosci. 7, 831–840.

Sinnegger-Brauns, M.J., Huber, I.G., Koschak, A., Wild, C., Obermair, G.J., Einzinger, U., Hoda, J.-C., Sartori, S.B., Striessnig, J., 2009. Expression and 1,4-dihydropyridine-binding properties of brain L-type calcium channel isoforms. Mol. Pharmacol. 75, 407–414. https://doi.org/10.1124/mol.108.049981.

Sloot, W.N., Gramsbergen, J.B., 1994. Axonal transport of manganese and its relevance to selective neurotoxicity in the rat basal ganglia. Brain Res. 657, 124–132.

Sloot, W.N., van der Sluijs-Gelling, A.J., Gramsbergen, J.B., 1994. Selective lesions by manganese and extensive damage by iron after injection into rat striatum or hippocampus. J. Neurochem. 62, 205–216.

Takeda, A., Ishiwatari, S., Okada, S., 1998. In vivo stimulation-induced release of manganese in rat amygdala. Brain Res. 811, 147–151.

Tippens, A.L., Pare, J.-F., Langwieser, N., Moosmang, S., Milner, T.A., Smith, Y., Lee, A., 2008. Ultrastructural evidence for pre- and postsynaptic localization of Cav1.2 L-type Ca2+ channels in the rat hippocampus. J. Comp. Neurol. 506, 569–583. https://doi.org/10.1002/cne.21567.

Tucciarone, J., Chuang, K.-H., Dodd, S.J., Silva, A., Pelled, G., Koretsky, A.P., 2009. Layer specific tracing of corticocortical and thalamocortical connectivity in the rodent using manganese enhanced MRI. Neuroimage 44, 923–931. https://doi.org/10.1016/j.neuroimage.2008.07.036.

Van Horn, S.C., Sherman, S.M., 2004. Differences in projection patterns between large and small corticothalamic terminals. J. Comp. Neurol. 475, 406–415. https://doi.org/10.1002/cne.20187.

Wang, J., Braskie, M.N., Hafzalla, G.W., Faskowitz, J., McMahon, K.L., de Zubicaray, G.I., Wright, M.J., Yu, C., Thompson, P.M., 2016. Relationship of a common OXTR gene variant to brain structure and default mode network function in healthy humans. Neuroimage 147, 500–506. https://doi.org/10.1016/j.neuroimage.2016.12.062.

Wang, L., Lu, H., Brown, P.L., Rea, W., Vaupel, B., Yang, Y., Stein, E., Shepard, P.D., 2015. Manganese-enhanced MRI reflects both activity-independent and activity-dependent uptake within the rat habenulomesencephalic pathway. PLoS One 10, e0127773. https://doi.org/10.1371/journal.pone.0127773.

Weick, J.P., Groth, R.D., Isaksen, A.L., Mermelstein, P.G., 2003. Interactions with PDZ proteins are required for L-type calcium channels to activate cAMP response element-binding protein-dependent gene expression. J. Neurosci. 23, 3446–3456.

Westenbroek, R.E., Ahlijanian, M.K., Catterall, W.A., 1990. Clustering of L-type Ca2+ channels at the base of major dendrites in hippocampal pyramidal neurons. Nature 347, 281–284. https://doi.org/10.1038/347281a0.

Yang, P.-F., Chen, D.-Y., Hu, J.W., Chen, J.-H., Yen, C.-T., 2011. Functional tracing of medial nociceptive pathways using activity-dependent manganese-enhanced MRI. Pain 152, 194–203. https://doi.org/10.1016/j.pain.2010.10.027.

Yu, X., Chung, S., Chen, D.-Y., Wang, S., Dodd, S.J., Walters, J.R., Isaac, J.T.R., Koretsky, A.P., 2012. Thalamocortical inputs show post-critical-period plasticity. Neuron 74, 731–742. https://doi.org/10.1016/j.neuron.2012.04.024.

Yu, X., Qian, C., Chen, D., Dodd, S.J., Koretsky, A.P., 2014. Deciphering laminar-specific neural inputs with line-scanning fMRI. Nat. Methods 11, 55–58. https://doi.org/10.1038/nmeth.2730.

Yu, X., Wadghiri, Y.Z., Sanes, D.H., Turnbull, D.H., 2005. In vivo auditory brain mapping in mice with Mn-enhanced MRI. Nat. Neurosci. 8, 961–968. https://doi.org/10.1038/nn1477.

Yu, X., Zou, J., Babb, J.S., Johnson, G., Sanes, D.H., Turnbull, D.H., 2008. Statistical mapping of sound-evoked activity in the mouse auditory midbrain using Mn-enhanced MRI. Neuroimage 39, 223–230. https://doi.org/10.1016/j.neuroimage.2007.08.029.

145

BIBLIOGRAPHY

Agid Y, Javoy F, Glowimski J (1974) Chemical or electrolytic lesion of the substantia nigra: early effects on neostriatal dopamine metabolism. Brain Res 74:41-49.

Alaverdashvili M, Lapointe V, Whishaw IQ, Cross AR (2017) Manganese-Enhanced Magnetic Resonance Imaging and Studies of Rat Behavior: Transient Motor Deficit in Skilled Reaching, Rears, and Activity in Rats After a Single Dose of MnCl2. Magn Reson Insights 10:1178623X17706878.

Albrechet-Souza L, Borelli KG, Almada RC, Brandao ML (2011) Midazolam reduces the selective activation of the rhinal cortex by contextual fear stimuli. Behav Brain Res 216:631-638.

Almeida-Correa S, Czisch M, Wotjak CT (2018) In Vivo Visualization of Active Polysynaptic Circuits With Longitudinal Manganese-Enhanced MRI (MEMRI). Front Neural Circuits 12:42.

Andersen RA (1997) Multimodal integration for the representation of space in the posterior parietal cortex. Philos Trans R Soc Lond B Biol Sci 352:1421-1428.

Andres JI, Alcazar J, Cid JM, De Angelis M, Iturrino L, Langlois X, Lavreysen H, Trabanco AA, Celen S, Bormans G (2012) Synthesis, evaluation, and radiolabeling of new potent positive allosteric modulators of the metabotropic glutamate receptor 2 as potential tracers for positron emission tomography imaging. J Med Chem 55:8685-8699.

Anis NA, Berry SC, Burton NR, Lodge D (1983) The dissociative anaesthetics, ketamine and phencyclidine, selectively reduce excitation of central mammalian neurones by N-methyl-aspartate. Br J Pharmacol 79:565-575.

Aoki I, Tanaka C, Takegami T, Ebisu T, Umeda M, Fukunaga M, Fukuda K, Silva AC, Koretsky AP, Naruse S (2002) Dynamic activity-induced manganese-dependent contrast magnetic resonance imaging (DAIM MRI). Magn Reson Med 48:927-933.

Armbruster BN, Li X, Pausch MH, Herlitze S, Roth BL (2007) Evolving the lock to fit the key to create a family of G protein-coupled receptors potently activated by an inert ligand. Proc Natl Acad Sci U S A 104:5163-5168.

Aronoff R, Matyas F, Mateo C, Ciron C, Schneider B, Petersen CC (2010) Long-range connectivity of mouse primary somatosensory barrel cortex. Eur J Neurosci 31:2221-2233.

Asem JS, Holland PC (2013) Immediate response strategy and shift to place strategy in submerged T-maze. Behav Neurosci 127:854-859.

Attardo A, Fitzgerald JE, Schnitzer MJ (2015) Impermanence of dendritic spines in live adult CA1 hippocampus. Nature 523:592-596.

Augustinack JC, van der Kouwe AJ, Salat DH, Benner T, Stevens AA, Annese J, Fischl B, Frosch MP, Corkin S (2014) H.M.'s contributions to neuroscience: a review and autopsy studies. Hippocampus 24:1267-1286.

Baldi E, Lorenzini CA, Corrado B (2003) Task solving by procedural strategies in the Morris water maze. Physiol Behav 78:785-793.

Bangasser DA, Lee CS, Cook PA, Gee JC, Bhatnagar S, Valentino RJ (2013) Manganese-enhanced magnetic resonance imaging (MEMRI) reveals brain circuitry involved in responding to an acute novel stress in rats with a history of repeated social stress. Physiol Behav 122:228-236.

Barnes CA (1979) Memory deficits associated with senescence: a neurophysiological and behavioral study in the rat. J Comp Physiol Psychol 93:74-104.

Barry DN, Commins S (2011) Imaging spatial learning in the brain using immediate early genes: insights, opportunities and limitations. Rev Neurosci 22:131-142.

Bartelle BB, Szulc KU, Suero-Abreu GA, Rodriguez JJ, Turnbull DH (2013) Divalent metal transporter, DMT1: a novel MRI reporter protein. Magn Reson Med 70:842-850.

Barth TM, Parker SM, Sinnamon HM (1982) Unilateral lesions of the anteromedial cortex in the rat impair approach to contralateral visual cues. Physiol Behav 29:141-147.

Bearer EL, Falzone TL, Zhang X, Biris O, Rasin A, Jacobs RE (2007) Role of neuronal activity and kinesin on tract tracing by manganese-enhanced MRI (MEMRI). Neuroimage 37 Suppl 1:S37-46.

Becker JT, Walker JA, Olton DS (1980) Neuroanatomical bases of spatial memory. Brain Res 200:307-320.

Bedenk BT, Almeida-Correa S, Jurik A, Dedic N, Grunecker B, Genewsky AJ, Kaltwasser SF, Riebe CJ, Deussing JM, Czisch M, Wotjak CT (2018) Mn(2+) dynamics in manganese-enhanced MRI (MEMRI): Cav1.2 channel-mediated uptake and preferential accumulation in projection terminals. Neuroimage 169:374-382.

Berard DR, Coleman WR, Berger LH (1983) Electrical stimulation of the superior olivary complex can produce cortical evoked potential and behavioral discrimination correlates of pitch perception in the rat. Int J Neurosci 18:87-95.

Bissig D, Berkowitz BA (2009) Manganese-enhanced MRI of layer-specific activity in the visual cortex from awake and free-moving rats. Neuroimage 44:627-635.

Block AE, Dhanji H, Thompson-Tardif SF, Floresco SB (2007) Thalamic-prefrontal cortical-ventral striatal circuitry mediates dissociable components of strategy set shifting. Cereb Cortex 17:1625-1636.

Block F, Dihne M, Loos M (2005) Inflammation in areas of remote changes following focal brain lesion. Prog Neurobiol 75:342-365.

Bontempi B, Laurent-Demir C, Destrade C, Jaffard R (1999) Time-dependent reorganization of brain circuitry underlying long-term memory storage. Nature 400:671-675.

Bourassa J, Pinault D, Deschenes M (1995) Corticothalamic projections from the cortical barrel field to the somatosensory thalamus in rats: a single-fibre study using biocytin as an anterograde tracer. Eur J Neurosci 7:19-30.

Brendel M, Jaworska A, Probst F, Overhoff F, Korzhova V, Lindner S, Carlsen J, Bartenstein P, Harada R, Kudo Y, Haass C, Van Leuven F, Okamura N, Herms J, Rominger A (2016) Small-Animal PET Imaging of Tau Pathology with 18F-THK5117 in 2 Transgenic Mouse Models. J Nucl Med 57:792-798.

Bush D, Barry C, Burgess N (2014) What do grid cells contribute to place cell firing? Trends Neurosci 37:136-145.

Bussey TJ, Duck J, Muir JL, Aggleton JP (2000) Distinct patterns of behavioural impairments resulting from fornix transection or neurotoxic lesions of the perirhinal and postrhinal cortices in the rat. Behav Brain Res 111:187-202.

Butler WN, Taube JS (2015) The nucleus prepositus hypoglossi contributes to head direction cell stability in rats. J Neurosci 35:2547-2558.

Buursma AR, de Vries EF, Garssen J, Kegler D, van Waarde A, Schirm J, Hospers GA, Mulder NH, Vaalburg W, Klein HC (2005) [18F]FHPG positron emission tomography for detection of herpes simplex virus (HSV) in experimental HSV encephalitis. J Virol 79:7721-7727.

Carter AG, Sabatini BL (2004) State-dependent calcium signaling in dendritic spines of striatal medium spiny neurons. Neuron 44:483-493.

Cassaday HJ, Nelson AJ, Pezze MA (2014) From attention to memory along the dorsal-ventral axis of the medial prefrontal cortex: some methodological considerations. Front Syst Neurosci 8:160.

Cenquizca LA, Swanson LW (2007) Spatial organization of direct hippocampal field CA1 axonal projections to the rest of the cerebral cortex. Brain Res Rev 56:1-26.

Chang Q, Gold PE (2003) Switching memory systems during learning: changes in patterns of brain acetylcholine release in the hippocampus and striatum in rats. J Neurosci 23:3001-3005.

Chatziioannou AF, Cherry SR, Shao Y, Silverman RW, Meadors K, Farquhar TH, Pedarsani M, Phelps ME (1999) Performance evaluation of microPET: a high-resolution lutetium oxyorthosilicate PET scanner for animal imaging. J Nucl Med 40:1164-1175.

Chee SS, Menard JL, Dringenberg HC (2015) The lateral septum as a regulator of hippocampal theta oscillations and defensive behavior in rats. J Neurophysiol 113:1831-1841.

Chen G, Manson D, Cacucci F, Wills TJ (2016) Absence of Visual Input Results in the Disruption of Grid Cell Firing in the Mouse. Curr Biol 26:2335-2342.

Chen KH, Chen DY, Liang KC (2013) Functional connectivity changes during consolidation of inhibitory avoidance memory in rats: a manganese-enhanced MRI study. Chin J Physiol 56:269-281.

Chen LL, Lin LH, Green EJ, Barnes CA, McNaughton BL (1994) Head-direction cells in the rat posterior cortex. I. Anatomical distribution and behavioral modulation. Exp Brain Res 101:8-23.

Chen S, Raos V, Bentivoglio M (1992) Connections of the thalamic reticular nucleus with the contralateral thalamus in the rat. Neurosci Lett 147:85-88.

Chen W, Tenney J, Kulkarni P, King JA (2007) Imaging unconditioned fear response with manganese-enhanced MRI (MEMRI). Neuroimage 37:221-229.

Cho J, Sharp PE (2001) Head direction, place, and movement correlates for cells in the rat retrosplenial cortex. Behav Neurosci 115:3-25.

Cho YH, Friedman E, Silva AJ (1999) Ibotenate lesions of the hippocampus impair spatial learning but not contextual fear conditioning in mice. Behav Brain Res 98:77-87.

Chometton S, Charriere K, Bayer L, Houdayer C, Franchi G, Poncet F, Fellmann D, Risold PY (2017) The rostromedial zona incerta is involved in attentional processes while adjacent LHA responds to arousal: c-Fos and anatomical evidence. Brain Struct Funct 222:2507-2525.

Chuang KH, Lee JH, Silva AC, Belluscio L, Koretsky AP (2009) Manganese enhanced MRI reveals functional circuitry in response to odorant stimuli. Neuroimage 44:363-372.

Chung K, Deisseroth K (2013) CLARITY for mapping the nervous system. Nat Methods 10:508-513.

Chung K, Wallace J, Kim SY, Kalyanasundaram S, Andalman AS, Davidson TJ, Mirzabekov JJ, Zalocusky KA, Mattis J, Denisin AK, Pak S, Bernstein H, Ramakrishnan C, Grosenick L, Gradinaru V, Deisseroth K (2013) Structural and molecular interrogation of intact biological systems. Nature 497:332-337.

Ciocchi S, Passecker J, Malagon-Vina H, Mikus N, Klausberger T (2015) Brain computation. Selective information routing by ventral hippocampal CA1 projection neurons. Science 348:560-563.

Cohen NJ, Eichenbaum H, Deacedo BS, Corkin S (1985) Different memory systems underlying acquisition of procedural and declarative knowledge. Ann N Y Acad Sci 444:54-71.

Colombo PJ, Brightwell JJ, Countryman RA (2003) Cognitive strategy-specific increases in phosphorylated cAMP response element-binding protein and c-Fos in the hippocampus and dorsal striatum. J Neurosci 23:3547-3554.

Comoli E, Ribeiro-Barbosa ER, Negrao N, Goto M, Canteras NS (2005) Functional mapping of the prosencephalic systems involved in organizing predatory behavior in rats. Neuroscience 130:1055-1067.

Compton DM, Griffith HR, McDaniel WF, Foster RA, Davis BK (1997) The flexible use of multiple cue relationships in spatial navigation: a comparison of water maze performance following hippocampal, medial septal, prefrontal cortex, or posterior parietal cortex lesions. Neurobiol Learn Mem 68:117-132.

Condes-Lara M, Rojas-Piloni G, Martinez-Lorenzana G, Diez-Martinez DC, Rodriguez-Jimenez J (2012) Functional interactions between the paraventricular hypothalamic nucleus and raphe

magnus. A comparative study of an integrated homeostatic analgesic mechanism. Neuroscience 209:196-207.

Conejo NM, Gonzalez-Pardo H, Vallejo G, Arias JL (2007) Changes in brain oxidative metabolism induced by water maze training. Neuroscience 145:403-412.

Cook D, Kesner RP (1988) Caudate nucleus and memory for egocentric localization. Behav Neural Biol 49:332-343.

Cooper BG, Mizumori SJ (2001) Temporary inactivation of the retrosplenial cortex causes a transient reorganization of spatial coding in the hippocampus. J Neurosci 21:3986-4001.

Cordero MI, Just N, Poirier GL, Sandi C (2016) Effects of paternal and peripubertal stress on aggression, anxiety, and metabolic alterations in the lateral septum. Eur Neuropsychopharmacol 26:357-367.

Cornwall J, Phillipson OT (1988) Afferent projections to the parafascicular thalamic nucleus of the rat, as shown by the retrograde transport of wheat germ agglutinin. Brain Res Bull 20:139-150.

Cui Y, Lv G, Jin S, Peng J, Yuan J, He X, Gong H, Xu F, Xu T, Li H (2017) A Central Amygdala-Substantia Innominata Neural Circuitry Encodes Aversive Reinforcement Signals. Cell Rep 21:1770-1782.

Cummings JA, Mulkey RM, Nicoll RA, Malenka RC (1996) Ca2+ signaling requirements for long-term depression in the hippocampus. Neuron 16:825-833.

Dalley JW, Cardinal RN, Robbins TW (2004) Prefrontal executive and cognitive functions in rodents: neural and neurochemical substrates. Neurosci Biobehav Rev 28:771-784.

Dedeurwaerdere S, Gregoire MC, Vivash L, Roselt P, Binns D, Fookes C, Greguric I, Pham T, Loc'h C, Katsifis A, Hicks RJ, O'Brien TJ, Myers DE (2009) In-vivo imaging characteristics of two fluorinated flumazenil radiotracers in the rat. Eur J Nucl Med Mol Imaging 36:958-965.

Deisseroth K (2011) Optogenetics. Nat Methods 8:26-29.

Del Guerra A, Belcari N (2002) Advances in animal PET scanners. Q J Nucl Med 46:35-47.

Delatour B, Gisquet-Verrier P (2000) Functional role of rat prelimbic-infralimbic cortices in spatial memory: evidence for their involvement in attention and behavioural flexibility. Behav Brain Res 109:113-128.

Denic A, Macura SI, Mishra P, Gamez JD, Rodriguez M, Pirko I (2011) MRI in rodent models of brain disorders. Neurotherapeutics 8:3-18.

Denk W, Delaney KR, Gelperin A, Kleinfeld D, Strowbridge BW, Tank DW, Yuste R (1994) Anatomical and functional imaging of neurons using 2-photon laser scanning microscopy. J Neurosci Methods 54:151-162.

Depresseux JC (1977) The positron emission tomography and its applications. J Belge Radiol 60:483-500.

Devan BD, White NM (1999) Parallel information processing in the dorsal striatum: relation to hippocampal function. J Neurosci 19:2789-2798.

Dine J, Genewsky A, Hladky F, Wotjak CT, Deussing JM, Zieglgansberger W, Chen A, Eder M (2016) Local Optogenetic Induction of Fast (20-40 Hz) Pyramidal-Interneuron Network Oscillations in the In Vitro and In Vivo CA1 Hippocampus: Modulation by CRF and Enforcement of Perirhinal Theta Activity. Front Cell Neurosci 10:108.

Doyere V, Burette F, Negro CR, Laroche S (1993) Long-term potentiation of hippocampal afferents and efferents to prefrontal cortex: implications for associative learning. Neuropsychologia 31:1031-1053.

Drapeau P, Nachshen DA (1984) Manganese fluxes and manganese-dependent neurotransmitter release in presynaptic nerve endings isolated from rat brain. J Physiol 348:493-510.

Dusart I, Schwab ME (1994) Secondary cell death and the inflammatory reaction after dorsal hemisection of the rat spinal cord. Eur J Neurosci 6:712-724.

Elliott AE, Packard MG (2008) Intra-amygdala anxiogenic drug infusion prior to retrieval biases rats towards the use of habit memory. Neurobiol Learn Mem 90:616-623.

Escanilla OD, Victor JD, Di Lorenzo PM (2015) Odor-taste convergence in the nucleus of the solitary tract of the awake freely licking rat. J Neurosci 35:6284-6297.

Eschenko O, Canals S, Simanova I, Beyerlein M, Murayama Y, Logothetis NK (2010) Mapping of functional brain activity in freely behaving rats during voluntary running using manganese-enhanced MRI: implication for longitudinal studies. Neuroimage 49:2544-2555.

Euston DR, Gruber AJ, McNaughton BL (2012) The role of medial prefrontal cortex in memory and decision making. Neuron 76:1057-1070.

Farrell MS, Roth BL (2013) Pharmacosynthetics: Reimagining the pharmacogenetic approach. Brain Res 1511:6-20.

Feierstein CE, Quirk MC, Uchida N, Sosulski DL, Mainen ZF (2006) Representation of spatial goals in rat orbitofrontal cortex. Neuron 51:495-507.

Fenton AA, Arolfo MP, Nerad L, Bures J (1994) Place navigation in the Morris water maze under minimum and redundant extra-maze cue conditions. Behav Neural Biol 62:178-189.

Franklin KBJ, Paxinos G (2007) The Mouse Brain in Stereotaxic Coordinates Third Edition. San Diego, California: Academic Press (Elsevier).

Funahashi S, Kubota K (1994) Working memory and prefrontal cortex. Neurosci Res 21:1-11.

Fyhn M, Hafting T, Treves A, Moser MB, Moser EI (2007) Hippocampal remapping and grid realignment in entorhinal cortex. Nature 446:190-194.

Gaffan EA, Eacott MJ, Simpson EL (2000) Perirhinal cortex ablation in rats selectively impairs object identification in a simultaneous visual comparison task. Behav Neurosci 114:18-31.

Gavin CE, Gunter KK, Gunter TE (1990) Manganese and calcium efflux kinetics in brain mitochondria. Relevance to manganese toxicity. Biochem J 266:329-334.

Gittis AH, du Lac S (2006) Intrinsic and synaptic plasticity in the vestibular system. Curr Opin Neurobiol 16:385-390.

Goebbels S, Bormuth I, Bode U, Hermanson O, Schwab MH, Nave KA (2006) Genetic targeting of principal neurons in neocortex and hippocampus of NEX-Cre mice. Genesis 44:611-621.

Goldman S, Wikler D, Damhaut P, Monclus M, Levivier M, Pirotte B, De Witte O, Brotchi J, Hildebrand J (1997) Positron emission tomography and brain tumours. Acta Neurol Belg 97:183-186.

Grunecker B, Kaltwasser SF, Peterse Y, Samann PG, Schmidt MV, Wotjak CT, Czisch M (2010) Fractionated manganese injections: effects on MRI contrast enhancement and physiological measures in C57BL/6 mice. NMR Biomed 23:913-921.

Grunecker B, Kaltwasser SF, Zappe AC, Bedenk BT, Bicker Y, Spoormaker VI, Wotjak CT, Czisch M (2013) Regional specificity of manganese accumulation and clearance in the mouse brain: implications for manganese-enhanced MRI. NMR Biomed 26:542-556.

Guenthner CJ, Miyamichi K, Yang HH, Heller HC, Luo L (2013) Permanent genetic access to transiently active neurons via TRAP: targeted recombination in active populations. Neuron 78:773-784.

Guo C, Peng J, Zhang Y, Li A, Li Y, Yuan J, Xu X, Ren M, Gong H, Chen S (2017) Single-axon level morphological analysis of corticofugal projection neurons in mouse barrel field. Sci Rep 7:2846.

Guzowski JF, Timlin JA, Roysam B, McNaughton BL, Worley PF, Barnes CA (2005) Mapping behaviorally relevant neural circuits with immediate-early gene expression. Curr Opin Neurobiol 15:599-606.

Hamilton DA, Akers KG, Johnson TE, Rice JP, Candelaria FT, Redhead ES (2009) Evidence for a shift from place navigation to directional responding in one variant of the Morris water task. J Exp Psychol Anim Behav Process 35:271-278.

Hardung S, Epple R, Jackel Z, Eriksson D, Uran C, Senn V, Gibor L, Yizhar O, Diester I (2017) A Functional Gradient in the Rodent Prefrontal Cortex Supports Behavioral Inhibition. Curr Biol 27:549-555.

Harris RM (1986) Morphology of physiologically identified thalamocortical relay neurons in the rat ventrobasal thalamus. J Comp Neurol 251:491-505.

Hazrati LN, Pinault D, Parent A (1995) The thalamic reticular nucleus does not send commissural projection to the contralateral parafascicular nucleus in the rat. Brain Res 679:123-134.

Heidbreder CA, Groenewegen HJ (2003) The medial prefrontal cortex in the rat: evidence for a dorso-ventral distinction based upon functional and anatomical characteristics. Neurosci Biobehav Rev 27:555-579.

Henriksson J, Tallkvist J, Tjalve H (1999) Transport of manganese via the olfactory pathway in rats: dosage dependency of the uptake and subcellular distribution of the metal in the olfactory epithelium and the brain. Toxicol Appl Pharmacol 156:119-128.

Hires SA, Tian L, Looger LL (2008) Reporting neural activity with genetically encoded calcium indicators. Brain Cell Biol 36:69-86.

Hoch T, Kreitz S, Gaffling S, Pischetsrieder M, Hess A (2013) Manganese-enhanced magnetic resonance imaging for mapping of whole brain activity patterns associated with the intake of snack food in ad libitum fed rats. PLoS One 8:e55354.

Hok V, Save E, Lenck-Santini PP, Poucet B (2005) Coding for spatial goals in the prelimbic/infralimbic area of the rat frontal cortex. Proc Natl Acad Sci U S A 102:4602-4607.

Holland PC, Gallagher M (2006) Different roles for amygdala central nucleus and substantia innominata in the surprise-induced enhancement of learning. J Neurosci 26:3791-3797.

Hoogland PV, Welker E, Van der Loos H (1987) Organization of the projections from barrel cortex to thalamus in mice studied with Phaseolus vulgaris-leucoagglutinin and HRP. Exp Brain Res 68:73-87.

Hoogland PV, Wouterlood FG, Welker E, Van der Loos H (1991) Ultrastructure of giant and small thalamic terminals of cortical origin: a study of the projections from the barrel cortex in mice using Phaseolus vulgaris leuco-agglutinin (PHA-L). Exp Brain Res 87:159-172.

Hoover WB, Vertes RP (2007) Anatomical analysis of afferent projections to the medial prefrontal cortex in the rat. Brain Struct Funct 212:149-179.

Howles GP, Qi Y, Johnson GA (2010) Ultrasonic disruption of the blood-brain barrier enables in vivo functional mapping of the mouse barrel field cortex with manganese-enhanced MRI. Neuroimage 50:1464-1471.

Iaria G, Petrides M, Dagher A, Pike B, Bohbot VD (2003) Cognitive strategies dependent on the hippocampus and caudate nucleus in human navigation: variability and change with practice. J Neurosci 23:5945-5952.

Igarashi KM, Lu L, Colgin LL, Moser MB, Moser EI (2014) Coordination of entorhinal-hippocampal ensemble activity during associative learning. Nature 510:143-147.

Itoh K, Sakata M, Watanabe M, Aikawa Y, Fujii H (2008) The entry of manganese ions into the brain is accelerated by the activation of N-methyl-D-aspartate receptors. Neuroscience 154:732-740.

Jacobson TK, Gruenbaum BF, Markus EJ (2012) Extensive training and hippocampus or striatum lesions: effect on place and response strategies. Physiol Behav 105:645-652.

Jay TM, Witter MP (1991) Distribution of hippocampal CA1 and subicular efferents in the prefrontal cortex of the rat studied by means of anterograde transport of Phaseolus vulgaris-leucoagglutinin. J Comp Neurol 313:574-586.

Jeannerod M, Decety J, Michel F (1994) Impairment of grasping movements following a bilateral posterior parietal lesion. Neuropsychologia 32:369-380.

Jones MW (2002) A comparative review of rodent prefrontal cortex and working memory. Curr Mol Med 2:639-647.

Kapoor V, Provost AC, Agarwal P, Murthy VN (2016) Activation of raphe nuclei triggers rapid and distinct effects on parallel olfactory bulb output channels. Nat Neurosci 19:271-282.

Kesner RP, Churchwell JC (2011) An analysis of rat prefrontal cortex in mediating executive function. Neurobiol Learn Mem 96:417-431.

Kim JJ, Lee HJ, Han JS, Packard MG (2001) Amygdala is critical for stress-induced modulation of hippocampal long-term potentiation and learning. J Neurosci 21:5222-5228.

Kirby ED, Jensen K, Goosens KA, Kaufer D (2012) Stereotaxic surgery for excitotoxic lesion of specific brain areas in the adult rat. J Vis Exp:e4079.

Kita H, Kitai ST (1990) Amygdaloid projections to the frontal cortex and the striatum in the rat. J Comp Neurol 298:40-49.

Kleinknecht KR, Bedenk BT, Kaltwasser SF, Grunecker B, Yen YC, Czisch M, Wotjak CT (2012) Hippocampus-dependent place learning enables spatial flexibility in C57BL6/N mice. Front Behav Neurosci 6:87.

Kobayashi Y, Inoue Y, Isa T (2004) Pedunculo-pontine control of visually guided saccades. Prog Brain Res 143:439-445.

Kubik S, Miyashita T, Guzowski JF (2007) Using immediate-early genes to map hippocampal subregional functions. Learn Mem 14:758-770.

Kugler S, Kilic E, Bahr M (2003) Human synapsin 1 gene promoter confers highly neuron-specific long-term transgene expression from an adenoviral vector in the adult rat brain depending on the transduced area. Gene Ther 10:337-347.

Kuo YT, Herlihy AH, So PW, Bell JD (2006) Manganese-enhanced magnetic resonance imaging (MEMRI) without compromise of the blood-brain barrier detects hypothalamic neuronal activity in vivo. NMR Biomed 19:1028-1034.

Kyd RJ, Bilkey DK (2003) Prefrontal cortex lesions modify the spatial properties of hippocampal place cells. Cereb Cortex 13:444-451.

Laine MA, Sokolowska E, Dudek M, Callan SA, Hyytia P, Hovatta I (2017) Brain activation induced by chronic psychosocial stress in mice. Sci Rep 7:15061.

Lashley KS (1950) In Search of the Engram. Sym Soc Exp Biol 4:454-482.

Laurens J, Angelaki DE (2018) The Brain Compass: A Perspective on How Self-Motion Updates the Head Direction Cell Attractor. Neuron 97:275-289.

Lech RK, Koch B, Schwarz M, Suchan B (2016) Fornix and medial temporal lobe lesions lead to comparable deficits in complex visual perception. Neurosci Lett 620:27-32.

Lee AS, Duman RS, Pittenger C (2008) A double dissociation revealing bidirectional competition between striatum and hippocampus during learning. Proc Natl Acad Sci U S A 105:17163-17168.

Lehallier B, Coureaud G, Maurin Y, Bonny JM (2012) Effects of manganese injected into rat nostrils: implications for in vivo functional study of olfaction using MEMRI. Magn Reson Imaging 30:62-69.

Lein ES et al. (2007) Genome-wide atlas of gene expression in the adult mouse brain. Nature 445:168-176.

Leitner FC, Melzer S, Lutcke H, Pinna R, Seeburg PH, Helmchen F, Monyer H (2016) Spatially segregated feedforward and feedback neurons support differential odor processing in the lateral entorhinal cortex. Nat Neurosci 19:935-944.

Li N, Chen TW, Guo ZV, Gerfen CR, Svoboda K (2015) A motor cortex circuit for motor planning and movement. Nature 519:51-56.

Lin MZ, Schnitzer MJ (2016) Genetically encoded indicators of neuronal activity. Nat Neurosci 19:1142-1153.

Lin TH, Chiang CW, Trinkaus K, Spees WM, Sun P, Song SK (2014) Manganese-enhanced MRI (MEMRI) via topical loading of Mn(2+) significantly impairs mouse visual acuity: a comparison with intravitreal injection. NMR Biomed 27:390-398.

Lin YJ, Koretsky AP (1997) Manganese ion enhances T1-weighted MRI during brain activation: an approach to direct imaging of brain function. Magn Reson Med 38:378-388.

Liu Z, Turner LF, Bures J (1994) Impairment of place navigation of rats in the Morris water maze by intermittent light is inversely related to the duration of the flash. Neurosci Lett 180:59-62.

Lopez AJ, Kramar E, Matheos DP, White AO, Kwapis J, Vogel-Ciernia A, Sakata K, Espinoza M, Wood MA (2016) Promoter-Specific Effects of DREADD Modulation on Hippocampal Synaptic Plasticity and Memory Formation. J Neurosci 36:3588-3599.

Lopez Hill X, Pascovich C, Urbanavicius J, Torterolo P, Scorza MC (2013) The median raphe nucleus participates in the depressive-like behavior induced by MCH: differences with the dorsal raphe nucleus. Peptides 50:96-99.

Low AYT, Thanawalla AR, Yip AKK, Kim J, Wong KLL, Tantra M, Augustine GJ, Chen AI (2018) Precision of Discrete and Rhythmic Forelimb Movements Requires a Distinct Neuronal Subpopulation in the Interposed Anterior Nucleus. Cell Rep 22:2322-2333.

Lowe AS, Thompson ID, Sibson NR (2008) Quantitative manganese tract tracing: dose-dependent and activity-independent terminal labelling in the mouse visual system. NMR Biomed 21:859-867.

Luo L, Xu H, Li Y, Du Z, Sun X, Ma Z, Hu Y (2012) Manganese-enhanced MRI optic nerve tracking: effect of intravitreal manganese dose on retinal toxicity. NMR Biomed 25:1360-1368.

Lutkenhoff E, Karlsgodt KH, Gutman B, Stein JL, Thompson PM, Cannon TD, Jentsch JD (2012) Structural and functional neuroimaging phenotypes in dysbindin mutant mice. Neuroimage 62:120-129.

Maddock RJ (1999) The retrosplenial cortex and emotion: new insights from functional neuroimaging of the human brain. Trends Neurosci 22:310-316.

Madisen L et al. (2012) A toolbox of Cre-dependent optogenetic transgenic mice for light-induced activation and silencing. Nat Neurosci 15:793-802.

Martinet LE, Sheynikhovich D, Benchenane K, Arleo A (2011) Spatial learning and action planning in a prefrontal cortical network model. PLoS Comput Biol 7:e1002045.

Matin L, Li W (1995) Multimodal basis for egocentric spatial localization and orientation. J Vestib Res 5:499-518.

Mayford M, Bach ME, Huang YY, Wang L, Hawkins RD, Kandel ER (1996) Control of memory formation through regulated expression of a CaMKII transgene. Science 274:1678-1683.

McAlonan K, Brown VJ (2003) Orbital prefrontal cortex mediates reversal learning and not attentional set shifting in the rat. Behav Brain Res 146:97-103.

McDonald AJ, Mott DD (2017) Functional neuroanatomy of amygdalohippocampal interconnections and their role in learning and memory. J Neurosci Res 95:797-820.

McNaughton BL, Mizumori SJ, Barnes CA, Leonard BJ, Marquis M, Green EJ (1994) Cortical representation of motion during unrestrained spatial navigation in the rat. Cereb Cortex 4:27-39.

McNaughton BL, Barnes CA, Gerrard JL, Gothard K, Jung MW, Knierim JJ, Kudrimoti H, Qin Y, Skaggs WE, Suster M, Weaver KL (1996) Deciphering the hippocampal polyglot: the hippocampus as a path integration system. J Exp Biol 199:173-185.

McWilliams R, Lynch G (1978) Terminal proliferation and synaptogenesis following partial deafferentation: the reinnervation of the inner molecular layer of the dentate gyrus following removal of its commissural afferents. J Comp Neurol 180:581-616.

Milner B, Penfield W (1955) The effect of hippocampal lesions on recent memory. Trans Am Neurol Assoc:42-48.

Miranda R, Blanco E, Begega A, Rubio S, Arias JL (2006) Hippocampal and caudate metabolic activity associated with different navigational strategies. Behav Neurosci 120:641-650.

Mitra A, Guevremont G, Timofeeva E (2016) Stress and Sucrose Intake Modulate Neuronal Activity in the Anterior Hypothalamic Area in Rats. PLoS One 11:e0156563.

Monaco JD, Abbott LF (2011) Modular realignment of entorhinal grid cell activity as a basis for hippocampal remapping. J Neurosci 31:9414-9425.

Montero VM, Scott GL (1981) Synaptic terminals in the dorsal lateral geniculate nucleus from neurons of the thalamic reticular nucleus: a light and electron microscope autoradiographic study. Neuroscience 6:2561-2577.

Mook Jo S, Kuk Kim Y, Wang Z, Danscher G (2002) Retrograde tracing of zinc-enriched (ZEN) neuronal somata projecting to the olfactory bulb. Brain Res 956:230-235.

Morris R (1984) Developments of a water-maze procedure for studying spatial learning in the rat. J Neurosci Methods 11:47-60.

Morris RG, Garrud P, Rawlins JN, O'Keefe J (1982) Place navigation impaired in rats with hippocampal lesions. Nature 297:681-683.

Moser E, Moser MB, Andersen P (1993) Spatial learning impairment parallels the magnitude of dorsal hippocampal lesions, but is hardly present following ventral lesions. J Neurosci 13:3916-3925.

Moser EI, Moser MB (2008) A metric for space. Hippocampus 18:1142-1156.

Nakamura Y, Yanagawa Y, Morrison SF, Nakamura K (2017) Medullary Reticular Neurons Mediate Neuropeptide Y-Induced Metabolic Inhibition and Mastication. Cell Metab 25:322-334.

Negron-Oyarzo I, Espinosa N, Aguilar-Rivera M, Fuenzalida M, Aboitiz F, Fuentealba P (2018) Coordinated prefrontal-hippocampal activity and navigation strategy-related prefrontal firing during spatial memory formation. Proc Natl Acad Sci U S A 115:7123-7128.

Nishio N, Tsukano H, Hishida R, Abe M, Nakai J, Kawamura M, Aiba A, Sakimura K, Shibuki K (2018) Higher visual responses in the temporal cortex of mice. Sci Rep 8:11136.

Nordhoy W, Anthonsen HW, Bruvold M, Brurok H, Skarra S, Krane J, Jynge P (2004) Intracellular manganese ions provide strong T1 relaxation in rat myocardium. Magn Reson Med 52:506-514.

Notsu K, Tsumori T, Yokota S, Sekine J, Yasui Y (2008) Posterior lateral hypothalamic axon terminals are in contact with trigeminal premotor neurons in the parvicellular reticular formation of the rat medulla oblongata. Brain Res 1244:71-81.

O'Keefe J (1976) Place units in the hippocampus of the freely moving rat. Exp Neurol 51:78-109.

O'Keefe J (1991) An allocentric spatial model for the hippocampal cognitive map. Hippocampus 1:230-235.

O'Keefe J, Dostrovsky J (1971) The hippocampus as a spatial map. Preliminary evidence from unit activity in the freely-moving rat. Brain Res 34:171-175.

O'Keefe J, Nadel L (1978) The Hippocampus as a Cognitive Map: Oxford University Press.

Ohara PT, Lieberman AR (1981) Thalamic reticular nucleus: anatomical evidence that cortico-reticular axons establish monosynaptic contact with reticulo-geniculate projection cells. Brain Res 207:153-156.

Ohara PT, Lieberman AR (1985) The thalamic reticular nucleus of the adult rat: experimental anatomical studies. J Neurocytol 14:365-411.

Ohara PT, Sefton AJ, Lieberman AR (1980) Mode of termination of afferents from the thalamic reticular nucleus in the dorsal lateral geniculate nucleus of the rat. Brain Res 197:503-506.

Ohl FW, Scheich H, Freeman WJ (2001) Change in pattern of ongoing cortical activity with auditory category learning. Nature 412:733-736.

Olton DS, Samuelson RJ (1976) Remembrance of places passed: Spatial memory in rats. J Exp Psychol Anim Behav Process Volume 2:97-116.

Oualian C, Gisquet-Verrier P (2010) The differential involvement of the prelimbic and infralimbic cortices in response conflict affects behavioral flexibility in rats trained in a new automated strategy-switching task. Learn Mem 17:654-668.

Packard MG, McGaugh JL (1992) Double dissociation of fornix and caudate nucleus lesions on acquisition of two water maze tasks: further evidence for multiple memory systems. Behav Neurosci 106:439-446.

Packard MG, McGaugh JL (1996) Inactivation of hippocampus or caudate nucleus with lidocaine differentially affects expression of place and response learning. Neurobiol Learn Mem 65:65-72.

Packard MG, Wingard JC (2004) Amygdala and "emotional" modulation of the relative use of multiple memory systems. Neurobiol Learn Mem 82:243-252.

Packard MG, Cahill L, McGaugh JL (1994) Amygdala modulation of hippocampal-dependent and caudate nucleus-dependent memory processes. Proc Natl Acad Sci U S A 91:8477-8481.

Park C, Pan Z, Brietzke E, Subramaniapillai M, Rosenblat JD, Zuckerman H, Lee Y, Fus D, McIntyre RS (2018) Predicting antidepressant response using early changes in cognition: A systematic review. Behav Brain Res 353:154-160.

Pautler RG (2004) In vivo, trans-synaptic tract-tracing utilizing manganese-enhanced magnetic resonance imaging (MEMRI). NMR Biomed 17:595-601.

Pautler RG, Koretsky AP (2002) Tracing odor-induced activation in the olfactory bulbs of mice using manganese-enhanced magnetic resonance imaging. Neuroimage 16:441-448.

Pautler RG, Silva AC, Koretsky AP (1998) In vivo neuronal tract tracing using manganese-enhanced magnetic resonance imaging. Magn Reson Med 40:740-748.

Pautler RG, Mongeau R, Jacobs RE (2003) In vivo trans-synaptic tract tracing from the murine striatum and amygdala utilizing manganese enhanced MRI (MEMRI). Magn Reson Med 50:33-39.

Penfield W, Milner B (1958) Memory deficit produced by bilateral lesions in the hippocampal zone. AMA Arch Neurol Psychiatry 79:475-497.

Peterson NN, Arezzo JC (1994) Effects of a frontal lesion on the cortical potentials associated with voluntary movement in the awake monkey. J Neurotrauma 11:197-205.

Pinault D, Deschenes M (1998) Projection and innervation patterns of individual thalamic reticular axons in the thalamus of the adult rat: a three-dimensional, graphic, and morphometric analysis. J Comp Neurol 391:180-203.

Pinault D, Bourassa J, Deschenes M (1995) Thalamic reticular input to the rat visual thalamus: a single fiber study using biocytin as an anterograde tracer. Brain Res 670:147-152.

Pitkanen A, Pikkarainen M, Nurminen N, Ylinen A (2000) Reciprocal connections between the amygdala and the hippocampal formation, perirhinal cortex, and postrhinal cortex in rat. A review. Ann N Y Acad Sci 911:369-391.

Poole DS, Doorenweerd N, Plomp JJ, Mahfouz A, Reinders MJT, van der Weerd L (2017) Continuous infusion of manganese improves contrast and reduces side effects in manganese-enhanced magnetic resonance imaging studies. Neuroimage 147:1-9.

Ragozzino ME (2007) The contribution of the medial prefrontal cortex, orbitofrontal cortex, and dorsomedial striatum to behavioral flexibility. Ann N Y Acad Sci 1121:355-375.

Ragozzino ME, Detrick S, Kesner RP (1999) Involvement of the prelimbic-infralimbic areas of the rodent prefrontal cortex in behavioral flexibility for place and response learning. J Neurosci 19:4585-4594.

Raos V, Bentivoglio M (1993) Crosstalk between the two sides of the thalamus through the reticular nucleus: a retrograde and anterograde tracing study in the rat. J Comp Neurol 332:145-154.

Recio-Spinoso A, Joris PX (2014) Temporal properties of responses to sound in the ventral nucleus of the lateral lemniscus. J Neurophysiol 111:817-835.

Rees H, Roberts MH (1993) The anterior pretectal nucleus: a proposed role in sensory processing. Pain 53:121-135.

Reichel JM, Bedenk BT, Czisch M, Wotjak CT (2017) Age-related cognitive decline coincides with accelerated volume loss of the dorsal but not ventral hippocampus in mice. Hippocampus 27:28-35.

Reichel JM, Bedenk BT, Gassen NC, Hafner K, Bura SA, Almeida-Correa S, Genewsky A, Dedic N, Giesert F, Agarwal A, Nave KA, Rein T, Czisch M, Deussing JM, Wotjak CT (2016) Beware of your Cre-Ation: lacZ expression impairs neuronal integrity and hippocampus-dependent memory. Hippocampus 26:1250-1264.

Reivich M, Gur R, Alavi A (1983) Positron emission tomographic studies of sensory stimuli, cognitive processes and anxiety. Hum Neurobiol 2:25-33.

Renier N, Wu Z, Simon DJ, Yang J, Ariel P, Tessier-Lavigne M (2014) iDISCO: a simple, rapid method to immunolabel large tissue samples for volume imaging. Cell 159:896-910.

Renno-Costa C, Tort ABL (2017) Place and Grid Cells in a Loop: Implications for Memory Function and Spatial Coding. J Neurosci 37:8062-8076.

Rich EL, Shapiro ML (2007) Prelimbic/infralimbic inactivation impairs memory for multiple task switches, but not flexible selection of familiar tasks. J Neurosci 27:4747-4755.

Rich EL, Shapiro M (2009) Rat prefrontal cortical neurons selectively code strategy switches. J Neurosci 29:7208-7219.

Robinson FR, Straube A, Fuchs AF (1993) Role of the caudal fastigial nucleus in saccade generation. II. Effects of muscimol inactivation. J Neurophysiol 70:1741-1758.

Robinson L, Bridge H, Riedel G (2001) Visual discrimination learning in the water maze: a novel test for visual acuity. Behav Brain Res 119:77-84.

Rolls ET, Robertson RG, Georges-Francois P (1997) Spatial view cells in the primate hippocampus. Eur J Neurosci 9:1789-1794.

Roth BL (2016) DREADDs for Neuroscientists. Neuron 89:683-694.

Roth JA, Garrick MD (2003) Iron interactions and other biological reactions mediating the physiological and toxic actions of manganese. Biochem Pharmacol 66:1-13.

Ruediger S, Spirig D, Donato F, Caroni P (2012) Goal-oriented searching mediated by ventral hippocampus early in trial-and-error learning. Nat Neurosci 15:1563-1571.

Sauvage MM, Nakamura NH, Beer Z (2013) Mapping memory function in the medial temporal lobe with the immediate-early gene Arc. Behav Brain Res 254:22-33.

Schelbert HR (1985) Positron-emission tomography: assessment of myocardial blood flow and metabolism. Circulation 72:IV122-133.

Scheyltjens I, Laramee ME, Van den Haute C, Gijsbers R, Debyser Z, Baekelandt V, Vreysen S, Arckens L (2015) Evaluation of the expression pattern of rAAV2/1, 2/5, 2/7, 2/8, and 2/9 serotypes with different promoters in the mouse visual cortex. J Comp Neurol 523:2019-2042.

Schmidt MV, Sterlemann V, Ganea K, Liebl C, Alam S, Harbich D, Greetfeld M, Uhr M, Holsboer F, Muller MB (2007) Persistent neuroendocrine and behavioral effects of a novel, etiologically relevant mouse paradigm for chronic social stress during adolescence. Psychoneuroendocrinology 32:417-429.

Schoenbaum G, Eichenbaum H (1995) Information coding in the rodent prefrontal cortex. II. Ensemble activity in orbitofrontal cortex. J Neurophysiol 74:751-762.

Schrigten D, Breyholz HJ, Wagner S, Hermann S, Schober O, Schafers M, Haufe G, Kopka K (2012) A new generation of radiofluorinated pyrimidine-2,4,6-triones as MMP-targeted radiotracers for positron emission tomography. J Med Chem 55:223-232.

Schröder L, Faber C (2011) In vivo NMR Imaging: Humana Press.

Schwabe L, Wolf OT (2009) Stress prompts habit behavior in humans. J Neurosci 29:7191-7198.

Schwabe L, Dalm S, Schachinger H, Oitzl MS (2008) Chronic stress modulates the use of spatial and stimulus-response learning strategies in mice and man. Neurobiol Learn Mem 90:495-503.

Schwabe L, Tegenthoff M, Hoffken O, Wolf OT (2010a) Concurrent glucocorticoid and noradrenergic activity shifts instrumental behavior from goal-directed to habitual control. J Neurosci 30:8190-8196.

Schwabe L, Schachinger H, de Kloet ER, Oitzl MS (2010b) Corticosteroids operate as a switch between memory systems. J Cogn Neurosci 22:1362-1372.

Schwabe L, Schachinger H, de Kloet ER, Oitzl MS (2010c) Stress impairs spatial but not early stimulus-response learning. Behav Brain Res 213:50-55.

Schwabe L, Tegenthoff M, Hoffken O, Wolf OT (2013) Mineralocorticoid receptor blockade prevents stress-induced modulation of multiple memory systems in the human brain. Biol Psychiatry 74:801-808.

Schwabe L, Oitzl MS, Philippsen C, Richter S, Bohringer A, Wippich W, Schachinger H (2007) Stress modulates the use of spatial versus stimulus-response learning strategies in humans. Learn Mem 14:109-116.

Scoville WB, Milner B (1957) Loss of recent memory after bilateral hippocampal lesions. J Neurol Neurosurg Psychiatry 20:11-21.

Seamans JK, Floresco SB, Phillips AG (1995) Functional differences between the prelimbic and anterior cingulate regions of the rat prefrontal cortex. Behav Neurosci 109:1063-1073.

Semmler A, Hermann S, Mormann F, Weberpals M, Paxian SA, Okulla T, Schafers M, Kummer MP, Klockgether T, Heneka MT (2008) Sepsis causes neuroinflammation and concomitant decrease of cerebral metabolism. J Neuroinflammation 5:38.

Sepulveda MR, Dresselaers T, Vangheluwe P, Everaerts W, Himmelreich U, Mata AM, Wuytack F (2012) Evaluation of manganese uptake and toxicity in mouse brain during continuous MnCl2 administration using osmotic pumps. Contrast Media Mol Imaging 7:426-434.

Shires KL, Aggleton JP (2008) Mapping immediate-early gene activity in the rat after place learning in a water-maze: the importance of matched control conditions. Eur J Neurosci 28:982-996.

Sloot WN, Gramsbergen JB (1994) Axonal transport of manganese and its relevance to selective neurotoxicity in the rat basal ganglia. Brain Res 657:124-132.

Smith PF (1997) Vestibular-hippocampal interactions. Hippocampus 7:465-471.

Soma T, Kurakawa M, Koto D, Fujii H, Okada S, Nagata M, Matsushita T, Kusakabe Y, Yamazaki Y, Murase K (2011) Statistical parametric mapping for effects of verapamil on olfactory connections of rat brain in vivo using manganese-enhanced MR imaging. Magn Reson Med Sci 10:107-119.

Sparta DR, Stamatakis AM, Phillips JL, Hovelso N, van Zessen R, Stuber GD (2011) Construction of implantable optical fibers for long-term optogenetic manipulation of neural circuits. Nat Protoc 7:12-23.

Spiller M, Brown RD, 3rd, Koenig SH, Wolf GL (1988) Longitudinal proton relaxation rates in rabbit tissues after intravenous injection of free and chelated Mn2+. Magn Reson Med 8:293-313.

Squire LR (1986) Mechanisms of memory. Science 232:1612-1619.

Squire LR (1987) The organization and neural substrates of human memory. Int J Neurol 21-22:218-222.

Squire LR (1992) Memory and the hippocampus: a synthesis from findings with rats, monkeys, and humans. Psychol Rev 99:195-231.

Sugai T, Yamamoto R, Yoshimura H, Kato N (2012) Multimodal cross-talk of olfactory and gustatory information in the endopiriform nucleus in rats. Chem Senses 37:681-688.

Sumser A, Mease RA, Sakmann B, Groh A (2017) Organization and somatotopy of corticothalamic projections from L5B in mouse barrel cortex. Proc Natl Acad Sci U S A 114:8853-8858.

Sun XR, Badura A, Pacheco DA, Lynch LA, Schneider ER, Taylor MP, Hogue IB, Enquist LW, Murthy M, Wang SS (2013) Fast GCaMPs for improved tracking of neuronal activity. Nat Commun 4:2170.

Tai YC, Chatziioannou AF, Yang Y, Silverman RW, Meadors K, Siegel S, Newport DF, Stickel JR, Cherry SR (2003) MicroPET II: design, development and initial performance of an improved microPET scanner for small-animal imaging. Phys Med Biol 48:1519-1537.

Takeda A, Kodama Y, Ishiwatari S, Okada S (1998) Manganese transport in the neural circuit of rat CNS. Brain Res Bull 45:149-152.

Tambalo S, Daducci A, Fiorini S, Boschi F, Mariani M, Marinone M, Sbarbati A, Marzola P (2009) Experimental protocol for activation-induced manganese-enhanced MRI (AIM-MRI) based on quantitative determination of Mn content in rat brain by fast T1 mapping. Magn Reson Med 62:1080-1084.

Tang X, Wu D, Gu LH, Nie BB, Qi XY, Wang YJ, Wu FF, Li XL, Bai F, Chen XC, Xu L, Ren QG, Zhang ZJ (2016) Spatial learning and memory impairments are associated with increased neuronal activity in 5XFAD mouse as measured by manganese-enhanced magnetic resonance imaging. Oncotarget 7:57556-57570.

Taube JS (1998) Head direction cells and the neurophysiological basis for a sense of direction. Prog Neurobiol 55:225-256.

Taube JS, Wang SS, Kim SY, Frohardt RJ (2013) Updating of the spatial reference frame of head direction cells in response to locomotion in the vertical plane. J Neurophysiol 109:873-888.

Thierry AM, Gioanni Y, Degenetais E, Glowinski J (2000) Hippocampo-prefrontal cortex pathway: anatomical and electrophysiological characteristics. Hippocampus 10:411-419.

Tian L, Hires SA, Looger LL (2012) Imaging neuronal activity with genetically encoded calcium indicators. Cold Spring Harb Protoc 2012:647-656.

Tindemans I, Verhoye M, Balthazart J, Van Der Linden A (2003) In vivo dynamic ME-MRI reveals differential functional responses of RA- and area X-projecting neurons in the HVC of canaries exposed to conspecific song. Eur J Neurosci 18:3352-3360.

Tolman EC, Ritchie BF, Kalish D (1946) Studies in spatial learning; place learning versus response learning. J Exp Psychol 36:221-229.

Tovote P, Fadok JP, Luthi A (2015) Neuronal circuits for fear and anxiety. Nat Rev Neurosci 16:317-331.

Trageser JC, Burke KA, Masri R, Li Y, Sellers L, Keller A (2006) State-dependent gating of sensory inputs by zona incerta. J Neurophysiol 96:1456-1463.

Tukker JJ, Tang Q, Burgalossi A, Brecht M (2015) Head-Directional Tuning and Theta Modulation of Anatomically Identified Neurons in the Presubiculum. J Neurosci 35:15391-15395.

Van der Linden A, Van Meir V, Tindemans I, Verhoye M, Balthazart J (2004) Applications of manganese-enhanced magnetic resonance imaging (MEMRI) to image brain plasticity in song birds. NMR Biomed 17:602-612.

Vedder LC, Miller AMP, Harrison MB, Smith DM (2017) Retrosplenial Cortical Neurons Encode Navigational Cues, Trajectories and Reward Locations During Goal Directed Navigation. Cereb Cortex 27:3713-3723.

Veinante P, Lavallee P, Deschenes M (2000) Corticothalamic projections from layer 5 of the vibrissal barrel cortex in the rat. J Comp Neurol 424:197-204.

Vetere G, Kenney JW, Tran LM, Xia F, Steadman PE, Parkinson J, Josselyn SA, Frankland PW (2017) Chemogenetic Interrogation of a Brain-wide Fear Memory Network in Mice. Neuron 94:363-374 e364.

Vogel S, Fernandez G, Joels M, Schwabe L (2016) Cognitive Adaptation under Stress: A Case for the Mineralocorticoid Receptor. Trends Cogn Sci 20:192-203.

Vogel S, Klumpers F, Krugers HJ, Fang Z, Oplaat KT, Oitzl MS, Joels M, Fernandez G (2015) Blocking the mineralocorticoid receptor in humans prevents the stress-induced enhancement of centromedial amygdala connectivity with the dorsal striatum. Neuropsychopharmacology 40:947-956.

Wang L, Lu H, Brown PL, Rea W, Vaupel B, Yang Y, Stein E, Shepard PD (2015) Manganese-Enhanced MRI Reflects Both Activity-Independent and Activity-Dependent Uptake within the Rat Habenulomesencephalic Pathway. PLoS One 10:e0127773.

Wang S, Lees GJ, Rosengren LE, Karlsson JE, Stigbrand T, Hamberger A, Haglid KG (1991) The effect of an N-methyl-D-aspartate lesion in the hippocampus on glial and neuronal marker proteins. Brain Res 541:334-341.

Watanabe T, Radulovic J, Spiess J, Natt O, Boretius S, Frahm J, Michaelis T (2004) In vivo 3D MRI staining of the mouse hippocampal system using intracerebral injection of MnCl2. Neuroimage 22:860-867.

Weinstein EA, Ordonez AA, DeMarco VP, Murawski AM, Pokkali S, MacDonald EM, Klunk M, Mease RC, Pomper MG, Jain SK (2014) Imaging Enterobacteriaceae infection in vivo with 18F-fluorodeoxysorbitol positron emission tomography. Sci Transl Med 6:259ra146.

Welker E, Hoogland PV, Van der Loos H (1988) Organization of feedback and feedforward projections of the barrel cortex: a PHA-L study in the mouse. Exp Brain Res 73:411-435.

Wenk GL (2001) Assessment of spatial memory. Curr Protoc Toxicol Chapter 11:Unit11 13.

Wheeler AL, Teixeira CM, Wang AH, Xiong X, Kovacevic N, Lerch JP, McIntosh AR, Parkinson J, Frankland PW (2013) Identification of a functional connectome for long-term fear memory in mice. PLoS Comput Biol 9:e1002853.

White EL, DeAmicis RA (1977) Afferent and efferent projections of the region in mouse SmL cortex which contains the posteromedial barrel subfield. J Comp Neurol 175:455-482.

White MD, Milne RV, Nolan MF (2011) A Molecular Toolbox for Rapid Generation of Viral Vectors to Up- or Down-Regulate Neuronal Gene Expression in vivo. Front Mol Neurosci 4:8.

Whitlock JR, Sutherland RJ, Witter MP, Moser MB, Moser EI (2008) Navigating from hippocampus to parietal cortex. Proc Natl Acad Sci U S A 105:14755-14762.

Wiig KA, Bilkey DK (1994) The effects of perirhinal cortical lesions on spatial reference memory in the rat. Behav Brain Res 63:101-109.

Wiig KA, Bilkey DK (1995) Lesions of rat perirhinal cortex exacerbate the memory deficit observed following damage to the fimbria-fornix. Behav Neurosci 109:620-630.

Winn P, Tarbuck A, Dunnett SB (1984) Ibotenic acid lesions of the lateral hypothalamus: comparison with the electrolytic lesion syndrome. Neuroscience 12:225-240.

Woo CW, Krishnan A, Wager TD (2014) Cluster-extent based thresholding in fMRI analyses: pitfalls and recommendations. Neuroimage 91:412-419.

Wotjak CT, Pape HC (2013) Neuronal circuits of fear memory and fear extinction. Neuroforum 19:92-102.

Wright AK, Norrie L, Arbuthnott GW (2000) Corticofugal axons from adjacent 'barrel' columns of rat somatosensory cortex: cortical and thalamic terminal patterns. J Anat 196 (Pt 3):379-390.

Yang PF, Chen DY, Hu JW, Chen JH, Yen CT (2011) Functional tracing of medial nociceptive pathways using activity-dependent manganese-enhanced MRI. Pain 152:194-203.

Yasuda R, Nimchinsky EA, Scheuss V, Pologruto TA, Oertner TG, Sabatini BL, Svoboda K (2004) Imaging calcium concentration dynamics in small neuronal compartments. Sci STKE 2004:pl5.

Yu X, Wadghiri YZ, Sanes DH, Turnbull DH (2005) In vivo auditory brain mapping in mice with Mn-enhanced MRI. Nat Neurosci 8:961-968.

Yu X, Zou J, Babb JS, Johnson G, Sanes DH, Turnbull DH (2008) Statistical mapping of sound-evoked activity in the mouse auditory midbrain using Mn-enhanced MRI. Neuroimage 39:223-230.

Zakiewicz IM, Bjaalie JG, Leergaard TB (2014) Brain-wide map of efferent projections from rat barrel cortex. Front Neuroinform 8:5.

ACKNOWLEDGMENTS

Suellen de Almeida Corrêa

ALMEIDA-CORREA, S.; ALMEIDA-CORREA, SUELLEN.

Address: Max-Planck Institute of Psychiatry
Kraepelinstrasse 2-10, 80804 Munich - Germany
Phone: +49 (0) 89-30622-604
suellen_almeida@psych.mpg.de
suellenac@gmail.com

EDUCATION

2014 – 2018 - Doctorate in Neurobiology (Dr. rer. nat.) *magna cum laude*

Max-Planck-Institut für Psychiatrie (MPI-P) and Ludwig-Maximilians-Universität München (LMU), Germany

Title: *In vivo* identification of brain structures functionally involved in spatial learning and strategy switch in mice

Supervisor: Dr. Carsten T. Wotjak

Fellow of: Coordination of Improvement of Higher Education Personnel, CAPES, Brazil

2011 – 2013 - Master in Biochemistry

Federal University of Rio de Janeiro, UFRJ, Brazil

Title: Role of calcineurin in different components of the extinction of aversive memories in mice.

Supervisor: Dr. Olavo Bohrer Amaral

Fellow of: National Council for Scientific and Technological Development, CNPq, Brazil

2006 – 2011 – Bachelor Degree in Biomedicine

Federal University of the State of Rio de Janeiro, UNIRIO, Brazil

Title: Effects of calcineurin inhibition on different aspects of the extinction of aversive memories in mice

Supervisor: Dr. Olavo Bohrer Amaral

Fellow of: National Council for Scientific and Technological Development, CNPq, Brazil

PUBLICATIONS

ALMEIDA-CORRÊA, SUELLEN; CZISCH, MICHAEL; WOTJAK, CARSTEN T. *In vivo* visualization of active polysynaptic circuits with longitudinal manganese-enhanced MRI (MEMRI). Frontiers in Neural Circuits, v. 12, article 42, 2018.

BEDENK, BENEDIKT T.; **ALMEIDA-CORRÊA, SUELLEN**; JURIK, ANGELA; DEDIC, NINA; GRÜNECKER, BARBARA; GENEWSKY, ANDREAS; KALTWASSER, SEBASTIAN F.; RIEBE, CAITLIN J.; DEUSSING, JAN M.; CZISCH, MICHAEL; WOTJAK, CARSTEN T. Mn^{2+} dynamics in manganese-enhanced MRI (MEMRI): $CA_{v1.2}$ channel mediated uptake and preferential accumulation in projection terminals. NeuroImage,
v. 169, p. 374-382, 2018.

REICHEL, JUDITH M.; BEDENK, BENEDIKT T.; GASSEN, NILS C.; HAFNER, K.; BURA, S. ANDREEA; **ALMEIDA-CORRÊA, SUELLEN**; GENEWSKY, ANDREAS; DEDIC, NINA; GIESERT, F.; AGARWAL, AMIT; NAVE, K.-A.; REIN, THEO; CZISCH, MICHAEL; DEUSSING, JAN M. AND WOTJAK, CARSTEN T. Beware of your Cre-Ation: lacZ expression impairs neuronal integrity and hippocampus-dependent memory. Hippocampus, v. 26, issue 10, p. 1250–1264, 2016.

ALMEIDA-CORRÊA, SUELLEN; MOULIN, THIAGO C.; CARNEIRO, CLARISSA F. D.; GONÇALVES, MARINA M. C.; JUNQUEIRA, LARA S.; AMARAL, OLAVO B. Calcineurin inhibition blocks within-, but not between-session fear extinction in mice. Learning & Memory (Cold Spring Harbor Online), v. 22, p. 159-169, 2015.

ALMEIDA-CORRÊA, SUELLEN; AMARAL, OLAVO B. . Memory labilization in reconsolidation and extinction - Evidence for a common plasticity system?. Journal of Physiology (Paris), v. 108, p. 292-306, 2014.

LEO, LUCIANA M.; **ALMEIDA-CORRÊA, SUELLEN**; CANETTI, CLAUDIO A.; AMARAL, OLAVO B.; BOZZA, FERNANDO A.; PAMPLONA, FABRICIO A. Age-Dependent Relevance of Endogenous 5-Lipoxygenase Derivatives in Anxiety-Like Behavior in Mice. Plos One, v. 9, p. e85009, 2014.

AWARDS AND TITLES

2018   **Travel Award for Outstanding Students from Universities Abroad** for pre-application funded visits of the Weizmann Institute of Science, Israel.

2017   **Bilateral German-Brazilian grant** for the organization of two workshops on "Neural Basis of Stress, Fear and Anxiety", by BAYLAT (Germany) and FAPESP (Brazil). (Co-applicant)

Travel grant for the ECNP Workshop for Junior Scientists in Europe in Nice, France, by European College of Neuropsychopharmacology (ECNP).

2016   **EMCCS PERC/IBRO Travel grant / best poster prize** at the EMCCS-EBBS FENS satellite meeting in Copenhagen, by IBRO.

Travel grant for the Hotchkiss Brain Institute (HBI) – Munich Center for Neuroscience (MCN) partnership meeting in Calgary, Canada, by HBI-MCN, Canada/Germany.

2014   **Donders Summer School "Stress & Cognition" - Poster Award**, Donders Institute for Brain, Cognition and Behavior – Nijmegen, The Netherlands.

Full PhD fellowship for doctoral studies abroad, by CAPES (Brazil).

2013   **Master in Science** - Biochemistry (Focus on Neuroscience), UFRJ, Brazil.

Honor mention at the XXXVII Conference of the Brazilian Society of Neuroscience and Behavior, by Brazilian Society of Neuroscience and Behavior (SBNeC).

Travel grant for short internship / scientific visit to Max Planck Institute of Psychiatry (Munich, Germany), by IBqM – UFRJ, Brazil.

2012   **Travel grant** for the 8th FENS Forum of Neuroscience (Barcelona, Spain), by IBqM – UFRJ, Brazil.

2011   **Bachelor degree** in Biomedicine, UNIRIO, Brazil.